University of Strathclyde
Department of Naval Architecture and Marine Engineering

Estimation of Residual Stresses in Marine Structures

By XING SUN

Supervised By: Professor Nigel Barltrop

A thesis presented in fulfillment of requirements for the
Degree of Doctor of Philosophy

Glasgow, United Kingdom
March 2013

This thesis is the result of the author's original research. It has been composed by the author and has not been previously submitted for examination which has led to the award of a degree.

Signed:

Date: 11th March 2013

Acknowledgements:

First of all, I wish to express my limitless thank to my supervisor, Professor Nigel Barltrop. He made me realised that a Ph.D research work is a kind of training in how to think, present an idea, argue, debate, listen to other people, find a problem, formulate and solve it, etc. As such, I felt that it has been a painful process, requiring dedication, persistence, and patience to undertake it. Professor Barltrop always encouraged me when I felt "low" in conducting the research. He guided me through the research with his extensive knowledge, experience and ever optimism. Without him, this thesis could never have been accomplished.

I also want to express my limitless thank to my department for the financial support during my second and third year of my PHD study.

I express sincere gratitude to Professor Peilin Zhou who offered me the opportunity to study at University of Strathclyde and opened my eyes to the wider world and gave countless encouragement and full support throughout.

Special thank to Professor John Goldak and my colleagues at the Department of Mechanical and Aerospacing Engineering in Carleton University, Canada, for giving me the opportunity to visit his department and using VrWeld software. Another thanks to IMarEST and Main's Family for the financial support during my visiting in Canada.

I warmly thank all my colleagues, in particular Dr. Li Xu, Dr. Qiuxin Gao, Dr. Hao Cui, Dr. Nana Yang, Mr. Wei Jin, for their valuable advice and friendship during this period.

Finally, I would like to express my deep gratitude to my parents in China who have given me endless support and encouragement. I would not be able to succeed without their support.

Abstract

A finite element model that is capable of simulating the thermo-mechanical welding process was developed by using full thermal-elasto-plastic computational analysis and validated by comparison with experimental data. It shows that distortions predicted by the finite element model agree well with measured data from previous literature and that the numerically obtained residual stress distribution is compared and agreed by both ANSYS and VrWeld software. After that, a simple method for predicting butt-welding residual stresses based on force and moment equilibrium was derived in this section. The results calculated from this simple method were a good match with the FE results. Then the author performed detailed analysis for the distribution of transverse and longitudinal residual stresses of 2D butt welding process by using 3D elements, which illustrated how the butt-welding residual stresses were distributed and accumulated during the welding process and how the boundary conditions affect the final results. A detailed parametric study for butt welding residual stresses based on 2D butt-welding by using 3D element was demonstrated. The factors carried out in the parametric study involved cut-off temperature effect, welding power effect, welding velocity effect, plate length effect and plate width effect. Lastly, the author also presented a simulation and an optimization of welding sequences for residual stress and distortion of a typical, fatigue sensitive, ship's side shell connection detail under different welding sequences.

Table of Contents

List of Figures:

List of Tables:

List of Symbols

A	Section area of a beam
a	Breadth of Double Ellipsoid Model
$B^{t+\Delta t}$	The matrix of symmetric physical gradient operator
b	Depth of Double Ellipsoid Model
C	Specific heat
c_f	Front length of Double Ellipsoid Model
c_r	Rear length of Double Ellipsoid Model
[D]	The conduction matrix
D_{el}	The fourth order elasticity tensor
d	The thickness of the plate,
E	Young's modulus
F	Multiplicative deformation gradient
$F_{\Delta V}$	Thermal expansion and phase changes
F_{pl}	Visco-plastic deformation
F_{el}	Elastic deformation
F_1	The shrinkage force at solidified element part
F_2	The shrinkage force at non-solidified element part
$F_{Longitudinal}$·	Longitudinal shrinkage force
$F_{Transverse}$	Transverse shrinkage force
f	Body force per unit volume
f_f	The fractions of heat deposited in the front
f_r	The fractions of heat deposited in the rear
h	Specific enthalpy
h_c	Convection coefficient
I	Arc current
K_T	Tangent stiffness matrix
K_0	The first kind, zero order Bessel Function
K_B	Stiffness of a beam
K_S	Stiffness of a spring
K_{xx}	The conductivity in the x direction
K_{yy}	The conductivity in the y direction
K_{zz}	The conductivity in the z direction

k_w	Geometric parameter dependent on the shape of fusion zone
L	Length of a beam
L_S	Length of solidified elements
L_D	Length of non-solidified elements
$M_{Longitudinal}$·	Longitudinal bending moment
$M_{Transverse}$	Transverse bending moment
Q	Total heat power input
$\mathbf{q}$	Boundary flux
q_0	Maximum heat flux in the welding pool
$q(x,y,z,t)$	Double Ellipsoid heat source power
$q_s(r)$	Gaussian heat source power
$\{q_{hf}\}$	Heat Flux Vector (W/m^2)
q_{vol}	Internal heat generation rate per unit volume (J/m^3)
R	The radial parameter
$R^{t+\Delta t}$	Matrix of basis functions
r	Distance between current position and the origin of coordinates
∇T	Temperature difference
$T_{ambient}$	Ambient temperature
$T^{t+\Delta t}$	The surface traction exerted
T	Temperature (K)
T_0	The initial temperature and
t	Time
U	Arc voltage
dU	Vector of nodal displacement increment
v	Speed of heat source
$\{v\}^T = \{v_x\ v_y\ v_z\}$	Velocity vector for mass transport of heat
$\frac{s}{t_0}$	The relative depth of penetration of the weld
$\frac{b}{t_0}$	The relative width of the fusion zone on the surface
η	Arc efficiency
τ	Lag time to define the position of the heat source
ε_T	Total strain
ε_{th}	Thermal strain

ε_e	Elastic strain
ε_p	Plastic strain
σ	Cauchy stress tensor
σ_y	Yield stress
σ_{XX}	Nominal stress in x direction
σ_{YY}	Nominal stress in y direction
σ_{ZZ}	Nominal stress in z direction
σ_{XY}	Shear stress in xy plane
σ_{YZ}	Shear stress in yz plane
σ_{XZ}	Shear stress in xz plane
$(\sigma_1, \sigma_2, \sigma_3)$	Principal stresses
$\{\nabla\}^T = \{\frac{\partial}{\partial x}, \frac{\partial}{\partial y}, \frac{\partial}{\partial t}\}$	Vector Operator
Γ	The boundary
Ω.	The domain
ρ	Density
λ	The thermal conductivity
r_k	Residual vector
θ	The transverse angular deformation

Chapter 1 Introduction

1.1 Overview and Background

1.1.1 Brief Overview

Shipping is one of the main methods of transportation. The technology of shipbuilding and through-life management has developed significantly during the last hundred years. Methods of fabrication change all the time. During the last century, the shipbuilding time has decreased from four years to eight weeks, due to the introduction of several important innovations. First of all, from the middle of 1930s, welding was introduced as a new joining method in ship construction instead of riveted joints. Together with the introduction of prefabrication techniques, it has accelerated ship production by about three times.

A large number of complicated welded joints can be found in marine structures, and during their operations, these details are subjected cyclic loads caused by the irregular waves, the propulsion systems and changes in the loading conditions. In addition there are residual stresses from both the initial fabrication and later repair work. It is also standard practise in ship and offshore building that a complete structure is first of all built in separate modules before they are connected in the final building phase. The connection of two adjacent modules introduces residual stresses, which often contribute to fatigue cracking at the point of connection. Local stress concentrations at connections between longitudinal stiffeners and web frames are always found, which will also encourage fatigue cracking. So new friendly construction and more fatigue resistant designs are always of interest.

The fracture of the early welded 'Liberty' ships during 1940s made people pay attention to preventing fracture and fatigue failures. In the last decades, a significant insight has been gained in fatigue and fracture in various types of structures, including ships. Physical models for the description of many common fatigue cracks have been developed and many experiment works have been carried out in order to verify and support these models. However, no matter the efforts made in this subject, cracking

problems still frequently happen in marine structures today due to the poor alignment and welding of structures during fabrication.

1.1.2 Effect of Welding Residual Stresses

Some studies suggest that residual stresses are more responsible for fatigue crack growth than any other factor (Wästberg et al, 2006). For example, when Bussu and Irving (2003) investigated the effects of weld residual stresses on the propagation of fatigue cracks in FSW 2024-T351 joints, they found that crack growth behaviour in the Friction Stir Welds (FSW) joints was generally dominated by the weld residual stresses and that microstructure and hardness changes in FSW's had a minor influence. A similar investigation by John et al (2003) in FSW aluminium 7050-T7451 and titanium Ti–6Al–4V revealed that residual stresses produce large effects on the near-threshold fatigue crack growth. (Note: For structural stress and typical welding methods, the residual stress may not dominate the fatigue behaviour.

Sobczyk and Trebicki (2004) investigated the effect of random residual stresses on fatigue crack growth. First, they propose a probabilistic model for residual stresses and then they show how the basic statistical information on the residual stress distribution can be included into the evaluation of the residual stress intensity factor Kr(a) and then into the crack growth equations as well as in the life-time assessment.

High reliability, which is the key aim in designing these structures, is compromised by the presence of these stresses and the uncertainty in their estimation. Recent research has even suggested that in some critical details the residual stresses may be beneficial and it may be possible to use particular welding sequences to obtain this beneficial stress pattern and subsequently increased structural reliability. Fricke et al (2004a) on discovering the impact these residual compressive stresses had on his investigation (which were rather beneficial) also suggested that more research should be undertaken to harness them. Also the committee's report on fatigue and fracture during the 16th international ship and offshore structures congress held on 20-25 August, 2006 at Southampton, UK concluded that one important area where more research is needed is a better understanding of the influence of residual stresses and how to estimate them and understand how they evolve during variable amplitude loading and with time and not

least how to measure them. The committee also agreed there was need for more research where effects as welding sequence, detailed geometry, welding parameters and shakedown of residual stresses are all expected to be significant (Wartberg 2006)

1.2 Objective and Scope of Work

The overall scope of this study aims to develop a program for the estimation of residual stresses in marine structures (ships and floating offshore structures) so that decision making during initial design and their through-life management can be better informed, leading to structures which can be kept adequately (though not excessively) safe during their required life.

It is important to predict the residual stresses, both in a new and a repaired structure, and then guidance can be offered on how best to repair an old structure or design the welded connections and welding sequences of new ones. For example, the residual stresses in the old plate may become very small due to the shake-down effect, then keep the old structure instead welding a new one, will be a better choice.

This research will focus on estimating these residual stresses, how they are modified during the different geometry size, how they interact with welding defects, and their overall effect on the structural reliability of the hull of a ship or FPSO.

1.3 Structure of the Thesis

The study is subdivided into different sections dealing with different aspects of welding residual stresses, and organized in seven chapters.

In chapter two, a general review of the phenomena leading to welding residual stresses is presented. Present state of the art analytical and finite element thermo-elasto-plastic analysis related to the prediction of thermal transients and welding induced stresses are outlined. In particular, the review concentrated on work done to predict welding residual stresses using both simplified analysis and the full thermal-elasto-plastic computational analysis.

In chapter three, a finite element model that is capable of simulating the thermo-mechanical welding process was developed by using full thermal-elasto-plastic computational analysis and validated by comparison with experimental data. It shows that distortions predicted by the finite element model agree well with measured data from previous literature and that the numerically obtained residual stress distribution is compared and agreed by both ANSYS (www.ansys.com) and VrWeld software (Goldak J. , Vr Software Suite). In this model, the temperature dependent material properties were used to take the microstructure, material melting and phase changing effect into account; the element activate and deactivate technique was implemented in both thermal and mechanical simulations and is used for making the simulation more accurate and closer to practical. It is found that the advanced mesh technique and subdomain method is capable of accelerating the simulation speed dramatically by comparing the calculation speed of ANSYS and VrWeld.

In chapter four, the author performs a detailed analysis for the distribution of transverse and longitudinal residual stresses of 2D butt welding process by using 3D elements, which deeply illustrated how the butt-welding residual stresses were distributed and accumulated during the welding process and how the boundary conditions affect the final results.

Chapter five demonstrates a detailed parametric study for butt welding residual stresses based on 2D butt-welding by using 3D element, where the simulation technology used is the same as the model in Chapter 4. The factors carried out in the parametric study involved cut-off temperature effect, welding power effect, welding velocity effect, plate length effect and plate width effect.

Chapter six offers a simulation and an optimization of welding sequences for residual stress and distortion of a typical ship's side shell connection detail, which often suffers fatigue damage, under different welding sequences. The advanced welding simulation techniques were used, which were the same as introduced in Chapter 3.

Finally, chapter seven gives conclusions and recommendations for future work.

Chapter 2 Literature Review & Theoretical Background

There is a lot of literature about research work on computational welding mechanisms. The application of computational techniques in the simulation of welding processes has been an important topic of research since the early development of numerical methods. Because the welding process involves different types and different physical phenomena, there are several fields of application, depending on which aspect of the welding process needs to be predicted. This review is focusing on the state of art of modeling welding processes for the prediction of welding residual stresses and distortions. The application of the modeling techniques developed through this thesis focused on the Arc Welding Process, which is the main welding technique used in marine structures. But the technique, which has been used in the simulation, can be also carried out on other types of welding processes, such as laser welding and friction stir welding, due to the modeling techniques are relevant to a range of welding processes.

With the development of computer technology, numerical analysis becomes a powerful tool to help people to understand, design and predict welded structures. One of the prevailing numerical methods is the finite element method (FEM). Due to their huge capability to store, manage and process large amounts of data, computers have become necessary engineering tools, which allow data and computation to be processed in a cost and time efficient way. Modeling and simulation have become an essential stage in the design process of many engineering applications. With the aid of computer simulation, welding engineers can reduce the costs and time in testing process or establish optimum welding conditions.

Before the 1980s, when the finite element method (FEM) became popular for thermal analysis in welds, the transient temperature field in welds was usually not predicted, while some researchers (Rykalin R. R., 1974) (Hansbo, 1946) computed the steady state temperature field by solving the heat equation for moving heat sources. Today, with help of powerful computers, FEM is widely used for simulating the transient temperature field in welds. The transient Lagrangian formulation allowed complex geometry, and non-linear equations. Total and updated Lagrangian are two ways to look at the same conservation laws (mass, impulse, energy) - one uses material coordinates while the other uses space coordinates. Many successful three-dimensional transient analyses on welds

have been reported using Lagrangian FEM formulations (Goldak J. A., 1989) (Oddy, 1987).

Finite element techniques permit complex geometry and temperature dependent material properties to be taken into account. Various welding processes can be simulated by changing the welding procedure parameters, (such as preheat conditions, heat input, weld type, welding speed, and imposed cooling patterns, etc.), and materials.

In large welded structures the temperature field varies dramatically from huge temperature change around the weld pool to basically no temperature change in the area further than a certain thermal distance away from the weld pool (depending on thermal diffusivity and welding speed). For a pure thermal analysis, only a relatively small region near the weld needs to be analyzed. Therefore the part of the structure that has little or no change in temperature during welding can be excluded from the solving domain. In contrast, in a thermal-stress analysis, the complete structure being welded is in a quasi-static equilibrium and the stresses generated by the welding process will travel through the entire structure. If the whole welded assembly is not included in the stress analysis, it is difficult to define boundary conditions to take the parts, which are not in the domain, into account.

During the welding process, there exist many complex physical, chemical and metallurgical phenomena. An ideal simulation will consider each of these phenomena in relation with the others. However, this will make the simulation very complicated and difficult to achieve. A practical approach is to make some reasonable simplifications, and gradually enrich it according to computer capability and mathematical models.

One of the ways to simplify the simulation is to seperate the whole welding process into several problems, which deals with each problem at a time, but connect and couple them by data flows. For computational welding mechanics, the following topics should be investigated:

- Weld pool model for the geometry and temperature distribution of a weld pool;

- Thermal analysis for heat transfer;

- Phase transformation analysis for microstructure evolution;

- Stress analysis for plastic deformation, residual stress and distortion.

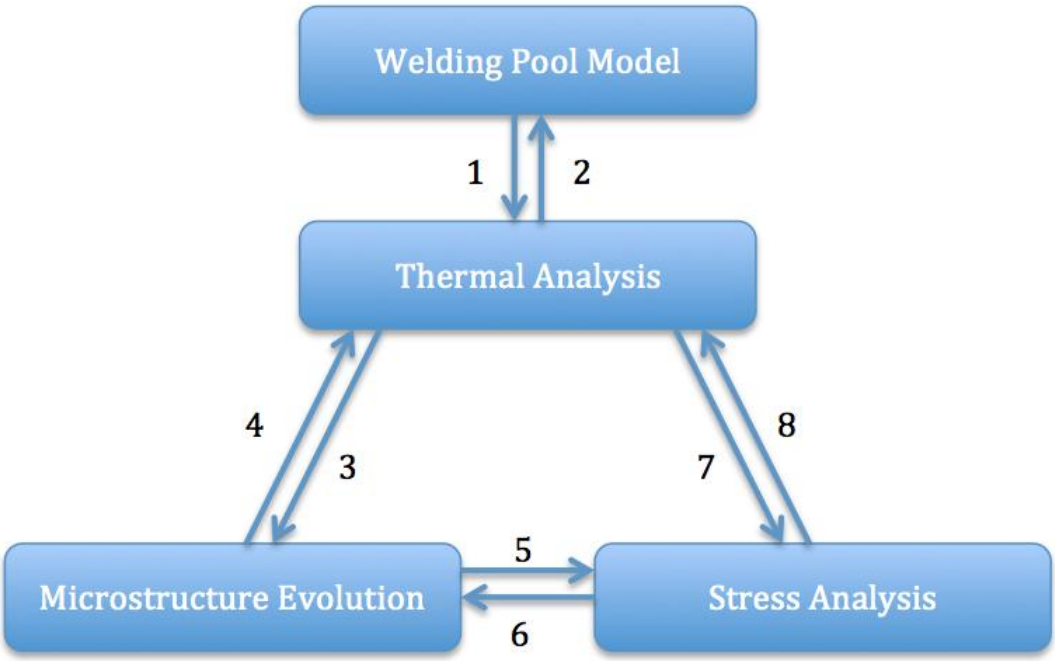

Figure 2-1: Data flows between different problems in welding analysis

Figure 2-1 describes the coupling between the different problems in the simulation of welding. The dominant coupling in welding is shown with odd number and the secondary coupling is shown with even number. The effect of temperature on the microstructure and thermal stress is dominant. Also phase transformations can dominate the stress analysis (Goldak J. A., 1989) (Oddy, 1987).

Details of data flows are explained as the followings:

- Process 1 passes the heat input calculated from the weld pool model to the thermal analysis

- Some weld pool models may need the temperature field or boundary conditions from the thermal analysis that could be done in process 2.

- Process 3 passes the temperature field from thermal analysis to microstructure evolution because it depends on temperature history.

- Each phase transformation can have an associated latent heat that could go from microstructure evolution to thermal analysis by process 4.

- The results of microstructure evolution, such as material properties (specific volume, yield stress and Young's modulus, etc.) and phase fractions, need to be passed to stress analysis by process 5.

- Process 6 could be needed if microstructure evolution depends on the mechanical deformation or stress field (stress dependent phase transformation, SDPT).

- Process 7 passes the temperature field from thermal analysis to stress analysis to account for the thermal expansion.

- The displacement field or deformed geometry and the heat generated by plastic deformation as a heat source could be passed from stress analysis to thermal analysis by process 8.

When the data flows from one problem to another problem, if the meshes of the two problems are the same, data just needs to be copied. If the meshes of the two problems are different, data needs to be mapped.

The primary step in welding simulation is getting an accurate result of temperature distribution throughout the whole welding process. There have been already both analytical and numerical methods developed for that, and these methods have also been validated by experiment results. But there are still some unknown factors involved in these techniques, such as material properties at high temperature and how to apply a proper boundary condition.

Because the welding process covered so many physical phenomena, the simulation needed to couple all of these factors, will increase the computational requirement. Though the computational power has been improved dramatically today, it is still not feasible to carry out such complex welding analysis. For this reason, the most important thing is to consider which parts of the welding process can be simplified, uncoupled and which assumptions are valid in order to calculate residual stresses and distortions. So there has been an amount of research work on the development of simplified methods. It has been proved that some of the coupling could be ignored. Lindgren, followed Boley and Weiner (Boley & Weiner, 1960), stated that the effect of metallurgical generated plastic heat is small while compare to the weld heat input. Furthermore, it is also feasible to neglect the influence on the changing geometry on the thermal behavior. In all couplings, the thermal dilatation, which is the sum of the thermal expansion and the volume changes due to phase transformations, is the main driver of the welding residual stresses. The effect on stresses resulting from phase changes is also often ignored; and with the exception of the thermal dilation, the material properties are usually a function of the temperature. Further simplifications can be performed by uncoupling the thermal transients and thermal strains, which can be called 'Indirect Coupling Method', it means two different analysis will be performed, thermal analysis followed by a structural elasto-plastic analysis. Because the effect of structure analysis on thermal analysis is relatively very small, the 'Indirect Coupling Method' can give reasonable results when compared to the full-coupled analysis. These methods have greatly reduced the computational efforts, and make it is possible to apply the analysis to relatively large structure types.

2.1 Thermal Analysis

There is no doubt that the high and uneven temperature generated during both heating and cooling in the welding process is the main driving force for the development of residual stresses and distortions. Therefore, the methods of simulating the thermal response during the welding process need to be investigated. There are many ways, ranging from the early analytical solution by Rosenthal (Rosenthal, 1946), Rykalin (Rykalin N. N., 1947) and Well (Well, 1952), to the finite element based methods, which was recently reviewed by Lindgren (Lindgen, 2001).

2.1.1 Fundamentals of Heat Flow

The heat flow equations are all based on first law of thermodynamics (Carslaw & Jaeger, 1950) (Chapman, 1987) (Burghardt & Harbach, 1993). The first law of thermodynamics states that the thermal energy is conserved within a control volume, and the relationship between the heat generation rate and the volume's temperature is described in Equation 2-1:

$$\rho c\left(\frac{\partial T}{\partial t}+\{v\}^T\nabla T\right)+\nabla^T\{q_{hf}\}=\frac{dq_{vol}}{dt}$$

Equation 2-1

Where:

$T=T(x,y,z,t)$	Temperature (K)
$\{\nabla\}^T=\{\frac{\partial}{\partial x},\frac{\partial}{\partial y},\frac{\partial}{\partial t}\}$	Vector Operator
$\{v\}^T=\{v_x\ v_y\ v_z\}$	Velocity vector for mass transport of heat
$\{q_{hf}\}$	Heat Flux Vector (W/m^2)
q_{vol}	Internal heat generation rate per unit volume (J/m^3)

According to the Fourier's law, the relationship between the heat flux vector to the gradients, which is shown in Equation 2-2:

$$\{q_{hf}\}=-[D]\{\nabla\}T$$

Equation 2-2

Where [D] is the conduction matrix:

$$[D]=\begin{matrix}K_{xx} & 0 & 0\\ 0 & K_{yy} & 0\\ 0 & 0 & K_{zz}\end{matrix}$$

K_{xx}, K_{yy} and K_{zz} is the conductivity in the x, y and z directions. Combining the above equations; the general equation is given as Equation 2-3:

$$\rho c\left(\frac{\partial T}{\partial t}+v_x\frac{\partial T}{\partial x}+v_y\frac{\partial T}{\partial y}+v_z\frac{\partial T}{\partial z}\right)=\frac{dq_{vol}}{dt}+\frac{\partial}{\partial x}\left(K_{xx}\frac{\partial T}{\partial x}\right)+\frac{\partial}{\partial y}\left(K_{yy}\frac{\partial T}{\partial y}\right)+\frac{\partial}{\partial z}\left(K_{zz}\frac{\partial T}{\partial z}\right)$$

Equation 2-3

2.1.2 Quasi-Stationary Thermal Analytical Solution

Some early studies provided analytical solutions of the thermal conduction for a moving heat source (Easterling, 1993), the equation is shown as Equation 2-4:

$$\frac{\partial^2 T}{\partial x^2}+\frac{\partial^2 T}{\partial y^2}+\frac{\partial^2 T}{\partial z^2}=2\lambda\frac{\partial^2 T}{\partial t^2}$$

Equation 2-4

Where T is the temperature, x, y and z is three-dimensional the coordinates, t is the time and λ is the thermal conductivity. Rosenthal (Rosenthal, 1946) derived linear, two-dimensional and three-dimensional temperature distribution pattern, which can be written as Equation 2-5 & Equation 2-6:

$$T-T_0=\frac{q}{2\pi\lambda dv}e^{\frac{v\xi}{2a}}K_0\left(\frac{vr}{2a}\right)$$

Equation 2-5

$$T-T_0=\frac{q}{2\pi\lambda rv}e^{\frac{-v\xi}{2a}}e^{\frac{-vr}{2a}}$$

Equation 2-6

Where K_0 is the first kind, zero order Bessel Function, d is the thickness of the plate, t is time, T_0 is the initial temperature and r is the distance between the current position and the origin of coordinates, which is defined as Equation 2-7:

$$r=\sqrt{\xi^2+y^2+z^2}$$

Equation 2-7

The equations above have also considered the heat input q and the thermal diffusivity a, and the ξ term is defined as Equation 2-8:

$$\xi = x - vt$$

Equation 2-8

Where v is the speed of heat source, and it is in the welding traveling direction; this analytical solution used a fixed coordinate system to represent the moving heat source, so that the following assumptions have been made:

- The size of the plate is assumed to be infinite
- The solution is assumed to be quasi-stationary
- Material properties are assumed to be a constant, which don't vary with temperatures

The utilization of these equations is dependent on the thickness of the plate relative to the other sizes (length or width). If the size of thickness can be compared to other sizes, the three-dimensional solution may be used; in contrast, if the thickness of the plate is relatively small, the two dimensional equation can be used. The Figure 2-2 shows an example of the plot, which used these equations for typical Gas Metal Arc Welding (GMAW) welding conditions.

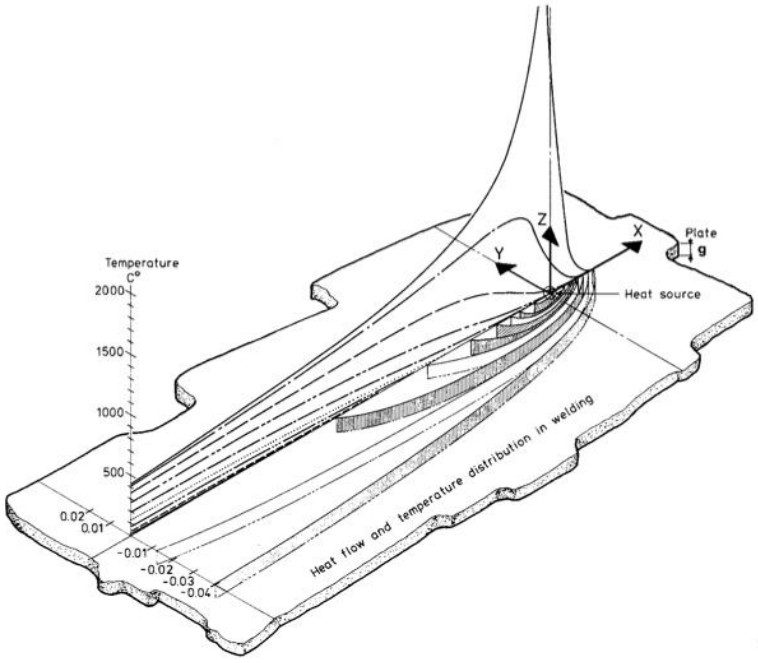

Figure 2-2: Graphical Representation of Rosenthal Thin Solution (Sorensen, 1999)

2.1.3 Finite Element Heat Source Model

With the increasing of computer efficiency, thermal transients of welding process can be calculated by finite element analysis. Compared to analytical solution, finite element analysis can offer more accurate simulation by applying temperature dependent material properties. Another advantage of finite element solution is that it is capable to model a detailed heat source. Different welding type or region of interest can employ different finite element based heat source model. According to the review by Radaj (1992), the analytical solution is sufficient if the region interested far away from the welding seam; but if the region near the welding seam is interest, the finite element heat source should be used.

The development of Finite Element Theory and computer capacity made the numerical methods for thermal analysis used widely. Professor John Goldak and his colleagues (Bibby & Goldak, 1988) made a review of different possible computational approaches. The whole temperature field can be split into three parts: the welding pool, the area near the welding pool (Heat Affected Zone) and the area far away from the welding pool. And they have proved that the numerical method can get much better results at the welding pool and Heat Affected Zone than the analytical solution; even more, it can also be adopted with a cut-off temperature technique (discussed in Chapter 3), so that the adoption of heat generation distributions can be applied as load in numerical analysis. Friedman (Friedman, 1975) used a Gaussian Circular heat input distribution in his study, which was also used by Camilleri (Camilleri D. , Comlekci, Lee, Tan, & Gray, 2003) and validated against experimental studies. Goldak (Goldak, Comlekci, & Bibby, A new finite element model for welding heat sources, 1984) proposed a general heat source model was made up by a double ellipsoid, which is widely used by many welding researchers as it has more accuracy and is suitable for implemention in numerical codes.

The Gaussian heat source is modeled as a surface heat flux having a radially symmetric normal distribution, and the heat flux can be described as Equation 2-9 & Equation 2-10 & Equation 2-11:

$$q_s(r) = q_0 e^{-\frac{3r^2}{R^2}}$$

Equation 2-9

$$q_0 = \frac{3}{\pi R^2} Q$$

Equation 2-10

$$Q = \eta UI$$

Equation 2-11

Where r is the distance from the center of the heat source; q_0 is the maximum heat flux in the welding pool, which determined by the magnitude and distribution of the heat input; R is the radial parameter, which determined the size and shape of the welding pool, and usually set it to 5mm (Younan, Will, & Fanous). The sketch of this model is shown in Figure 2-3:

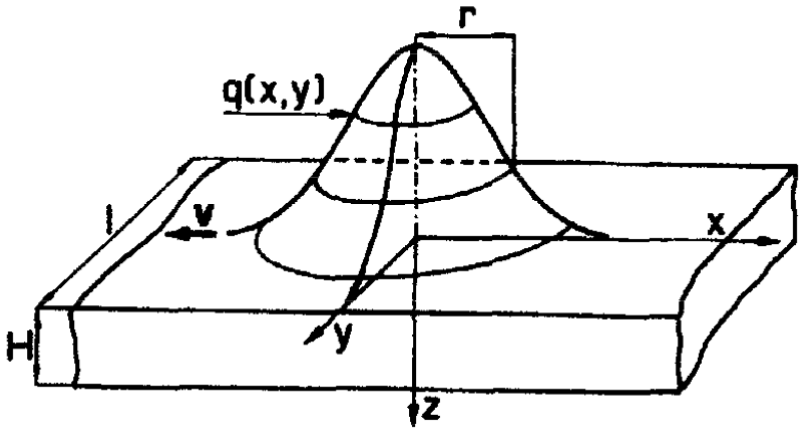

Figure 2-3 Graph Schemetic of Gaussian Heat Source

Because the Gaussian heat source doesn't take the welding arc penetration effect into account, a more advanced and significant heat source model was derived by Goldak, Comlekci and Bibby (1984), which is the Double Ellipsoidal Power Density Function. It distributes the heat throughout the volume of the molten zone. This model is defined spatially by a double ellipsoid, the front half of the source is the quadrant of the one ellipsoidal source, and the rear half is the quadrant of a second ellipsoidal source. The power density distribution is assumed to be Gaussian along the weld path, and it is convenient to introduce a moving coordinate, ξ, fixed on the heat source and moving with it. The moving reference frame on the heat source is related to the coordinate fixed on the work piece.

$$\xi = z + v(\tau - t)$$

Equation 2-12

Where v is the welding speed, τ is a lag time necessary to define the position of the heat source at time t = 0. In the double ellipsoid model, the fractions of heat deposited in the front and rear of heat source are labeled by f_f and f_r, respectively, and these fractions are specified to satisfy $f_f + f_r = 2$. This model is taken q denote the power density within the ellipsoid, and started from an ellipsoid with center at (0,0,0) and semi-axes, a, b, c parallel to the co-ordinate axes x, y, z. Then the power density distribution inside the front quadrant can be expressed by the Equation 2-13 & Equation 2-14:

$$q(x,y,z,t) = (\frac{6\sqrt{3}f_f Q}{abc_f})e^{-3(\frac{x^2}{a^2}+\frac{y^2}{b^2}+\frac{z^2}{c^2})}$$

Equation 2-13

And the power density in the rear quadrant is specified by

$$q(x,y,z,t) = (\frac{6\sqrt{3}f_r Q}{abc_r})e^{-3(\frac{x^2}{a^2}+\frac{y^2}{b^2}+\frac{z^2}{c_r{}^2})}$$

Equation 2-14

In the above equations, Q is the heat available at the source. For the arc welding, the heat available is

$$Q = \eta UI$$

Equation 2-15

Where η is the heat source efficiency, $0 \leq \eta \leq 1$, U is the arc voltage, and I is the arc current. The parameters a, b, c, and c_r are independent, which depend on the size of the welding pool. The sketch of this model is shown in Figure 2-4:

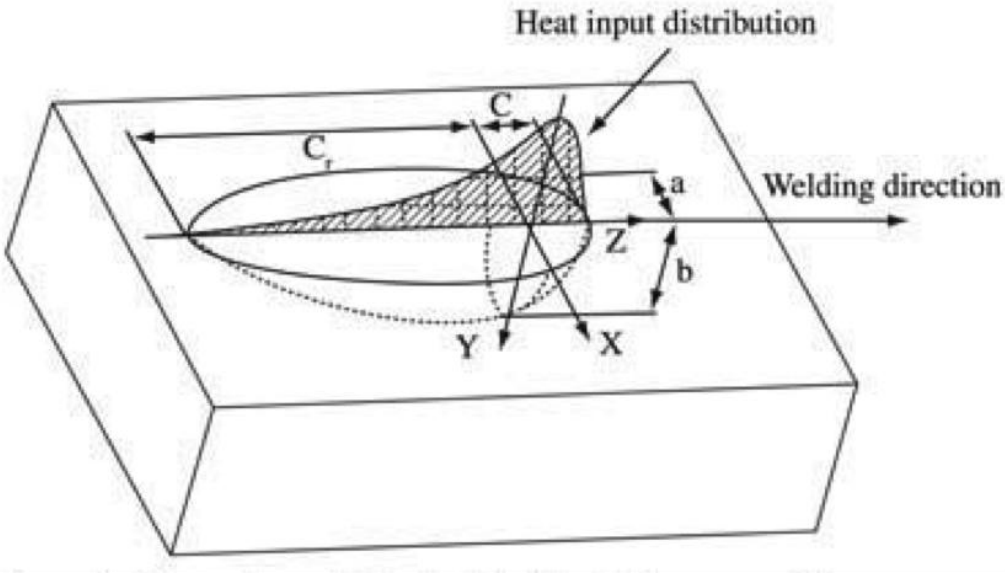

Figure 2-4 Double Ellipsoid Heat Source Model (Goldak & Akhlaghi, Computational Welding Mechanics, 2005)

2.1.4 Initial and Boundary Conditions

The initial condition for thermal analysis depends on the welding process: with or without pre-heating, single pass or multi-pass, and so on. Normally, for a single pass weld without preheating, the initial temperature field will be set to a constant value equal to the surrounding temperature.

The boundary conditions are the conditions of heat input or dissipation at the boundary surface of the welds. Three types of boundary conditions occur in the thermal analysis of welding process: (Gu M. , 1992)

- Isothermal boundary condition, which means the temperature is predefined;
- Heat flux boundary conditions, which predefined the heat flow density;
- Convection boundary conditions, the heat transfer to the surrounding medium is proportional to the difference between surface temperature and the surrounding temperature.

2.1.5 Melting and Solidification

In the molten pool region, the filler metal and base metal will first melt when heated, and then solidify during cooling. Latent heat should be considered in the thermal analysis for the weld process. In order to achieve that, the enthalpy method is used for melting and solidification, which defines a big enthalpy value change at the phase change temperature. In that case, we can use the specific enthalpy increment to compute the residual. The heat transfer Equation 2-16 could be written as:

$$\frac{\partial h}{\partial t} + \{v\}^T \nabla h + \nabla^T \{q_{hf}\} = \frac{dq_{vol}}{dt}$$

Equation 2-16

Where h is the specific enthalpy. (Wang, 2005)

2.2 Structural Analysis

2.2.1 Thermo-Elasto-Plastic Method

Some of the plasticity constitutive laws for metals are discussed in this section. Thermal effects are taken into account for in the mechanical analysis by including thermal strains and temperature dependent material properties. Also, the thermal state affects the plastic yield criterion. The constitutive laws relating stresses, strains, and temperature are nonlinear in the theory of plastic deformation of solids (Martin, 1975).

2.2.1.1 Fundamental Assumptions

The following assumptions apply to the formulations that follow (Hsu, 1986), which is only for steel:

1. The material is treated as a continuous medium or a continuum.
2. The material is isotropic, with its properties independent of direction.
3. The material has no "memory" such that the effect on the material in previous events does not impact the current event.

2.2.1.2 Fundamental Difference Between Elastic and Plastic Deformation

The following outlines some of the fundamental differences between elastic and plastic material behavior (Hsu, 1986).

1) Elastic deformation

   i) Very small deformation with the strain up to about 0.1%
   ii) Usually a linear relationship between the stress and strain.
   iii) Completely recoverable strain or deformation after the applied load is removed.

2) Plastic deformation

   i) Larger deformation.
   ii) Nonlinear relationship between the stress and strain.
   iii) Results in permanent deformation after the removal of the applied load.
   iv) No volumetric change in the solid during plastic deformation, often modeled with Poisson's ratio of 0.5. Deformation is caused by shear actions on the material. Only shape changes can be observed.
   v) The total strain, ε_T, is the sum of the elastic components ε_e and the plastic component ε_p as shown in Figure 2-5

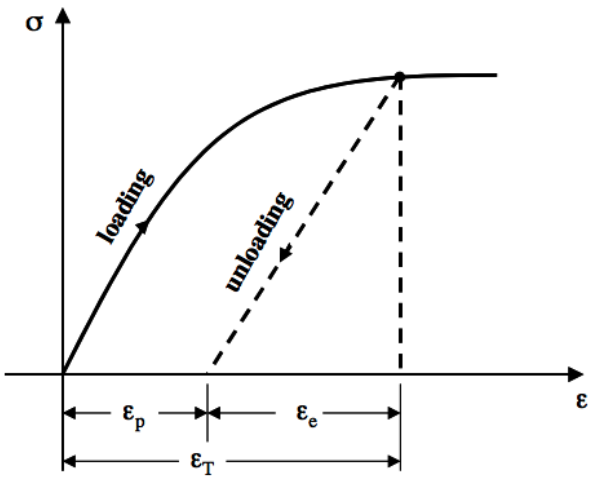

Figure 2-5: Uniaxial elastic-plastic loading and elastic unloading of a material (Hsu, 1986)

2.2.1.3 Idealized Uniaxial Stress-Strain Curves

Three idealized stress-strain curves for a prismatic, metal bar subjected to uniaxial tension are shown in Figure 2-6. Rigid, perfectly plastic, elastic, perfectly plastic, and elastic, strain-hardening behaviors are shown in parts (a), (b), and (c), respectively, of the figure. The yield strength of the material is denoted by σ_y in the plots. The rigid, perfectly plastic idealization neglects elastic strains and hardening. The elastic, perfectly plastic curve includes elastic strains but neglects hardening. The elastic, strain-hardening curve includes elastic strains and assumes linear hardening. When a surrounding elastic material prevents the large deformations, then plastic deformation is contained. For contained plastic deformation, neglecting strain- hardening, or work hardening, is a reasonable assumption. Large deformations by cold working occur in metal-forming processes such as drawing, rolling, and extrusion. Cold working involves hardening and the plastic deformations in these processes are much larger than elastic deformations, so that neglecting elastic deformation is a reasonable assumption.

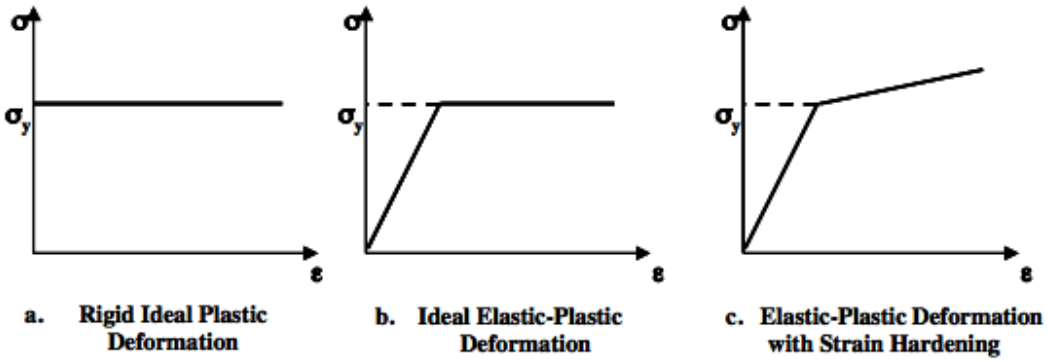

Figure 2-6: Idealized flow curves from uniaxial tension test (Hsu, 1986)

The yield strength of a metal is measured in the tension test, which is a uniaxial state of stress. The question of what governs yielding in a multi-axial state of stress is determined from experiments, since there is no theoretical way to correlate yielding in a three-dimensional stress state with yielding in the uniaxial tensile test. The yield condition now can only be defined by the yield criterion (Hsu, 1986).

2.2.1.4 Von Mises Yield Criterion

The Von Mises yield criterion was first derived from the distortion energy theory. Let σ denote the Mises effective stress defined by Equation 2-17

$$\sigma = \frac{1}{\sqrt{2}}[(\sigma_{XX} - \sigma_{YY})^2 + (\sigma_{YY} - \sigma_{ZZ})^2 + (\sigma_{XX} - \sigma_{ZZ})^2 + 6(\sigma_{XY}{}^2 + \sigma_{YZ}{}^2 + \sigma_{XZ}{}^2)]^{0.5}$$

Equation 2-17

Where σ_{XX}, σ_{YY}, σ_{ZZ}, σ_{XY}, σ_{YZ}, σ_{XZ} are the Cartesian stress components at a point in the material. Mises criterion states that yielding initiates in a three-dimensional state of stress when the effective stress equals the yield strength of the material determined from the uniaxial tensile test. Expressed mathematically the criterion is simply

$$\sigma = \sigma_y \qquad \text{at the initiation of yielding}$$

For the uniaxial state of stress, where $\sigma_{XX} \neq 0$, and all other stresses components are equal to zero, Mises criterion predicts yield initiation when $\sigma_{XX} = \pm\sigma_y$. For the state of pure shear where $\sigma_{XY} \neq 0$ and all other stress components are equal to zero, Mises criterion predicts the initiation of yielding when $\sigma_{XY} = \pm\sigma_y/(\sqrt{3})$. Thus, Mises criterion implies that the yield stress in tension is $\sqrt{3}$ times the yield stress in shear. This relationship between the yield stresses in tension and pure shear closely approximates many tests of polycrystalline metals (Malvem, 1969). Mises criterion can be visualized in principal stress space, where the principal stresses are denoted (σ_1, σ_2, σ_3). The criterion plots as right circular cylindrical surface of radius $\sqrt{2}/3\ \sigma_y$, with the axis of the cylinder equally inclined with respect to the positive principal stress axes. For $\sigma_3 = 0$, Mises criterion plots as an ellipse in the (σ_1 - σ_2) plane as is shown in Figure 2-7.

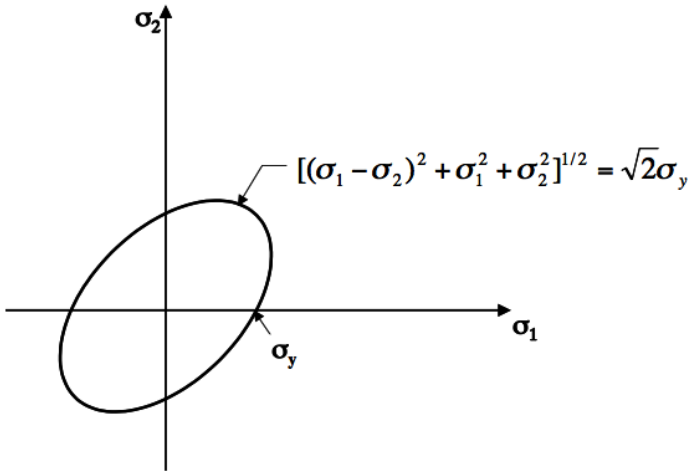

Figure 2-7: Two-dimensional Von Mises yield surface (Hsu, 1986)

2.2.1.5 Strain Hardening

Strain hardening is defined as the increase in hardness and strength of a metal as it is plastically deformed (Callister, 1995). Initial plastic yielding takes place when a material is loaded beyond its elastic limit. Theoretically, the material starts to "flow" without any additional load as depicted in Figure 2-6 (b). However, in reality most materials retain some of their original stiffness after yielding. Additional loading is required to further plastically deform the material as shown in Figure 2-6 (c). The material also becomes "harder" after some plastic deformation as a higher applied load is required to cause the same material to deform plastically again after the completion of one previous loading cycle (Hsu, 1986). Two types of strain-hardening schemes are typically used in finite element analysis:

Isotropic hardening.

Figure 2-8 illustrates the principle of isotropic hardening of a material. First the material is loaded beyond its initial yield strength σ_y to an instantaneous strain ε_1 and then unloaded upon reaching point A. A permanent strain ε_2 is introduced in the material after unloading. If the solid is loaded again, the material is found to yield at a higher strength σ_y' which coincides with the stress σ_A at the last load point. The biaxial stress states for the isotropic strain-hardening behavior can be graphically represented by the uniform expansion of the initial yield surface of Figure 2-7, or as shown in Figure 2-9 (Hsu, 1986).

The yield surface maintains its shape and does not translate, while its size increase is controlled by a single parameter depending on the plastic deformation.

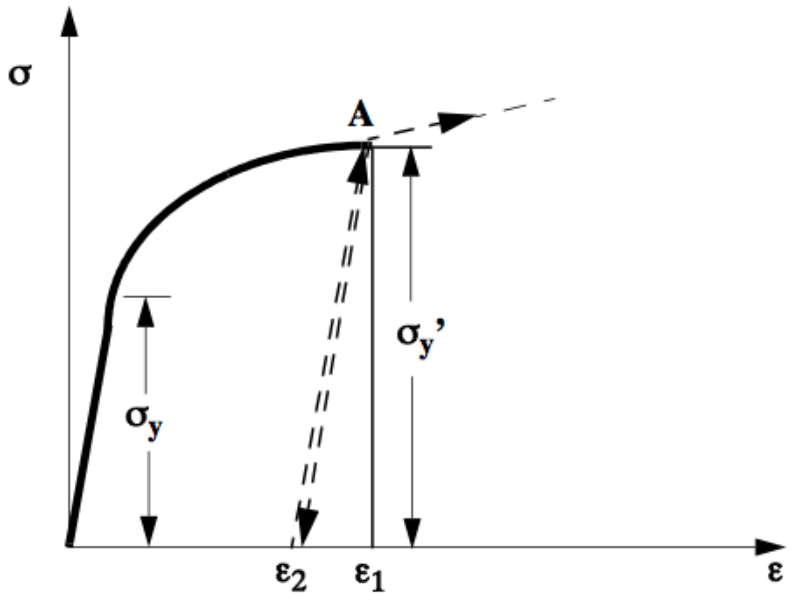

Figure 2-8: Paths for loading, unloading and reloading for an isotropic hardening solid (Hsu, 1986)

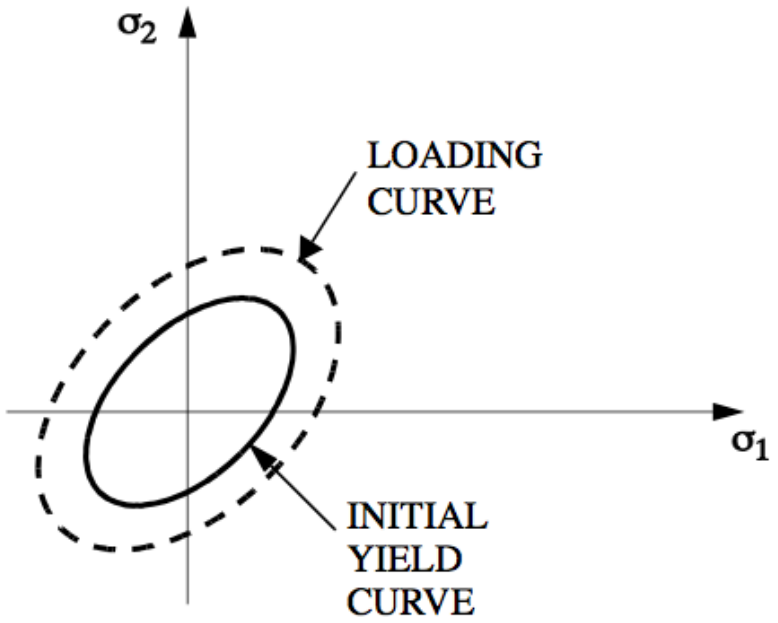

Figure 2-9: Biaxial loading surfaces for isotropic hardening solids (Hsu, 1986)

Kinematic hardening.

A material which exhibits kinematic hardening has the characteristic that when the material is plastically deformed in tension followed by loading in the reverse direction, the compressive yield strength in reverse loading is reduced in the same amount as the tensile yield strength is increased during the initial loading. The lowering of the compression yield following a first loading in tension is called the Bauschinger effect. The isotropic hardening model would predict a compression yield strength at $\sigma_{zz} = -(\sigma_y + \alpha_{zz})$ in Figure 2-10. Thus, the isotropic hardening model cannot predict the Bauschinger effect, but the kinematic model can predict it. Kinematic hardening results in the strain hysteresis observed after a complete tension-compression load cycle, as shown in Figure 2-10. For the multi-axial loading situation, the size and shape of the yield surface does not change, but it merely translates in stress space as is shown in Figure 2-11 (Hsu, 1986). The translation is in a direction of the plastic-deformation-increment vector.

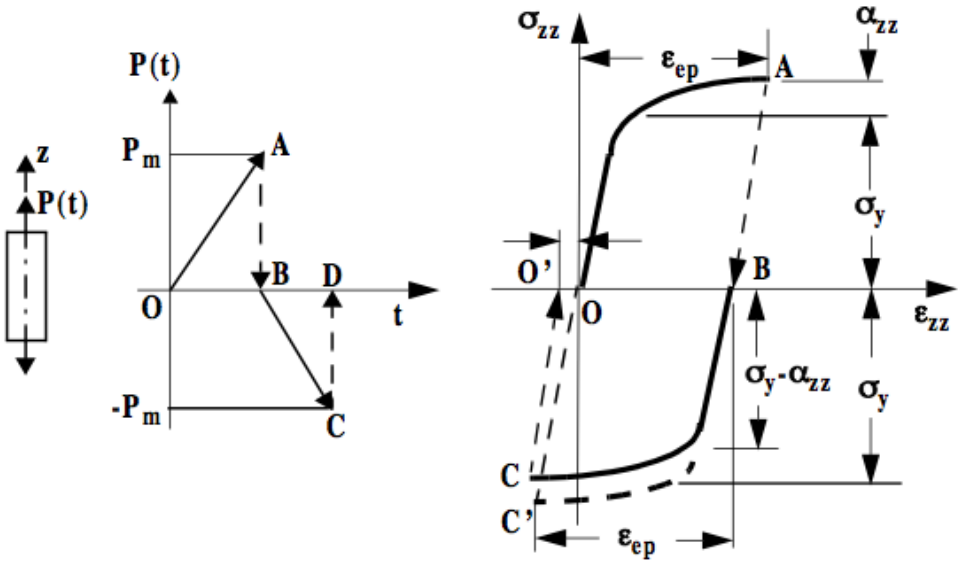

Figure 2-10: Paths for a uniaxially loaded bar under kinematic hardening plastic deformation (Hsu, 1986)

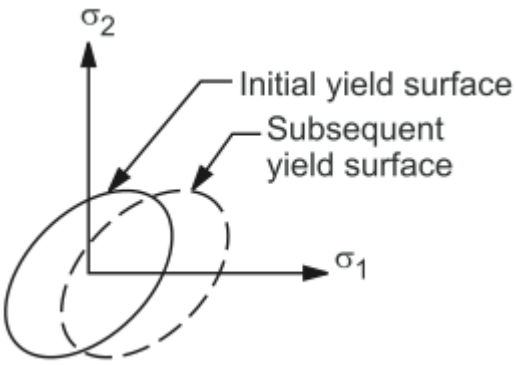

Figure 2-11: Translation of the yield surface with kinematic hardening rule under biaxial loading condition (Hsu, 1986)

2.2.2 FEM Formulation and Implementation

From conservation of momentum, if we neglect the inertial force term, we can obtain a local spatial equilibrium equation for quasi-static state: (Asadi & Goldak, 2010)

$$\nabla \cdot \sigma + f = 0$$

Equation 2-18

Where σ is the Cauchy stress tensor, f is the body force per unit volume. This equation is valid for both Lagrangian and Eulerian reference frame.

For the FEM formulation, the above equation will be integrated over the physical configuration, or a reference configuration with unique mapping to that physical configuration.

The Lagrangian formulation or the Updated Lagrangian (UL) formulation, which is the one most commonly used in solid mechanics, has dominated computational weld mechanics for more than a decade. To avoid the spot welding effect, many small time steps would be necessary, which means if the time step is not small enough, the heat source will stay in one position too long and make the simulation has similar effect as spot welding.

For an incremental step-by-step analysis, the Updated Lagrangian formulation may be more numerically efficient based on the fact that in the total Lagrangian formulation, which the strain displacement matrix is more complex (Bathe, 1996). It will be more convenient to use an Updated Lagrangian formulation, which updates all static and kinematic variables at the end of every time step.

For the time step from t to t+Δt, the solution for the discrete time t is assumed to be known and is assigned to be the initial condition in the UL formulation. The solution for the discrete time t+Δt is required. To solve the problem by FEM, the equilibrium conditions of a system of finite elements representing the body under consideration domain can be expressed as:

$$f_{int}^{\mathrm{t+\Delta t}} + f_{ext}^{\mathrm{t+\Delta t}} = 0$$

Equation 2-19

Where the left upper script means at time t+Δt, the lower script int means the nodal internal force vector, which corresponding to the element stresses in this configuration and ext means the nodal external force vector applied in this configuration. This also means that the equilibrium equation above is evaluated in the configuration at the current time t+Δt. For each element, the internal and external nodal force vector can be computed as:

$$f_{int}^{\mathrm{t+\Delta t}} = \oint B^{\mathrm{t+\Delta t}T} \cdot \sigma^{\mathrm{t+\Delta t}} d\Omega$$

Equation 2-20

$$f_{ext}^{\mathrm{t+\Delta t}} = \int R^{\mathrm{t+\Delta t}T} \cdot T^{\mathrm{t+\Delta t}} d\Gamma - \oint R^{\mathrm{t+\Delta t}T} \cdot f^{\mathrm{t+\Delta t}} d\Omega$$

Equation 2-21

Where $B^{t+\Delta t}$ and $R^{t+\Delta t}$ are the matrix of symmetric physical gradient operator and matrix of basis functions, respectively. $T^{t+\Delta t}$ is the surface traction exerted on the boundary, Γ, of the domain Ω. Normally, with the thermo-elasto-plastic finite strain analysis, Equation 2-19 is nonlinear. In a displacement based FEM analysis, by introducing the tangent stiffness matrix K_T, a linearized matrix equation can be obtained for the time step from t to t+ Δt:

$$K_T dU = f_{ext}^{t+\Delta t} - f_{int}^{t}$$

Equation 2-22

Where dU is a vector of nodal displacement increment in this time step.

By using the Newton-Raphson iterative scheme, the linearized equation above is iteratively solved until a solution to the non-linear problem in Equation 2-19 is found. The equations used in the Newton-Raphson, at iteration k, are:

$$K_T^{t+\Delta t}{}_{k-1} du_k = f_{ext}^{t+\Delta t} - f_{int}^{t+\Delta t}{}_{k-1}$$

Equation 2-23

$$dU^{t+\Delta t}{}_k = dU^{t+\Delta t}{}_{k-1} + du_k$$

Equation 2-24

With the initial conditions:

$$dU_0{}^{t+\Delta t} = 0$$

Equation 2-25

$$dK_{T_0}{}^{t+\Delta t} = K_T{}^t$$

Equation 2-26

$$f_{0_{int}}^{t+\Delta t} = f_{0_{int}}^{t}$$

Equation 2-27

For each Newton-Raphson iteration, the residual vector

$$r_k = f_{ext}^{t+\Delta t} - f_{int}^{t+\Delta t}{}_k$$

Equation 2-28

and its Euclidean norm is calculated. If the Euclidean norm or energy norm of the residual vector is smaller than a tolerance, or the convergence ratio is smaller than a tolerance, the linearized Equation 2-22 is considered to be converged, and thus, the equation is solved. The solution (displacement field) satisfies the equation of continuity and the boundary conditions. Thus, the stress computed here is called kinematically

admissible stress. However the error between the FEM solution and the exact solution cannot be predicted by residual type error estimates.

A more reliable error measurement has been proposed by considering both kinematically admissible stress (KAS) and statically admissible stress (SAS) fields (Mashaie, 1990) (Cheng, 2003). A statically admissible stress field is defined as the stress field that satisfies the static equilibrium conditions in the interior and on the Neumann boundaries of domain. (Mashaie, 1990) pointed out that the difference between the energy norm (defined in strain energy) of the kinematically admissible stress field and that of the statically admissible stress field is an upper bound for the difference between the energy norm of the kinematically admissible stress field and that of the exact solution of the problem.

The statically admissible stress field can be computed from the kinematically admissible stress field, together with enforcing the Neumann constraints.

With the error bound in each element computed, one can efficiently determine when the problem is solved, or where the mesh needs to be refined or coarsened for certain accuracy or efficiency requirements.

2.2.3 Simplified Methods

In order to reduce the computational time, some simplified methods have been developed. The first simplification is the utilization of Indirect Coupling Method，which has been investigated by many researchers (Roberts, Hunziker, Reed, Dye, & Stone, 1999) (Teng, Fung, Chang, & Yang, 2001) (Olden & Leggat, 1999) (Dong, Hong, & Bouchard, 2005), and the procedure has been shown in Figure 2-12. Jiang (Jiang, Yahiaoui, Hall, & Laoui, 2005) carried out a study in comparison of direct and indirect methods in regard to their capability of predicting residual stresses and distortion; and Lindgren (Lindgen, 2001) has also investigated the effect of the indirect method on the simulation process. It has been found that using indirect coupling method greatly reduced the computational time without losing significant level of accuracy.

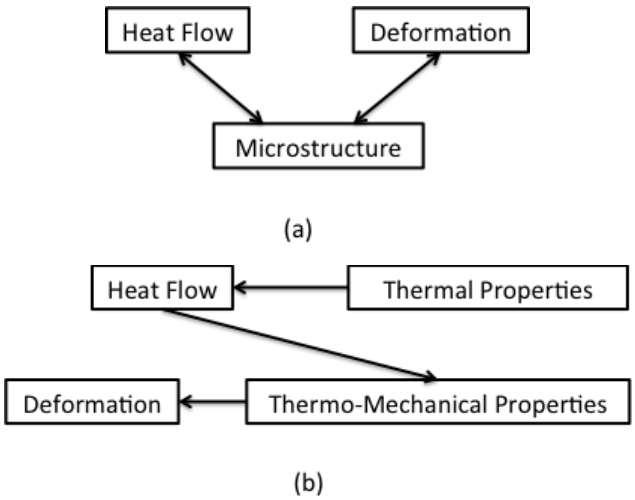

Figure 2-12: Simulation Procedure for (a) Coupled and (b) Uncoupled Thermal-Mechanical Welding Physical Phenomena

The second simplification is to reduce the complex elasto-plastic analysis to a simple analysis by a deeper understanding of the relationship between stresses and strains during the welding process. The simple and basic method is the Shrinkage Volume Method, which was proposed by Bachorski (Bachorski, Painter, Smailes, & Wahab, 1999). This method simplified the elasto-plastic analysis to a simple elastic finite element analysis, which give a contraction strain $(-\alpha\Delta T)$ to the elements associated with the welding pool. In order to achieve a steady state during the calculations, it ignored the heat process when assigning the initial temperatures to each element. This assumption means the history of stress during heating will be ignored, so that the magnitude of the predicted residual stresses cannot be accurate. And another disadvantage of this method is that the results are seriously dependent on the assumed weld pool shape in the thermal simulation.

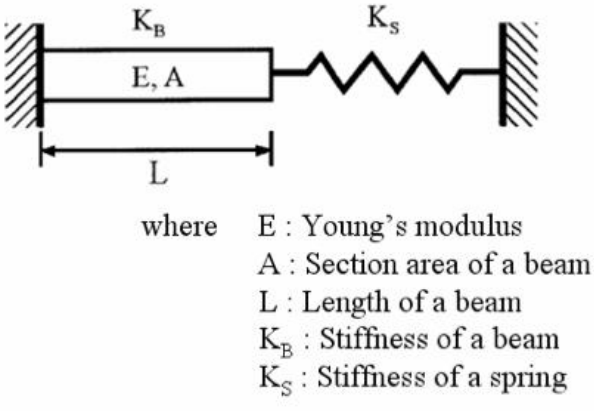

Figure 2-13: Simplified spring & bar model

Ueda (Ueda & Nakacho, 1982) derived a simplified method called Inherent Strain Method. In a welding process, the heat input causes an uneven temperature distribution of thermal stresses, therefore the plastic strain remains around the weld bead so that the permanent deformation occurs after welding. Ueda deems that the plastic strain is the main reason causing the welding deformations and defined it as the inherent strain. In general, the inherent strain induced by welding has six components according to their directions. However, in the case of where a plate has a large length thickness ratio such as ship hull plate, only the longitudinal and transverse in plane components need to be considered. This method, based on a spring & bar model, is schematically shown in Figure 2-13. The spring models the weld pool and the bar represents the surrounding material.

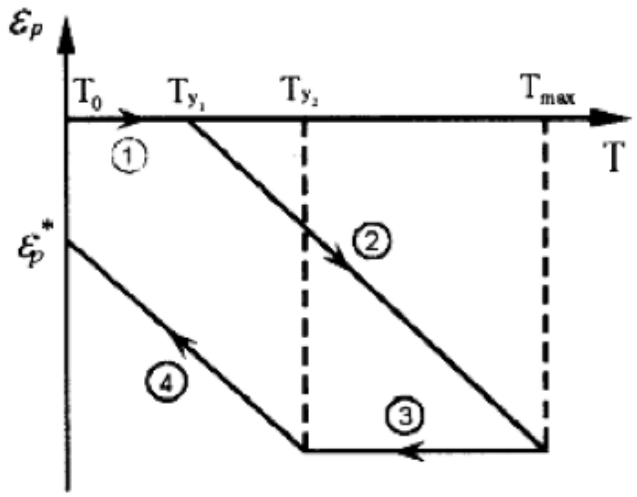

Figure 2-14: Thermal history of plastic strain

According to the temperature change, the thermal history of the inherent strain of a bar can be divided into four parts, which is schematically shown in Figure 2-14. After all the thermal history, the remaining compressive plastic strain is ε_p^*, and the magnitude of residual plastic strain is calculated from the total strain, the stress strain relationship and the equilibrium equation of a bar & spring system which can be expressed by the following equations:

Total Strain: $$\varepsilon = \varepsilon_{th} + \varepsilon_e + \varepsilon_p$$

Equation 2-29

Stress Strain Relation: $\sigma = E\varepsilon_e$

Equation 2-30

Equilibrium equation: $F_B = F_S$

Equation 2-31

The degree of restraint is the level of resistance against thermal deformation of the welding region, and the amount of plastic strain is determined for each case and used to formulate equivalent loads (longitudinal and horizontal force and moment) to be applied to the structure by means of an elastic finite element analysis.

Another simplified technique is proposed by Deo (Deo, Michaleris, & Sun, 2003). This illustrates how de-couple, two dimensional welding simulations and can be carried out in conjunction with three dimensional buckling analysis on structures where displacement is restrained. The author used a simplified approach in a two dimensional welding simulation followed by a three-dimensional buckling analysis. This approach has some similarities with the Inherent Strain Method; the difference is that the applied stress strain field comes from a two dimensional analysis rather than an empirical determination based on the temperature field and the spring bar model. Firstly, a two dimensional indirect coupling thermal mechanics analysis is performed, which is an elasto-plastic analysis carried out in a quasi-static Lagrangian form subdivided in several small static steps. Generalized plane strain conditions were assumed, which imply linear variation of the longitudinal strain. A constant negative thermal load is applied at the weld region to introduce the effect of welding in the three dimensional structure. Furthermore, the author also simplify the analysis by assuming the same material model for the weld and parent material, based on the previous work that showed a 20% difference in yield strength of the weld material causes only a 3% change in residual stress. Finally, the longitudinal residual stress obtained from the two dimensional elasto-plastic analysis is compared with the buckling critical stress to determine if the structure will indeed buckle. Eigenvalue analyses were used for determining the buckling stress. The models were verified experimentally and an in-house FE-code was produced. This method was successful in predicting whether the plates bucked or not and recommendations could be made regarding the influence of geometric parameters on buckling.

Camilleri proposed another simplified approach which focused on reducing the computational time (Camilleri & Gray, 2005) (Camilleri, Comlekci, & Gray, 2005). Similar to all the simulation procedures described so far (in this section), firstly, the thermal part is performed with a thermal analysis. Then the structural part is based on the early idea from Okerblom (Okerbolm, 1958). This approach contains two algorithms: Thermal Contraction Strain (TCS) and Mismatch Thermal Strain (MTS). TCS is used to determine the angular deformation and MTS is for carrying out the longitudinal contraction calculations. These algorithms are based on key characteristics of the temperature distribution generated by the fast-moving, intense heat sources: the temperature gradient on the approach side of the thermal source is steep, as the forward heat flow rate is relatively small, and for similar reasons, the temperature profile transverse to the weld is steep, but the gradient in the trailing region where cooling takes place is relatively slow (Camilleri D. 1., 2005). Okerblom was the first to pay attention to these features and suggest that the thermal mechanical process may be modeled by considering as a transverse plane strain slice, which would be passed through the quasi-stationary temperature field in the direction of welding.

The TCS algorithm assumes the transverse angular deformation is controlled by the contraction across the pre-defined welding pool, which depends on the transverse width across the thickness. Because the maximum temperature in reality is usually over the melting point, the material will act as a liquid, but liquid properties cannot be used in this analysis, as the finite element method doesn't allow the Young's Modulus or Yield Stress to be zero, so that a cut off temperature is set (in Camilleri's research, 1000℃) which is the level at which is the material starts to provide some strength. Similar to the Shrinkage Volume Method (Bachorski, Painter, Smailes, & Wahab, 1999), the TCS algorithm also neglects the heating process and assumes a defined zone contracts. The transverse contraction can be extended to express the transverse angular deformation in the following equation:

$$\theta = \frac{s}{t_0}\frac{b}{t_0}\alpha T_s[3(1-k_w^2) - 2\frac{s}{t_0}(1-k_w^3)]$$

Equation 2-32

Where:

$\frac{s}{t_0}$ The relative depth of penetration of the weld

$\frac{b}{t_0}$	The relative width of the fusion zone on the surface
k_w	Geometric parameter dependent on the shape of fusion zone

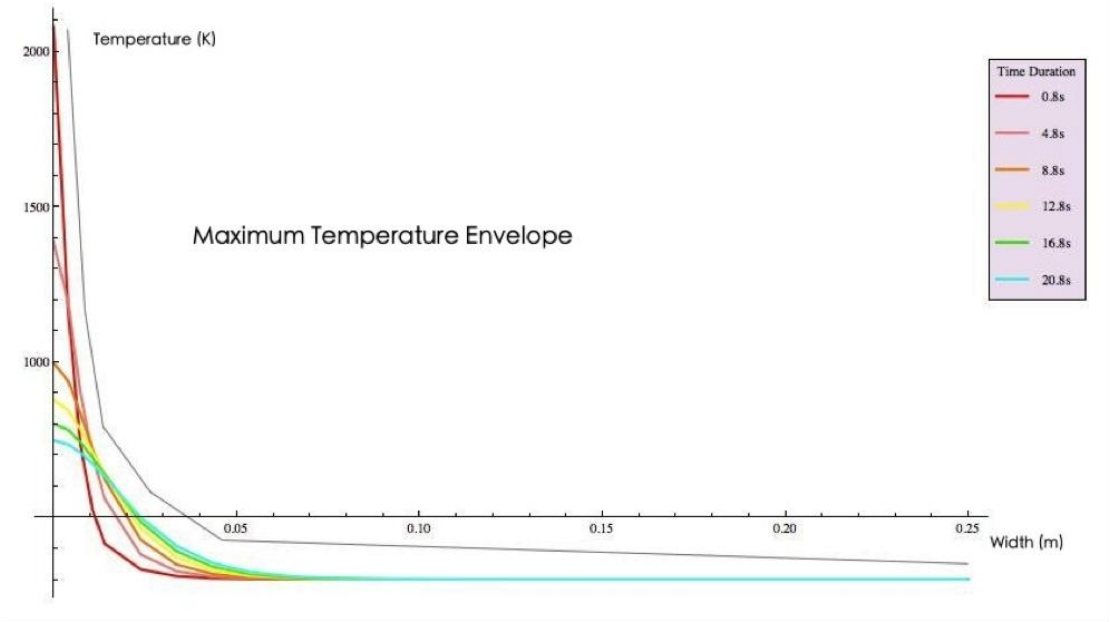

Figure 2-15: Envelope of maximum temperatures across a slice for butt-welding

The MTS algorithm is used to develop the strain in the longitudinal direction. In this case, the longitudinal contraction forces are derived from the thermal strain mismatches, which were developed during the cooling phase of the welding process. Then a plane strain slice can be used to pass through the temperature distributions that in turn gradually extent outwards. As a result, the development of the longitudinal stress is mainly driven by the envelope of maximum temperatures across the slice, which used by (Camilleri D. 1., 2005) is shown in Figure 2-15. From this figure, the maximum temperatures are reached at different times at each transverse location. However it has been found that it is not necessary to take account of the time offset in this approach. As this method is based on representing the shrinkage volume by the behavior of a defined region, it doesn't matter that whether the full temperature field or just a local field determines the contraction force.

In this approach, the longitudinal stress is the most difficult to analyze, due to the complexity of material behavior mentioned earlier. However, substantial simplifications are admissible because the longitudinal stress level in the welding pool regions where the

complex behavior takes place is limited by the final yield strength. The authors also show that the typical profile of the maximum transverse temperatures is inversely proportional to the distance from the center line of the weld, which results in a weak dependence on the actual yield strength value, leaving the expansion as the major driving force. The expansion and yield characteristics in a perfect elasto-plastic model for steel are a relatively small temperature difference (about 120℃) that causes yielding in a typical case. Hence the mechanics of contraction force development are driven primarily by the cooling phase of the cycle within a relatively low temperature range within which the material properties are almost constant. The resulting MTS algorithm is implemented within a three-dimensional, elastic, finite-element formulation by applying a load profile which corresponds to an artificial temperature reduction at points across the width of the plane strain slice. In the welding line region, yield magnitude stresses, which are defined by thermal strain that exceed twice yield strain, are applied. No load is applied in the other regions that remain elastic, defined by thermal strain less than yield strain ε_Y. In the zones between the fully plastic and elastic regions, loads corresponding to $(\alpha T_M - \varepsilon_Y)$ are applied, where T_M is the maximum temperature reached at the location (Camilleri & Gray, 2003). The comparison between the results and the average experimental deformation was good, which proved this algorithm is a good basis on which to develop further simplified methods for different cases such as single (Camilleri, Comlekci, & Gray, 2006) and multi-stiffened plate structures (Camilleri, Comlekci, & Gray, 2005).

Because there are some common drawbacks in most simplified methods; it is necessary to make correct use of them to obtain meaningful results. Much research effort is still put into simplified simulation techniques, which are usually verified by experimental data or more complex modeling techniques.

2.3 Conclusions

The above literature review illustrates the current practices and trends for simulation of welding induced residual stress and distortion. Control of weld residual stresses and distortion is a very important task in marine structure manufacturing. Attempts have been made by many researchers since 1930 to understand weld residual stresses and distortion using predictive methodology, parametric experiments or empirical formulations. Attempts have also been made in the last three decades to predict weld

residual stresses and distortion through computer simulations of welding process using the finite element analysis (FEA) method. One significant conclusion from these studies is that the weld residual stresses and distortion are not influenced much by the weld heating cycle but instead occur as a result of shrinkage in the weld metal and its adjacent base metal during cooling when the yield strength and modulus of elasticity of the material are recovered to their higher values at lower temperatures. Therefore, analysis of the shrinkage phenomena of welds alone may be sufficiently accurate to predict the state of weld residual stresses and distortion, which gives the insight of the simple method for calculation welding transverse residual stresses in Chapter 4.

In principle, all finite element software can simulate the welding process, but the specialist software has pre-coded the welding heat source, material properties, element activate and deactivate technique, advanced mesh technique, microstructure calculation abilities and sub-domain technique, which can make more efficient simulation of welding process than a standard finite element package. So the author used both standard and specialist finite element software in this study (See Chapter 3).

Chapter 3 Simulation of Butt and Fillet Welding Processes by FEM

3.1 Finite Element Software Packages

After a review of the limited number of commercial finite element software package, which are capable of welding process simulation, ANSYS and VrWeld were chosen to be used in this research due to their particular capabilities. ANSYS is a general-purpose finite element modeling package that can simulate any physical process; but VrWeld is a finite element software package especially for simulation of welding process. The results and the capabilities for simulating the welding process of both software packages will be compared and discussed.

3.1.1 ANSYS

ANSYS (www.ansys.com) offers a comprehensive range of engineering simulation solution sets providing access to virtually any field of engineering simulation that a design process requires. The multi-physics simulation solutions from ANSYS allow engineers and designers to create virtual prototypes of their designs operating under real-world multi-physics conditions. As the range of need for simulation expands, companies must be able to accurately predict how complex products will behave in real-world environments, where multiple types of coupled physics interact. Industry leading software from ANSYS (www.ansys.com) enables engineers and scientists to simulate the interaction between structural mechanics, heat transfer, fluid flow and electromagnetics all within a single, unified engineering simulation environment. So the welding process, which is a thermal and structural coupled multi-physical problem, can be simulated by using ANSYS.

One of the ANSYS program's most powerful features for thermal analysis is its ability to analyze phase change problem, such as a melting or solidification process. In order to analyze a phase change problem, a nonlinear transient thermal analysis needs to be performed. In nonlinear analysis, the latent heat will be accounted for by defining the enthalpy of the material as a function of temperature. Enthalpy, which has units of heat

per unit volume, is the integral of density times specific heat with respect to temperature. In this research, the latent heat was accounted for by defining the temperature dependent specific heat of the material.

The function tool in ANSYS allows the user to define a dependent variable as a function of one or more independent variables. By using the function tool, complicated boundary conditions or loads, like the heat source model, can be defined on a model, and the nonlinear material behavior can also be defined by taking advantage of this tool. After defining the equations in the function tool, the equation is loaded into a table as a coded equation. This code equation is processed in ANSYS when the table is called for evalution.

The GUI (Graphical User Interface) of ANSYS is easy to learn and ready for use, but it is only suitable for relative simple problems, not complex problems, like simulating the welding process. As the welding process is a thermal and mechanical coupled physical phenomena, which contains the phase change and utilization of element death and birth technique, the simulation process needs to be controlled. The APDL (ANSYS Parametric Design Language) is a scripting language that can be used to automate common tasks or even build the model in terms of parameters. By using APDL in ANSYS, a tailor made model for the structural analysis was created. The indirect coupled method was used in this research, which means the thermal transient simulation would be finished first to acquire the temperature distribution; then the structural transient analysis was performed with the thermal temperature distribution input as body loads.

The element death and birth technique was used to simulate the welds deposition. In order to achieve the element death effect, the ANSYS program doesn't actually remove dead elements, it just multiplies their conductivity or stiffness by a very small factor (default set it as 1E-6). Element loads, mass, damping, specific heat and other such effects associated with the dead elements are all set as zero. The mass and energy of dead elements are not included in the summations over the model. The element's strain is also set to zero as soon as that element is dead. When the elements are birthed, they are not actually added to the model, it is just their stiffness, mass, element loads, etc. that are recovered to the original values with no record of strain history. The elements are deactivated (or activated) in the first time sub-step of the load step, and maintain that

status through the rest of the load step. When implementing this technique, it is necessary to be aware that the nodes that are not connected to any active elements may 'float', in such case, the inactive DOFs (Degree of Freedoms) need to be constrained to reduce the number of equations to be solved and to avoid ill-conditioning, then the artificial constraints will be removed when the elements are reactivated.

3.1.2 VrWeld

VrWeld (Goldak J. , 2007) is a finite element code for the simulation of welding process. It was a predefined material deposition process via a silent element technique and moving heat sources. The silent element technique uses the same principles as the element death and birth technique in ANSYS, in which the deactivated elements stiffness or conductivity are multiplied by a very small reduction factor, any loads applied to deactivated elements from the global load vector are removed. Another key feature of VrWeld code which sets it apart from other commercial finite element software, is the ability to model metallurgical transformations. Metallurgical transformations include volume changes due to phase transformations as well as the change of mechanical properties due to the phase transformation. Also included is a library of temperature dependent material properties for both common steel and aluminum. VrWeld code has many other capabilities, but those presented here are the only ones of concern for this research.

The input data to VrWeld are: (Asadi & Goldak, 2010)

1. The 3D geometry of all parts and fixtures in the structure to be welded. These are usually imported as Stereo lithographic (STL) files. If the 3D transit geometry of each filler metal pass is not provided as STL files, then it must be modeled and the data for the geometry of the filler metal models must be provided.

2. The composition, temperature dependent thermal and mechanical material properties for each alloy type for each part in the structure including filler metal of welds must be specified.

3. The weld process parameters including weld current, weld voltage, power density distribution in the weld pool are needed. For a MIG welding process the filler metal wire size and speed are needed. The start time and start position of each weld pass and the speed as the arc travels along the weld path is needed. The delay time between the ends of one weld pass and the start of the next weld pass is important.

4. If fixtures are applied or released, the appropriate time dependent boundary conditions must be defined to model the action of each fixture.

5. A cool-down time after the welds have been completed is chosen to allow the structure to cool to temperature.

6. The initial state of the temperature, microstructure and strain or stress is needed.

7. If sensors such as thermocouples, strain gauges, displacement transducers, residual stress sampling volumes are of interest, then the position and the times of interest of each transducer are specified as a virtual sensor.

The output data from VrWeld include the following fields in the structure:

1. Transient temperature field

2. Transient displacement field

3. Transient elastic, thermal, plastic and total strain vector or strain tensor field.

4. Transient stress and deviatoric tensor field and principle stress fields as scalars or vectors.

In welding simulation, the nonlinear thermal-elasto-plastic calculation is only implemented in the region near the welds, as there is not much temperature change in the far field region, where only the linear thermal-elastic calculation is needed. In principle, substructure technique could be used in stantard finite element software

package, like ANSYS, ABAQUS, etc., but the standard finite element can only consider all elements in the nonlinear welding simulation in practice, which results in long computation time and a waste of computation resources. It is feasible to separate the linear and nonlinear into different parts, and calculate each by the appropriate calculation method.

In VrWeld, the model is initially set by body part (the far field region) and weld joint; the designer can define the size of each part. Furthermore, the weld joint can be defined by several subdomains, as illustrated in Figure 3 1. During the calculations, only the active subdomain, where the heat source locates, is calculated by nonlinear analysis, the remaining parts are treated as linear. User can define other requirements for the active subdomain, such as the maximum temperature of an element, the maximum temperature difference in current time step, etc. This technique could dramatically save the calculation resources and increase the computation speed.

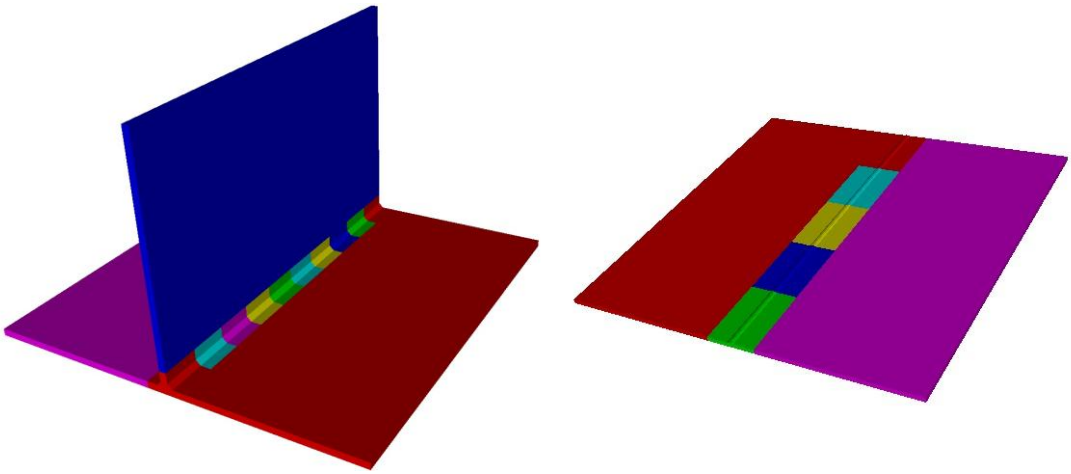

Figure 3-1: Schematic of Subdomain Method

3.2 Thermal Analysis in Welding

During the welding process, there is a moving local high intensity power source generating a steep thermal profile in the welding pool, heat affected zone (HAZ) and around the weld. This causes a local change in microstructure, stress and strain state, which can have a large effect on the whole structure. The 3D transient temperature is

determined by solving the partial differential equation for the conservation of energy, which is given in Equation 3-1 for a Lagragian or material formulation.

$$\dot{h} + \nabla \cdot (-K\nabla T) = Q$$

Equation 3-1

In welding simulation, heat source models are used to formulate the boundary conditions and heat sources near the weld pool to take either transient flux or temperature. The Goldak double ellipsoid power density function is used in this research. The double ellipsoid model (Goldak & Akhlaghi, Computational Welding Mechanics, 2005) is the heat source model used most frequently in published papers. This model prescribes a Gaussian distribution of power density in a weld pool shape characterized by four parameters: width, depth, front length, and rear length of the double ellipsoid as shown in Figure 3-2. Heat power density used in the each of front and rear sections of the double ellipsoid is defined by Equation 3-2 and Equation 3-3 respectively.

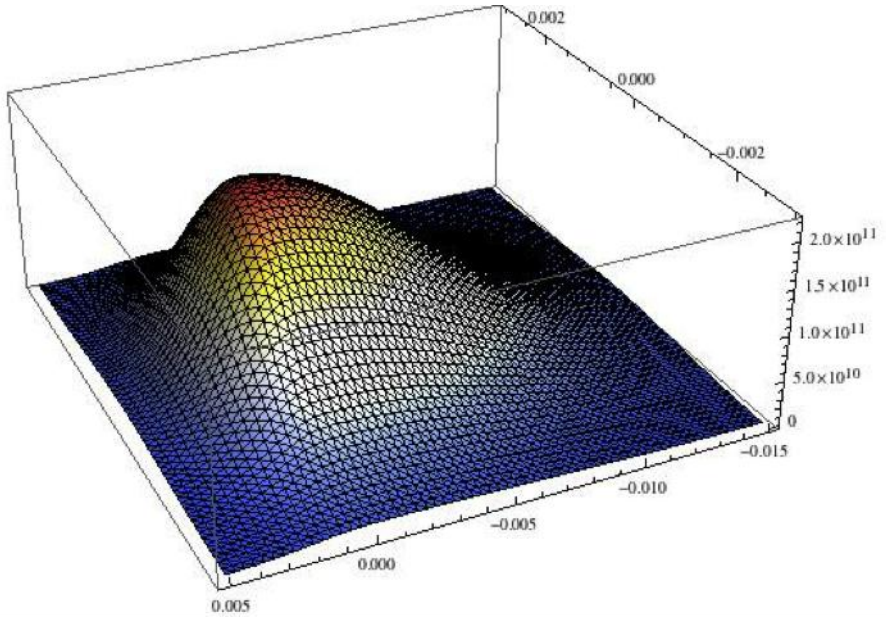

Figure 3-2: Schematic of Power Input in Double Ellipsoid Heat Source Model

$$q(x,y,z,t) = \left(\frac{6\sqrt{3}f_f Q}{abc_f}\right)e^{-3\left(\frac{x^2}{a^2}+\frac{y^2}{b^2}+\frac{z^2}{{c_f}^2}\right)}$$

Equation 3-2

$$q(x,y,z,t) = (\frac{6\sqrt{3}f_r Q}{abc_r})e^{-3(\frac{x^2}{a^2}+\frac{y^2}{b^2}+\frac{z^2}{c_r{}^2})}$$

Equation 3-3

Because the heat source is moving, a Eulerian frame with origin at the center of the heat source is defined. Using a Eulerian frame enables longer time steps for the weld when the analysis approaches steady state. But the Eulerian frame introduces an advection term as in Equation 3-4 into the FEM equation. This term is nonlinear and difficult to solve. Gu (Gu & Goldak, Steady State Thermal Analysis of Welds with Filler Metal Addition, 1993) implemented a weld model in the Eulerian frame. This is basically a Eulerian mesh fixed in space tied to the arc and the part moves under the arc. CWM (Computational Welding Mechanics) analyses usually use a material frame for modeling where the heat source moves in discretized time as steps in series of spot welds. This frame requires sufficiently small time steps to approximate a continuous heat source. The transient heat equation can be solved by the standard Lagrangian finite element method (O. & R., 1989). It maps the Eulerian thermal field into the material mesh by tracking along the flow lines for each time step. Because the elements can be deformed in the forward time step, a semi-Lagrange algorithm can be used that starts from the last time step and back tracks along the flow lines to update the state.

$$\frac{DT(X,t)}{Dt} = \frac{\partial T(x,t)}{dt} + V \cdot \nabla T$$

Equation 3-4

The initial temperature in thermal analysis is usually set to the ambient temperature. A convection boundary condition generates a boundary flux **q** [w/m2] on all external surfaces. This flux is computed from Equation 3-5 with convection coefficient $\mathbf{h_c}$. The equation that could be used to evaluate the convection coefficient $\mathbf{h_c}$, are given in Equation 3-6 (Kumar, Coulombe, Tchernov, Goldak, Johnson, & El-Zein, 2008) for steels in [w/m^{2}K]. **T** is in [K].

$$q = h_c(T - T_{ambient})$$

Equation 3-5

$$h_c = 5 + 0.05(T - 300) + 6 \times 10^{-7}(T - 300)^3$$

Equation 3-6

The model in this paper solves the time dependent system of partial differential equation on a domain defined by an FEM mesh. The domain is dynamic in that it changes with each time step as filler metal is added to the weld pass. The initial condition is often assumed to be a constant temperature of 300 K but the domain can be initialized to any initial temperature field. The material properties are set as temperature dependent. A convection boundary condition is applied to external surfaces. The FEM formulation of the heat equation leads to a set of ordinary differential equations that are integrated in time using a backward Euler integration scheme.

3.3 Stress Analysis in Welding

In the welding process, the stress analysis is quasi-static as the inertial or dynamic forces are sufficiently small that they can be neglected. Therefore at each instant of time, the domain is in static equilibrium. However, the temperature is time dependent and therefore the thermal strain due to thermal expansion is time dependent. If microstructure evolution is included in the model, then the microstructure is time dependent. When a phase changes, then the specific volume, **V**, or density, **ρ**, of the phase changes. The incremental volumetric strain tensor in a time step is $\mathbf{I\Delta V/V}$.

In a time step, the multiplicative deformation gradient **F** contains thermal expansion and phase changes $\mathbf{F}_{\Delta V}$, visco-plastic deformation $\mathbf{F}_{pl}$ and elastic deformation $\mathbf{F}_{el}$, which can be written as the following equation (Mahyar, 2011):

$$F = F_{\Delta V} F_{pl} F_{el}$$

Equation 3-7

$$F_{\Delta V} = I + I\frac{\Delta V}{V}$$

Equation 3-8

$$F_{el} = F F_{\Delta V}^{-1} F_{pl}^{-1}$$

Equation 3-9

The initial condition for each time step is the state at the start of the time step, which is constrained to be an equilibrium state. Given the density **ρ**, and the fourth order elasticity tensor $\mathbf{D}_{el}$ as a 6×6 matrix, the body force **b** and the Green-Lagrange elastic

strain ε_{el}, the program then solves the conservation of momentum equation at the end of each time step that can be written in the form of Equation 3-10, in which inertial forces are ignored.

$$\nabla \cdot \sigma + f = 0$$

Equation 3-10

$$\sigma = D_{el}\varepsilon_{el}$$

Equation 3-11

$$\varepsilon_{el} = \frac{F_{el}^{T}F_{el} - I}{2}$$

Equation 3-12

The initial state often is assumed to be stress free. The classic 3 nodes 6 degree of freedom dirichlet boundary condition (see Figure 3-9) is used to constrain the rigid body modes. The system is solved using a time marching scheme with time step lengths of approximately 1 second during welding and usually an exponentially increasing time step length after welding has stopped. See (Gu & Goldak, Steady State Formulation for Stress and Distortion of Welds, 1994) and (Goldak & Akhlaghi, Computational Welding Mechanics, 2005) for more details.

3.4 Material Description

The steels used in marine structures must meet the specified minimum of the yield strength values, they must be resistant to the initiation of the brittle fracture, and they must be resistant to fatigue.

The steels for commercial ships are commonly subdivided into two strength classes: normal strength (235 MPa yield strength) and higher strength (355 MPa yield strength). (Tither, 1992)

The material that investigated in this research is ASTM A131, Grade DH36, which commonly used in shipyard. This steel is higher strength steel; it belongs to the family of micro-alloyed high strength low alloy steels. The yield strength in it is elevated by precipitation mechanisms and grain refinement through the presence of small amounts

of vanadium, niobium and copper. The chemical composition of this steel is given in Table 3-1.

Component Elements Properties	Metric
Carbon, C	<= 0.18 %
Iron, Fe	98.00%
Manganese, Mn	1.25%
Phosphorous, P	<= 0.040 %
Silicon, Si	0.30%
Sulfur, S	<= 0.050 %

Table 3-1: Chemical composition of ASTM A131, Grade DH36 Steel

In welding simulation, the material properties are dependent on different temperatures. For the simulations, the following properties are needed:

- General properties (Density, Thermal Expansion Rate)
- Thermal properties (Thermal Conductivity, Enthalpy)
- Elastic mechanical properties (Young's Modulus, Poisson's ratio)
- Inelastic mechanical properties (Yield Stress, Work Hardening Rate)

The temperature dependent material properties for thermal and structural calculations are listed in Table 3-2 & Table 3-3.

Temperature	Density	Conductivity	Enthalpy
Kelvin	kg/m^3	W/(m*K)	J/kg
273	7865	46	8.594.E+08
500	7803	45	1.709.E+09
1023	7608.9	29	4.696.E+09
1073	7667.9	26	5.129.E+09
1123	7566.9	26	5.483.E+09
1750	7364.88	32	8.197.E+09
1800	7077.82	320	1.048.E+10
2250	6452.32	320	1.260.E+10

Table 3-2: Thermal Material Properties

Temperature	Young's Modulus	Possion's Ratio	Thermal Expansion Coefficient	Yield Stress	Work Hardening Rate
Kelvin	GPa	-	1/K	MPa	GPa
293	210	0.3	1.38.E-05	355	3.6
673	171	0.3	1.38.E-05	260	2.76
873	87	0.3	1.38.E-05	119.8	1.798
1073	39	0.3	-9.10.E-06	34.2	0.513
1473	11.53	0.3	3.15.E-04	5	0.05
1773	1	0.48	3.15.E-04	5	0.05

Table 3-3: Structural Material Properties

From the mechanical properties, when the temperature is higher than about 1073 K, which is the material soften temperature, this steel would lose strength. At this point, the material has not melted, it is still solid, but acting like a rubber.

3.5 Mesh Grading

In welding simulation, the choice of finite elements has a significant influence on both accuracy and computational speed. For most applications, the linear hexahedron is preferred to both linear and the quadratic tetrahedron (Cifuentes, 1992). Mesh refinement is usually divided into h-refinement, p-refinement or a combination. In h-refinement, the polynomial degree of the shape function is preserved whereas the element density is changed and vice versa for p-refinement. Szabo (Szabo, 1984) showed that h-refinement is superior to p-refinement in non-smooth stress field, which as in welding process. And in result of that, the linear hexahedrons and h-refinement are chosen for welding.

The basic problem in welding is discretization of a domain holding a localized region with large gradients in field variables. Thermal, microstructure and mechanical effects require the weld zone to be solved under a very fine mesh, in contrast the far field region can be solved by a relatively coarse mesh. The variation in such a mesh density may be several orders of magnitude in welding process simulations. Mesh grading in three dimensions using standard elements, illustrated in Figure 3-3, usually results in distorted element shapes and inefficient grading. The three-dimensional grading with regular undistorted elements, as shown in Figure 3-4, can be obtained by using constraint

equations to couple DOFs or by a transition element such as the graded element developed by McDill (McDill, J., J., & Bibby, 1987).

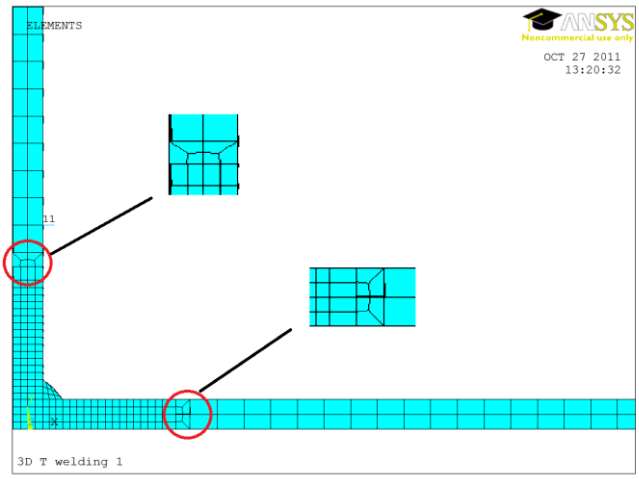

Figure 3-3: 3D Mesh Grading Using Standard Method

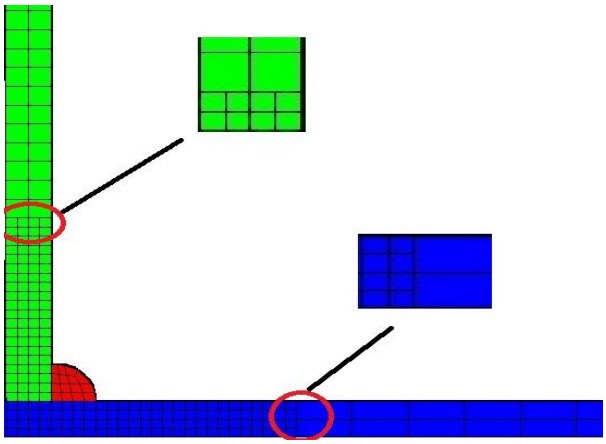

Figure 3-4: Improved 3D Mesh Grading

In this research, the standard three-dimensional grading was used in ANSYS as it is very complicated and time consuming to implement the improved three-dimensional grading in ANSYS; in VrWeld, the improved three-dimensional grading with regular undistorted elements by using the displacement constraint equations is chosen. This is extremely efficient as it allows large variation in mesh density within a short distance and the number of elements is therefore minimized. The use of this technique is formulated by a set of meshing parameters describing the basic element size, the maximum levels of refinement allowed, the position of the heat source and the additional scaling parameters. These parameters are defined as the input variables in VrWeld.

3.6 Weld Metal Deposition

The finite element welding simulation consisted of sequential transient thermal and nonlinear structural analysis. The thermal analysis used a moving heat source to represent the welding torch, where each load step represented as an increment in the position of the heat source along the weld path. In this research, the element active and deactivate technique was used in both ANSYS (element death and birth) and VrWeld (silent element).

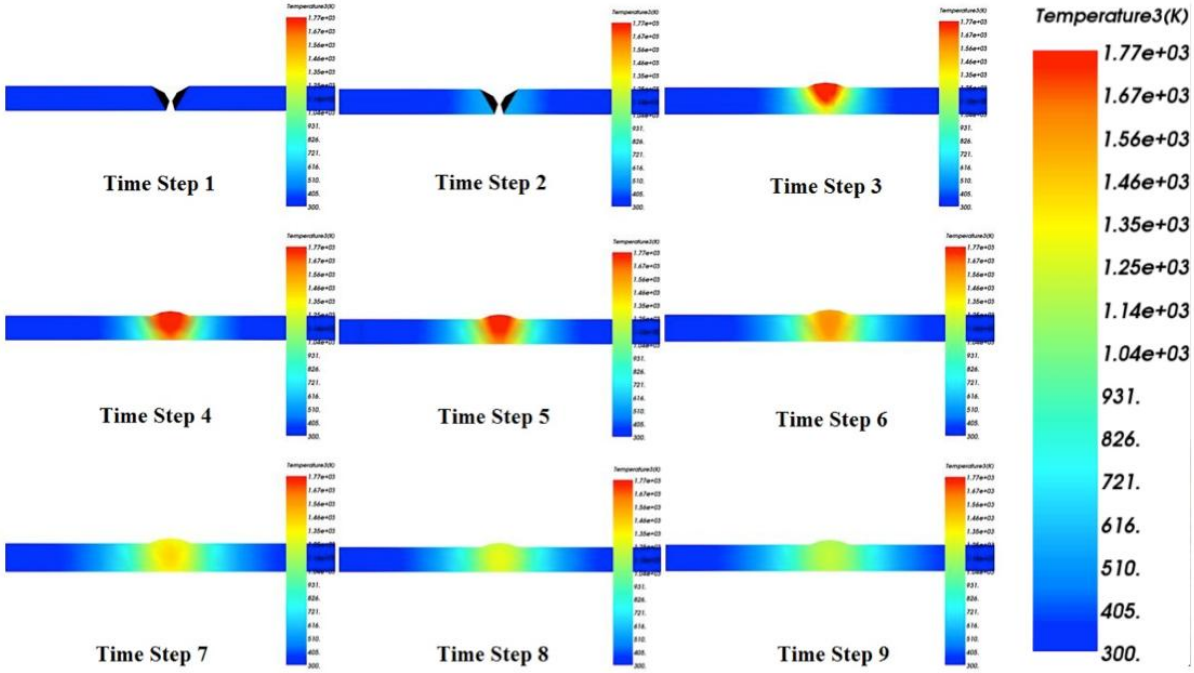

Figure 3-5: Schematic of Temperature During Heat Source Passing Through

At first, all the weld filling material elements are deactivated, as they do not exist in practice. As the heat source progressed along the weld path, the model defined which weld elements were activated while the welding pool center approached, Figure 3-5 shows how the temperature distributed while the heat source passed through. The transient temperature field from the thermal analysis was used as a series of loads in the subsequent structural analysis where each load step represented an increment in the welding torch position along the weld path. The element active and deactivate was also used in the structural analysis to activate weld elements behind the welding torch once their temperature fell below the cut-off temperature, which is a temperature above that the material is deemed to have lost considerable strength. When the temperature was

above that temperature, the material was treated as melted and the stress is set as zero, which is shown in Figure 3-6.

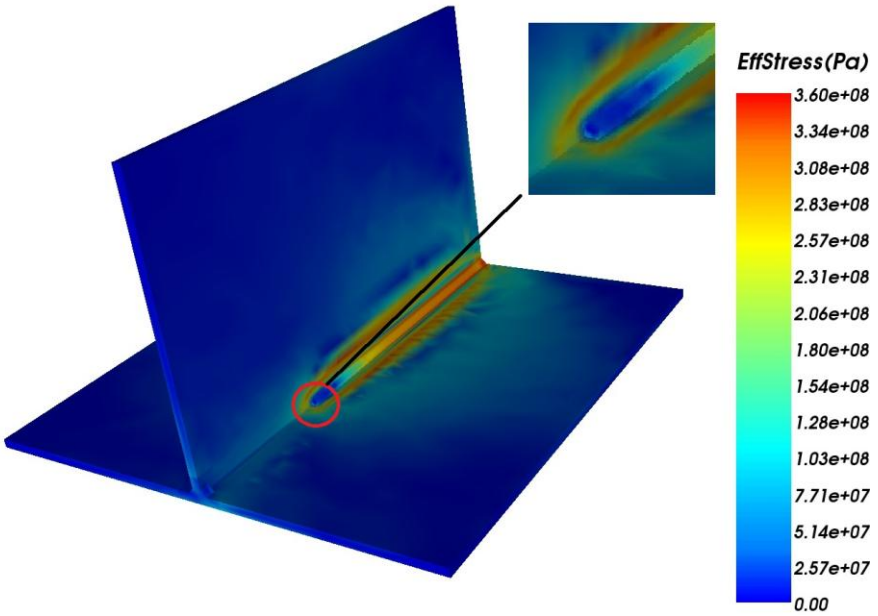

Figure 3-6: Example of Effective Stress by using Element active and deactivate

3.7 Implementation In FEM Software

Together with the discussed in the above sections, the study performed on the three – dimensional transient thermal-elasto-plastic analysis used the indirect coupling method. In the simulation, a thermal modeling is used to calculate the temperature distribution during the welding process, in the thermal model, the double ellipsoidal density power function was use as heat source and the element activate and deactivate technique need to represent the weld filling. At first, all the weld filling material elements are deactivated. As the heat source progressed along the weld path, the model defined the weld elements to be reactivated as the welding pool center approached. The detailed procedure is illustrated in Figure 3-7.

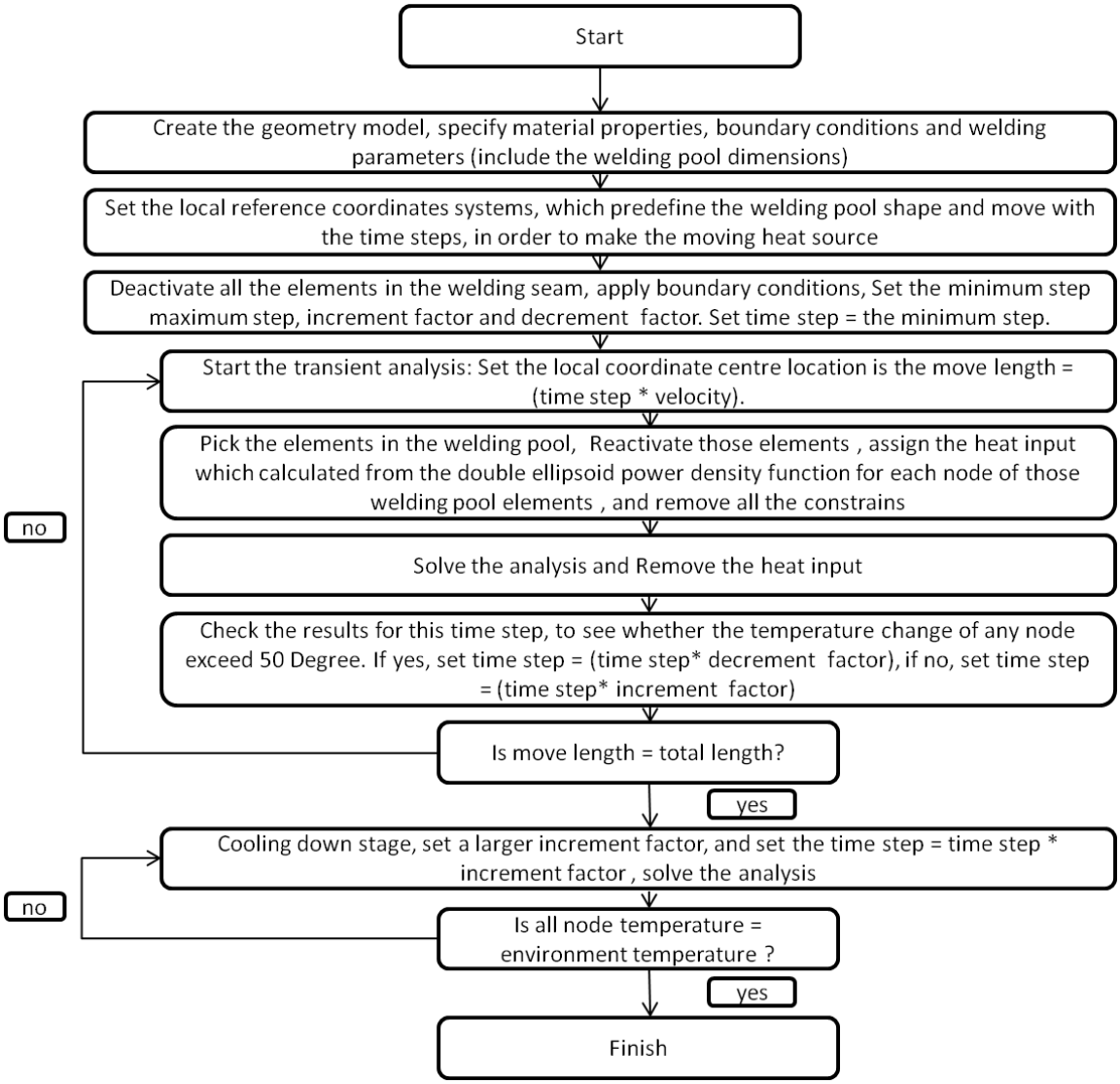

Figure 3-7: Procedure of Thermal Analysis

In the structural analysis, the weld filling was simulated by the same method as the thermal analysis, but the cut-off temperature was adopted. The thermal model results are used to determine the maximum temperature throughout the weld cycle. If the average nodes temperature of the element has reached the designed cut-off temperature, the element is deactivated, its material properties are set to fusion zone values and the reference temperature set to cut-off temperature in order to get the correct thermal strain. Once the elements have been through the above steps, the structure analysis will start a transient analysis by loading the corresponding load step from the thermal analysis. For the heating process, the whole model will be checked for each load step to determine which nodes have reached values equal to or greater that the cut-off temperature. When this happens the corresponding element is reactivated and all of its body loads set to the

cut-off temperature value. This is repeated until all elements have been activated, then the structural analysis is continued until the structure has cooled to the room temperature. The detailed procedure is illustrated in Figure 3-8.

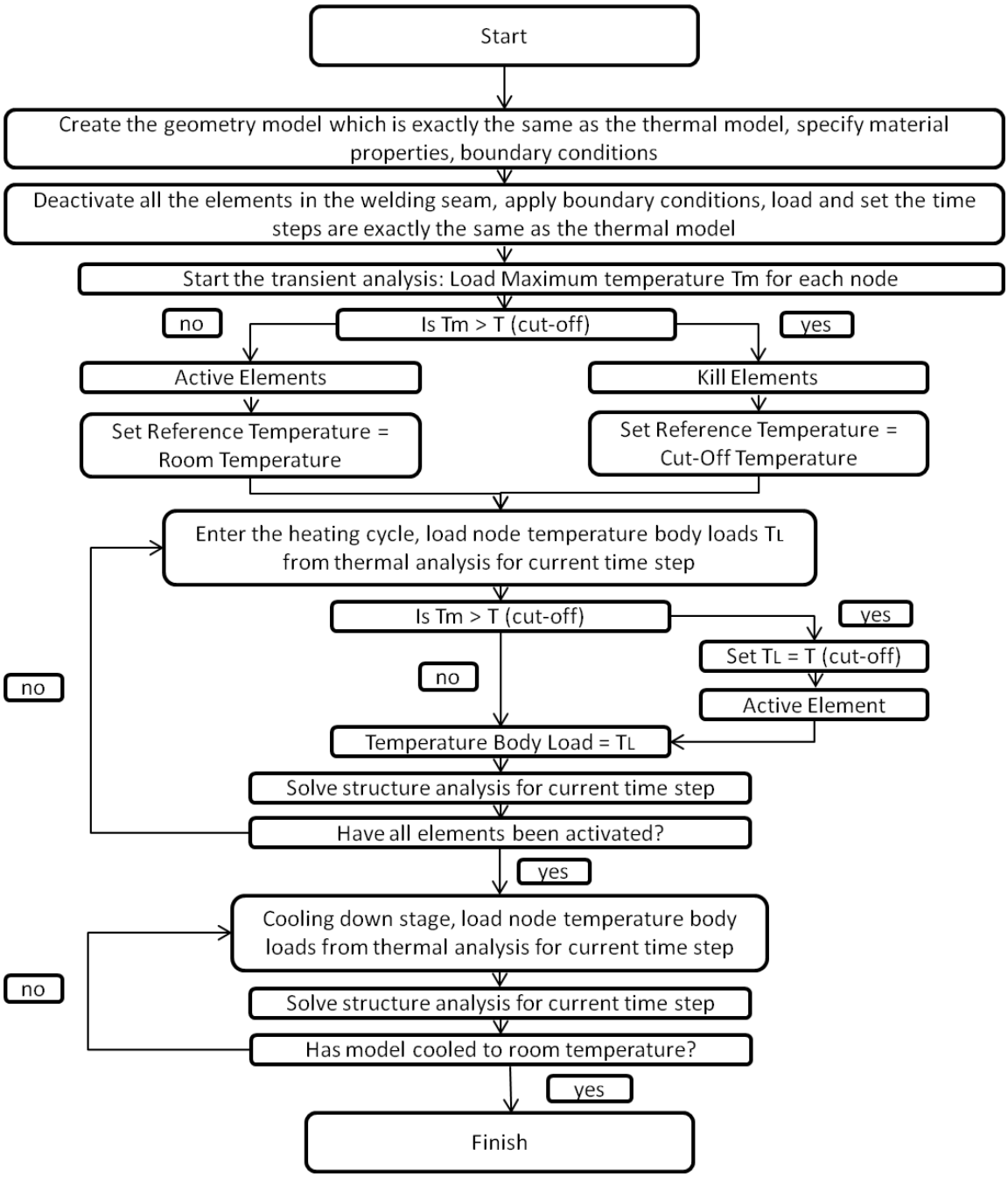

Figure 3-8: Procedure of Structural Analysis

The simulation methodology described above was implemented in both ANSYS and VrWeld. When implementing it in ANSYS, as the calculation process is not stable by the

un-convergence problem, the author also write a command to modify the time step automatically, which make sure the temperature increment is smaller than 50 K during each time step. And this method has not been implemented in ANSYS before.

3.8 Simulation of Butt and Fillet Welding Process

3.8.1 Butt Welding

Structural and thermal finite element analyses were performed using VrWeld to calculate temperature distribution, residual stresses and distortions in a fillet welding process. The simulation consisted of two analyses. The first was a transient thermal analysis where the temperature distribution caused by a travelling heat source was determined. The second step consisted of a nonlinear structural analysis that was solved as a series of sequential load steps. Each load step represented an increment in the position of the heat source in the direction of welding. The temperatures from the thermal analysis associated with each load step were applied as loads in the structural analysis. This process was repeated several times until the welding was completed.

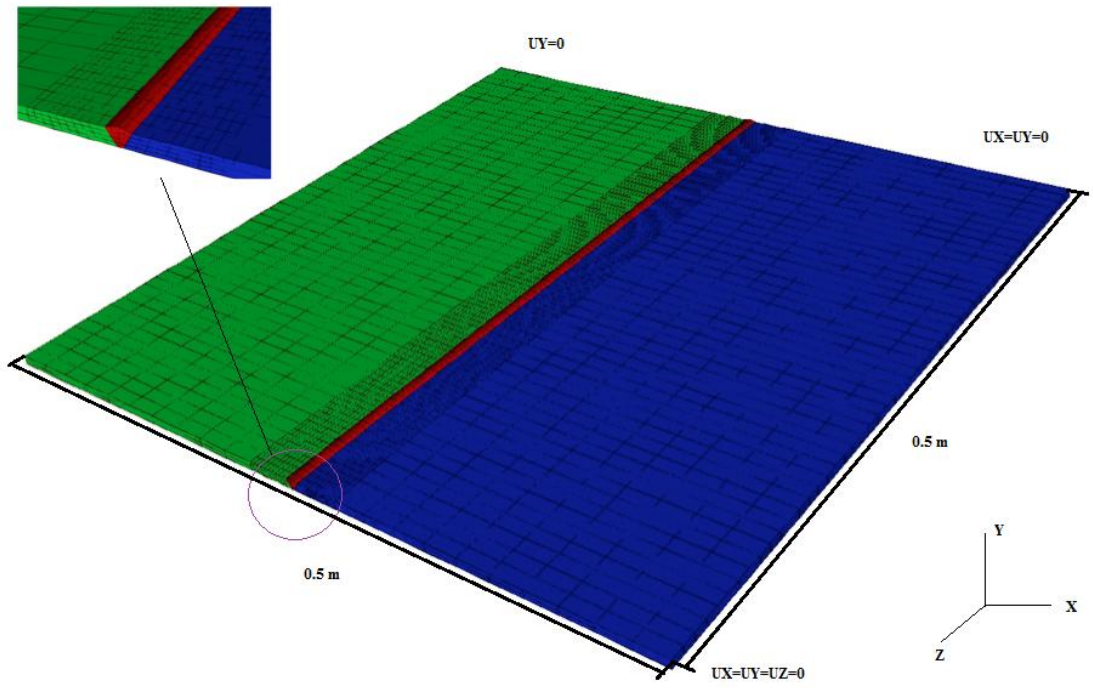

Figure 3-9: Butt-Welding Geometry, Mesh & Boundary Conditions

The plates are made from ASTM A131, Grade DH36 steel, for which the temperature dependent material properties have been listed before, and the size is 250 mm x 500 mm with a thickness of 6 mm. The geometry, mesh and the boundary conditions of this model are shown in Figure 3-9. The mesh size in the weld joint is 0.002 m and the mesh size in the body part is 0.02 m. According to the figure, the advanced mesh technique is used and the boundary condition is the classic three nodes, six degree of freedoms constraint, which can prevent the structure rigid body movement but the structure can be stretched and compressed freely The complete model contains approximately 14,804 elements and 19,259 nodes. The moving heat source uses the double heat ellipsoid power density function and the welding method and parameters are listed in Table 3-4.

Shielding Gas	Pass Number	Length of welds (m)	Current (A)	Voltage (V)	Speed (m/s)
CO2	1	0.5	150	22	0.005

Table 3-4: Butt Welding Method and Conditions

During the simulation process, the element activate and deactivate technique was used to simulate the welding deposition. This is a good model of the welding process. The procedure of how to perform it in the FEM software has been given in Figure 3-7. And the cut off temperature is set as the melting temperature 1773 K. From Figure 3-10, the results shows the plates are not connected at the beginning, then once the welding pool is formed, it will keep moving forward until the welding process finishes. It can be seen that the temperature distribution and the magnitudes around the welding pool do not change during the welding process. As time passes, only the location of the temperature field changes, which indicates that this kind of temperature distribution is in a quasi-steady state. Due to the use of the element activate and deactivate technique, all the elements in the welding seam do not have a heating part but only a cooling process because while they are reactivated, they have been already given a melting temperature. The elements, which are in the heat affected zone, have both heating and cooling process, which is also one of reasons that the element death and birth technique make the calculations more accurate.

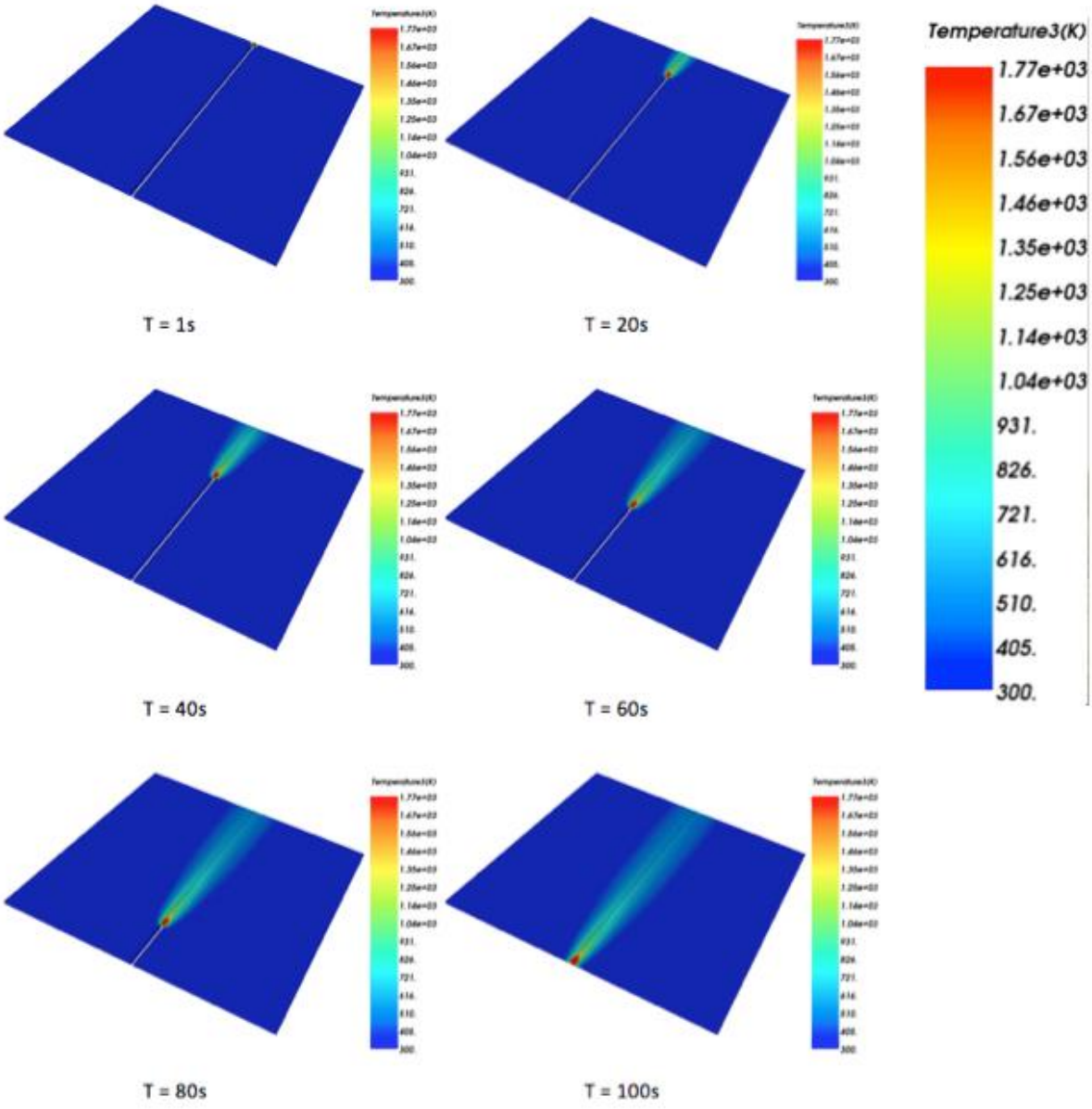

Figure 3-10: Dynamic temperature distribution during welding process

Figure 3-11 verifies the above conclusions about the quasi-steady state, which shows the temperature profiles at each time steps are exactly the same and the maximum temperature is 2078.41 K. The solid-liquid temperature for this material is 1773 K and the material softening temperature is 1073 K. According to Figure 3-11, it can be found that the lengths of liquid part and the material softening part in the welding line direction are 0.012 m and 0.047 m during the welding process. The heat caused by a moving heat source has a consistent typical, though complicated effect on the stress in the areas

around the welding pool created by the source. So it is necessary to analyze the size of the liquid part and softened material part during the welding process.

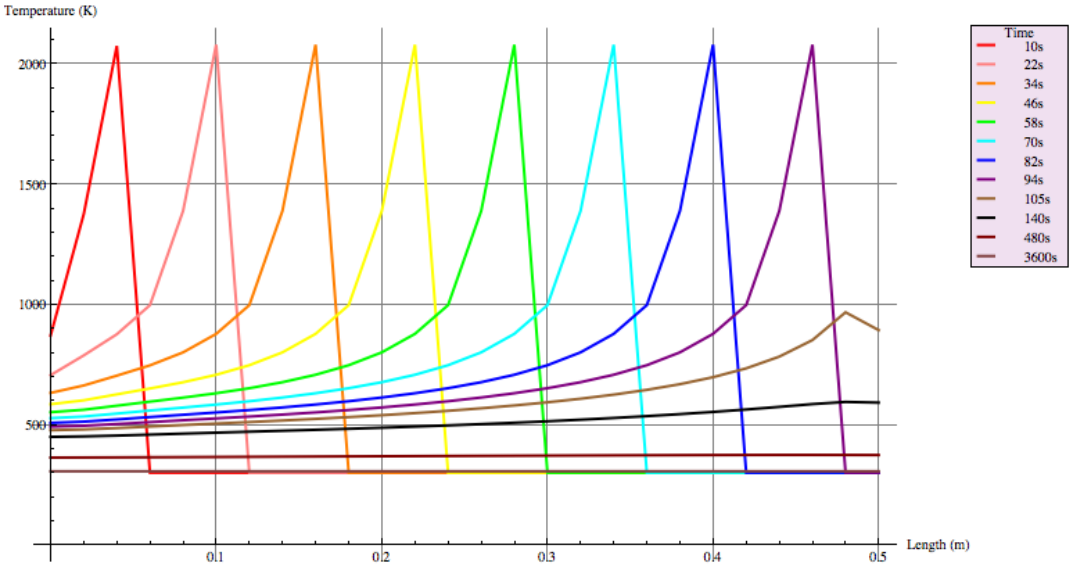

Figure 3-11: Temperature Distribution of Welding Line at different time

From Figure 3-12, it can be seen that the expanding cells push the butt edges of two plates together at the start of welding; and at the end of welding, the expanding cells ahead of the welding pool and the contracting cells after the welding pool push the butt edges of two plates apart. During the welding process, the base metal area ahead of the welding pool swells due to the expansion force caused by heating but the area in the welding pool doesn't bear any forces as it is liquid; the area after the welding pool shrinks as the contraction force caused by cooling. The boundary conditions used in this model allow all movement except the rigid body movement, furthermore, the element activate and deactivate technique makes sure the welding seam is empty before the welding deposition. This kind of simulation, which is most accurate, could not be found in any literature as the reported studies did not use the element active and deactivate technique in the structural simulation of welding process as it introduces a serious convergence problems into the thermal stress analysis when reviewed by (Pilipenko, 2001).

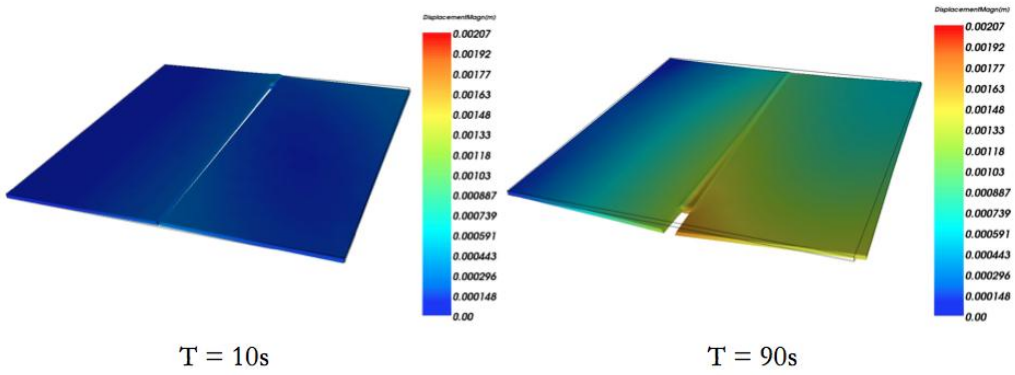

Figure 3-12: Displacement representation of start and end of the welding process

Figure 3-13 & Figure 3-14 give an overall representation of the residual stress distributions calculated for the butt-welding process. These figures are the result of 3D-model runs and help to create an overall impression of the complexity of stress-state caused by the welding procedure.

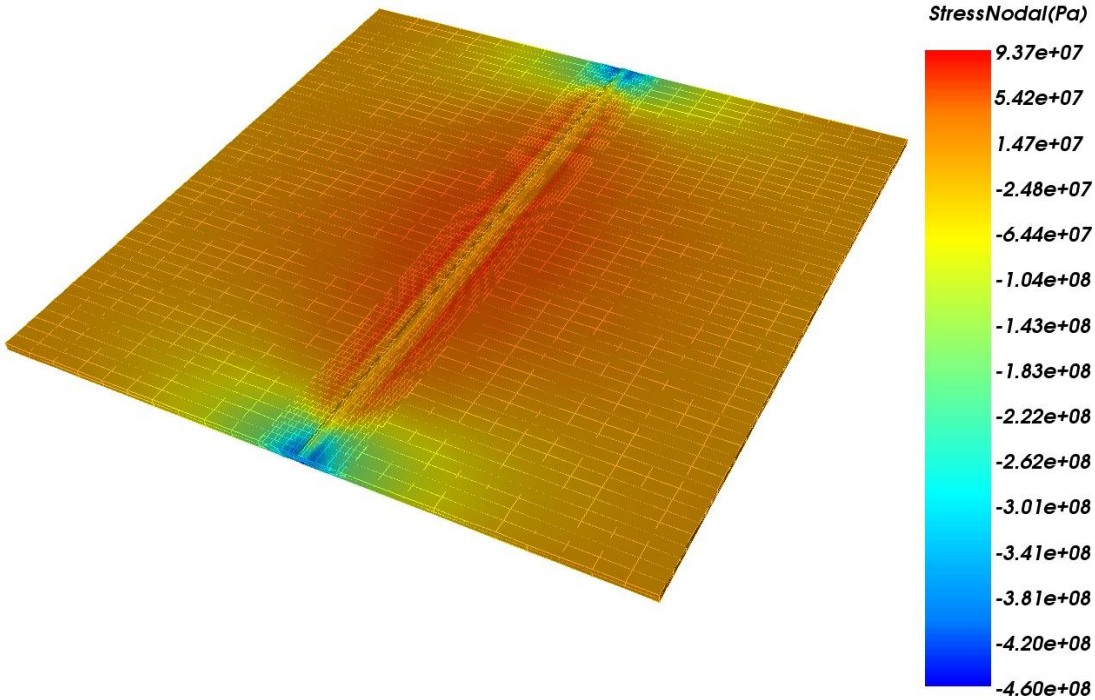

Figure 3-13: Distribution of the transverse stress

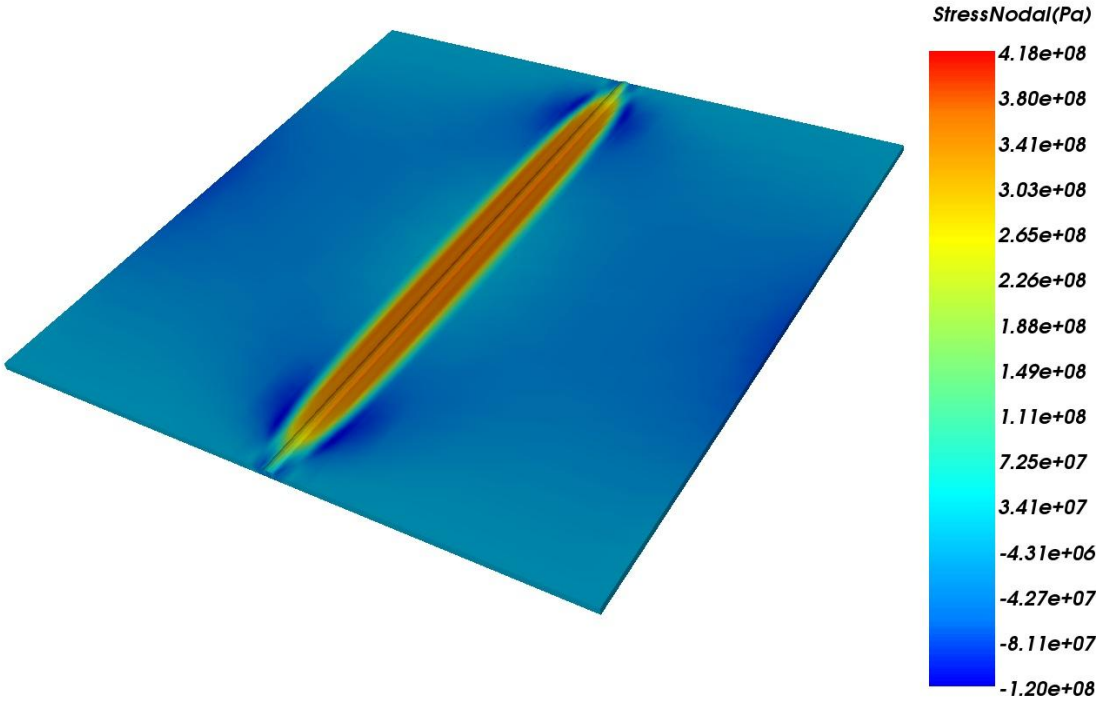

Figure 3-14: Distribution of the longitudinal stress

The diminishing of end effects agrees with Saint-Venant's principle. "For bodies extended in two or three dimensions the stress or strain due to loading on a small part of the body may be expected to diminish with distance on account of geometrical divergence whether or not the resultant is zero" (S P Timoshenko, 1970). From the above figures, it can be seen that the length of the chosen model is not sufficient to unify the stress distribution in the middle of the plate from the end effects. In other words, if the length were great enough, the stress distribution would not change with longitudinal direction after some distance from the edge.

With increasing temperature ahead of the moving heat source, the points close to the weld line start to experience compression in the longitudinal direction. Then, due to higher temperature lowering the yielding point, the value of the longitudinal stress reduces to zero. Stresses in the regions a short distance from the arc are compressive, because the expansion of these areas is restrained by the surrounding metal where the temperature is lower. However, stresses in the areas further away from the weld arc are tensile and balance with compressive stresses in the areas near the weld. At some distance behind the weld arc, the temperature drops sufficiently for the material to be

stiff enough to resist the deformation caused by the temperature change. Due to cooling the areas close to the weld contract and cause tensile stresses. After a certain time, the temperature change due to welding diminishes. High tensile longitudinal stresses are produced near the weld. The longitudinal stresses reach a value about 20% higher than the yielding point for room temperature. Also, in the regions away from the weld, compressive stresses arise, which balance the temperature along the welds.

3.8.2 Fillet Welding

The simulation of fillet-welding process was also performed using both VrWeld and ANSYS to calculate the temperature distribution, residual stresses and distortions

Shielding Gas	Pass Number	Length of Leg (m)	Current (A)	Voltage (V)	Speed (m/s)
CO2	2	0.006	270	28	6.67

Table 3-5: Fillet Welding Method and Conditions

The plate and stiffener are both made from ASTM A131, Grade DH36 steel. The plate is 500 mm x 500 mm with a thickness of 9 mm and the stiffener is 300 mm x 500 mm with a thickness of 9 mm. The stiffener is connected to the plate by 6 mm fillet welds deposited on both sides of the stiffener with the welding conditions illustrated in Table 3-5. The geometry of this model is shown in Figure 3-15. Tack welds with a length of approximately 10 mm were pre-welded on both sides of the stiffener at the middle of the length and at both ends. And the two weld passes are sequential welded. The complete model in this model by VrWeld contains approximately 17,000 elements and 19,000 nodes.

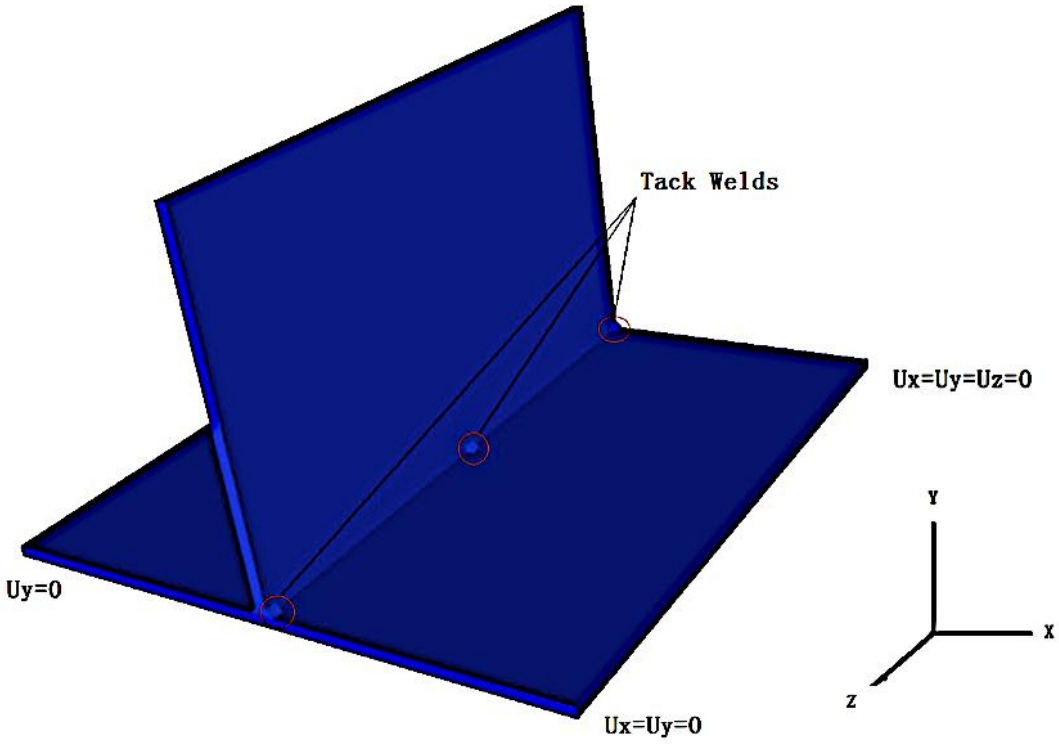

Figure 3-15: Stiffened Plate Geometry and Boundary Conditions

In order to validate the welding simulation by comparison with published experimental data, the boundary conditions were set up as the same as the experiment published by Deng et. (Deng, Liang, & Murakawa, 2007). The boundary condition applied ensure the model could deform freely in any direction and rigid body motions were prevented as shown in Figure 3-15.

The total welding time in this simulation is 150 seconds and the time step is 0.75 s. Due to the use of advanced mesh and subdomain methods to improve the computation efficiency, the whole analysis only took about 2 hours CPU time on a 6 Core i7 X980 @ 3.33GHz processor with 12 GB of memory. The author also ran exactly the same model, but without advanced mesh and sub-domain methods in ANSYS, which took the smaller time step as 0.25 s and used a more fine mesh. A coarse mesh caused a serious convergence problem. In ANSYS, the element type of solid model meshes used is Solid70 and Solid185. Since the weld does not fully penetrate the stiffener, the contact between the plate and stiffener was modeled using Combin39 nonlinear spring elements to connect coincident nodes at the plate-stiffener interface. Nonlinear springs were used in place of contact elements to avoid the extensive computation time associated with

contact algorithms. The spring elements were given a high compressive stiffness and low tensile stiffness in the direction normal to the plate-stiffener interface and zero stiffness in the other two orthogonal directions so that sliding and separation were permitted. An elasto-plastic material model is used with von Mises failure criteria and associated flow rule, which states that the plastic flow is orthogonal to the yield surface. Nonlinearities due to large strain and displacement are considered. The model took about 38 hours by using the same computer. And the results predicted by these models are almost the same. From Figure 3-16, it can be seen that the tack welds in the center of longitudinal direction present the maximum VonMise stress, because they have experienced both heating and cooling processes. Furthermore, they are also used to prevent the rigid body movement of the stiffener. Figure 3-17 shows the simulated distribution of longitudinal residual stress in the upper surface of the plate for a transverse cross section at the middle of length for both VrWeld and ANSYS. From the comparison, the biggest difference happened where the welds are deposited, which is due to the different mesh densities from the two models. The simulated results showed that the highest tensile residual stress also occurred at where the welds were deposited and the values are 422 MPa (VrWeld) and 435 MPa (ANSYS), which are both higher than the yield stress of the material due to work hardening which has been included in both simulations.

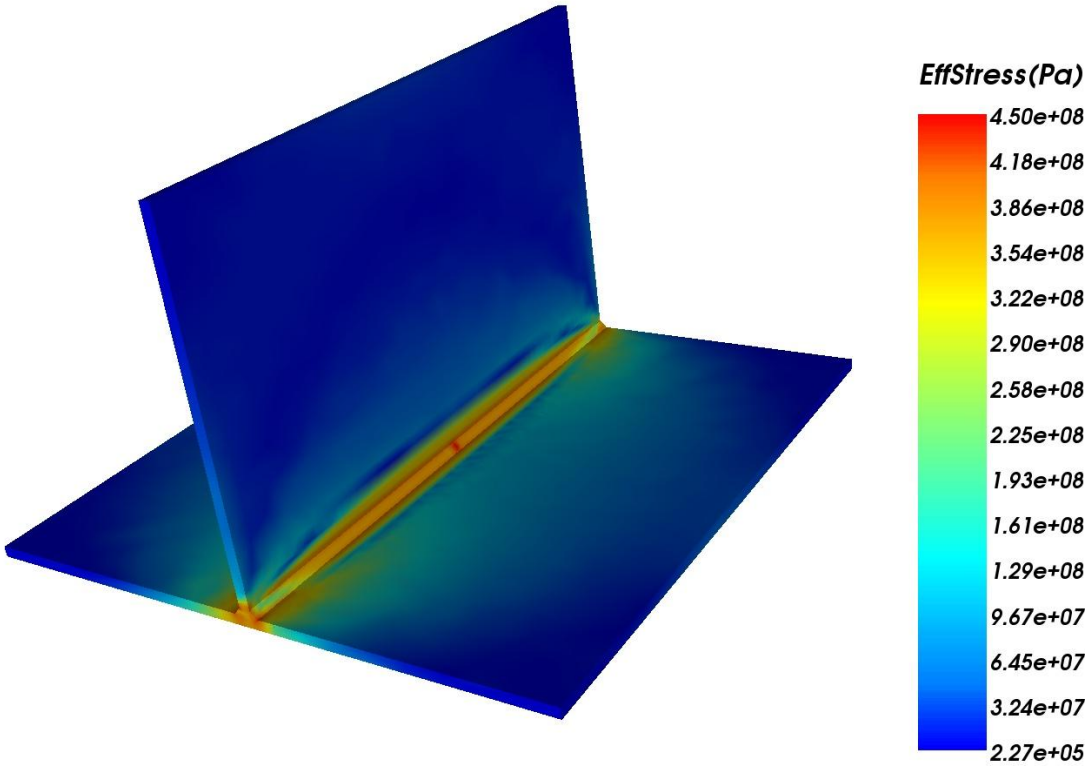

Figure 3-16: Distribution of the overall VonMise stress

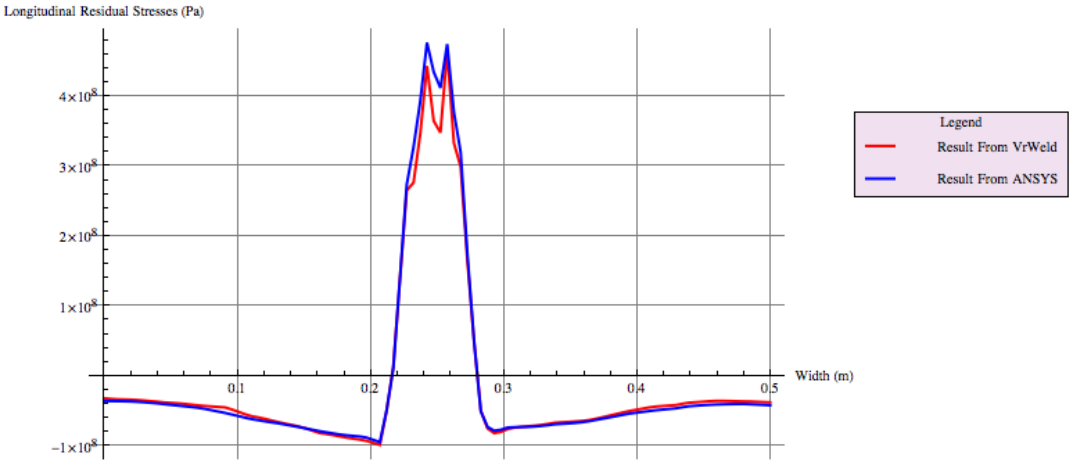

Figure 3-17: Longitudinal Residual Stresses at Upper Surface of The Mid-Length in Plate

The finite element model was validated by comparison the simulated deformation with the experimental results published by (Deng, Liang, & Murakawa, 2007). This publication was useful due to it contains the temperature dependent material properties, which is essential for the accurate welding simulation. There are also some other welding experiments are available, but none of them consider the flat bar stiffened plate jointed by GMAW process. In this experiment, the stiffener and the plate were first tack welded and then a welding robot continuous a single pass fillet welds of approximately 6 mm on both sides of the stiffener. The conditions were just the same as setting in finite element model of this study. Figure 3-18 shows the deformed shape of the stiffened plate after welding obtained from the finite element model.

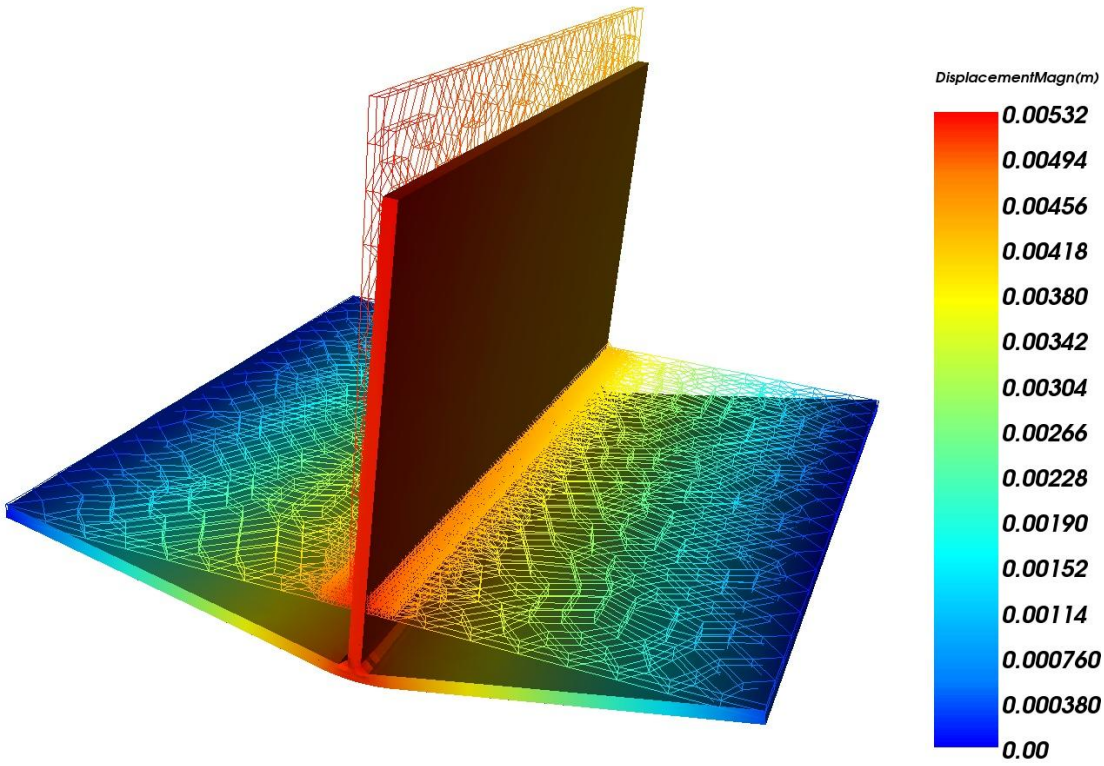

Figure 3-18: Welding deformation predicted by FEM for validation

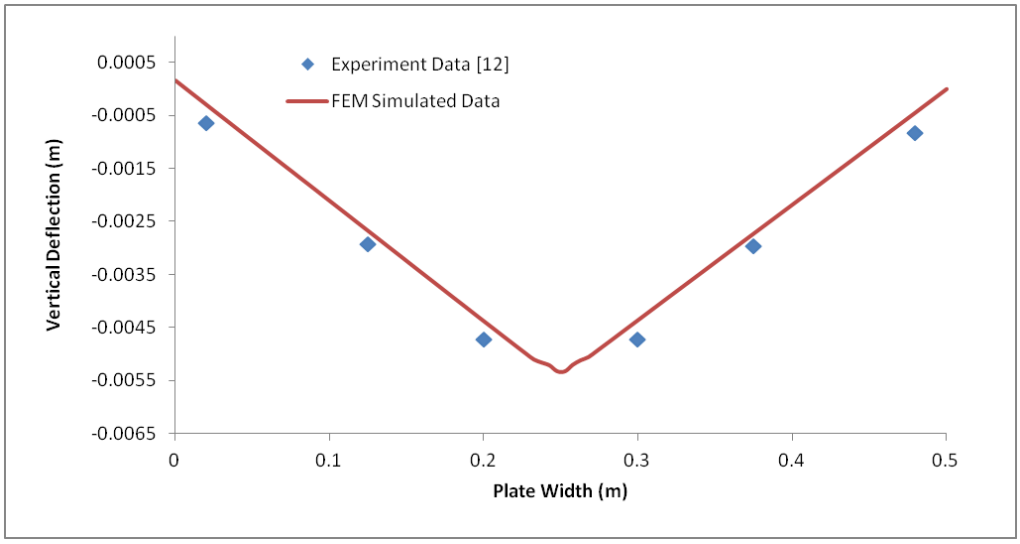

Figure 3-19: Vertical Deflection of Plate at The Middle of Length

A comparison of vertical deflection at the middle length of the plate, which shows in Figure 3-19, demonstrated good agreement between the finite element model predictions using the current model and experimental results. The FEM simulated vertical deflection at the middle of the plate is 0.00532 m, and the angular distortion is 0.02. The average

difference between the simulated data and experiment one is about 6.46%, which is acceptable. The residual stresses results were not given in this literature, so that the simulated data was not compared.

According to the idealized weld induced residual stress distribution used in ship design, the tensile longitudinal stress and compressive transverse stress is assumed as material yield stress. And the following process is how to consider the weld induced distortion effect in the ship industry:

b/t (plate) = 500 / 9 = 55.5

δ_0 = 0.005

δ_0 /t = 0.005 / 0.009 = 0.556 = 0.19β^2

Which means the welding induced distortion for this fillet welding is average. But in this model, the boundary condition applied is not the same as the real situation, because the main purpose of this study is to understand the residual stresses distributions.

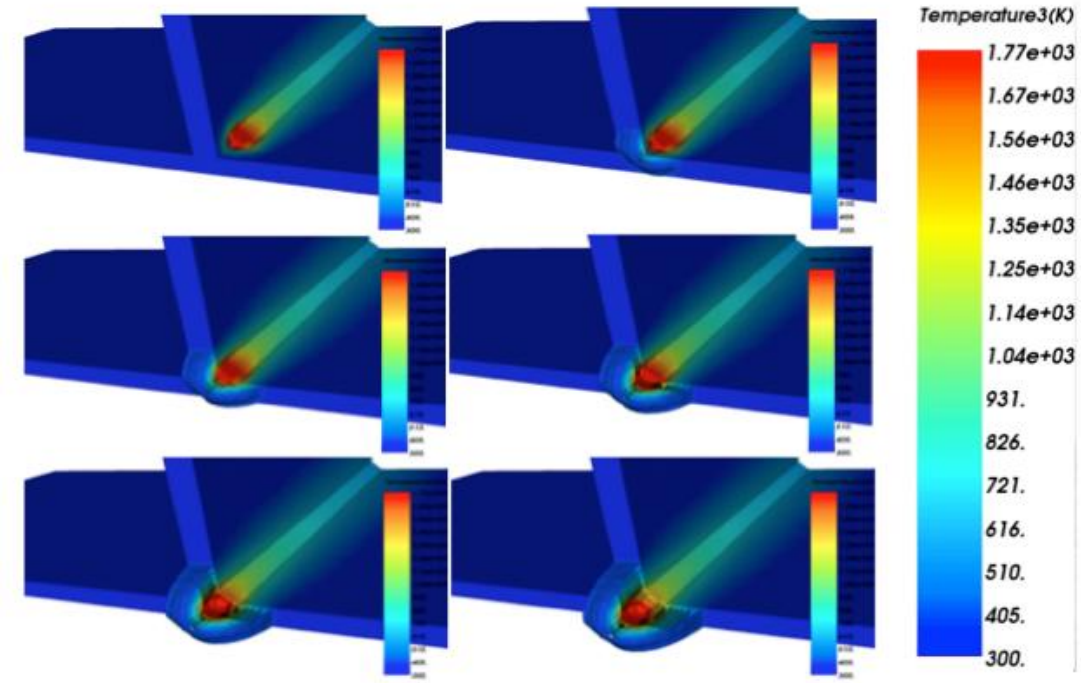

Figure 3-20: Moving Welding Pool

Figure 3-20 shows how the welding pool temperature profile pass the mid-cross section, it can be seen that the filling metal and a small portion of base material was full melt, which ensured a good welding quality. The temperature histories at point A and B at the middle of length in the first 250 seconds was plotted in Figure 3-21. Before the heat source reached this section, there is no filling material and the temperature remains as the ambient temperature 293K, which shows that the conduction effect is not dramatic in the direction of welding compare to the welding speed. When the heat source reached this cross section, the temperature suddenly rose to 1872 K at point A, and the peak temperature at point B was 790 K, which was obtained 5.22 seconds later than point A. After the maximum temperatures passed, there are also smaller peaks followed when the filling material was deposited on the other side of the stiffener. The results of peak temperatures at point A and B, which predicted by Deng (Deng, Liang, & Murakawa, 2007), were 1973 K and 688 K. The different predicted results are mainly due to the material properties used in these models have a slightly difference and the use of element active and deactivate technique in the present analysis.

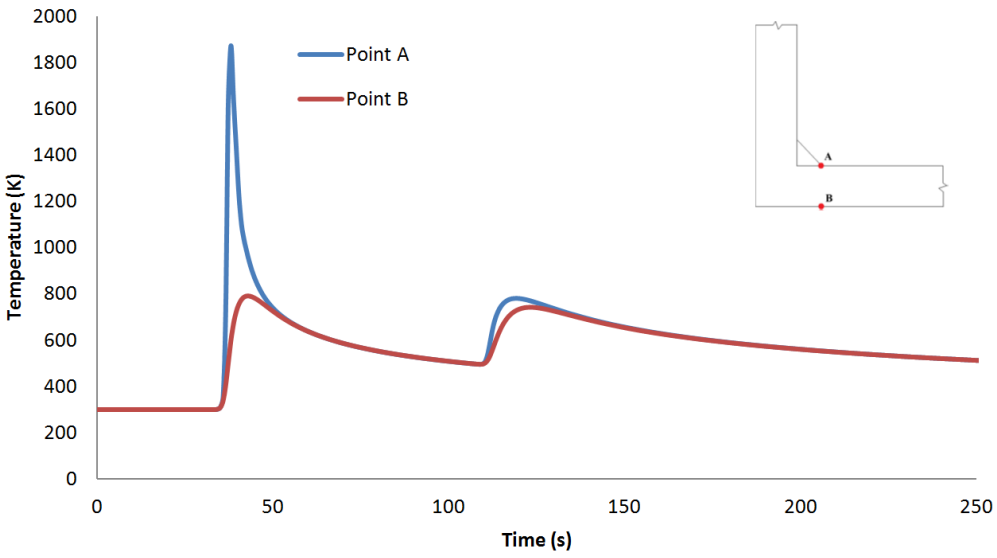

Figure 3-21: Temperature Histories at Point A and B

3.9 Conclusions

In this chapter, a finite element model based on ANSYS and VrWeld software that is capable of simulating the thermo-mechanical welding process was developed and validated by comparison with experimental data. It has been shown that distortions

predicted by the finite element model agree well with measured data from previous literature and that the numerically obtained residual stress distribution is compared and agreed by both ANSYS and VrWeld software. In this model, the temperature dependent material properties were used to take the microstructure, material melting and phase changing effect into account; the element activate and deactivate technique, which implemented in both thermal and mechanical simulations, is used for making the simulation more accurate and closer to practical; it is found that the advanced mesh technique and subdomain method is capable of accelerating the simulation speed dramatically by comparing the calculation speed of ANSYS and VrWeld.

Chapter 4 Analysis of Welding Residual Stress Distributions

Welding stresses can be temporary or residual. The temporary stresses only exist in a specific moment of the non-stationary heating and cooling process. The residual stresses can be found after the whole welding process and the cooling down are completed. The welding residual stresses are internal stresses, which exist in a body without external forces applied; they are in equilibrium with themselves within the limits of the structure, and an isotropic material formulation is usually suitable for the determination of such stresses.

In this chapter, a detailed study for the butt-welding residual stresses is reported. In marine structures, the welding size is usually big, so the thickness effect can be neglected and the transverse (perpendicular to the welding seam) and longitudinal (parallel to the welding seam) residual stresses are usually the center of attention. For a better analysis on these subjects, it is necessary to obtain the results on the entire histories of stresses to which the material is subjected during the process of welding. During the welding process, the welds and a limited portion of the base material are heated to a very high temperature and then cooled down to room temperature. Within the thermal cycle, the temperature distribution changes with time and the material properties depend on temperature. In order to perform a reliable analysis, the above-mentioned factors should be taken into account, so the model of a 2D butt-welding by using 3D element was chosen. And a simplified method is also derived for comparing with the FEM results.

The plates are made from ASTM A131, Grade DH36 steel, for which the temperature dependent material properties have been listed in Chapter 3, and the size is 250 mm x 500 mm with a thickness of 6 mm. The geometry, mesh and the boundary conditions of this model are shown in Figure 4-1. This boundary condition is the classic three node support with a total of six degree of freedoms constrained, which can prevent the structure from the rigid body movement but can be stretched and compressed freely (see Figure 4-1). In this model, the element activate and deactivate technique is also used for simulating the welds deposition and there is no tack welds. The complete model contains approximately 5,600 elements and 11,716 nodes. The moving heat source still using the double heat ellipsoid power density function and the welding method and parameters are listed in Table 4-1.

Shielding Gas	Pass Number	Length of welds (m)	Current (A)	Voltage (V)	Speed (m/s)
CO2	1	0.5	150	20	0.005

Table 4-1: Welding Method and Conditions

During the simulation, the cut-off temperature is set as 1773 K, and the silent elements technique is used to perform the weld metal deposition and the subdomain method is used to increase the calculation efficiency, as described in Chapter 3.

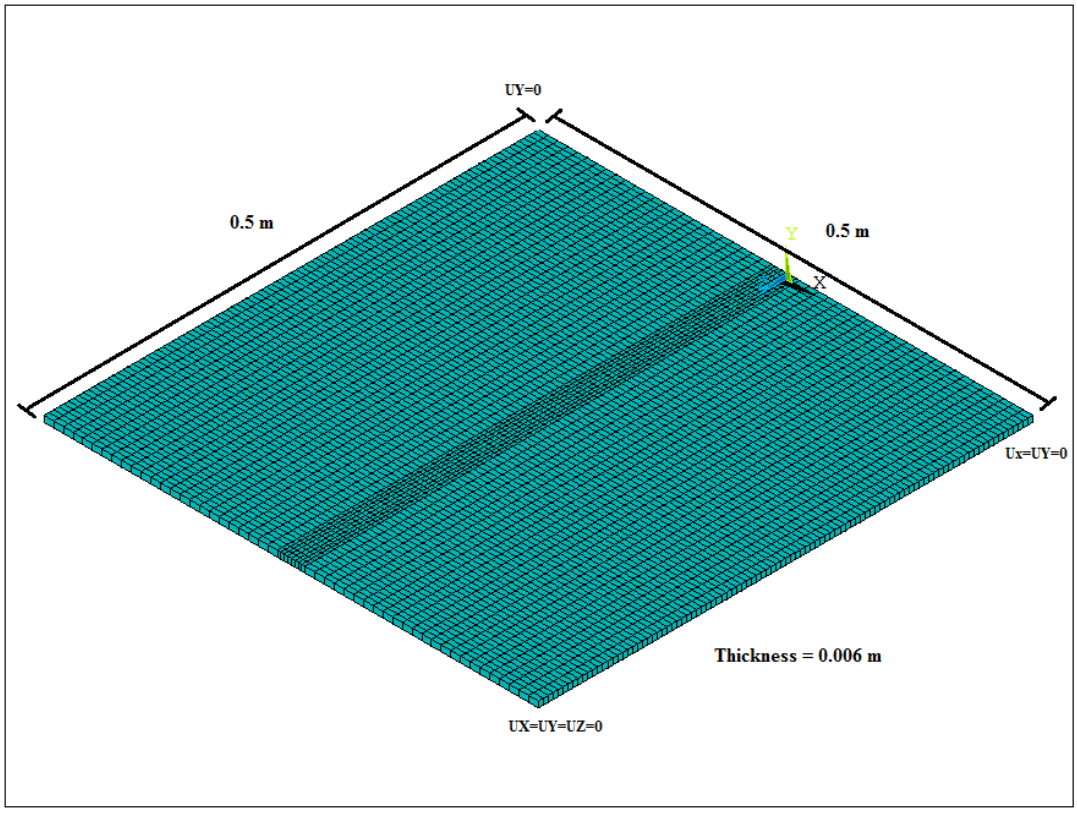

Figure 4-1: Butt Welding Geometry and Boundary Conditions

Due to the symmetrical nature of the geometry and the boundary condition applied to this model, the results are also symmetrical to the (Y, Z) cross section. There is no need to look at the whole results but a half. The author outputs all the results from the Finite

Element Software into Mathematica Software, which was more convenient to program for post processing the results.

4.1 Simple Method of Residual Stress Prediction

4.1.1 Force and Moment Equilibrium For Butt Welding

Welding residual stresses remain from the previous welding operation, they are internal self equilibrating stresses. The model discussed in this chapter doesn't have any external load, so the residual stresses are always in equilibrium during the welding process.

Figure 4-2 shows that after the welding and cooling process, the welds have both transverse and longitudinal shrinkages which, because they are restrained by the plates, are the main reason for the production of welding residual stresses.

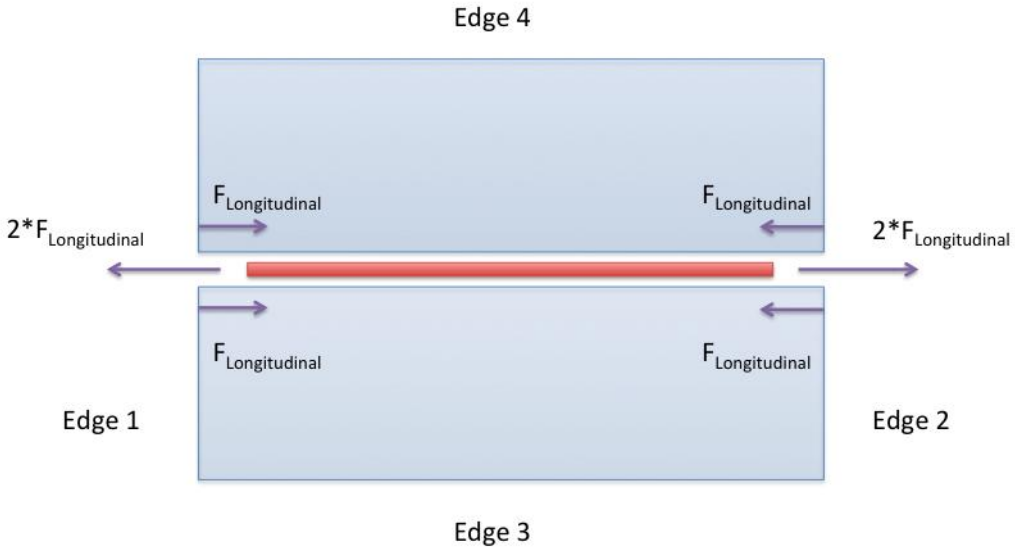

Figure 4-2: Schematic of longitudinal force and edges

The transverse residual stresses result from transverse shrinkage of the filling material and, in equilibrium, are distributed as Figure 4-3. In a continuous structure the forces would depend on restraint against pulling in on the edge 3 and 4 (see Figure 4-2)

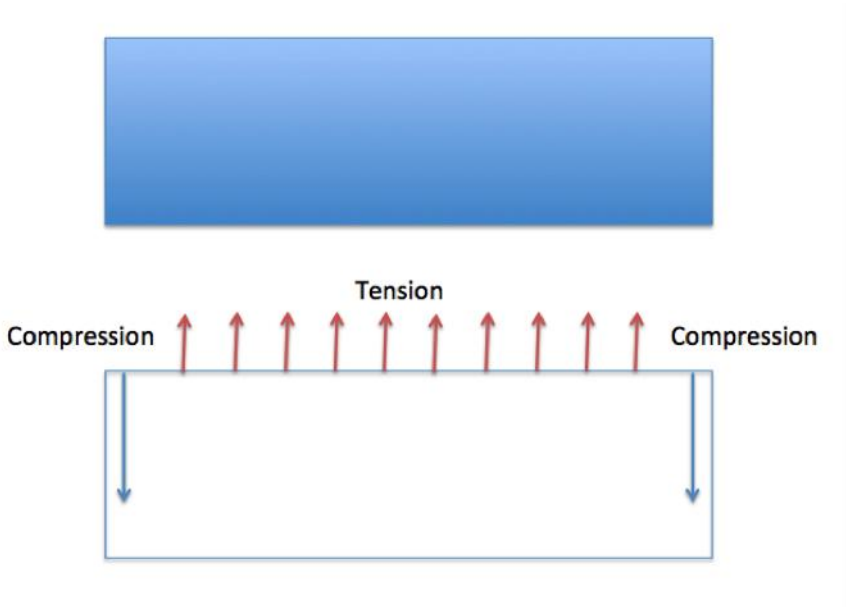

Figure 4-3: Schematic of transverse force distribution

If only a quarter of the whole plate is investigated (see Figure 4-4), it can be seen that the transverse residual stress induced transverse moment should be equilibrium with the longitudinal moment $M_{Longitudinal}$. This longitudinal moment is the part that results from the transverse shrinkage; the longitudinal force produced from the longitudinal shrinkage of the filling material results in the bending moment $M_{Longitudinal}$, and $M_{Transverse}$, as shown in Figure 4-5 which, in some proportion, to resist the applied compression from the weld to achieve equilibrium. This longitudinal moment is the part that results from the longitudinal shrinkage.

From the above discussion, it can be seen that the longitudinal residual stresses are coming from both transverse and longitudinal shrinkages, and the transverse residual stresses should equilibrate the part of longitudinal residual stresses resulting from the transverse shrinkage.

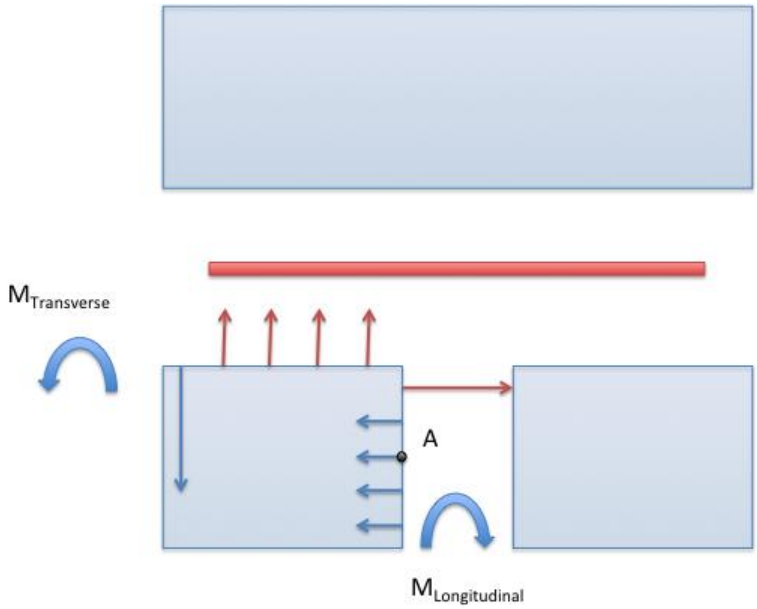

Figure 4-4: Schematic of moment equilibrium for transverse shrinkage

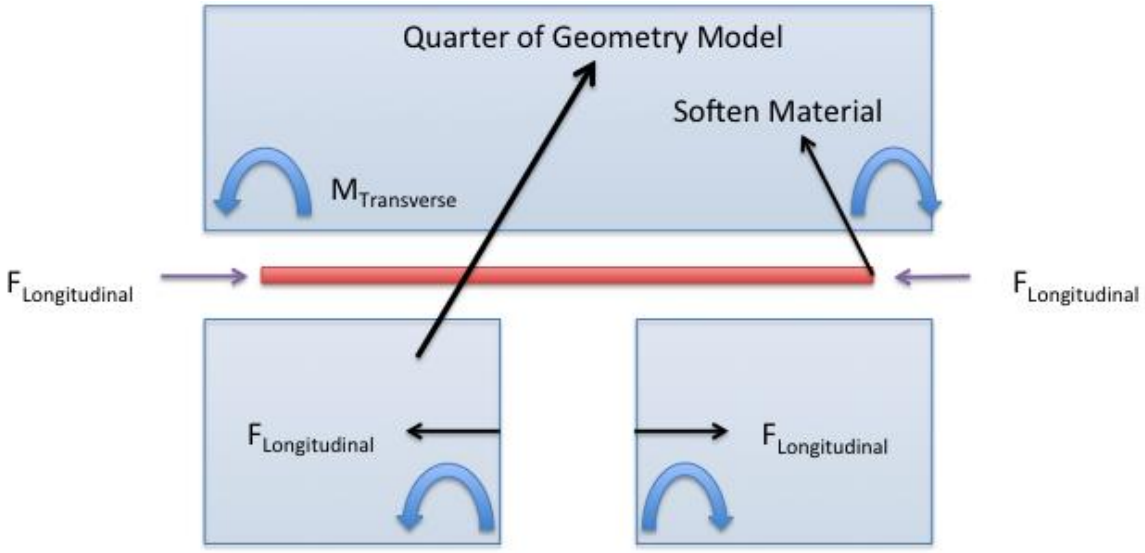

Figure 4-5: Bending moment induced from longitudinal shrinkage

4.1.2 Simple Calculation of Transverse Residual Stresses

A simple program to estimate average transverse residual stresses in a linear butt weld based on force and moment equilibrium is derived in Appendix 1. The simple method separates the filling material into many small pieces, see Figure 4-7 (in Appendix 1, the number has been set as 100), the main theory of this simple calculation assumed that the weld cannot rotate in-plane so an in-plane bending stress develops to balance the force

applied as the weld pool shrinks. The method then finds the effect of each piece of the filling material on each position along the plate length, the summation of results along all time steps at each plate position should be equilibrium.

During the welding and cooling process, the materials are yielding and the material properties are temperature dependent, so the yield stress of the material is changing with temperature. The temperature at any position change with time step, the stress that can be resisted by the material is the difference of the yield stress between the time steps, in other words, the resisted stress is related to the rate of change of the yield stress with temperature. In linear theory, once the material is at yield, it can't resist any more loads, which means no matter how big the loading is, the maximum load can be applied in the material is the load which can be afforded. Figure 4-6 shows the yield stress and load can be applied at different temperatures. It can be seen that at very high temperature, both yield stress and the stress that can be applied have very small values, close to 0, until the temperature is smaller than 1293 K. The yield stress is increasing as the temperature drops from 1293K to 293K; but the stress that can be applied is increasing from 1293K to 793K, and decreasing from 793K to 293K.

The most important result is that the stress of interest is the rate of material yield stress with temperature, which is the other one of the most important factors affect the welding residual stress distribution except the changing rate of temperature.

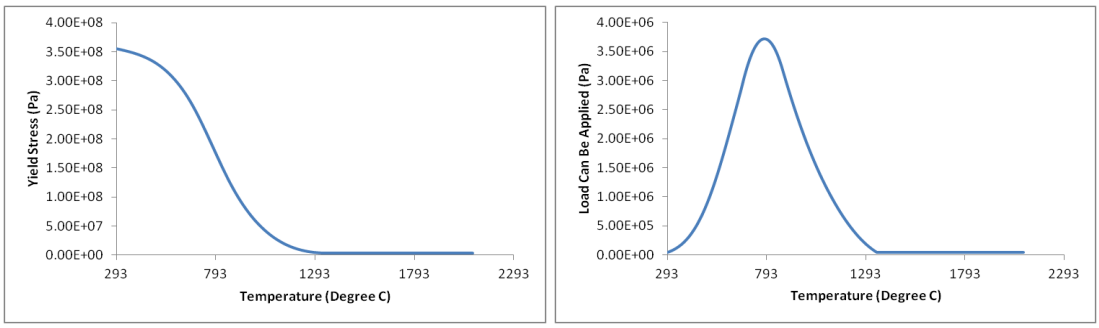

Figure 4-6: Yield stress and load can be applied at different temperatures

Because the weld is deposited in the welding seam gradually, the element death and birth technique was used in FE method to represent the welding process; but in this simple method, the author separates the welding seam into solidified elements and non-solidified elements at the length position where the temperature is 793K, corresponding

to the maximum value of load that can be applied. From Figure 4-7, it can be seen that both parts can resist loads, therefore the load applied at each time step will be assigned at both parts in some proportion. From Figure 4-8, it can be seen that when the welding started, the loads are mainly applied on the solidified element part, but at the end of welding process and the whole cooling process, the loads are mainly applied on the non-solidified element part. And at the dividing line (see Figure 4-7), the load applied is not the maximum value, due to the load applied is the rate of material yield stress with temperature, the value also depends on the temperature difference between load steps. If the temperature changes evenly at each load step, the peak value should appear at the dividing line, but the temperature change is uneven, especially at the area near the welding pool. So the peak value of load applied is located ahead of the dividing line, where the temperature change between load steps is the largest.

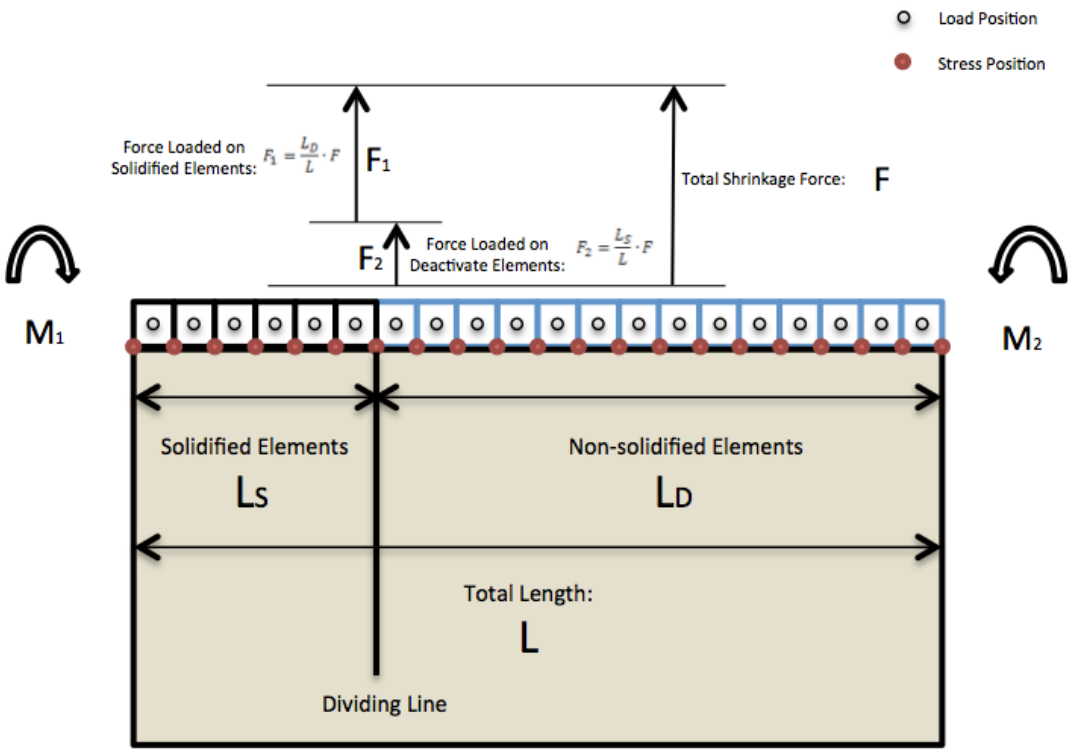

Figure 4-7: Schematic of transverse residual stress analysis for simple method

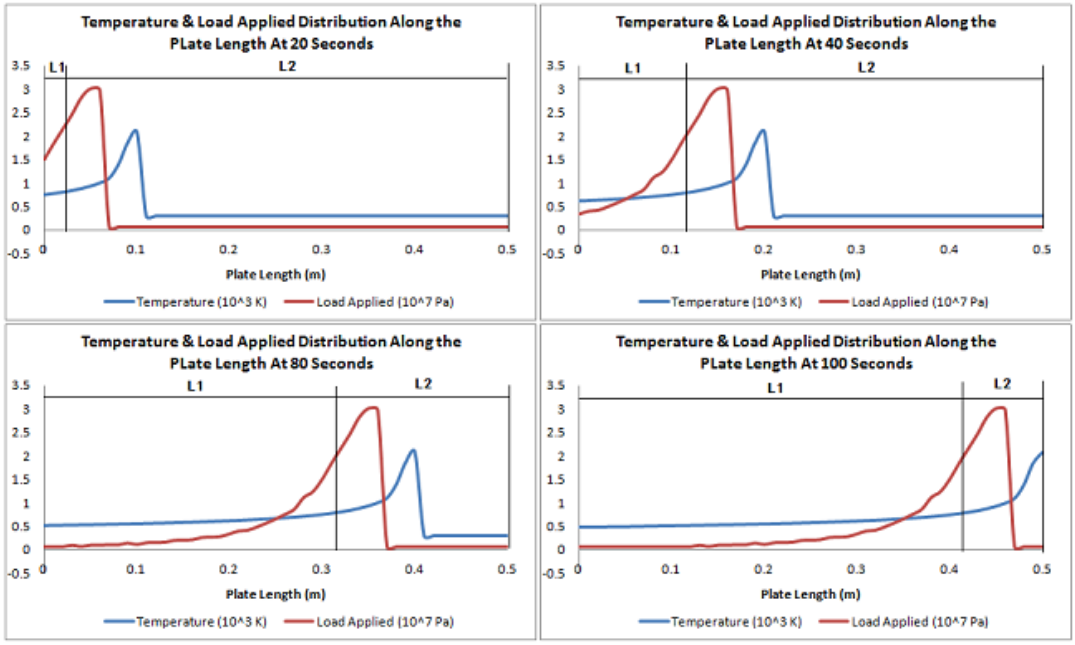

Figure 4-8: Temperature and load applied distribution along plate length at different load steps (for both transverse and longitudinal directions)

Although the value of load applied depends on the temperature at each position, this simple method does not calculate the temperature during the welding process as keeping its simplicity, in order to present the load distribution at each time step. Instead the author makes an assumption for the proportion of the shrinkage force applied on the solidified element part and non-solidified element part: the shrinkage F_1, which applied on the solidified element part; and the shrinkage force F_2 is also evenly applied on the non-solidified element part. F_1 and F_2 have the following relationship:

$$F = F_1 + F_2$$

Equation 4-1

$$F_1 = F * [L_D / (L_S+L_D)]$$

Equation 4-2

$$F_2 = F * [L_S / (L_S+L_D)]$$

Equation 4-3

The maximum stress from transverse shrinkage is set as the yield stress at normal temperature (293K), because the material is assumed as ideal elastic and yielding during the welding process, and from Figure 4-6, it can be seen that the stress is from 0 to yield stress at room temperature, so the transverse shrinkage force on each increment piece is calculated by Equation 4-4, then the moment is calculated by Equation 4-5, finally, the stress contributed to each position along the plate length can be obtained from Equation 4-6.

$$Force = \frac{\sigma_{Yield} \cdot (t \cdot \Delta L)}{2}$$

Equation 4-4

$$Moment = Force \cdot x$$

Equation 4-5

$$Stress = \frac{M \cdot y}{I}$$

Equation 4-6

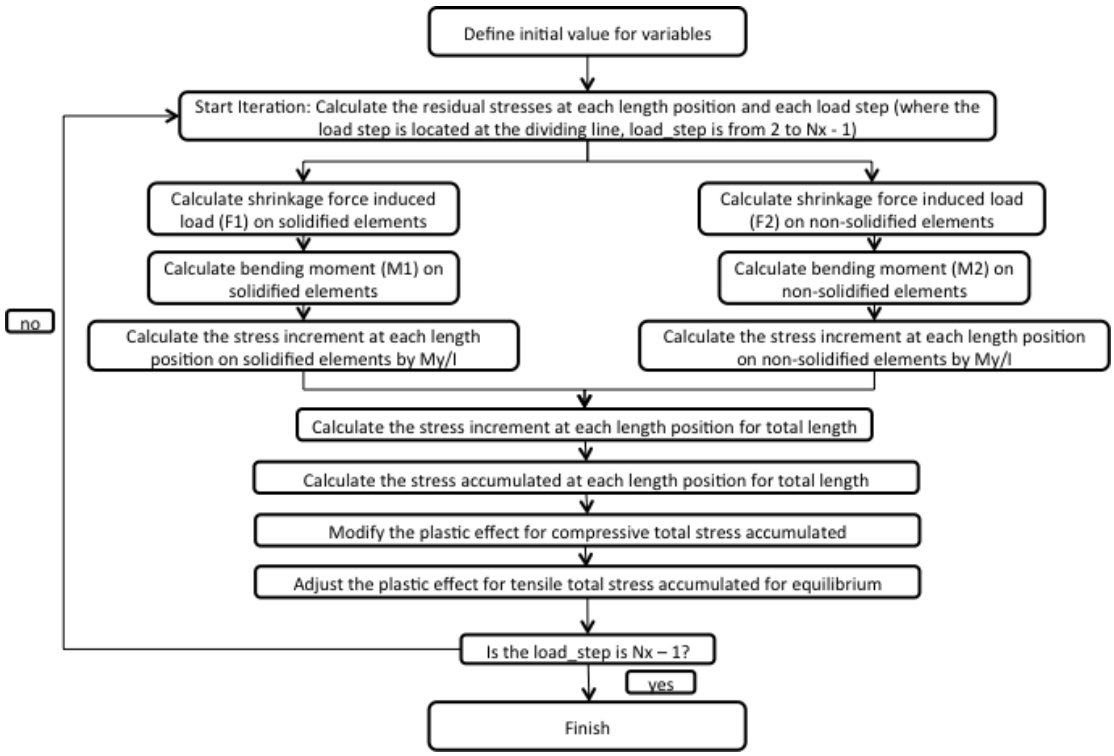

Figure 4-9: The calculation procedure of the transverse equilibrium stresses

The procedure for implementing this simple method is given in Figure 4-9. It can be seen that at each load step, the stress increment at each length position on both solidified and non-solidified elements were calculated first, and then the stress increment along the plate length can be determined, see Figure 4-10. After that, by integrating the stress increments with load step, the residual stress distribution at current load step is calculated, as shown in Figure 4-11. According to Figure 4-11, it can be seen that the value of stresses are very large, due to the calculation here being purely elastic, which does not take the plastic effect into account. Lastly, therefore, the result is modified for the adding plastic effect, the peak compressive stress value is cut off at yield stress at the room temperature (355Mpa) and then the residual stresses are adjusted to make the system achieve force and moment equilibrium at the current load step. The modified residual stress distribution is shown in Figure 4-12.

The load step in this simple method is not exactly following the time step in FE analysis, instead it is based on the understanding of the residual stress distribution in the whole process, when combining the welding and cooling process together. Figure 4-13 shows the transverse residual stress distribution along the welding line at final load step from both this simple method and finite element analysis in Section 3.8.1. It can be seen that the transverse residual stresses calculated from this simple method (blue line) shows compression at the both ends of the weld and tension in the centre. It is a good match to the FEM result (red line).

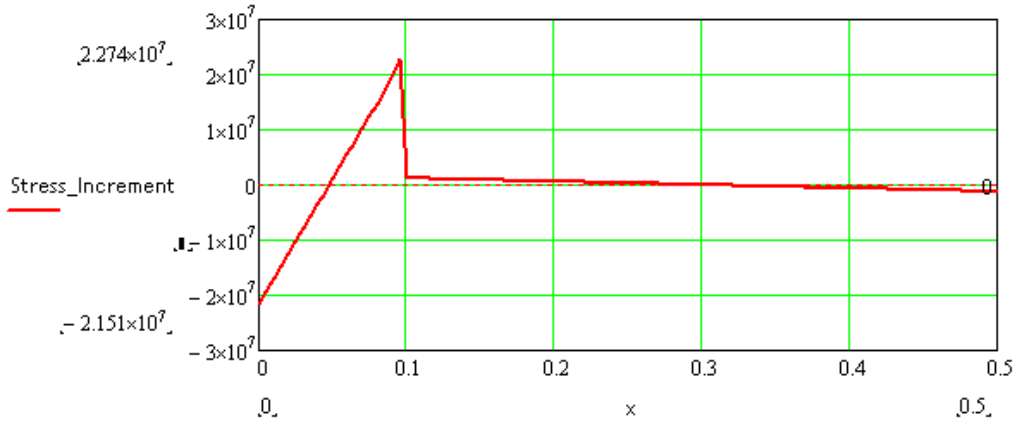

Figure 4-10: Stress increment distribution along plate length at load step 20

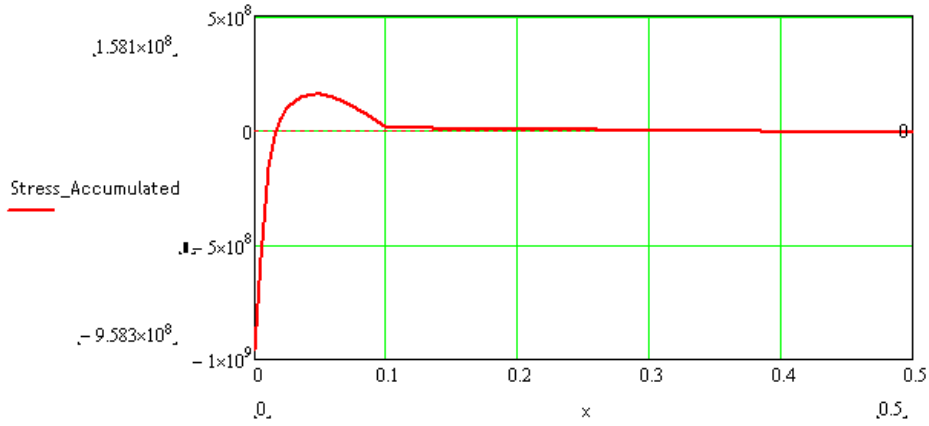

Figure 4-11: Residual stress distribution along plate length at load step 20

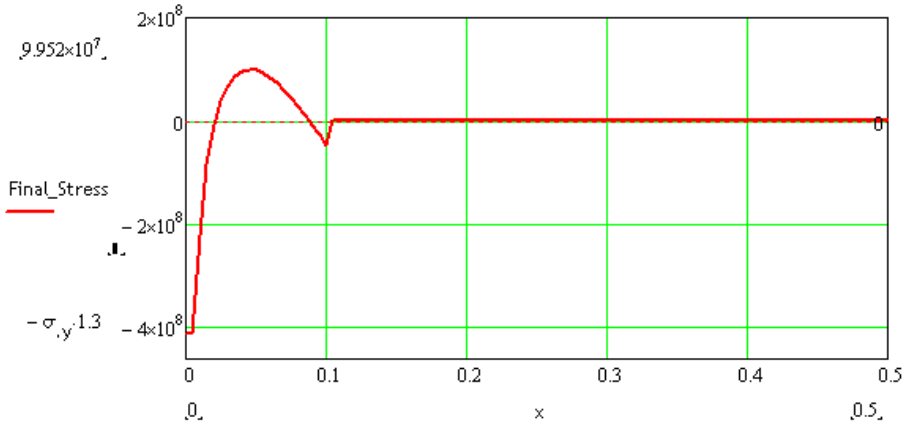

Figure 4-12: Modified residual stress distribution along plate length at load step 20

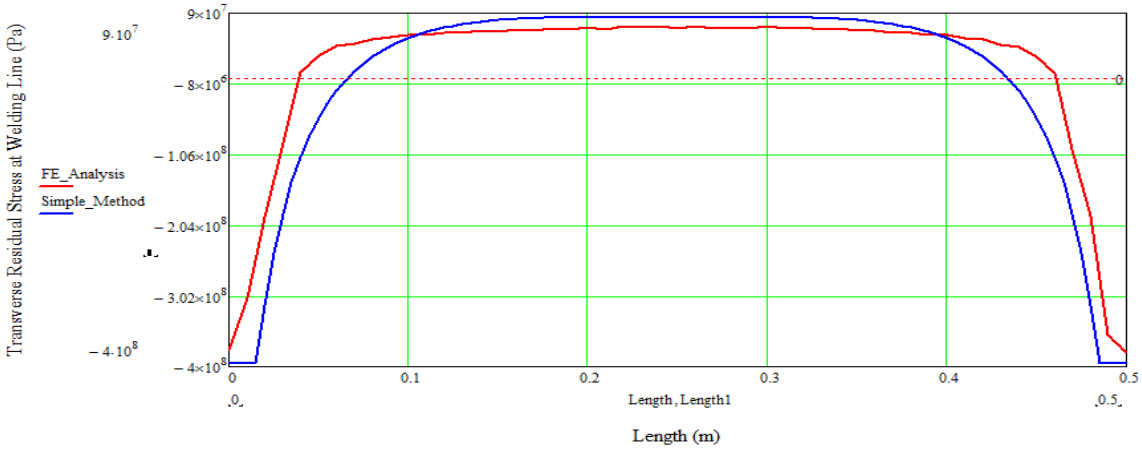

Figure 4-13: Transverse residual stress distribution along the welding line at final load step from simple method and finite element analysis

The final results are then checked for equilibrium. The author integrates the final stress along the welding line to get the shear force at each position, then integrates the shear force along the welding line to get the bending moment. In order to check the stress distribution achieves the force and moment equilibrium, the integrated shear force and bending moment at the two ends of the weld should be zero, which is shown to be the case in Figure 4-14.

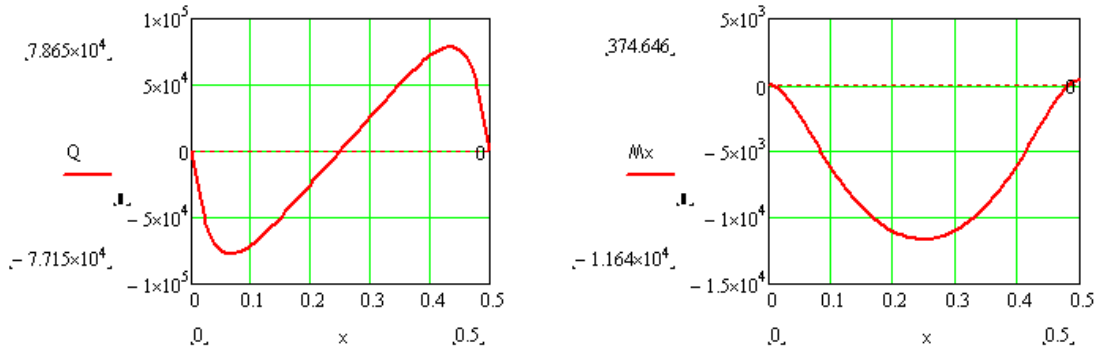

Figure 4-14: Integrated shear force and bending moment along the length of the weld

4.1.3 Simple Calculation of Longitudinal Residual Stress

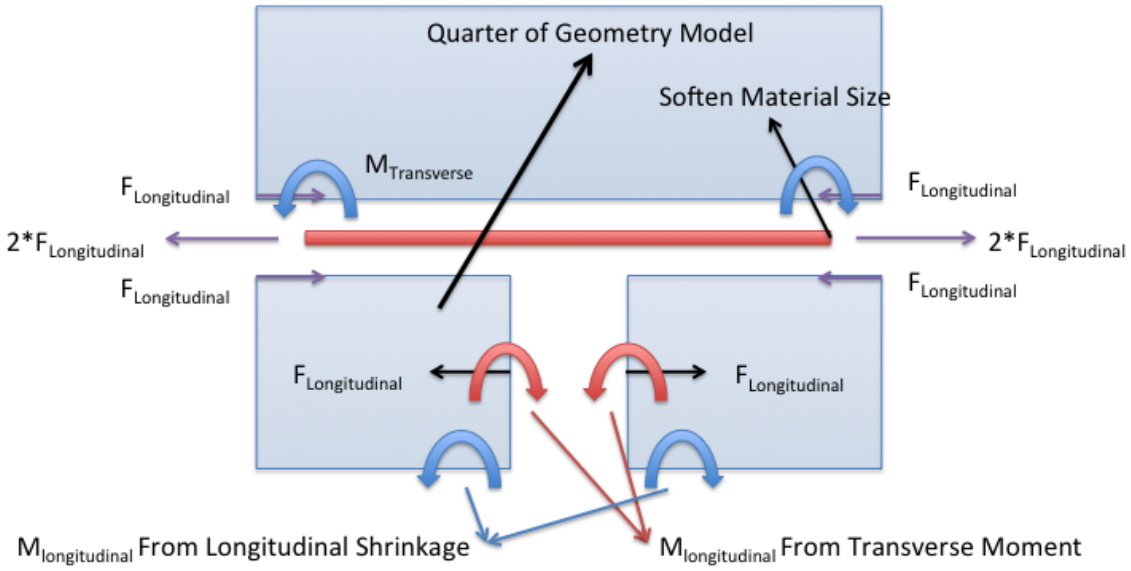

Figure 4-15: Schematic of transverse and longitudinal shrinkages induced moments

As discussed in Section 4.1.1, the longitudinal residual stress has two sources, one is the longitudinal shrinkage and the other one is the transverse bending moment. A simple program to estimate longitudinal residual stresses in a linear butt weld based on force and moment equilibrium is also derived in Appendix 1. This method is able to calculate the longitudinal residual stress distribution in different longitudinal positions and the cross section investigated in the example of Appendix 1 is located at the mid-length. In this simple method, the size of softened material in transverse direction (Variable 'weld' in Appendix 1, see Figure 4-16) needs to be specified (i.e. where the material is yielding). After that, only a quarter of the geometry model was considered as the model is symmetrical about both transverse and longitudinal directions (see Figure 4-15).

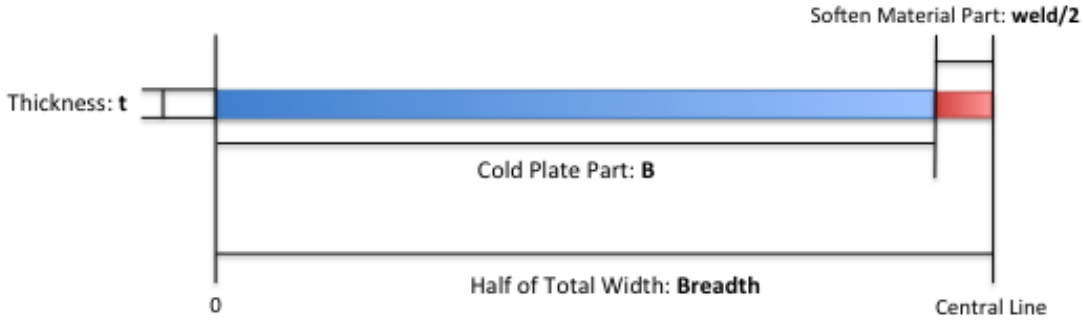

Figure 4-16: Schematic of half plate width cross-section-area

From Figure 4-15, it can be seen that $F_{longitudinal}$ comes from the longitudinal shrinkage and the value is half of the shrinkage force. In order to achieve force equilibrium, there a force needs to balance $F_{longitudinal}$, if there is tack welding before the welding process, the balance force may act at the tacks; but if there is no tack welding, which the balance must act on the solidified cross section. According to Equation 4-6, whether the term of F/A exists depends on whether there is tack welding. The tack welding does not primarily influence the transverse moment, but it does affect the longitudinal residual stress distribution only on the cross-section that has the tack welding. In this case, the author sets there is no tack welding.

The calculation routine for longitudinal residual stress from longitudinal shrinkage at the plate without a softened material part has been shown in Figure 4-17 and the distribution has been plotted in Figure 4-18.

$$LStress_{LS} := \left| \begin{array}{l} LForce \leftarrow -\sigma_y \cdot t \cdot weld \\ LMoment \leftarrow \dfrac{\dfrac{LForce}{2} \cdot \left(\dfrac{B}{2}\right) \cdot B^3}{\left(x_{LPI}\right)^3 + B^3} \\ \text{for } ixcw \in 1 .. Ny \\ \quad \left| \begin{array}{l} c \leftarrow \text{"P/A +My/I is now calculated on the cross section at length position LPI"} \\ \sigma_{ixcw} \leftarrow \dfrac{LForce}{B \cdot t \cdot 2} \cdot Tack + \dfrac{LMoment \cdot \left(\left(y_{ixcw} - \dfrac{B}{2}\right)\right)}{t \cdot \dfrac{(B)^3}{12}} \end{array} \right. \\ \sigma \end{array} \right.$$

Calculation of Longitudinal Shrinkage Force ($2*F_{longitudinal}$ in Figure 4-15)

Calculation of the bending moment from Longitudinal Shrinkage by Equation 4-5

Figure 4-17: The calculation routine of longitudinal residual stress from longitudinal shrinkage

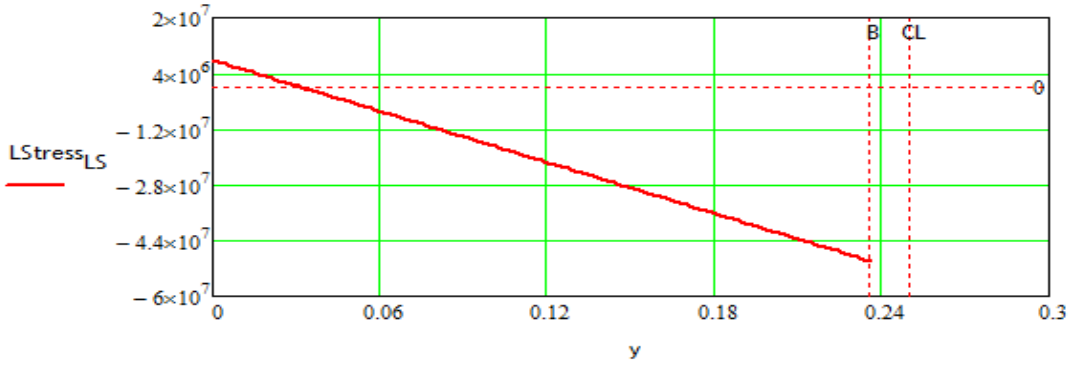

Figure 4-18: Transverse distribution of plate longitudinal residual stress from longitudinal shrinkage

For calculating the longitudinal residual stress from the transverse bending moment at the plate, without a softening material part, the transverse bending moment at the length position of cross section investigated needs to be calculated first, and then Equation 4-6 is used to calculated the final results. The calculation routine has been shown in Figure 4-19 and the distribution has been plotted in Figure 4-20.

$LStress_{TS} :=$ | $LMoment \leftarrow -Mx_{ini_{LPI}}$ Calculation of the bending moment from Transverse Shrinkage, which from the transverse residual stress analysis

for $ixcw \in 1 .. Ny$

$c \leftarrow$ "My/I is now calculated on the cross section at length position LPI"

$$\sigma_{ixcw} \leftarrow \frac{LMoment \cdot \left(\left(y_{ixcw} - \frac{B}{2} \right) \right)}{t \cdot \frac{(B)^3}{12}}$$

σ

Figure 4-19: The calculation routine of longitudinal residual stress from transverse bending moment

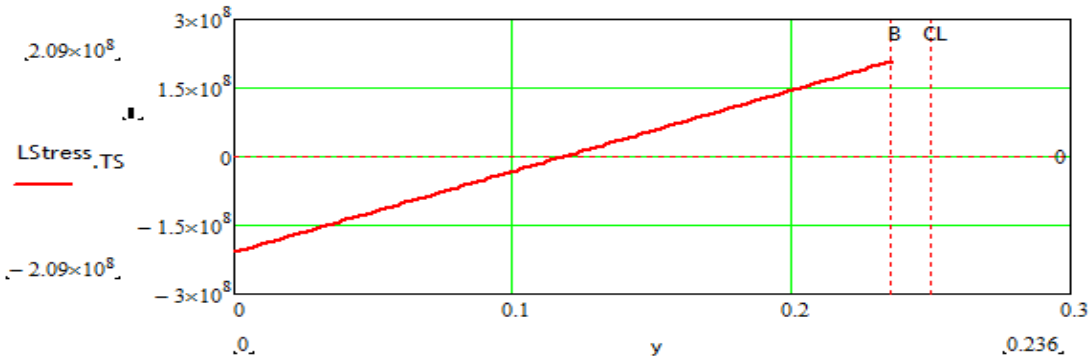

Figure 4-20: Transverse distribution of longitudinal residual stress from transverse bending moment

Next, the total longitudinal residual stress distribution at the plate without a softening material can be obtained by sum of the longitudinal stress from longitudinal shrinkage and transverse moment together. Finally the stress in the softened material is set as the yield stress because the material there was yielding during the welding and cooling process. The longitudinal residual stress distribution at the cross section located at mid-length is plotted in Figure 4-21 (blue line); it is also a good match to the FEM result in Section 3.8.1 (red line).

By comparing Figure 4-21 (blue line) to Figure 5-5 (red line), it can be seen that the result from simple method is almost exactly the same as the case 673 K COT. Because the

simple method take the constant yield stress at the room temperature instead of temperature dependent, it makes the material stiffer, which has the same effect as decreasing the COT.

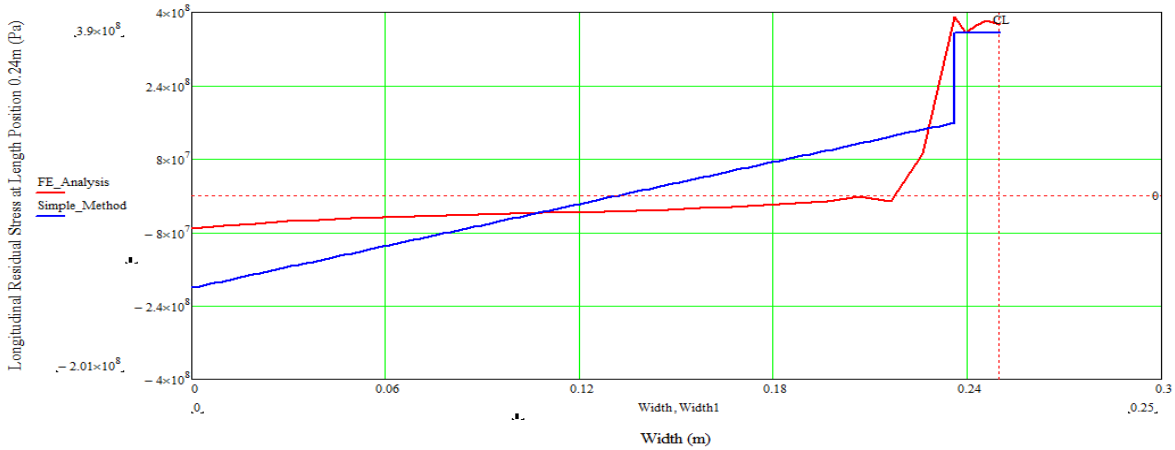

Figure 4-21: Transverse distribution of total longitudinal residual stress at mid-length from simple method and finite element analysis

The longitudinal residual stress distribution is symmetrical with the welding line, so only the force equilibrium check (see Figure 4-22) was done in this case, the bending moment has to be in equilibrium.

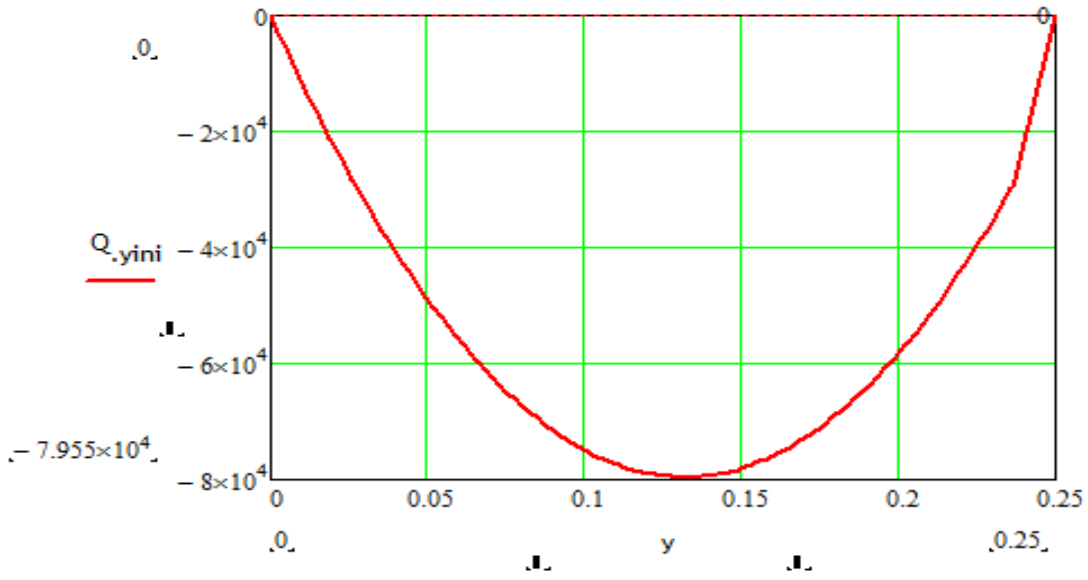

Figure 4-22: Transversely integrated longitudinal force distribution at the centre of the length of the weld

4.1.4 Discussion

A simple method for predicting the butt-welding residual stresses based on force and moment equilibrium was derived in this section. The results calculated from this simple method were pretty match with the result in Section 3.8.1, and further comparison with the finite element results is done in the following sections in this chapter (Figure 4-51).

4.2 Transverse Residual Stresses From FE Analysis

As mentioned before, internal stresses are in a self-equilibrium state, so the development of the welding residual stresses is caused by two parts, one is the heating and cooling effect on a single element, the other is the self balance of the whole plate. Figure 4-23 shows that at the two ends of the weld, the transverse residual stress is compressive and the magnitude is around the yield stress of this material; and other parts present a tensile residual stress, which have a relatively lower maximum magnitude located around the welding line. The result looks symmetric, and the maximum tensile stress is not occurring at the weld line, which cannot be simply explained by first principles analysis. In this section, the transverse residual stresses developing history at different lines parallel to the welding line will be analyzed, in order to explain how the transverse residual stresses is formed.

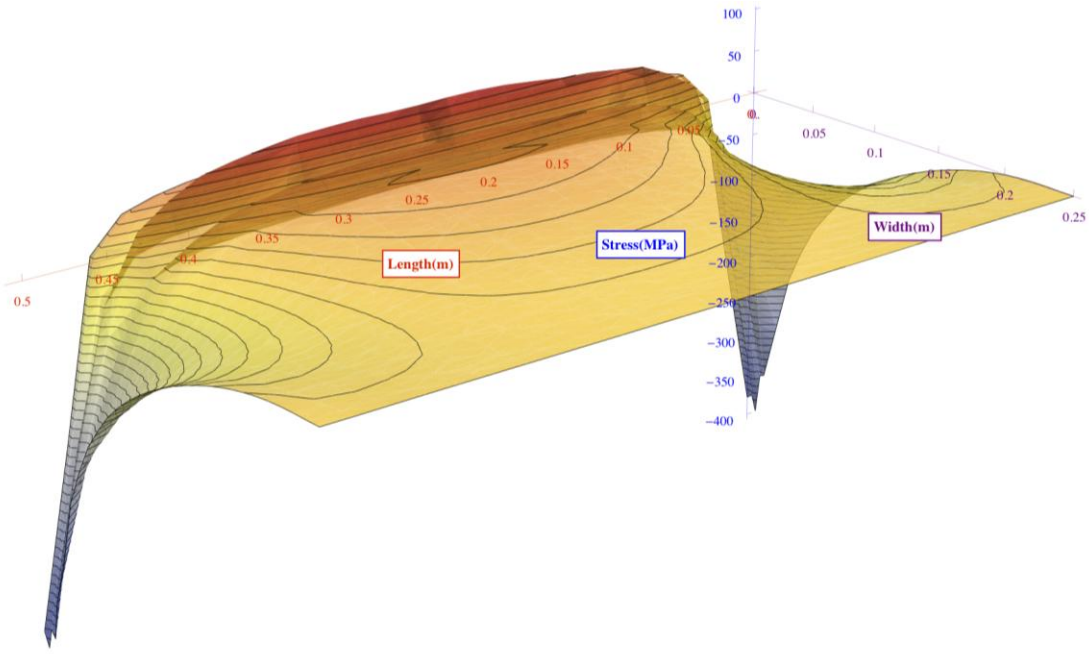

Figure 4-23: Overall transverse residual stress distribution

4.2.1 Welding Line

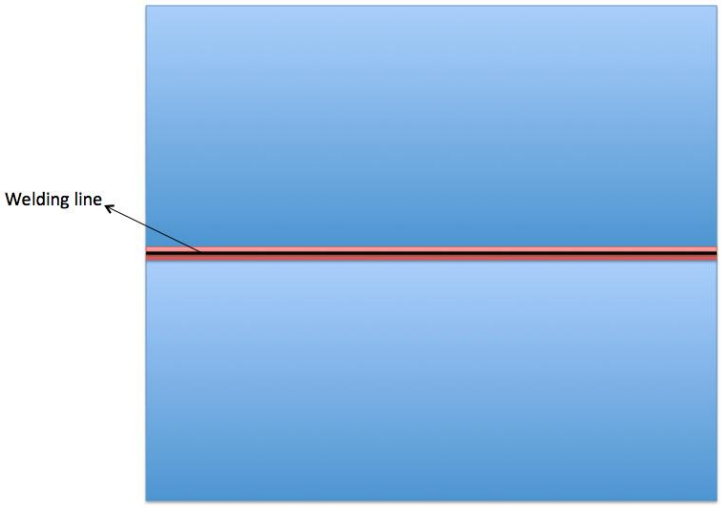

Figure 4-24: Schematic of location of welding line

The welding line (see Figure 4-24) is where the welding pool is located, and where the element activate and deactivate technique is used, so the results here are different from the other lines. Figure 4-25 shows how the element activate and reactivate worked in this

simulation, which is represented by the stress being zero before the welding pool passing. From this figure, it can be also seen that at 48 second, the welding pool center is located at 0.24 m, but the stress at 0.24 m is zero, which is due to the material in the welding pool is melt, the non-zero stress happened at 0.21 m, where the temperature is 1073K (material soften temperature), which also indicates that the material softening time is 6 seconds.

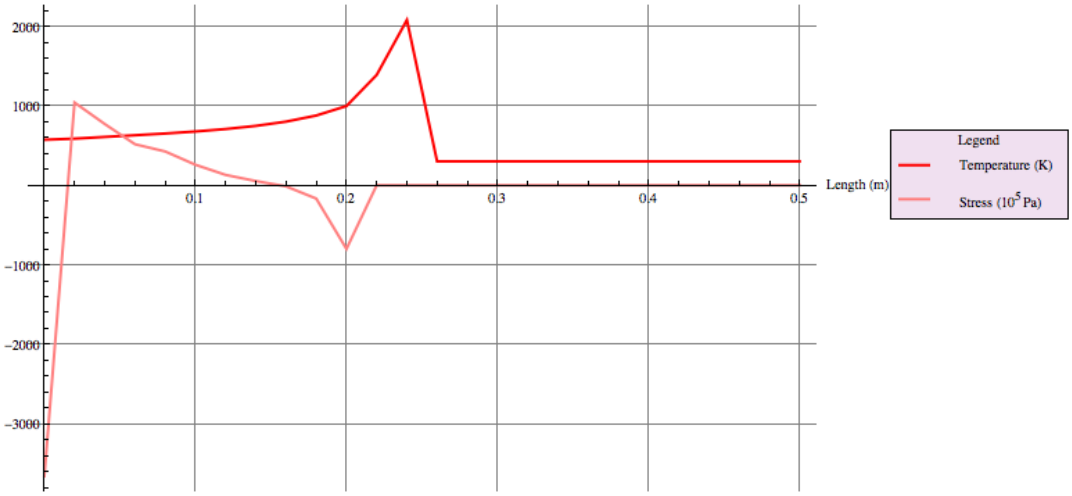

Figure 4-25: Temperature VS Transverse Stresses at the Welding Line at 50 second

Figure 4-26 presents the transverse residual stress distribution in the welding line under different time. Until 10 second, there is no stress at all, as all the elements in the welding seam were deactivated at first, and are melt liquid when they are first reactivated in the welding pool. After 22 second, the stresses keeps the same format moving forward, which presents compression at the two ends and tension at the center, the compression part is 'steep' (which means rapidly changing with distance along weld) especially the stress at the start of welding line which has a maximum value of 387 MPa in compression, however the tension part becomes flat as the time passes. At 105 second, when the welding process has been finished for 5 seconds, it can be seen that stress at the end the welding line is still zero as the material is still melt, but the overall format of the stress distribution along the welding line is the same as earlier. During the cooling process, the compressive stress at the start of welding line keeps the high value, but at the end of the welding line, the stress suddenly changes to the same high compression, and then maintains it, which is mainly due to the self-balance of the force and the moment. At first, the tensile stresses have the maximum of around 100 MPa at outer of the line center in

both directions, which is used to balance the neighboring compressive stress at the local position, then the tensile stresses at the center of the line are getting bigger and bigger, which is gradually decreased while moving outwards, until at 3600 second, when the whole plate has been cooled down to the room temperature, the final result plot can be found in Figure 4-26, which shows there are very large and rapidly changing compressive residual stresses at the two ends and relatively small magnitude and flat tensile stresses from the outer to the center of the line, and the tensile stress and compressive stress are 71.3 MPa and 380 MPa. By comparing this result with the results calculated from the simple method in Section 4.1 (see Figure 4-13), it can be seen that the results have a good match.

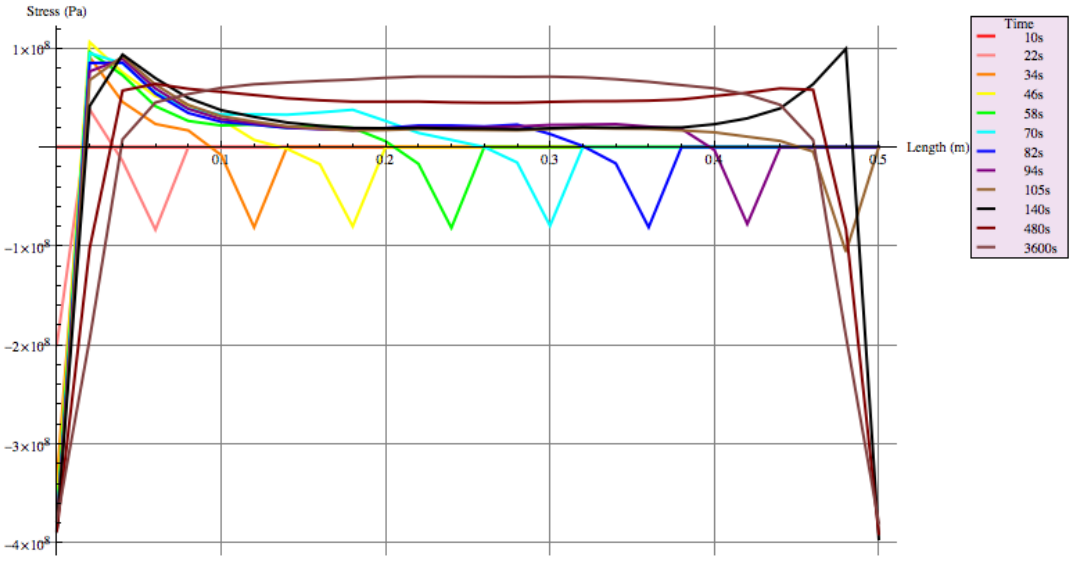

Figure 4-26: Transverse Residual Stress Distribution of Welding Line at Different Time

Figure 4-27 shows at position 0 m and 0.5 m, there are almost no tensile stresses at all during the whole welding process. This is due to the edge effect, the force and moment equilibrium dominate the result totally. At other locations, the stresses are all present as compressive, which is due to the element ahead of this location is deactivate, that location is the edge at that specific time; after that, as the element ahead is reactivate, the location is not the edge any more, the edge effect is disappeared gradually, the stresses become tensile due to the shrink at the cooling stage; the final results are dominated by the force and momentum equilibrium again, so that it presents as symmetrical.

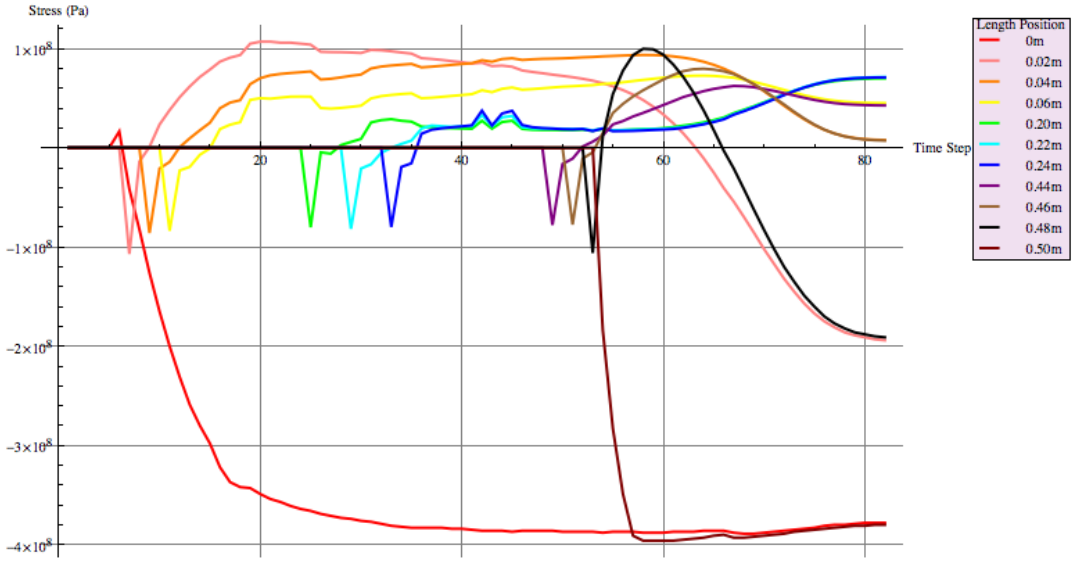

Figure 4-27: Time history of transverse residual stress at different positions in welding line

4.2.2 0.004 m From Welding Line

The line located at 0.004 m from welding line (see Figure 4-28) is in the heat-affected zone (HAZ), where the element activate and deactivate technique is not used. From Figure 4-29, the compressive stress at the mid-length is due to this part of material being heated, which results in the element expansion. Then the stress changes to zero at 0.22 m, because the temperature at that point exceeds 1073 K; after that, the stress becomes tensile. From the temperature, it can be seen that those points are in the cooling stage, so that those tensile stresses come from the elements shrinkage; about the compressive stress at the start of this line, which is due to the edge effects.

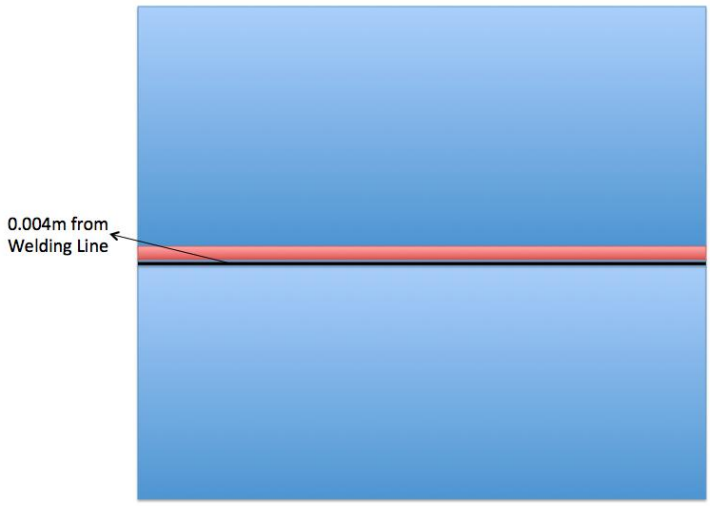

Figure 4-28: Schematic of location of 0.004m from welding line

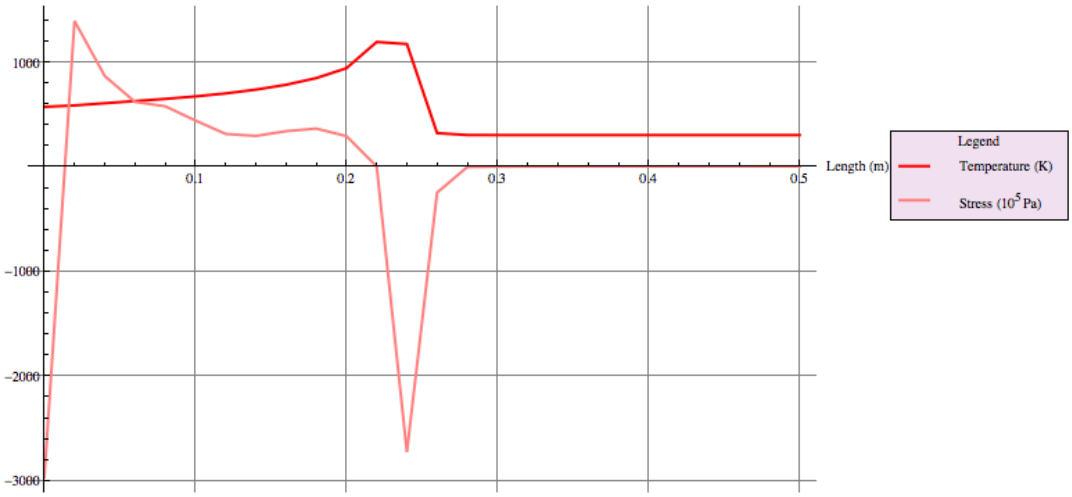

Figure 4-29: Temperature VS Transverse Stresses at 0.004m from Welding Line

Figure 4-30 presents the transverse residual stress distribution at 0.004 m from welding line under different time. At 10 second, there is a tensile stress at the start of this line though this location is the edge, the reason why the edge effect are not working is only this point's temperature below the material soften temperature and start cooling. After 22 second, the stresses keep the same format moving forward, which presents compression at the two ends and tension at the center. At 105 second, 5 seconds after the welding process has finished, it can be seen that stress at the end the welding line is still zero as the material is still soft, but the overall format of the stress distribution has been changed to only have one compression part at the start, which is different from the results at the

welding line due to the element activate and deactivate technique is not being used here as there is no weld deposition. During the cooling process, the format of the changing the stress distribution with time is the same as the results at the welding line. And the final result also shows there are very large magnitude and steep compressive residual stresses at the two ends and relatively small magnitude and flat tensile stresses from the outer to the center of the line, but the magnitude of tensile stress and compressive stress are 70.9 MPa and 396 MPa, which is a little different from the result in welding line. However, this slight difference can be neglected, so it can be concluded that once the temperature exceeds the material soften temperature during the welding process, the final transverse residual stress distribution at this line has the same result as the welding line.

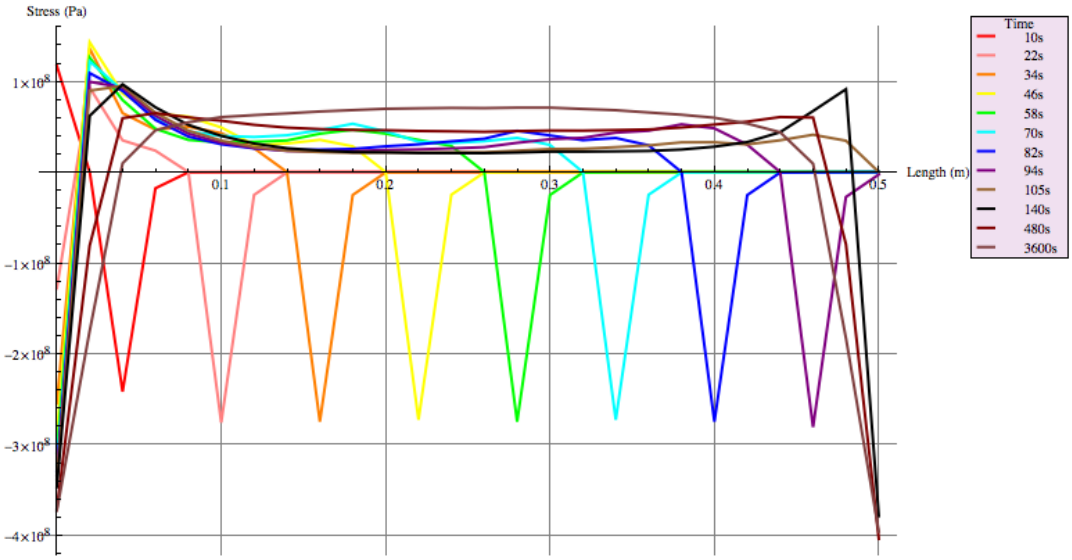

Figure 4-30: Transverse Residual Stress Distribution at Different Time

By comparing Figure 4-27 & Figure 4-31, it can be found that the compression magnitude is larger than the value in welding line, because the temperature is not so high, and all the points on both lines have almost the same stress history after their temperature below the material soften temperature, which explains why the both lines have the same final residual stress distribution.

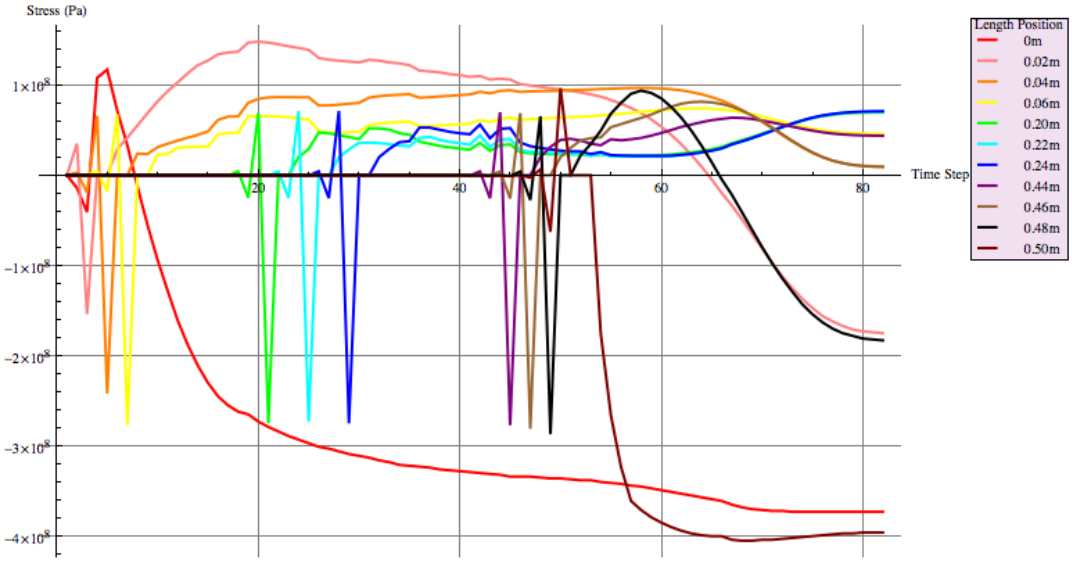

Figure 4-31: Time history of transverse residual stress at different position

4.2.3 0.007 m From Welding Line

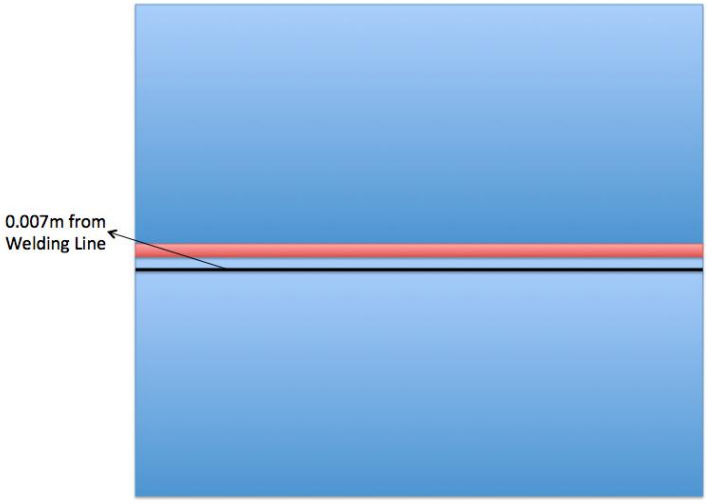

Figure 4-32: Schematic of location of 0.007m from welding line

From Figure 4-33, the compressive stress between the length position 0.1 m and 0.24 m is due to this part of the material being heated, which results in the element expansion; then it start to become tensile from 0.22 m due to the temperature starting to decrease. It is about the compressive stress at the start of this line due to the edge effects.

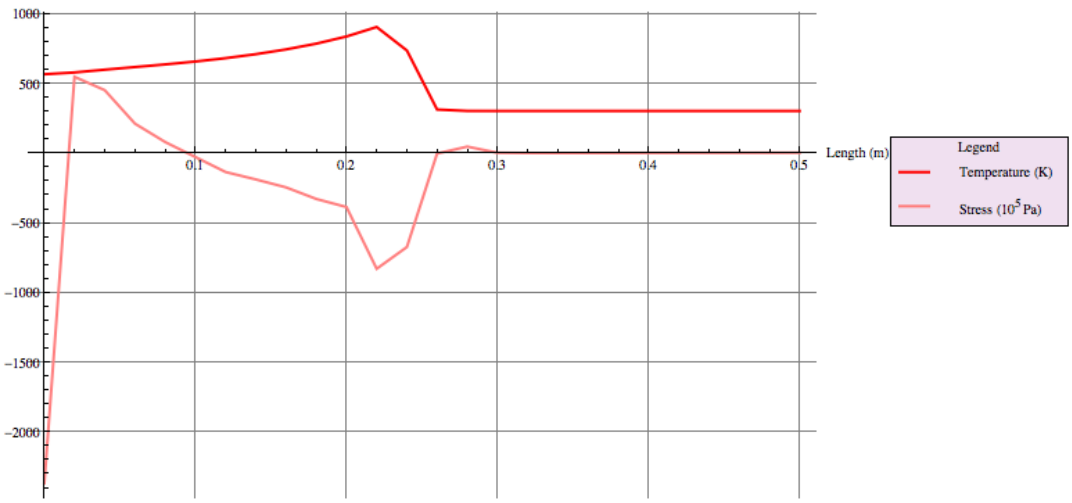

Figure 4-33: Temperature VS Transverse Stresses at 0.007m from Welding Line

Figure 4-34 presents the transverse residual stress distribution at 0.007 m from welding at different times. Until 22 second, there is no tensile stress at all, as the temperature change in this line is not significant. When the material was heated, it produces the compressive stresses. As the temperature start decreasing, the stress gradually changes to tension; after 34 second, the stresses keeps the same format moving forward. This results in compression at the two ends and tension at the center, but the compression zone gets larger due to the flatter temperature distribution and the time of reaching the maximum temperature is later than the lines discussed before. The final result also shows there are very large and steep compressive residual stresses at the two ends and relatively small magnitude and flat tensile stresses from the outer to the center of the line. The tensile stress and compressive stresses are 40.5 MPa and 391 MPa, which gives the same level compressive stress as along the weld line, but smaller tensile stress, because during the welding process in this line, there is no temperature higher than the material soften temperature, there is no stress suddenly changing to zero as the material softens; the stresses of all the elements in the line change to tensile gradually from compressive.

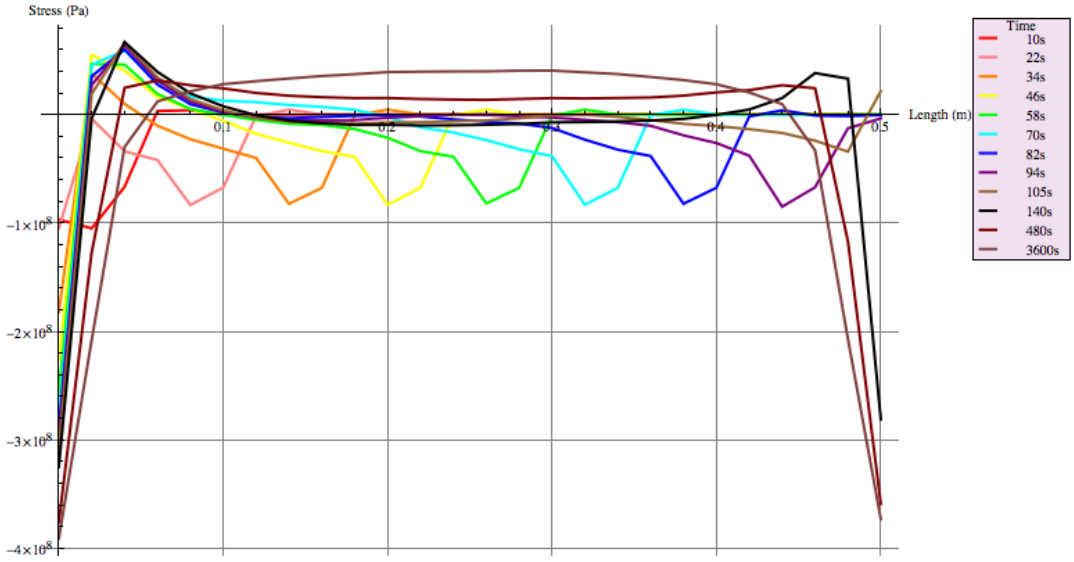

Figure 4-34: Transverse Residual Stress Distribution at Different Time

According to Figure 4-35, all the stresses are mainly dominated by the force and moment equilibrium. The direct effect of the temperature change is relatively flat and the maximum temperature is low. There is small plastic strain produced, which results in the heating expansion but is largely cancelled by the cooling shrinkage. At the start and end edge, the material was heated first, so they present compressive stresses, and the compressive stresses start to decrease as the temperature decreases. Because of the edge effects, high magnitude compressive stress are still produced eventually. At points located in the center of the line, the stresses firstly produce compressive stresses, then cancelled by the cooling shrinkage to zero, and then, due to the self-balance effect, the stresses change to tensile at the final stage.

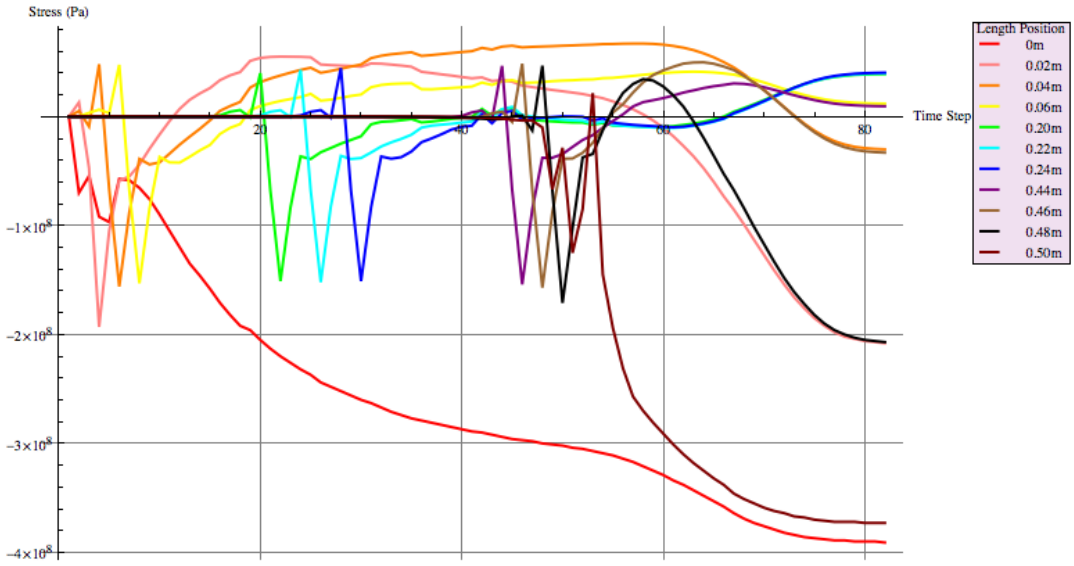

Figure 4-35: Time history of transverse residual stress at different position

4.2.4 0.014 m From Welding Line

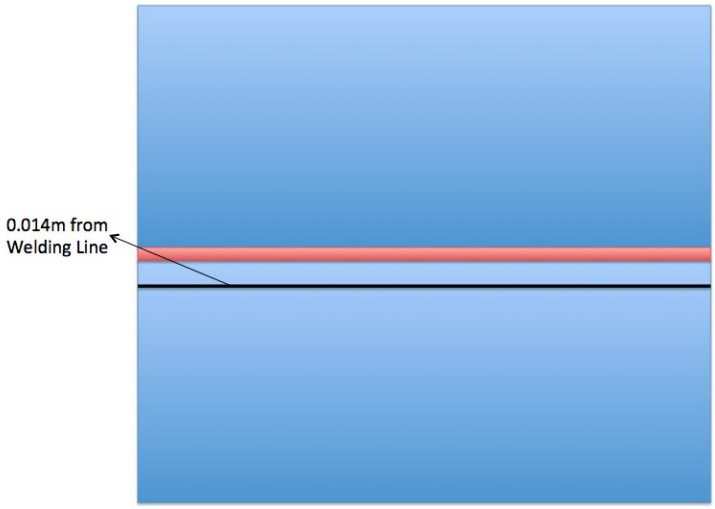

Figure 4-36: Schematic of location of 0.014m from welding line

From Figure 4-37, the temperature slope is flatter, and the maximum temperature is 638 K. It can be seen that there is almost no tensile stress. As the temperature starts to increase, the compressive stress is produced, then after the temperature reaches the maximum value, the stresses start to decrease to zero, due to the edge effect, which increases at the start of line.

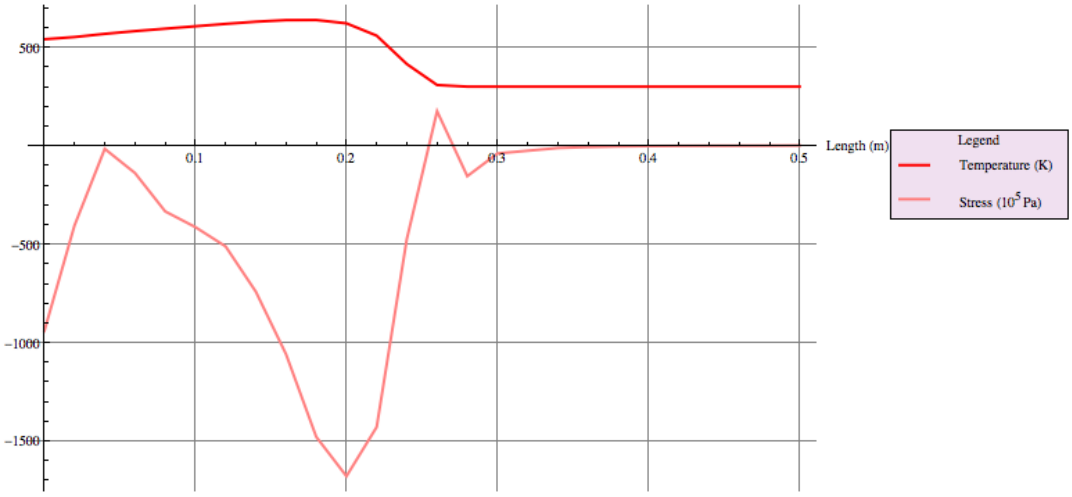

Figure 4-37: Temperature VS Transverse Stresses at 0.014m from Welding Line

According to Figure 4-38, there is no temperature change induced tensile stress in the whole welding process. The final result also shows there are very large magnitude and steep compressive residual stresses at the two ends and relatively small magnitude and flat tensile stresses from the outer to the center of the line, but the tensile stress and compressive stress are 93.3 MPa and 342 MPa, which gives the same level compressive magnitude as along the weld line, but the maximum tensile magnitude in the whole plate.

By comparing Figure 4-35 & Figure 4-39, the shape of the stress history of all the points from these two lines are almost the same, although the scales are different. Because the maximum temperature of the line previous is 720 K while the maximum temperature of this line is 638 K. According to Table 3-3: Structural Material Properties, the temperature 673 K is a kind of boundary, when the temperature is higher than that, the material strength decreases faster, and vise versa. So the reason why the dramatic magnitude difference happens is a result of the temperature dependent material property effect, besides the final stress distribution is mainly dominated by the force and moment equilibrium due to the temperature change which is relatively flat and the maximum temperature is low.

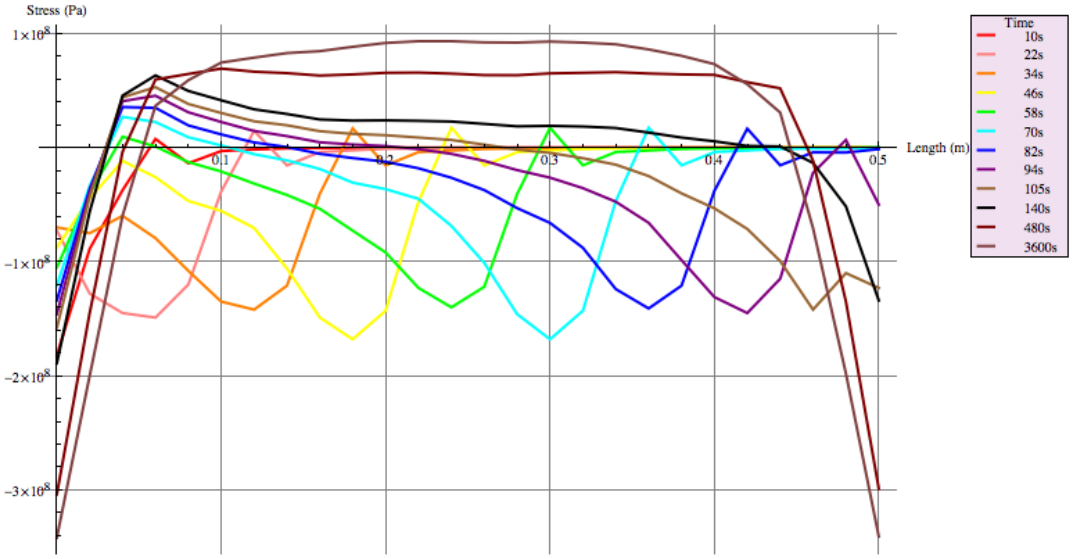

Figure 4-38: Transverse Residual Stress Distribution at Different Time

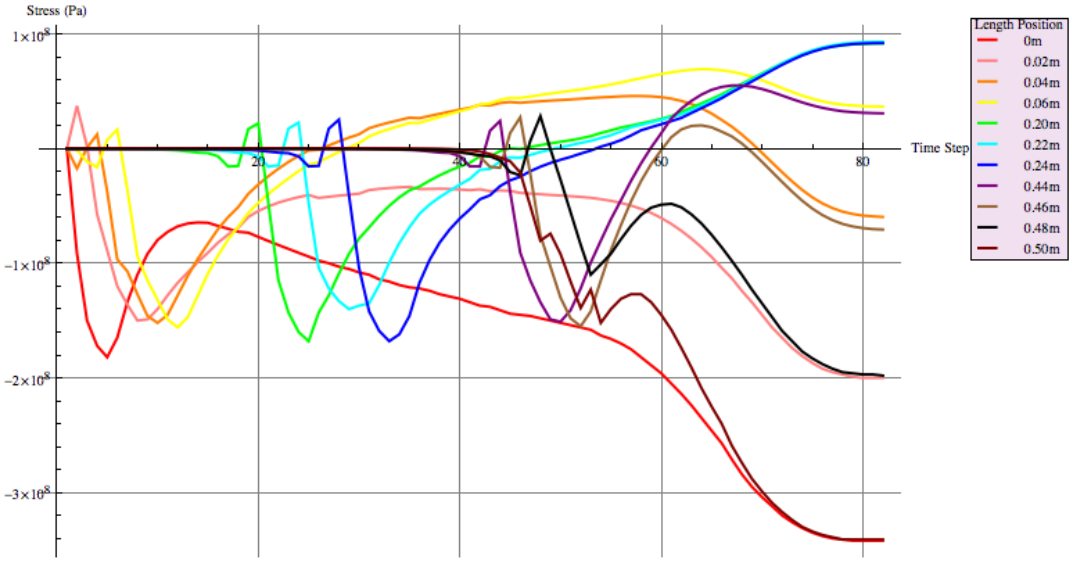

Figure 4-39: Time history of transverse residual stress at different position

4.2.5 0.024 m From Welding Line

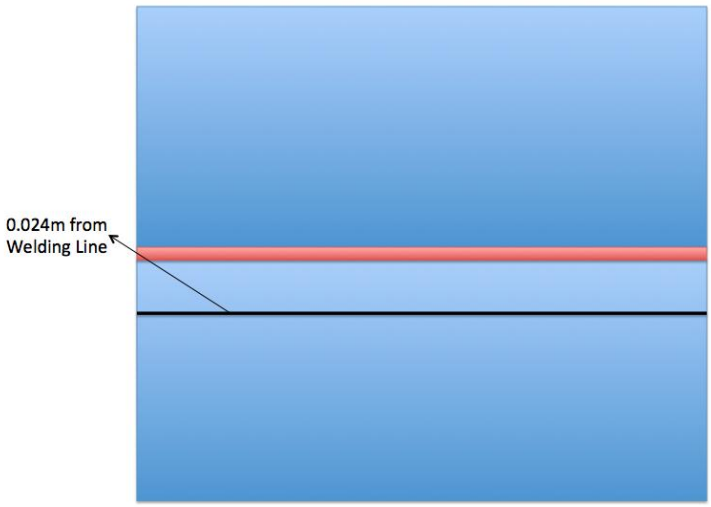

Figure 4-40: Schematic of location of 0.024m from welding line

From Figure 4-41, it can be seen that before the material was heated, there has been already tensile stresses produced, which is obviously due to the force equilibrium as no temperature change has get occurred. As the temperature goes up, the tensile stress starts to decrease and change to compressive gradually. When the temperature decreases, the stress becomes tensile again.

According to Figure 4-42, there is mainly tensile stress producing during the welding process, because material was heated relatively late and as a result of the force and moment equilibrium. The tensile stress and compressive stress of final results are 15.6 MPa and 287 MPa.

Figure 4-43 shows all the points experience a high tensile stress first, because the temperature at that time is low, and the material stiffness is large. Because of that, there is no material yielding, so the heating resulted compressive stress can be cancelled by the cooling tensile stress. So the final results is fully explained by the internal force and moment equilibrium effect. Furthermore, the final stress results of all the other lines, which further from welding line than this line, is formed due to the whole plate self-balance effect, the heating and cooling induced stresses can be cancelled at the end of the whole process as there is no plastic strain.

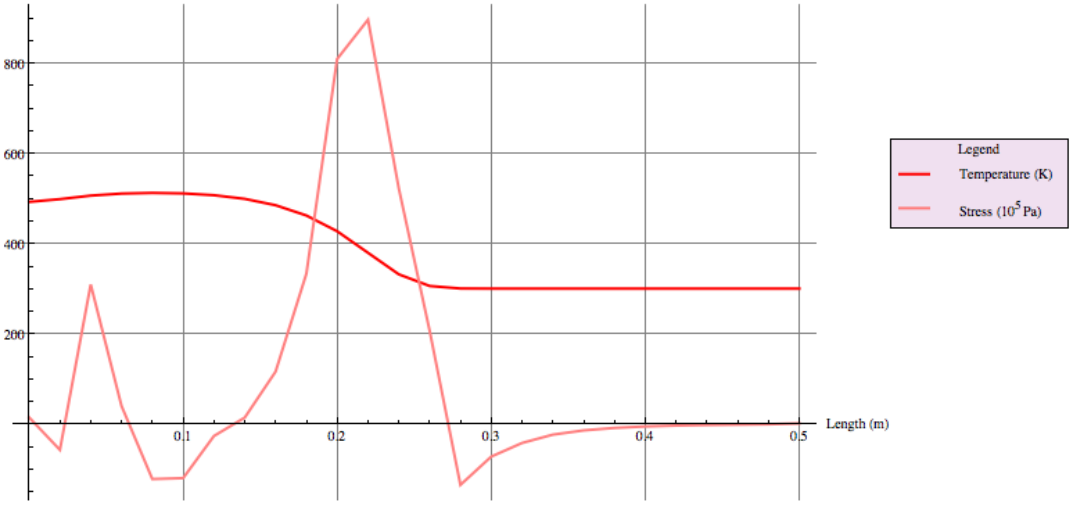

Figure 4-41: Temperature VS Transverse Stresses at 0.024m from Welding Line

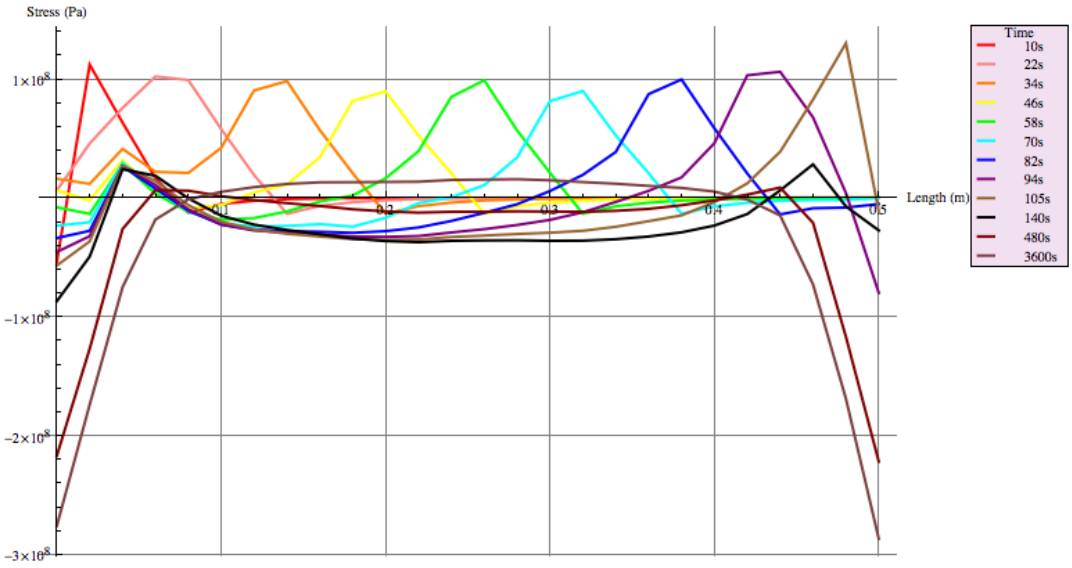

Figure 4-42: Transverse Residual Stress Distribution at Different Time

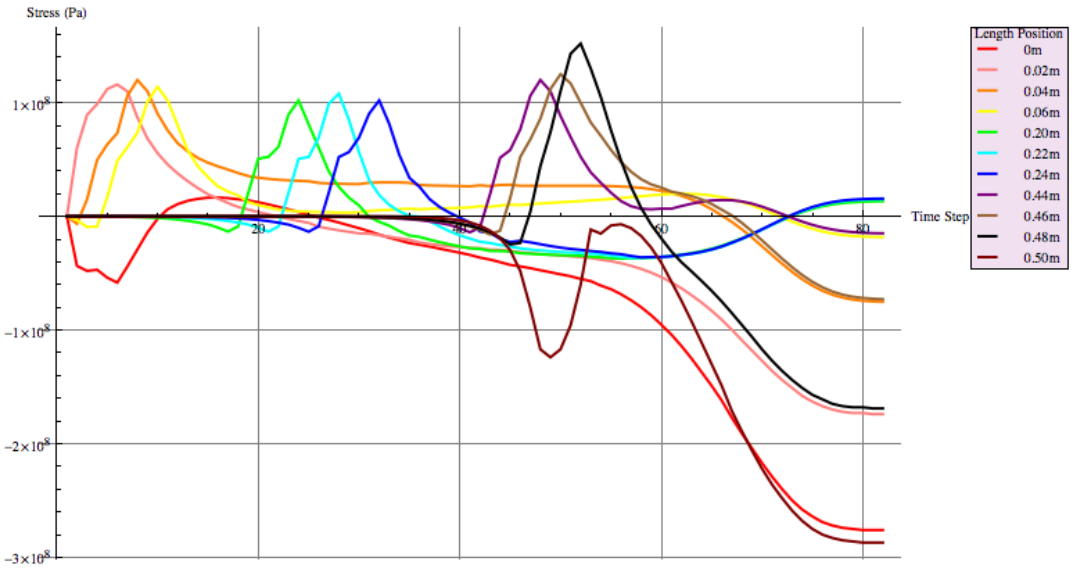

Figure 4-43: Time history of transverse residual stress at different position

4.2.6 Discussion

Figure 4-44 shows that the temperature distribution at different lines parallel to the welding line at 48 second. From this diagram, it can be seen that only the first three lines have a relatively high temperatures and a steep slope during the welding process; all are located in the welding pool or heat-affected zone. So the stresses along these lines include elastic stresses and plastic stresses, which are the original source of residual stresses. The temperature change dominates the stress distribution during the welding process and the force and moment equilibrium dominate the stress distribution during the cooling process in this area; other lines located away from the welding line show that the temperature increased very slow and the slope is quite flat, because the temperature change along those lines results from the heat conduction; there is no direct power input, so the stresses here are equilibrate the whole plate and they are all elastic reversible stresses, which are mainly dominated by the force and moment equilibrium during both the welding and cooling process.

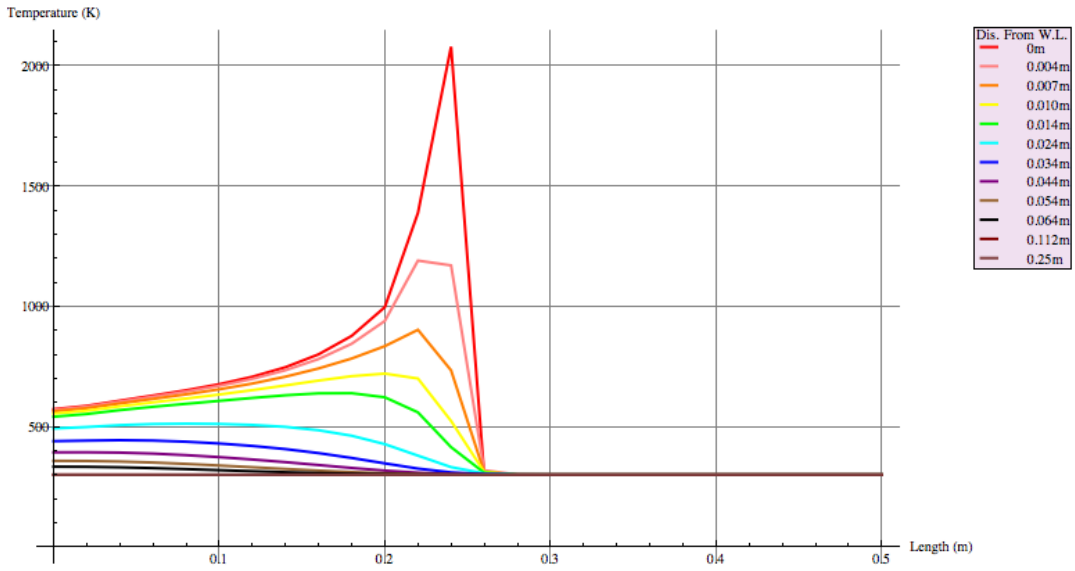

Figure 4-44: Longitudinal temperature distribution at different transverse positions at 48 second

From Figure 4-45 & Figure 4-46, it can be seen that the maximum tensile stress happened in the line which is located at about 0.014m from welding line, which is the location of the end of heat affected zone. In the other word, this is the approximate boundary of the plastic strain generated. The maximum transverse tensile stress is 93 MPa, which is relatively small. The transverse compressive stresses, generated at the longitudinal edges of the plate, have a maximum of 396 MPa at the welding line. The results look like quite symmetrical, which is due to in this model to using the element activate and deactivate facility, so during the welding process, the stress in the welding line is affected by the edge effect at each time step, and it keeps the form of compression at the two ends and tension at the center, due to the force and moment equilibrium, the final result is symmetrical. Furthermore, the stresses generated here is the main original source of the welding residual stresses, which means the stresses in other places are generated followed this, so the whole results should have the same symmetrical format seen along t he welding line.

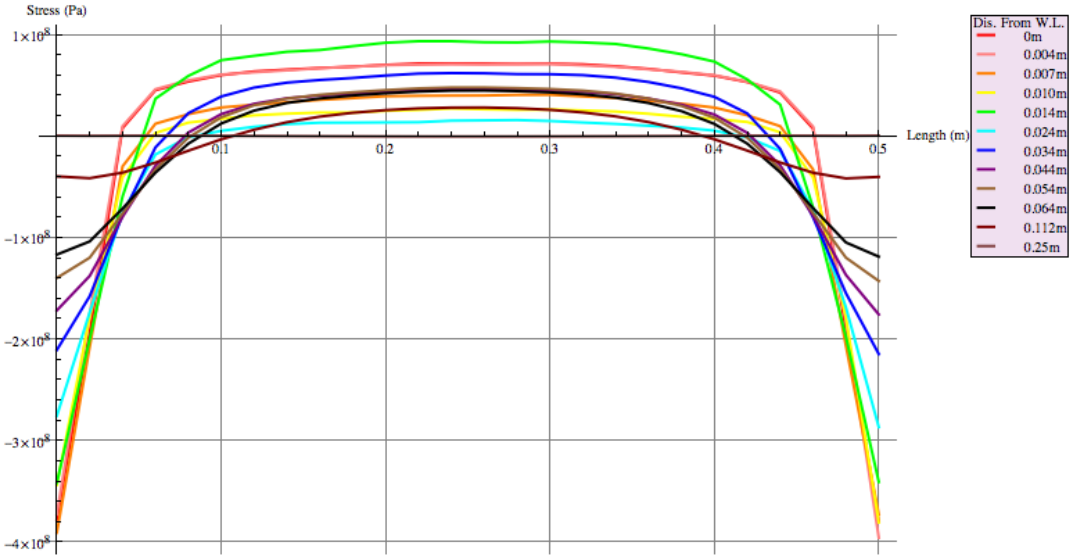

Figure 4-45: Final transverse residual stress distribution of different width position in longitudinal direction

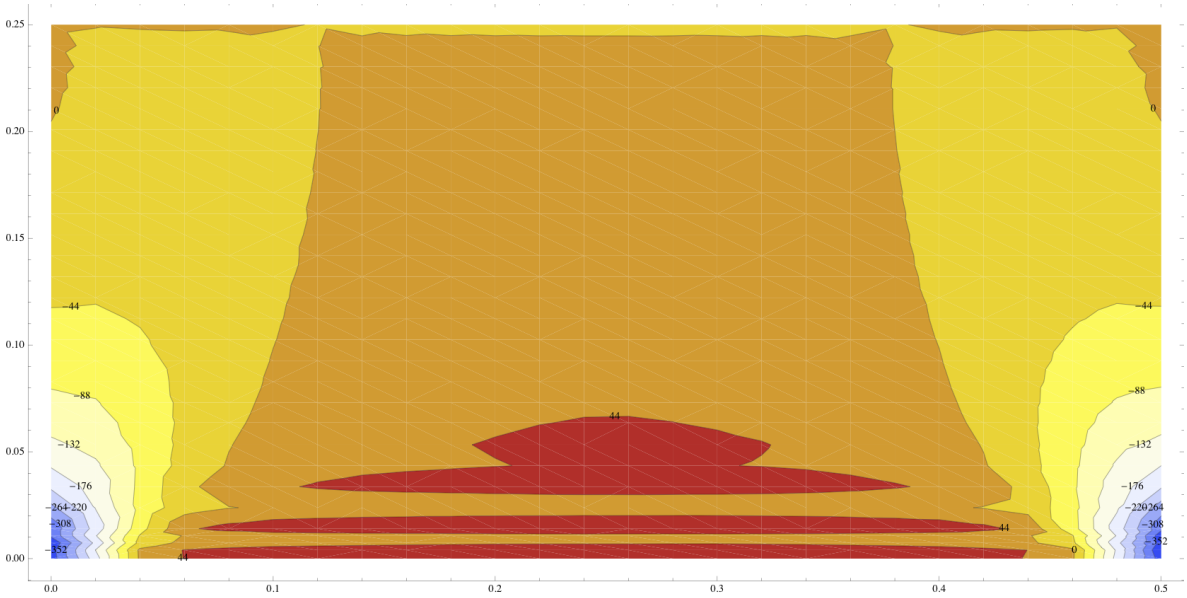

Figure 4-46: Transverse residual stress distribution plot

Overall the internal stresses must be in a self-equilibrium state; the transverse residual stresses should be equilibrium along lines parallel to the welding line, but some results showed in Figure 4-45 apparently were not. This is due to this model using 3-D elements and there is a three-dimensional effect producing a through thickness stress variation. From Figure 4-47, which shows the results from 3-D butt-welding model in Chapter 3, it can be seen the transverse residual stress represents higher value in the middle of the

thickness direction and relatively lower value on the surfaces, which caused the results are not equilibrium if only look at the results on the surfaces. And this effect is mainly worked on the positions near to the welding line, for those lines far from the welding line, the results are quite equilibrium, as shown in Figure 4-45.

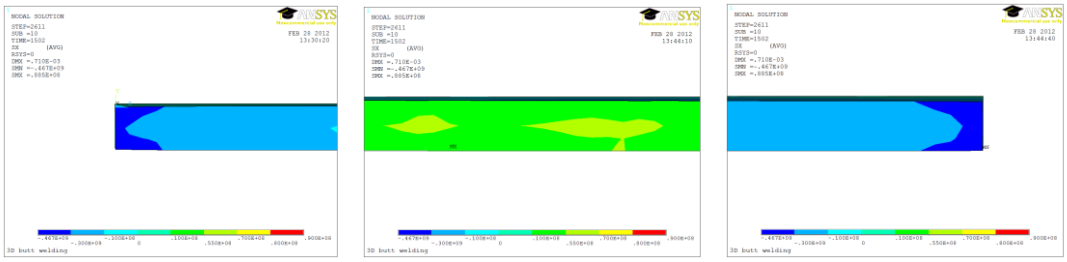

Figure 4-47: Transverse residual stress distribution through thickness direction at the welding line

4.3 Longitudinal Residual Stresses From FE Analysis

The longitudinal residual stress is of concern to most researchers because it has been deemed as one of the most responsible factors for the fatigue and fracture of marine structures. Figure 4-48 also shows how the longitudinal residual stress is affected by the edge effects. And according to the discussions in Section 4.2, the longitudinal residual stresses also presented symmetrical distribution about the mid-length line. There is a tensile residual stress near the welding line and compressive residual stress on the other parts far from the welding joint, the tensile residual stress is very large, a little larger than the yield stress of this material; and the compressive stress is relatively low. The maximum tensile stress is not at the welding line, but at 0.014 m from the welding line, for the same reason as the transverse residual stress distributions. In this section, the longitudinal residual stresses developing history along the transverse direction at length location 0.04 m and 0.24 m will be analyzed.

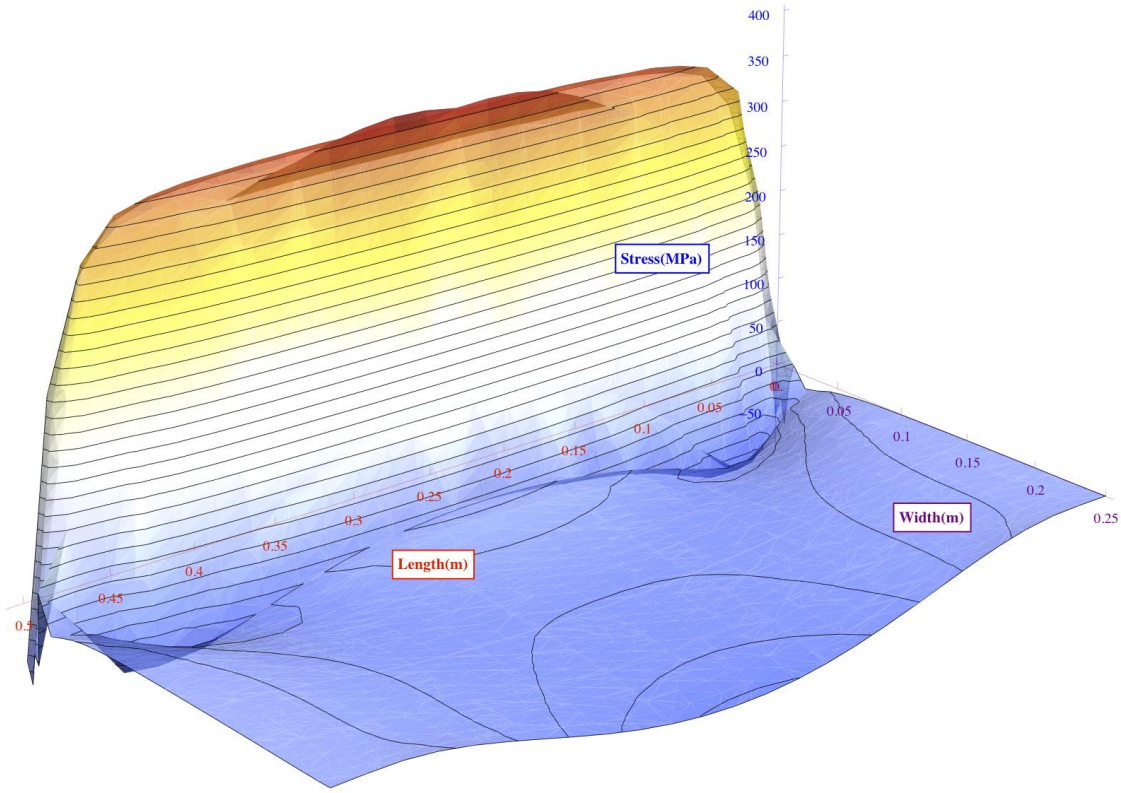

Figure 4-48: Overall transverse residual stress distribution

4.3.1 Length Position at 0.04 m

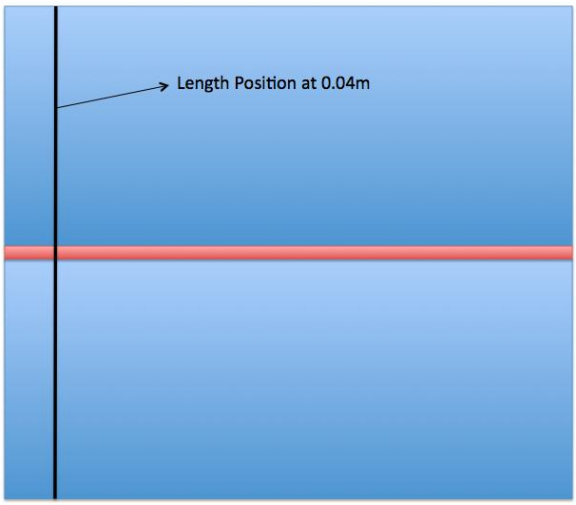

Figure 4-49: Schematic of location of length position 0.04m

Figure 4-50 shows the longitudinal residual stress distribution along the transverse direction at length position 0.04 m from the start of the weld. At the area near the welding line, the longitudinal residual stress is tensile with a value 329 MPa. The stresses away from the welding line is compressive with a maximum value of 80.4 MPa, the stress starts becoming compressive from tensile at the width position 0.016 m from the weld line. From Figure 4-51, it can be seen that the FE results and the simple method results are a good match.

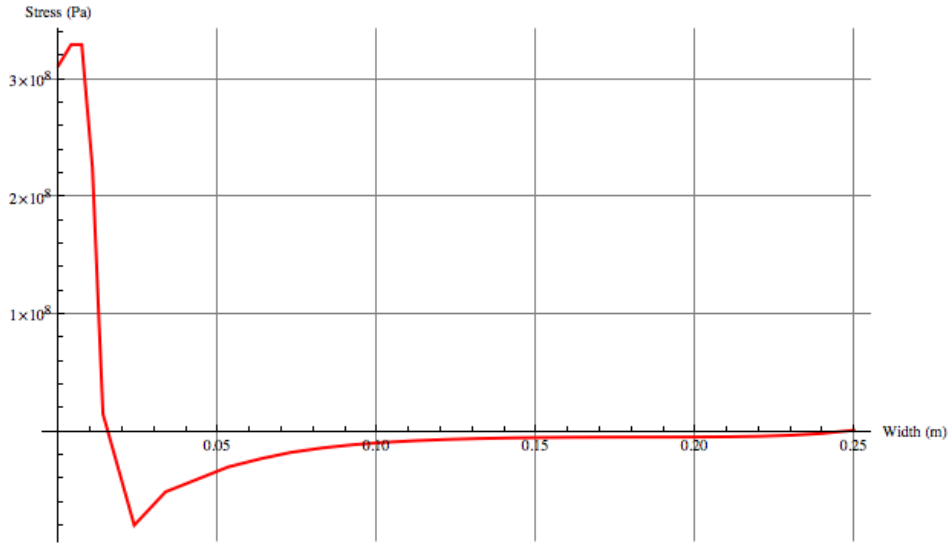

Figure 4-50: Final time step longitudinal residual stresses at length position 0.04 m in transverse direction

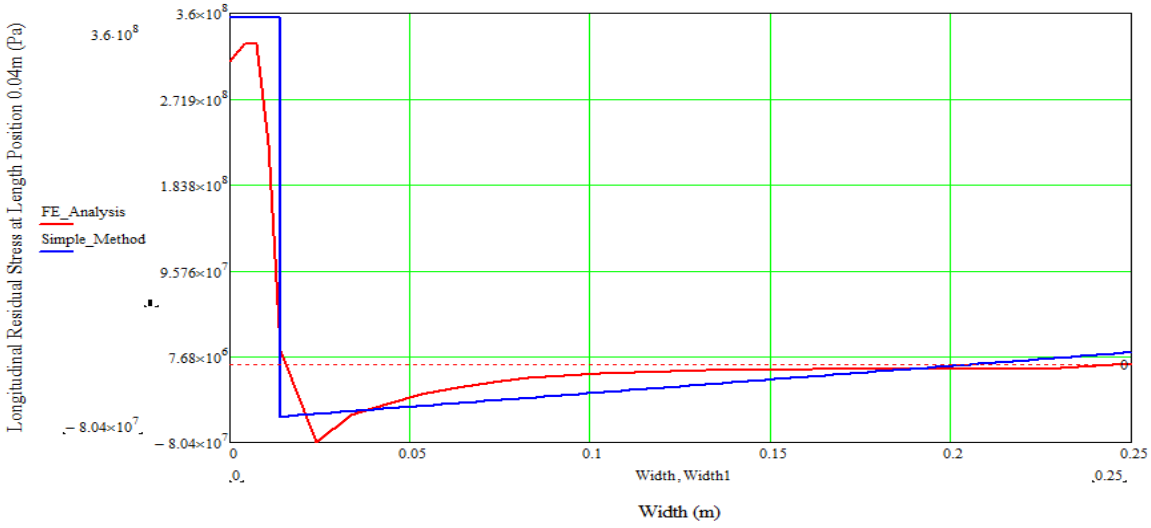

Figure 4-51: Results comparison between simple method and FE analysis

Figure 4-52 illustrates how the temperature changes during the whole welding process. It can be seen that at 8 seconds, the welding pool center has just arrived, and the temperature has reached the maximum value, and then start to cool down. The time interval in this figure is 12 seconds. The figure shows that the cooling rate near to the welding line is changing; at first the cooling rate is big and then become smaller due to the temperature dependent convection and conduction coefficient (mentioned in Section 3.2 & 3.4). From Figure 4-52, it can be seen that at the width positions from 0.024 m to 0.25 m, the temperature almost remains the same after reaching the maximum value. The maximum temperature during the whole process is around 500 K, which means when this region starts to cool, the temperature distribution only has a slightly change.

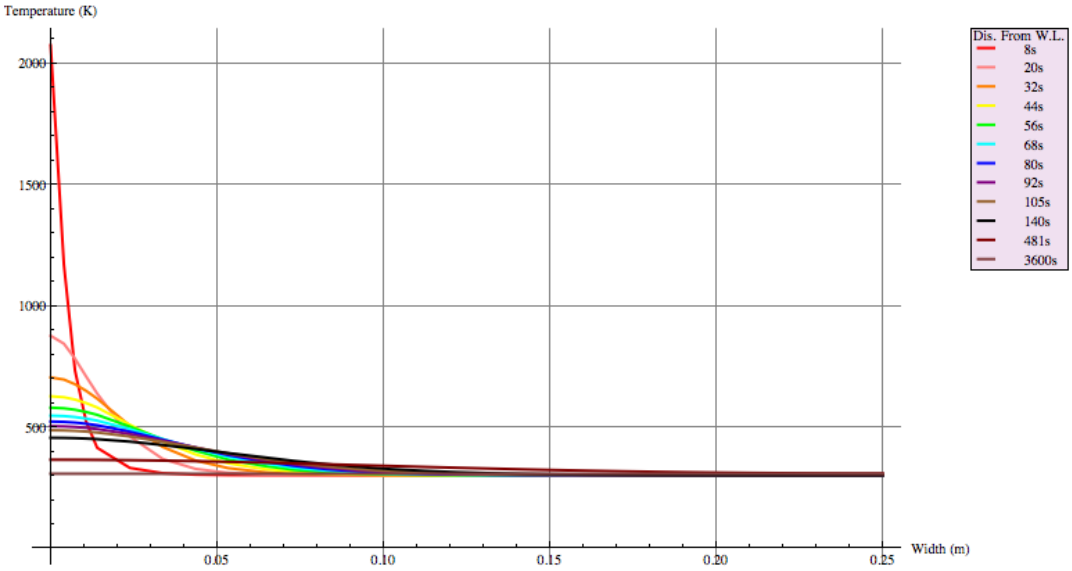

Figure 4-52: Time history of temperature at length position 0.04m in transverse direction

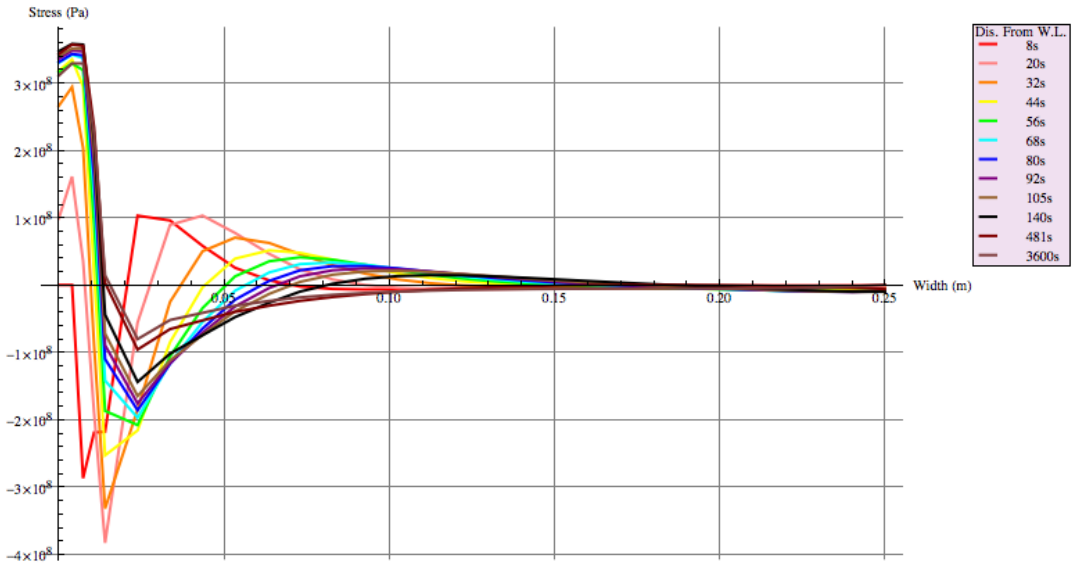

Figure 4-53: Time history of longitudinal residual stress at length position 0.04m in transverse line

Figure 4-53 shows how the longitudinal residual stress changes during the whole welding process. This corresponds along with the temperature distribution in Figure 4-52. When the welding pool center reached this line, the stress at the welding line is zero due to the melted material. The area near the welding line presents a compressive stress due to heating expansion and area next shows the tensile stress, which is produced for force equilibrium. The part away from the welding line has a zero stress. During the cooling process, it can be seen that the compressive part start to change to tensile and the tensile part starts to become compressive, the part away from the welding line remains zero. From Figure 4-53, the change of longitudinal residual stress distribution comes from the area near the welding line. The width position 0.007 m is a turning point while the welding pool center arrived (see the red line in Figure 4-53), because the temperature start to be lower than the material soften temperature from this point; and this point is also the turning point at the final time step (see the darker pink line in Figure 4-53). According to the discussion in temperature history, the width position from 0.024 m to 0.25 m, in this region, the stress produced here is mainly used for balancing purpose, because the maximum temperature in this region is 500 K, which makes the structure analysis in this region a purely elastic analysis, so that the stress produced due to the temperature change could be reversed.

4.3.2 Length Position at 0.24 m

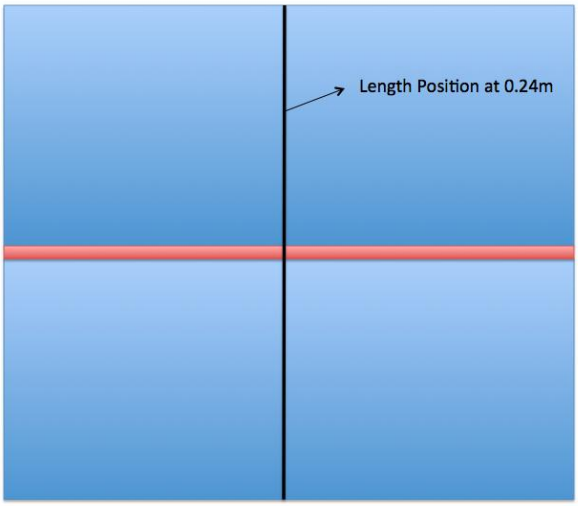

Figure 4-54: Schematic of location of length position 0.24m

Figure 4-55 shows the longitudinal residual stress distribution along the transverse direction at length position 0.24 m, which gives a different result from the length position 0.04 m. It can be seen the tensile stress region is wider and the maximum tensile stress is 390 MPa at width position 0.014 m; the maximum compressive stress 72 MPa occurs at the transverse edge of the plate. By comparing this result with Figure 4-21, it can be seen that those results have the same distribution pattern, but the results from the simple method seems stiffer, because the material work hardening effects is not used in the simple method.

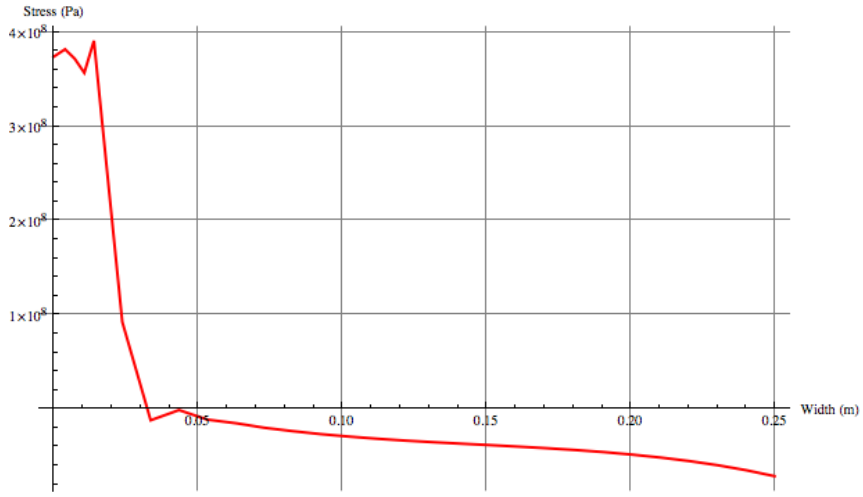

Figure 4-55: Final time step longitudinal residual stresses at length position 0.24 m in transverse direction

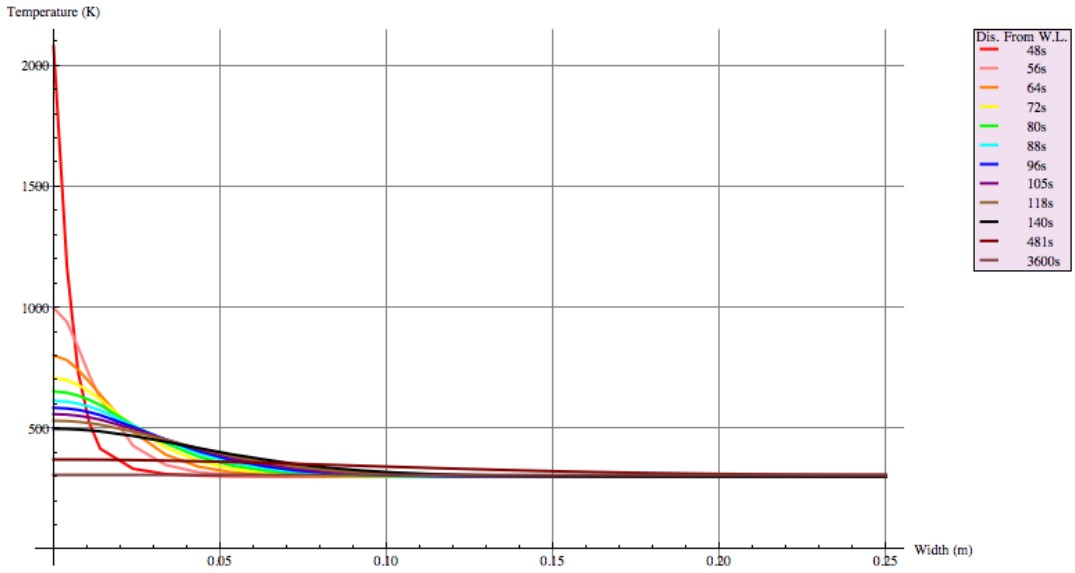

Figure 4-56: Time history of temperature at length position 0.24m in transverse direction

Figure 4-56 illustrated how the temperature changes during the whole welding process. It can be seen that it is almost the same temperature history as that at length position 0.04 m, except for the time of welding pool center arriving. Because of that, it can be concluded that all the length positions have the same temperature history along the transverse direction.

By comparing Figure 4-57 with Figure 4-53, it can be seen that the longitudinal residual stress distribution histories at these two lines are different. At 48 second, the welding pool center reached this line, the stress in the welding line is zero due to the melted material, and the area near the welding line presents a compressive stress due to heating expansion. The area next shows a tensile stress, which is produced for balancing, and the part away from the welding line has a relatively small compressive stress. During the cooling process, it can be seen that the stress acting at the area around the welding line start to change to tensile and the tensile part start to become compressive, the part away from the welding line remains compressive. From Figure 4-57, the width position 0.014 m is a tuning point while the welding pool center arrived (see the red line in Figure 4-53), which is twice of the previous line; and this point is also the turning point at the final time step (see the darker pink line in Figure 4-53). Furthermore, the stress started changing to compressive from tensile at the width position 0.032 m at the final time step, which is also twice that of the previous line.

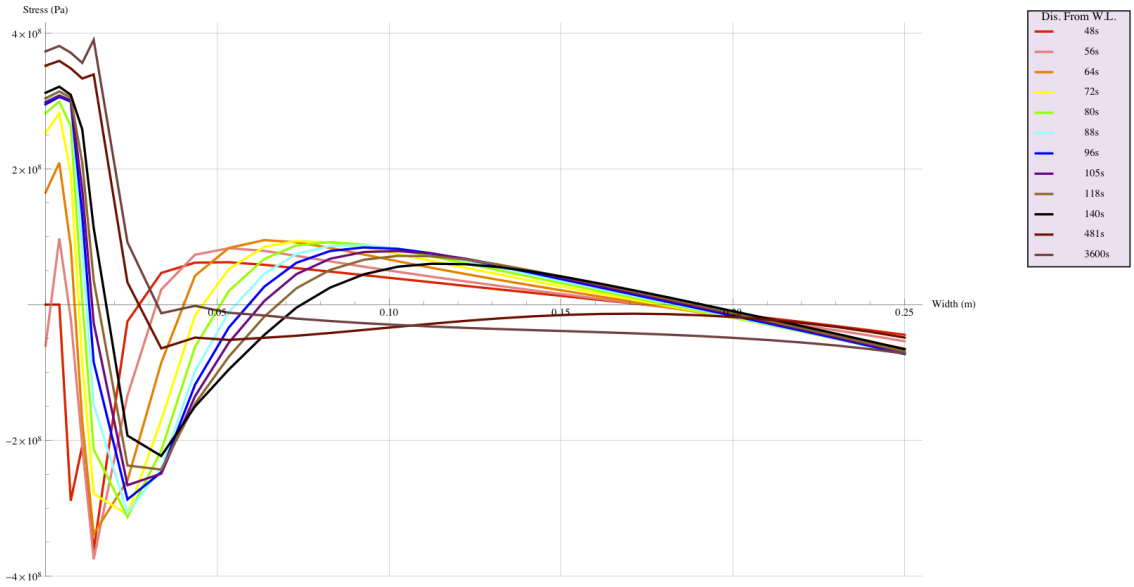

Figure 4-57: Time history of longitudinal residual stress at length position 0.24m in transverse line

As the time history of these two lines being almost the same, the longitudinal residual stress history might also be expected to be the same. However, these two lines belong to a whole plate, in which the stress distributions are also affected by the force and moment equilibrium. In other words, the heating and cooling effect is the driving force for producing the residual stresses, but the force and moment equilibrium is the key factor leading to the final welding residual stress distributions.

4.3.3 Discussion

Figure 4-58 shows that the longitudinal residual stress distributions at any width locations along with the longitudinal direction are symmetrical about the mid-length line, so in Figure 4-59, only the longitudinal residual stress distributions at length position from 0 m to 0.24 m are shown. According to the Figure 4-58 & Figure 4-59, it can be seen that at the width position from 0 m to 0.014 m (the welding line and the heat affected zone), there are very high tensile stress and the magnitudes are over the material yield stress, the stresses produced here result from the heating and cooling effects, which should not be affected much by the model geometry dimension; at the width position from 0.034 m to 0.25 m, the stresses here are compressive, which is produced for as a result of the force

and moment equilibrium, so that the stresses distribution here will change as different model geometry dimension. The width position from 0.014 m to 0.034 m is a transition area.

The internal stresses should be in a self-equilibrium state and the longitudinal residual stress at the two ends in the longitudinal direction should be zero because there is no external force during the whole welding process. However the simulation results showed a small compressive value, because in VrWeld software, each element has eight Gaussian Points inside; the non-linear analysis is carried out at the Gaussian Points; as mentioned in Section 3.5, the displacement constraint equations is chosen, and kinematically admissible displacement field is used in the VrWeld software, which is used to define the principle of minimum potential energy, so it needs only to satisfy compatibility condition and the displacement boundary conditions, but not the traction boundary conditions or equilibrium.

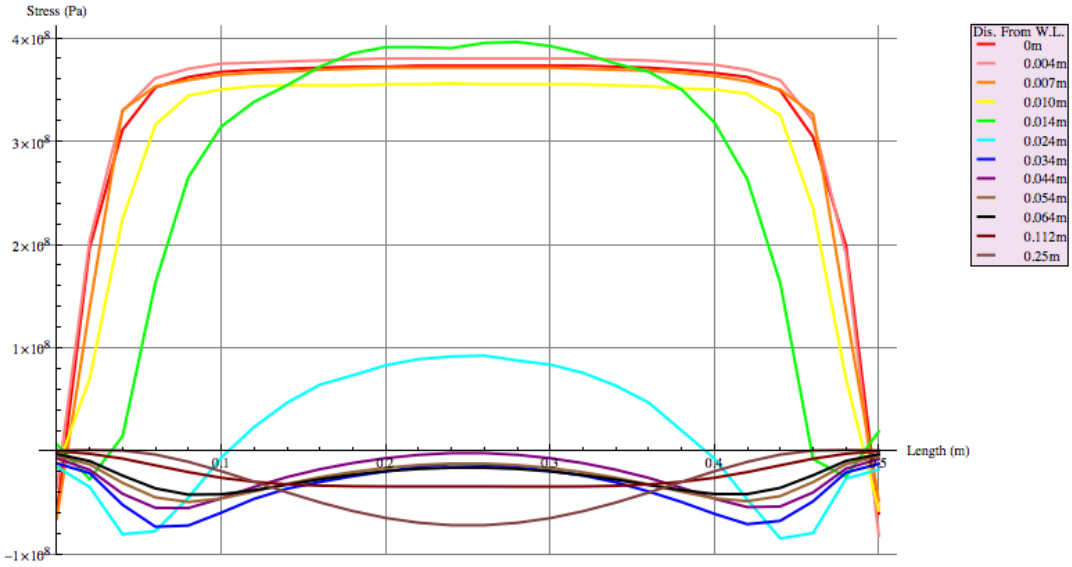

Figure 4-58: Final longitudinal residual stress distribution of different width position in longitudinal direction

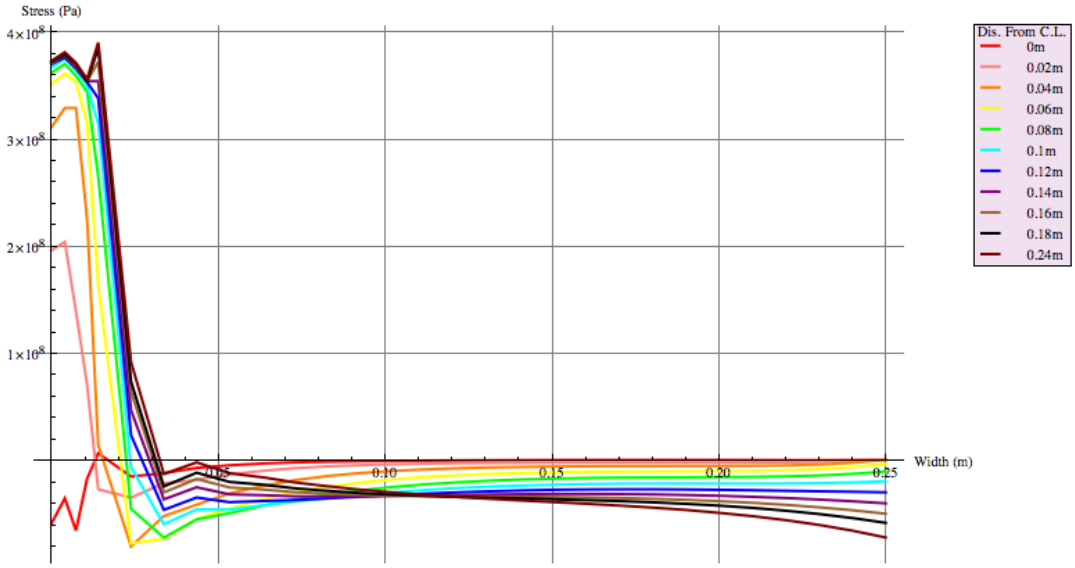

Figure 4-59: Longitudinal residual stress distribution of different length position in transverse direction

4.4 Boundary Conditions

Different boundary conditions can affect the structural analysis results, including the stress significantly. In order to present the internal reaction force at the welding line, the author did a half model by using symmetrical boundary condition, which is labeled as Model 1 in this section and the schematic can be seen in Figure 4-60. According to Figure 4-61, it can be seen that the reaction force is self-balanced and the distribution pattern also verified the transverse residual stress distribution discussed in the previous section.

Model 2 (see Figure 4-62) is used to present the displacement tendency at the welding line without internal restriction, in order to get a deeper understanding of the welds' behavior. From Figure 4-63, it can be seen that at the two ends of the welding line, there is a large shrinkage in both transverse and longitudinal directions, which can explain why there is such a massive compressive transverse residual stress at the edges of the welding line. So the edge effect is induced by both transverse and longitudinal shrinkage, but due to the heating and cooling effect at any length position should be the same, which means the transverse shrinkage should be also the same if it is analyzed separately. According to

that, the author assumed the main reason caused the large compressive transverse residual stress is the longitudinal shrinkage.

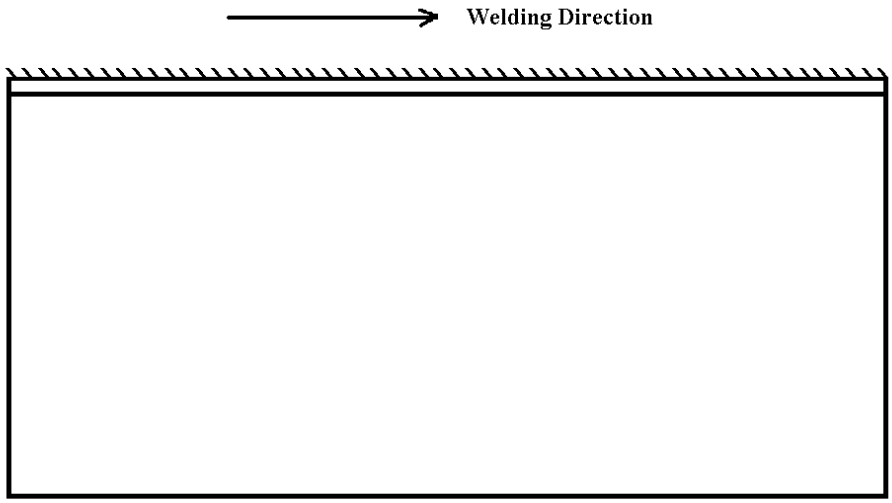

Figure 4-60: Boundary condition schematic of Model 1

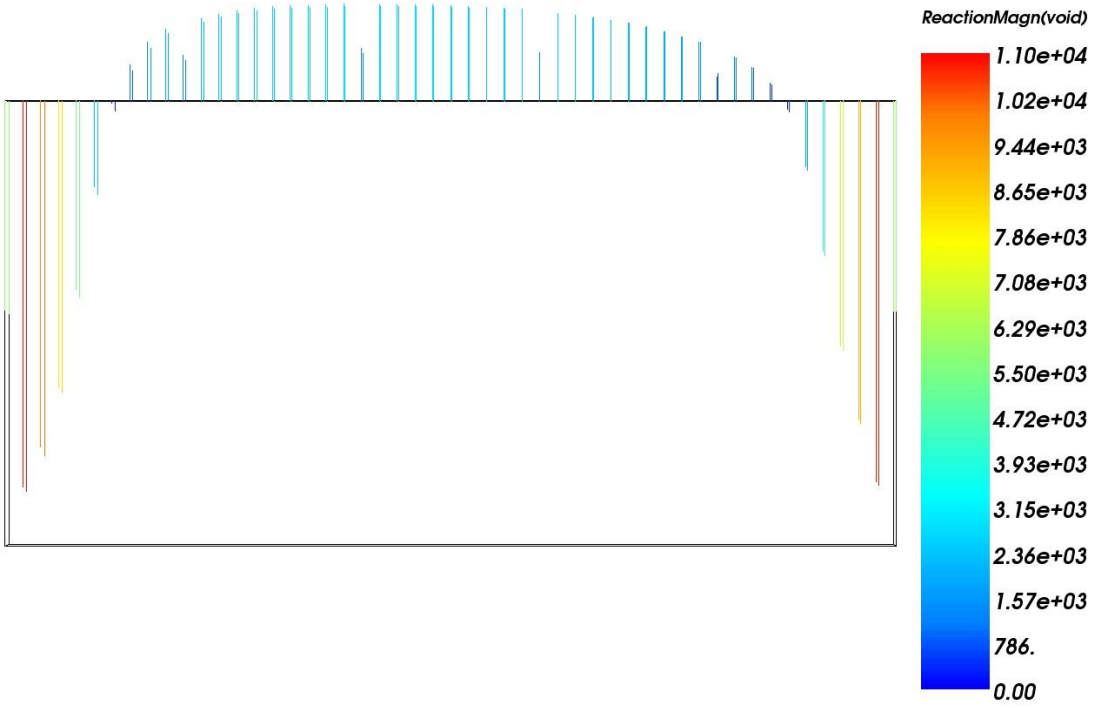

Figure 4-61: Reaction force distribution at welding line in Model 1

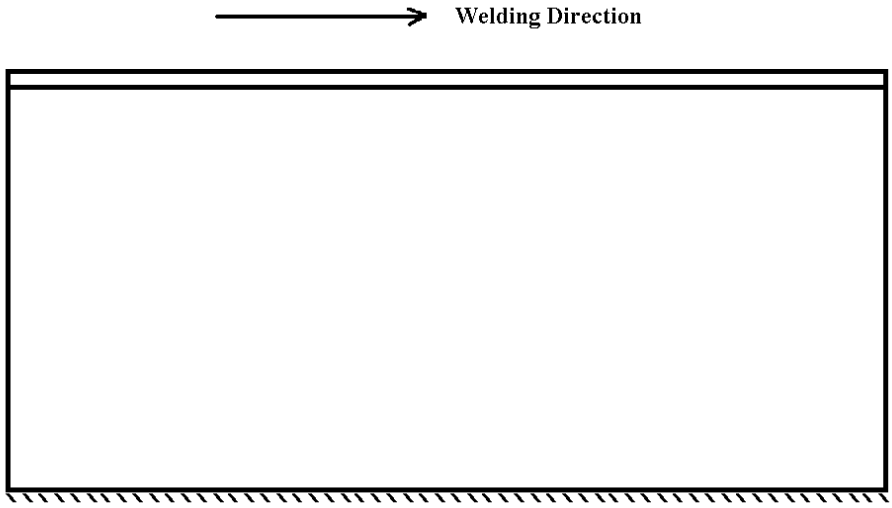

Figure 4-62: Boundary condition schematic of Model 2

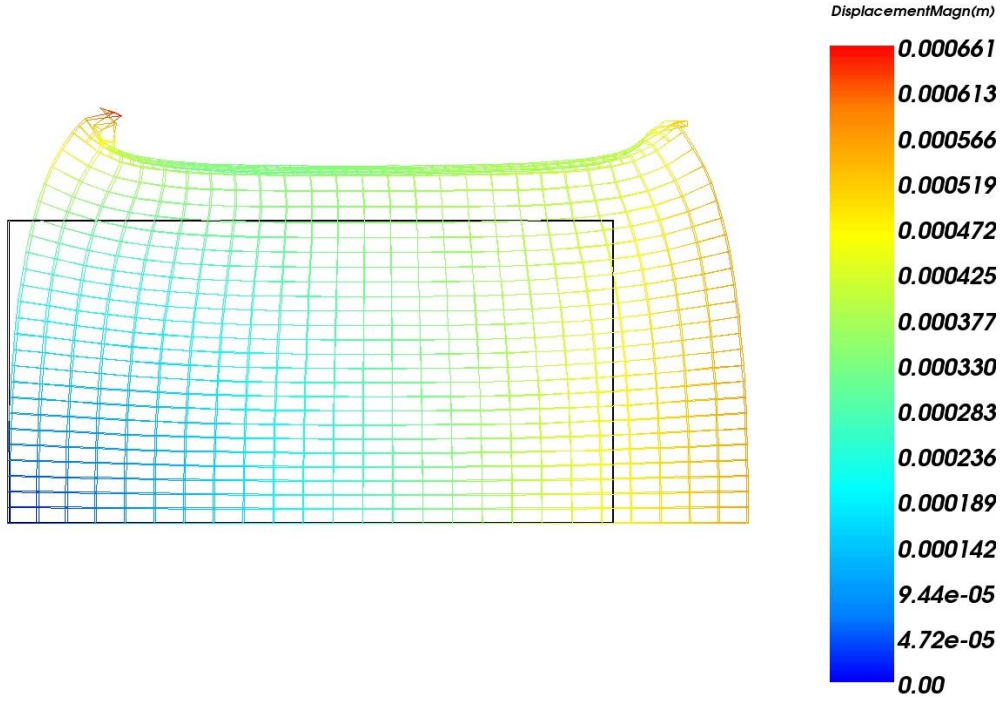

Figure 4-63: Displacement schematic of Model 2

Model 3 (Figure 4-64) was built to verify the author's assumption above. It can be seen from the schematic that the boundary condition restrict the longitudinal displacement of the model, and Figure 4-65 shows that the transverse shrinkage is flat in longitudinal direction after preventing the model from the longitudinal shrinkage, there is no edge effect at all, which proved that the main reason causing the edge effect is the longitudinal shrinkage.

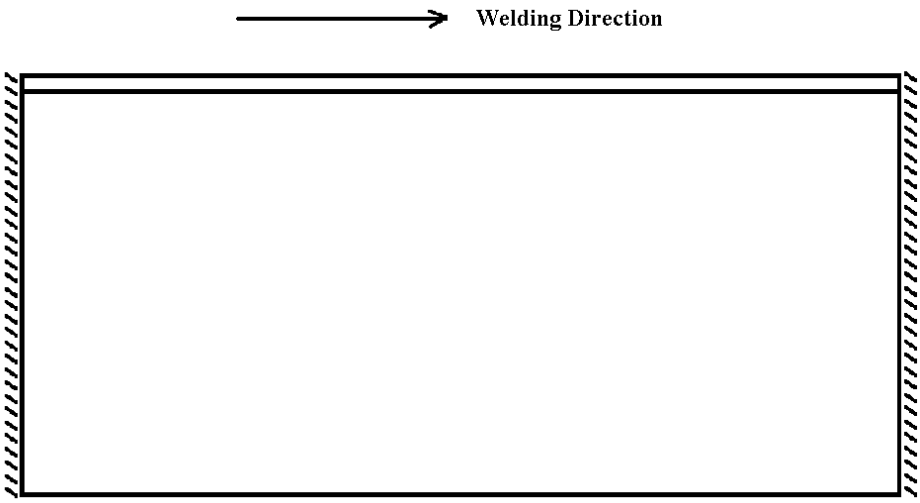

Figure 4-64: Boundary condition schematic of Model 3

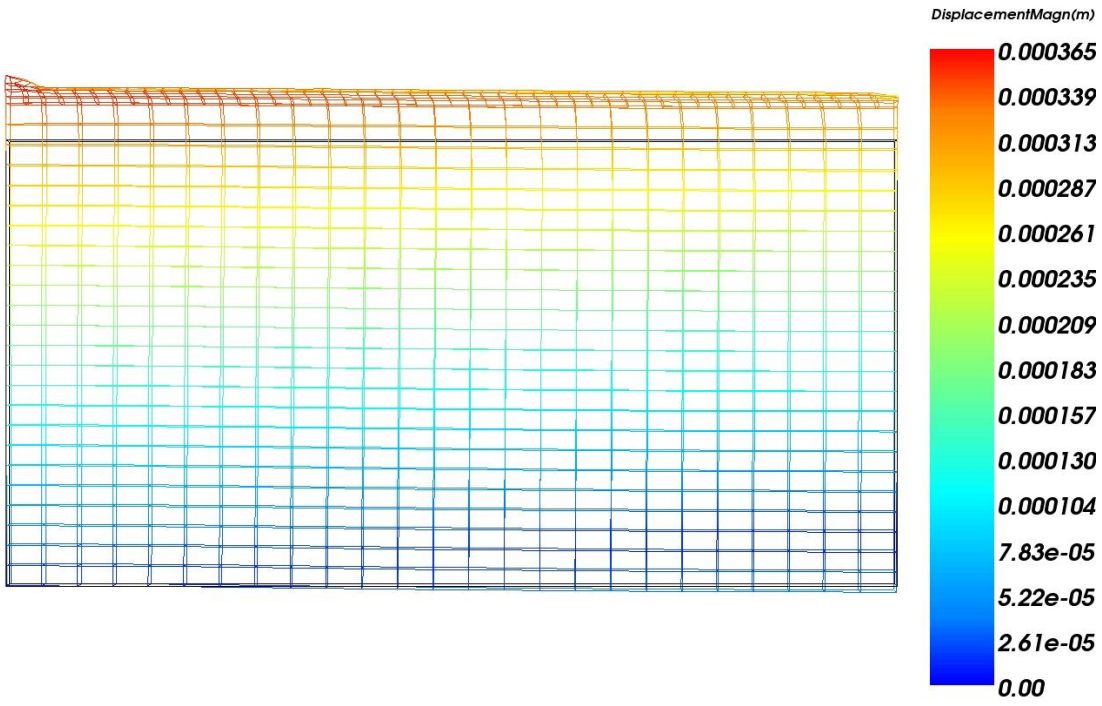

Figure 4-65: Displacement schematic of Model 3

Lastly, Model 4 is used to analyze the residual stress behavior against the longitudinal shrinkage. From Figure 4-66, it can be seen that in this model, the symmetrical boundary condition and longitudinal constraint at the two edges were applied.

According to Figure 4-67, the magnitude of transverse residual stress in the whole plate is from -84 MPa to 84 MPa, there is no longer the large compressive stress, which indicates that the large compressive residual stress comes from the longitudinal shrinkage. The longitudinal residual stress distribution shows that each cross section has the same longitudinal stress distribution along the welding line, but the compressive stress magnitude increased tens to hundreds MPa, which is due to the constraint at the two edges that were applied prevent the longitudinal shrinkage, but it also provide a reaction force at the boundary, which stopped the stress releasing at the edge.

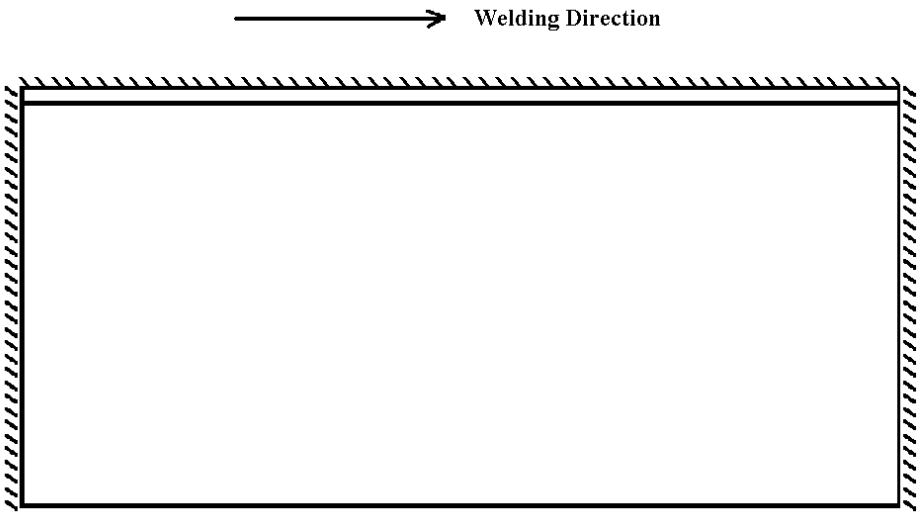

Figure 4-66: Boundary condition schematic of Model 4

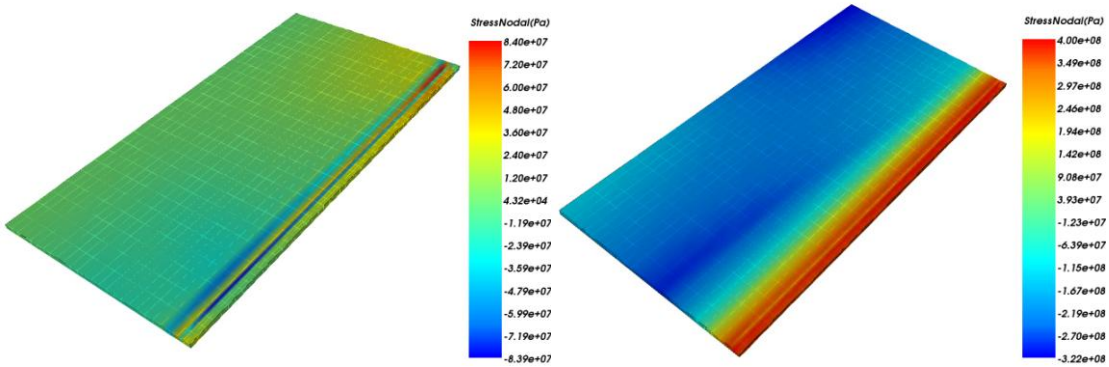

Figure 4-67: Transverse and longitudinal residual stress distribution of Model 4

4.5 Conclusions

In this chapter, a simple method for predicting the butt-welding residual stresses based on force and moment equilibrium was derived, with results that are a reasonable match with the results from FE analysis. The author also did a detailed analysis for the distribution of transverse and longitudinal residual stresses, which deeply illustrated how the butt-welding residual stresses was distributed and accumulated during the welding process. The boundary condition analyses illustrate the cause of the edge effect graphically, which is due to the longitudinal shrinkage at the two edges of the welding line. According to Figure 4-68, it can be seen that the high value residual stresses are located near the welding line, and the following conclusions can be drawn:

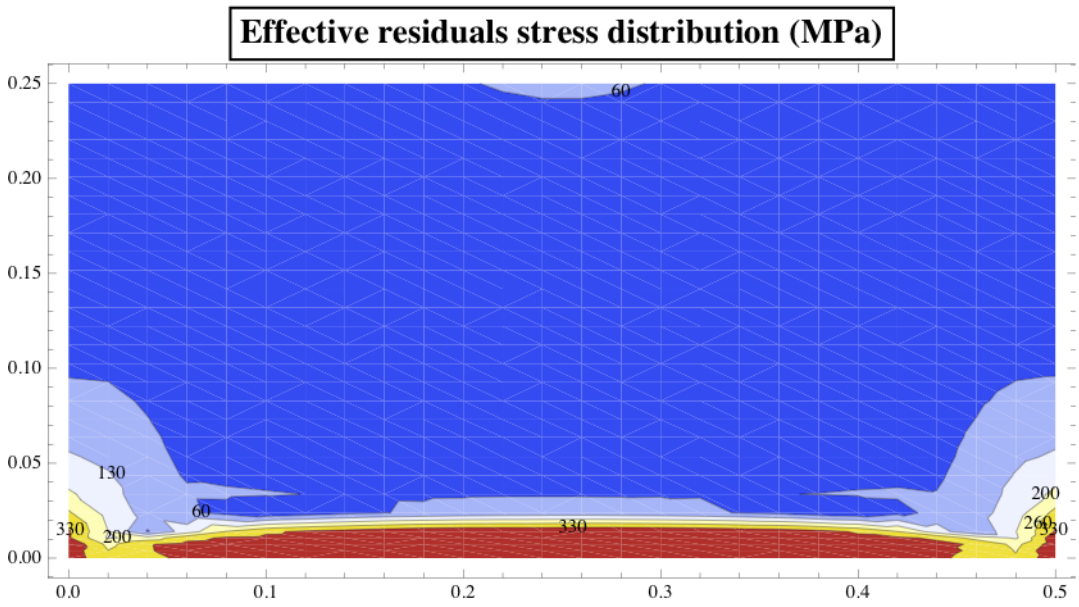

Figure 4-68: Effective residuals stress distribution (MPa)

- The welding residual stresses are symmetrical in both transverse and longitudinal directions. This results from the use of element activate and deactivate technique and the force and momentum equilibrium effect, which has been detailed explained in Section 4.2.1;

- The main factors dominating the welding residual stress distribution are the heating and cooling during the welding process and the internal force and moment equilibrium effect; the former mainly dominates the stress produced at

the areas near the welding line, which is the origin of the driving force, not substantially affected by the model geometry dimensions; the stresses well away from the weld line are mainly balancing overall forces and moments.

- The maximum residual stress magnitude does not occur at the welding line, but at the position at 0.014 m from the welding line, due to the temperature dependent material properties and performances.

- The transverse welding residual stresses have relatively small tensile value, but a large compressive value, which exceeds the material yield stress, located at the region of both ends of the welding line.

- The longitudinal welding residual stresses have a relatively small compressive value, but a large tensile value, which also exceeds the material yield stress and are located at the region around the welding line.

Chapter 5 Parametric Study of Welding Residual Stress Distributions

In this chapter, a detailed parametric study for butt welding residual stresses based on 2D butt-welding by using 3D element is reported. The simulation technology used is the same as in Chapter 4. The parametric study considered cut-off temperature, welding power, welding velocity, plate length and plate width. According to the analysis carried out in Chapter 4, the following key aspects are compared for the different cases in each parametric study:

- The stress produced at the welding line, which is the origin of the driving force of the final residual stress distribution;

- The transverse welding residual stresses at the cross section of the welding. These have a large compressive value at both ends of the welding line, which exceeds the material yield stress;

- The longitudinal welding residual stresses at the cross section of the mid-length. These have a large tensile value at the region around the welding line center, which also exceeds the material yield stress.

5.1 Cut-Off Temperature (COT) Effect

The definition of the cut-off temperature has been introduced in Section 3.6. This is an important factor in the structure analysis. By changing the cut-off temperature, the temperature dependent mechanical material property affect on the welding residual stresses is determined. In this analysis, the model parameters are exactly the same as the model in Chapter 4, and the different cut-off temperatures chosen are 673 K, 873 K, 1073 K, 1473 K and 1773 K. As the only difference in this parametric study is the COT, the temperature simulations are all the same as for the model in Chapter 4, so only the welding residual stresses results are discussed.

5.1.1 Transverse Residual Stress Comparison Under Different COT

Figure 5-1 shows the time history of the transverse residual stress at the start point of the welding line, it can be seen that when the COT is 673 K and 873 K, the material is not melt and gets some level of strength, the residual stress presents tensile first on the material is cooling, and the case of 673 K resulting a larger stress than 873 K as the material has more strength at 673 K. Then as the welding center moves forward, the edge effect drives the residual stress into compressive. When the COT is 1073 K, which is just the material soften temperature, the residual stress oscillate by small amount between tension and compression, which is because the material temperature is decreasing and the material strength is recovering gradually, in addition, the residual stress also needs to satisfy the force and moment equilibrium. When the COT is 1473 K and 1773 K, due to both COT are higher than the material soften temperature, it can be seen that the residual stress history are exactly the same, which illustrate that once the material strength is recovered, the residual stress is affected by the edge effect and becomes compressive.

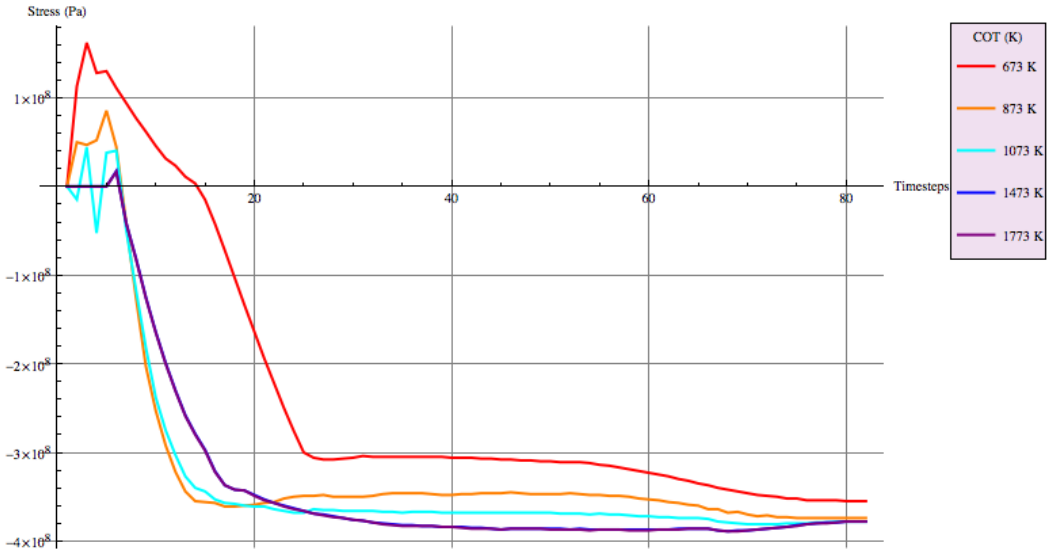

Figure 5-1: Transverse residual stress history at the start point of welding line under different Cut-Off-Temperature

According to Figure 5-2, it can be seen that the transverse residual stress distributions in the welding line under different COT have the same pattern, with very rapidly changing compressive residual stresses at the two ends and relatively small magnitude and flat

tensile stresses from the outer to the center of the line, but the stress and the positions where the stress change from compressive to tensile are different. From the results in thermal analysis, the duration of the temperature above each COT is different, which has been listed in Table 5-1.

Cut-Off Temperature (K)	Duration (s)
673	30
873	16
1073	9
1473	5.25
1773	3.75

Table 5-1: Duration of the temperature above each COT

So in each model, the temperature load defined in the structure analysis for any point, which temperature is higher than 673K, is different in the first 30 seconds, due to the material property is temperature dependent, the Young's Modulus, Yield Stress and the Work Hardening Rate are different at each COT, the residual stress in the welding line produced during the welding process are different, which means the origin driving force of the final residual stress distribution is different; furthermore, the force and moment equilibrium leads to the different final residual stress distribution, which presents that the higher COT, the lower magnitude of tensile stress.

From Figure 5-3, the high magnitude compressive transverse residual stress distributions are different under different COT. As the higher COT, the changing rate of the stress is higher, but the stress changing ranges are almost the same, when the COT is 1073 K, there is the biggest compressive stress; and when the COT is 673 K, the smallest compressive stress results; the other three cases are similar.

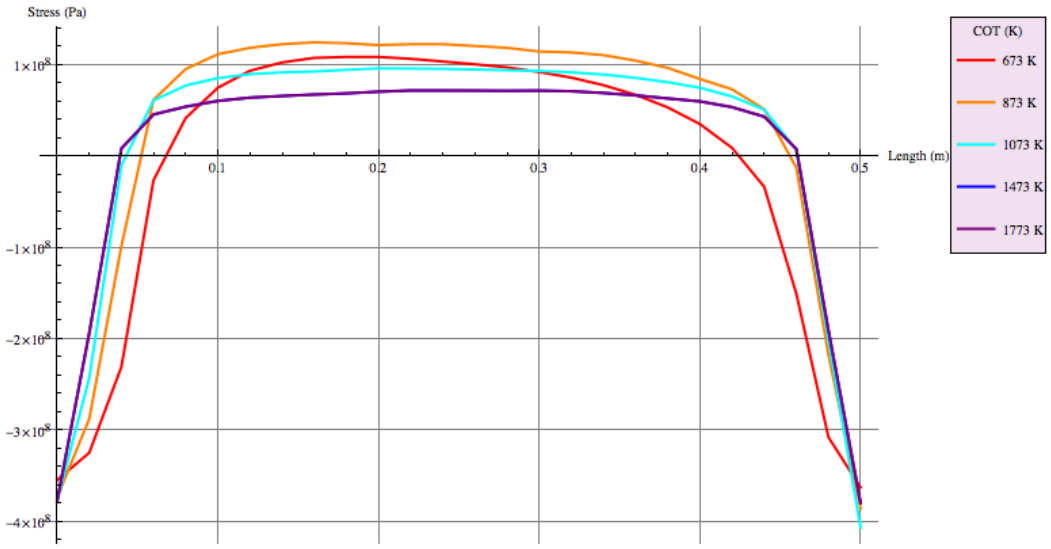

Figure 5-2: Transverse residual stress distribution at welding line under different Cut-Off-Temperature

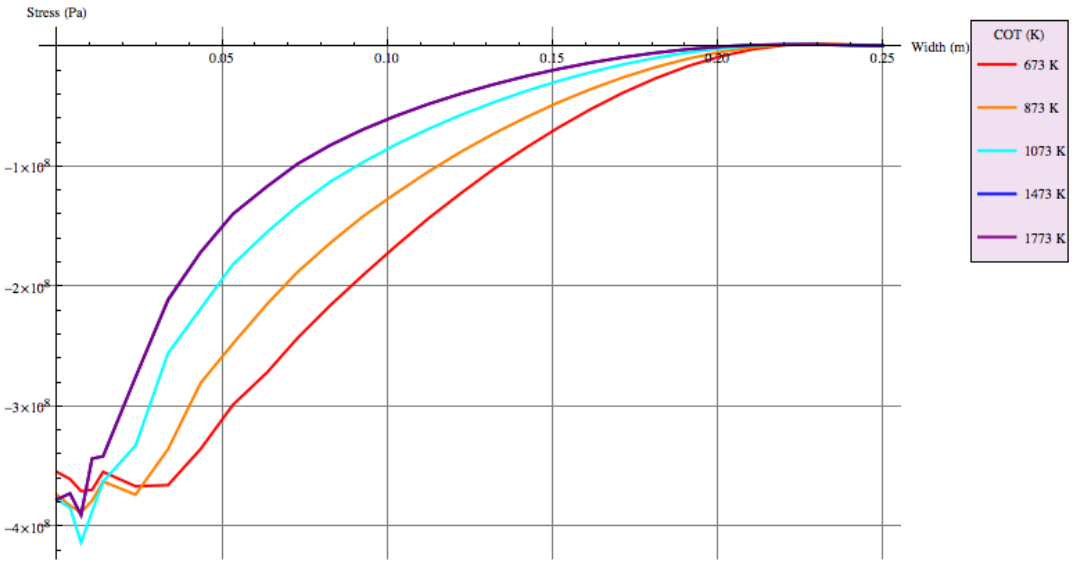

Figure 5-3: Transverse residual stress distribution at the cross section of welding beginning under different Cut-Off-Temperature

5.1.2 Longitudinal Residual Stress Comparison Under Different COT

Figure 5-4 shows that the longitudinal residual stress distributions in the welding line under different COT have the same pattern, but different stress values and changing rate

of the stress at the two ends of the plate. It can be seen that the tensile residual stress value and rate of change increase as the COT increases, and once the COT is higher than 1073 K, the changing rates become the same and the magnitude start to decrease. The largest magnitude of the longitudinal residual stress occurs when the COT is 1073 K and the smallest one when the COT is 673 K. Because the models are using the kinematic hardening scheme, and when the COT is 673 K, the material has relatively more strength even at the COT, it will produce tensile stress first due to the cooling effect, then the edge effect drives it into compression. According to the kinematic hardening scheme, the material is plastically deformed in tension followed by loading in the reverse direction, the compressive yield strength in reverse loading is reduced in the same amount as the tensile yield strength is increased during the initial loading.

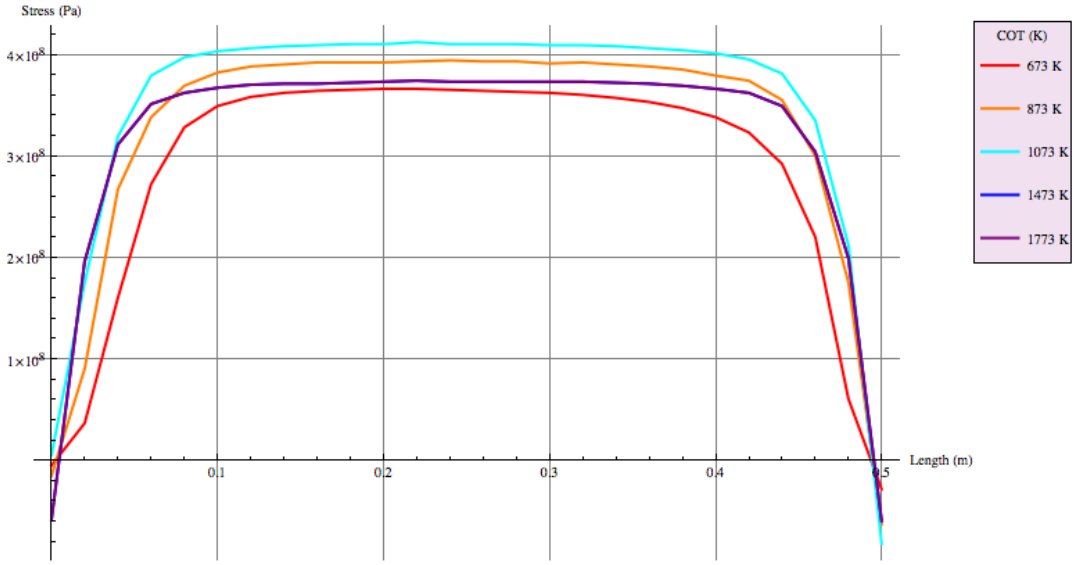

Figure 5-4: Longitudinal residual stress distribution at welding line under different Cut-Off-Temperature

Figure 5-5 indicates that different COT doesn't substantially affect the longitudinal residual stress in the area near the welding. From the figure, it can also be seen that in the area away from the welding line, the stress is higher at lower COT. Because the stiffer weld at low COT results in a bigger overall in-plane bending of the plate, at high COT, the balance of compression is more uniform. And the residual stress at that region is using for balancing the stress produced near the welding line, where the maximum temperature is different, so the different micro-structural form results in a different

material yielding and work hardening situation, furthermore, which creates the different plastic strain distribution, which is an important factor to lead different force and momentum equilibrium impact for the stress distribution.

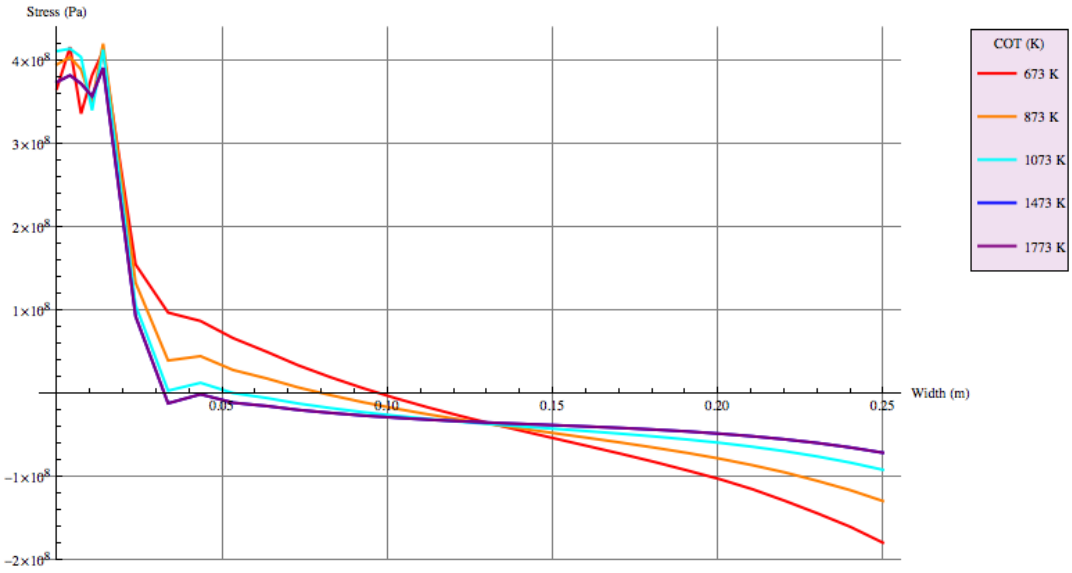

Figure 5-5: Longitudinal residual stress distribution at the cross section of mid-length under different Cut-Off-Temperature

5.1.3 Discussion

The different COT defines the different maximum temperature loading in the structure analysis, it doesn't change the temperature analysis for the welding process, just modified the results from it, which can be seen in Figure 5-6. The investigation of COT effect can be used to find how the high temperature material property affects the simulation results. It is important to note that the material property performance at the high temperature is the main input factor when carrying out a welding simulation.

From Figure 4-4, the transverse moment should be in equilibrium with the longitudinal moment. Combining Figure 5-5 and Figure 5-2, there is a larger transverse moment with lower COT. Therefore the longitudinal moment needed to balance the transverse moment also becomes larger at lower COT. So the author concludes that the longitudinal in-plane bending should be a reaction to the transverse end compression.

As mentioned before, 1073 K is the material softening temperature, according to the analysis above; when the COT is over 1073 K, the stress simulation results don't change and the analysis can simulate the material melt effect during the welding process. Visually, the higher COT results are more reliable, but the simulation process is more complicate to carry out. If the COT is set lower than 1073 K, the material is too stiff as it does not melt even at the maximum temperature. The lower the COT, the easier it is to find a simple method for calculation of the residual stress (by neglecting the material melt effect), but the residual stress distribution is changed not only in scale, but also in the distribution pattern.

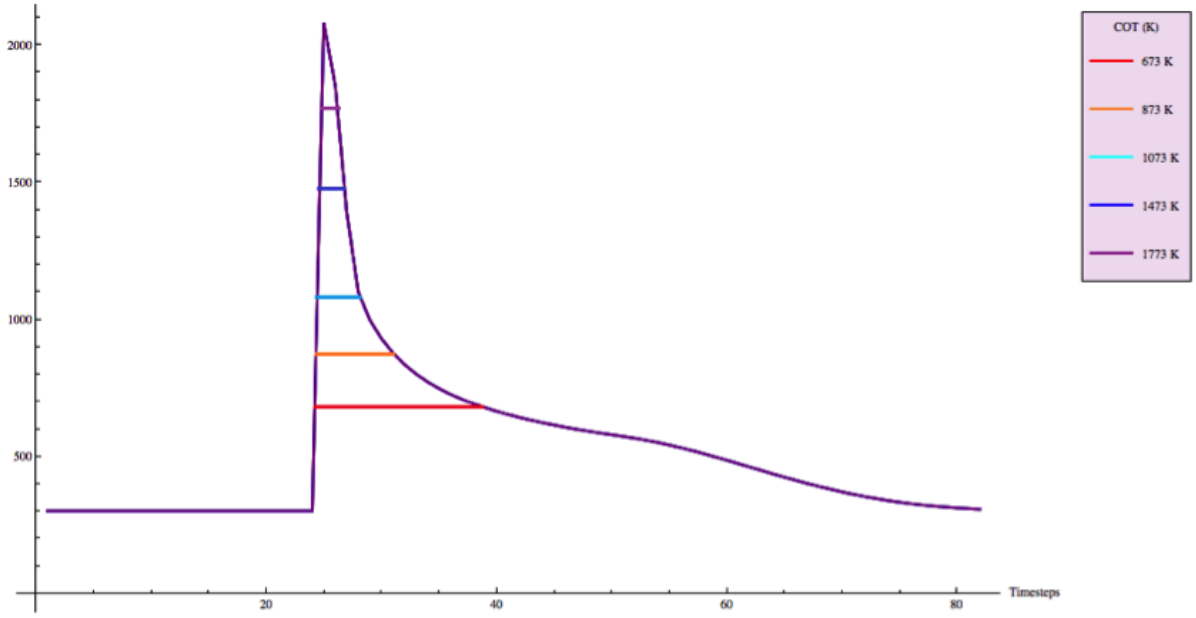

Figure 5-6: Temperature input time history in the structure at the start point of the welding line for different COT

5.2 Welding Power Effect

Welding power is the product of the arc voltage, current and the welding efficiency according to Equation 2-11. The welding power has a significant effect on the thermal analysis of the welding process. By changing the welding power, the whole temperature profile will be changed, like maximum temperature, the duration of material melt and welding pool size. In this analysis, the model parameters are exactly the same as the

model in Chapter 4, the COT will be set as the melting point 1773 K, and the different power chosen are 2250 W, 3000 W, 3750 W, 4500 W and 5250 W.

5.2.1 Temperature Comparison Under Different Welding Power

From Figure 5-7, it can be seen that as the welding power increasing, the maximum temperature during the welding process changing from 1571 K to 3485 K, which all exceed the material soften temperature 1073 K. The maximum temperature increment is not proportional to the power increment, because when the temperature reaches the melt point, part of power is needed to make up the latent heat during the phase transition process. Also the heat conduction and convection rate are temperature dependent.

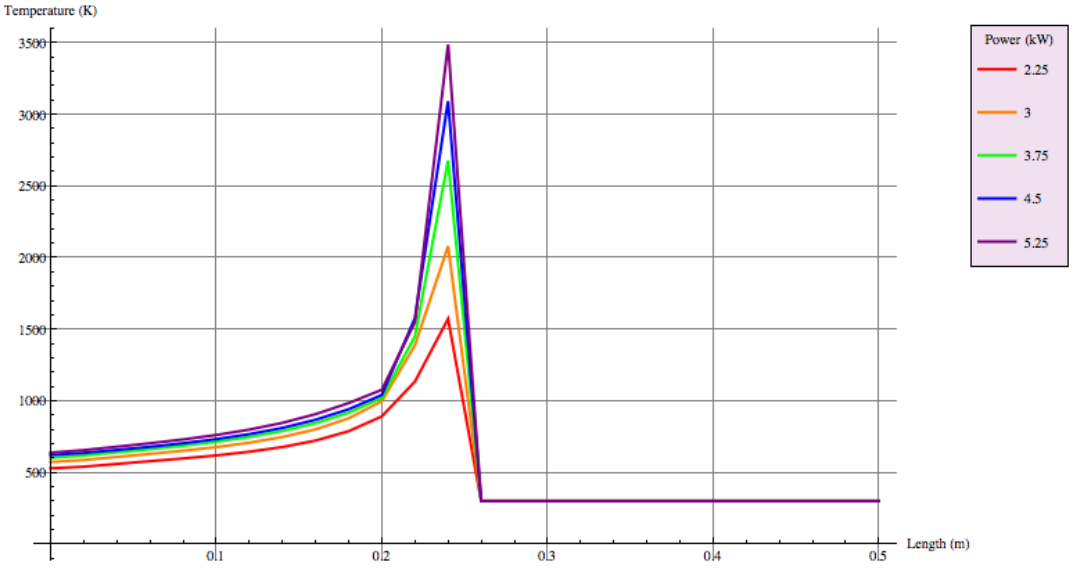

Figure 5-7: Temperature distribution at welding line under different welding power

Once the temperature of material is over the material soften point, the material starts to lose mechanical strength, the micro-structure change is not considered in this study, so no matter how high the temperature is, once it is over 1073 K, the material mechanical behavior is almost the same, the main difference between each case is the duration for which the temperature over 1073 K. Figure 5-8 shows the temperature history at the mid-length of the welding line, where the welding pool is passing. The duration of the material soften are different for the different welding power input, which can be seen in Table 5-2.

Welding Power Input (W)	Duration (s)
2250	7.4
3000	9.1
3750	10
4500	10.28
5250	10.7

Table 5-2: Duration of the temperature over 1073 K

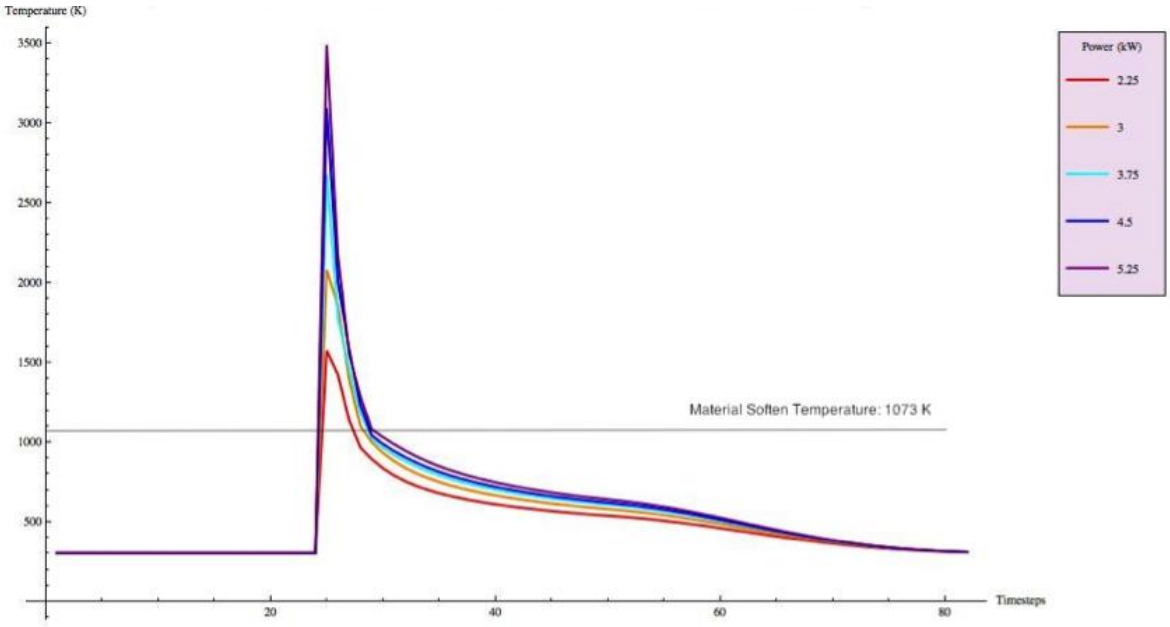

Figure 5-8: Temperature history at the mid-length of welding line under different welding power

5.2.2 Transverse Residual Stress Comparison Under Different Welding Power

According to Figure 5-9, it can be seen that the transverse residual stress distributions in the welding line under different welding power have the same pattern, and there is a slightly difference in the magnitude. All the distributions looks quite symmetrical except the case 2250 W, because the maximum temperature didn't reach the melting point 1773K in this case.

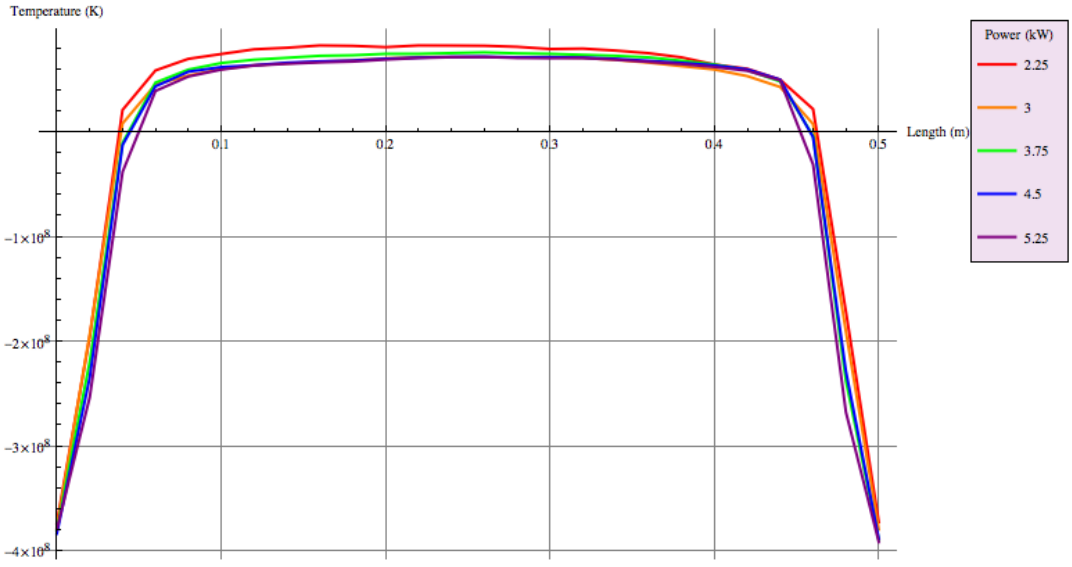

Figure 5-9: Transverse residual stress distribution at welding line under different welding power

From Figure 5-10, it can be seen that the transverse residual stress distributions at the cross section of welding start also keep the same pattern, and the magnitude are almost the same too, which can be concluded that the transverse residual stress distribution at this kind of position is mainly affected by the edge effect.

Figure 5-11 shows that the transverse residual stress distributions at the cross section of mid-length keep the same pattern, but the magnitude changed significantly, especially from the width position 0.007 m to 0.024 m from the welding line. As the welding power increases, the magnitude of the stress is increased, but the increments are decreased. While the welding power is higher than 3750 W, the stress distributions do not change significantly. Because the maximum temperature of each point and the size of welding pool is increasing with the welding power input, the region and duration of maximum temperature over 1073 K is increased; according to Table 5-2, the bigger the welding power, the smaller increment of the duration, which explains the trend in transverse residual stress shown in Figure 5-10.

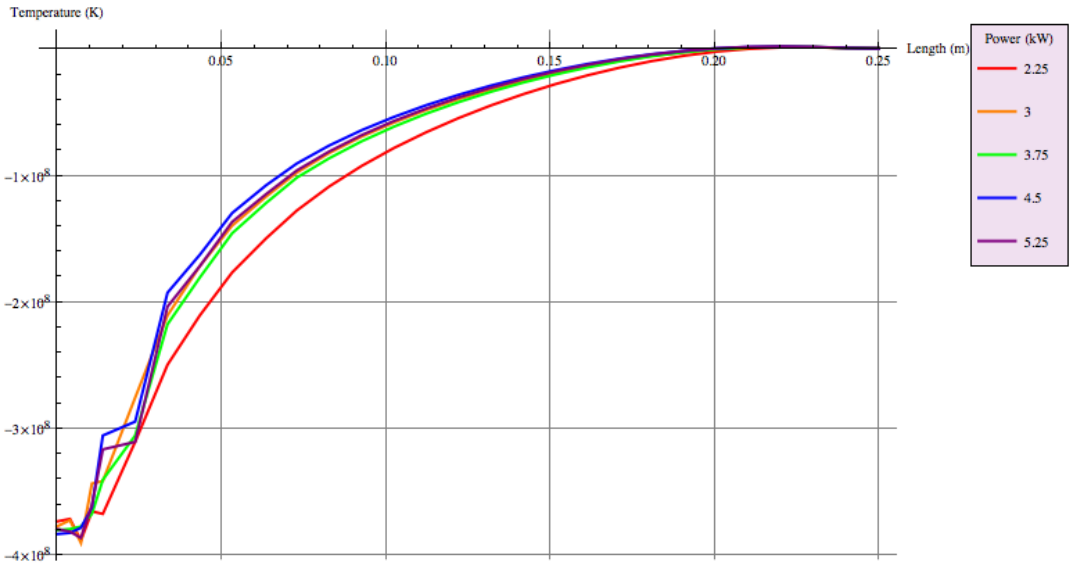

Figure 5-10: Transverse residual stress distribution at the cross section of welding beginning under different welding power

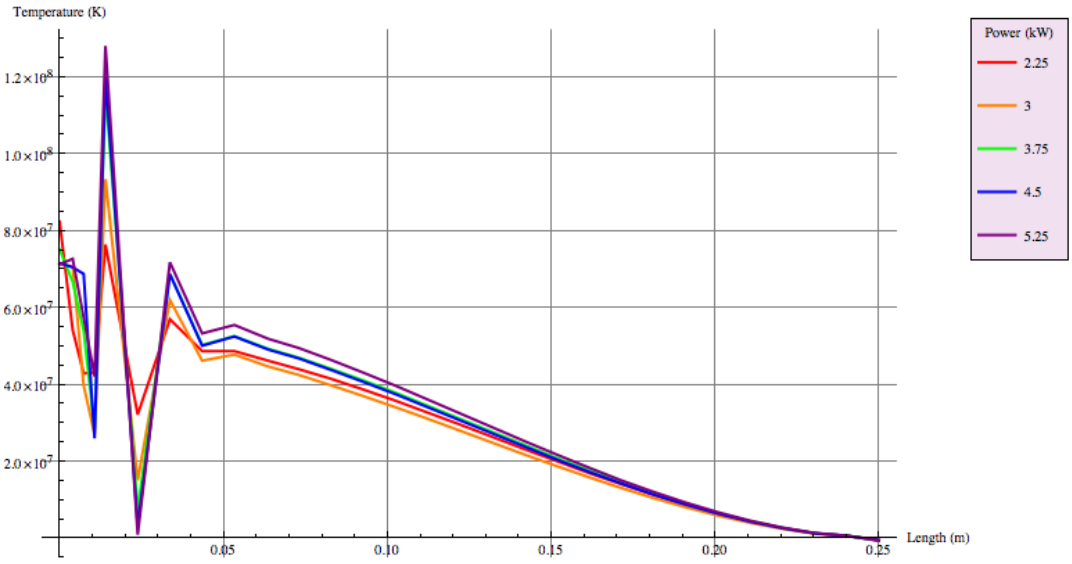

Figure 5-11: Transverse residual stress distribution at the cross section of mid-length under different welding power

5.2.3 Longitudinal Residual Stress Comparison Under Different Welding Power

Figure 5-12 shows that the longitudinal residual stress distributions in the welding line under different welding power are almost the same. It can be seen that the tensile residual stress-changing rate and the magnitude decrease a little bit as the welding power increasing.

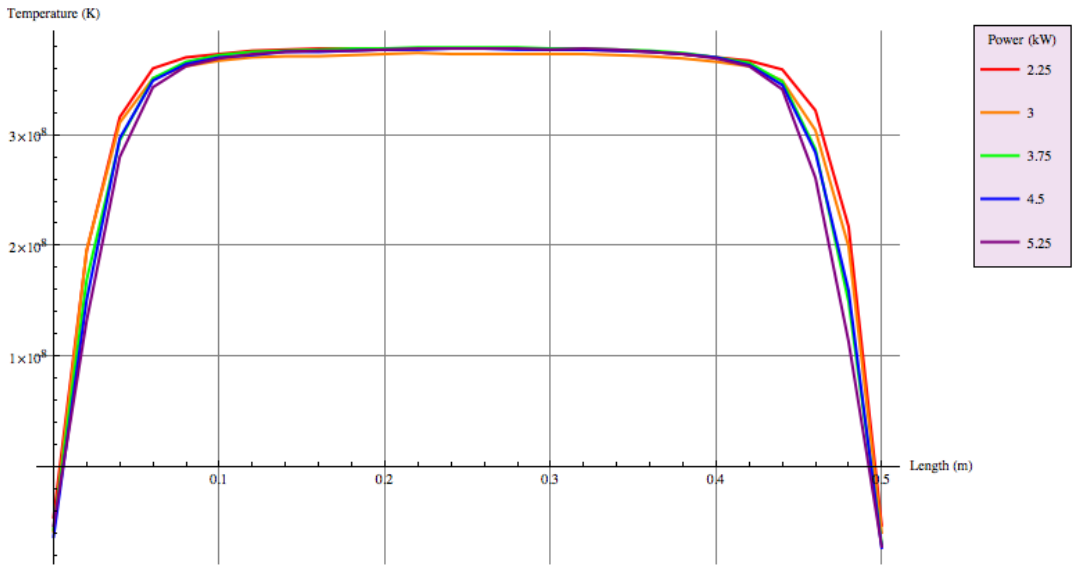

Figure 5-12: Longitudinal residual stress distribution at welding line under different welding power

Figure 5-13 also indicates that different welding power doesn't affect the longitudinal residual stress distribution pattern in the transverse direction, but the magnitudes from width position 0.007 m to 0.024 m from the welding line also have a relatively significant difference.

In general, the longitudinal residual stress distribution in the whole plate doesn't change significantly with welding power.

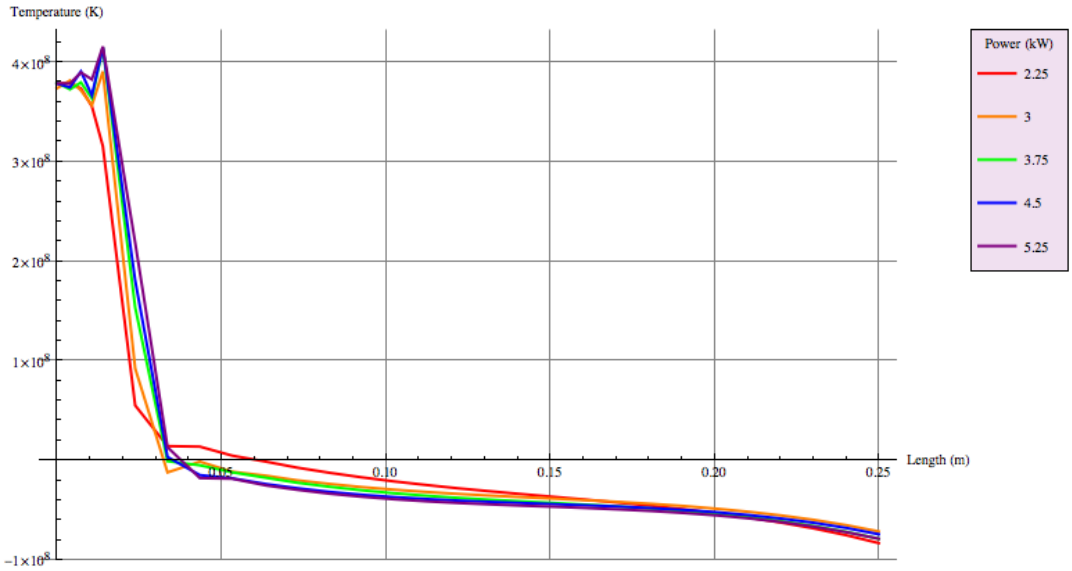

Figure 5-13: Longitudinal residual stress distribution at the cross section of mid-length under different welding power

5.2.4 Discussion

In this section, a detailed parametric study regarding the welding power input effect has been carried out. It showed that the residual stress distribution at welding line doesn't change very much except when the welding power is 2250 W. Because when power is 2250 W, the maximum temperature in the welding pool doesn't exceed the 1773 K, which means the material was not melt during the whole welding process, besides the duration of temperature over 1073 K is relatively shorter than other cases. So the material of the case 2250 W is stiffer than other cases in this study, and the final transverse and longitudinal moments are bigger.

The magnitudes of the residual stress at the width position from 0.007 m to 0.024 have a significant difference regarding the different welding power input. Because this region is the heat affected zone, the power input changes the temperature distribution in this region significantly, and there is no welding deposition and melting, so the material here experienced both heating and cooling process, the different maximum temperature defined different plastic strains, which is the origin of the residual stress.

5.3 Welding Velocity Effect

Many researchers characterize the welds they study by power per unit length (M.F.Ashby & K.E.Easterling, 1982) (Ion, Easterling, & Ashby, 1984) (Henwood, Bibby, Goldak, & Watt, 1988) (Myhr & Grong, 1991). The classical Rosenthal-Rykalin solutions to the transient heat equation for welding process, see Equation 2-5 & Equation 2-6, the term q/v in this equation satisfy the above assumption. But according to those equations, the temperature is clearly not a function of the parameter power per unit length. It is a function of both weld power and weld speed.

In this study, it is necessary to model the same maximum temperature during the welding process in order to analyze the effect of the welding velocity. The models set up for the welds are shown in Table 5-3, the COT is set as 1773 K, and the other parameters for the simulation are also exactly the same as the model in Chapter 4.

Welding Velocity (m/s)	Welding Power Input (W)
0.002	1840
0.005	3000
0.01	4740
0.015	6400
0.02	7800

Table 5-3: Welding power input for the different welding velocities

According to Table 5-3, the welding power input is not proportional to welding velocity, so in author's opinion, the welds cannot be characterized by power per unit length if the velocity is not sufficient high. As shown in Table 5-4, if the power per unit length of weld is held constant and the power is reduced while maintaining the same dimensions of the double ellipsoid weld heat source model, a stage is reached where there is not sufficient power to maintain the maximum temperature. But as the welding velocity increases, the change of power per unit length is getting smaller, which is because at high welding speeds, heat flow is constrained to flow almost normal to the weld joint, so the author concludes that at such high welding speeds, power per unit length of weld does tend to characterize a weld joint.

Welding Velocity (m/s)	Power Per Unit Length (kJ/m)
0.002	920
0.005	600
0.01	474
0.015	427
0.02	390

Table 5-4: Power per unit length calculated regarding to the different welding velocities

5.3.1 Temperature Comparison Under Different Welding Speed

From Figure 5-14, it can be seen that the maximum temperature during the welding process at the welding line in the same for each case when using the welding power setup in Table 5-3, which value was investigated by many tests. As mentioned before, the highly uneven temperature distribution at the area near the welding line is the driving force for the welding residual stresses, so keeping the maximum temperature same, I can isolate and focus on the velocity effect from other factors. As the welding velocity increases, there is a longer distance along the welding line with high temperature. Because there is less time for cooling down during the welding process, at high welding velocity the welding pool length has a significantly longer.

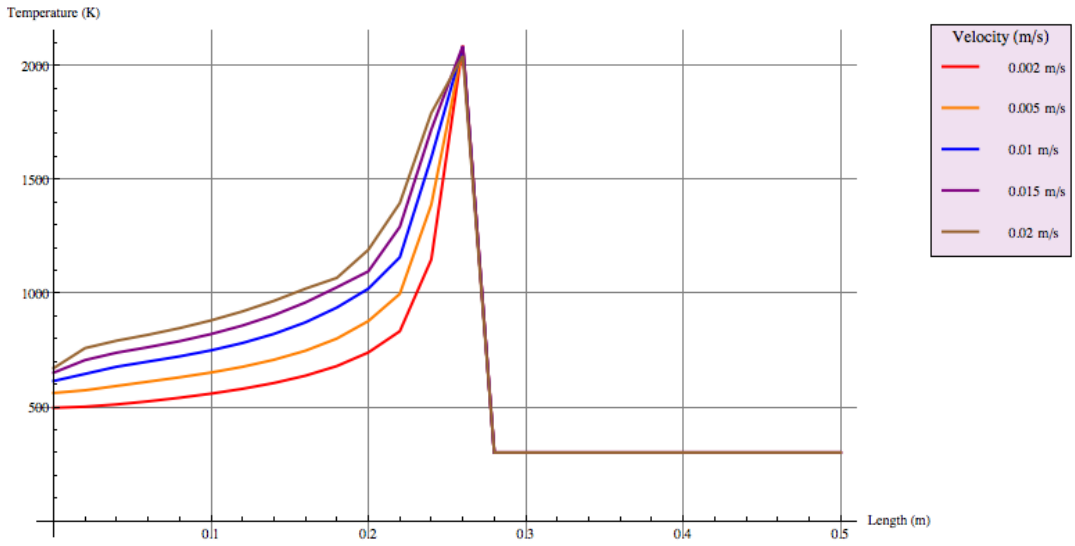

Figure 5-14: Temperature distribution at welding line under different welding velocity

It needs to be mentioned that the timeframes in Figure 5-14 for each case are not the same. From Figure 5-15, it can be seen that the time needed for the welding pool center to reach mid-length are different for the different welding velocities; and when the welding velocity is low, the time of heating for each point in the weld seam becomes longer, but the cooling rate remains the same, so the duration when the temperature is over 1073 K gets longer, as shown in Table 5-5.

Welding Velocity (m/s)	Duration (s)
0.002	14.7
0.005	9.1
0.01	5.5
0.015	4.5
0.02	4.1

Table 5-5: Duration of the temperature over 1073 K

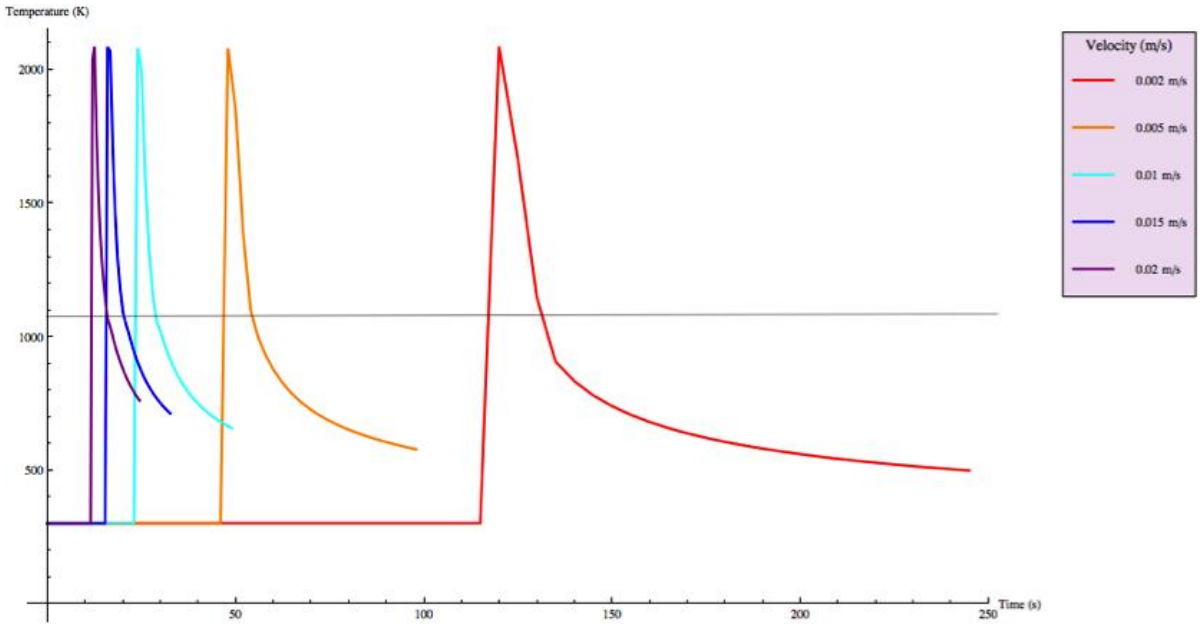

Figure 5-15: Temperature history at the mid-length of welding line under different welding velocity

5.3.2 Transverse Residual Stress Comparison Under Different Welding Speed

According to Figure 5-16, it can be seen that the transverse residual stress distributions in the welding line under different welding velocity have the same pattern, but the tensile stress magnitudes at the center are different. It indicates that when the welding velocity is low, there is a smaller tensile residual stress produced in the center, and when the velocity is 0.01 m/s, the tensile magnitude reaches a peak, then no matter how high the velocity is, the transverse residual stress distribution remains the same.

From Figure 5-17, it can be seen that the transverse residual stress distributions at the cross section of welding start also keep the same pattern, and the stresses are almost the same.

Figure 5-18 shows that the transverse residual stress distributions at the cross section of mid-length keep the same pattern, but still the magnitude changed significantly, especially from the width position 0.007 m to 0.024 m from the welding line. According to the figure, it can be seen that when the welding velocity is 0.01 m/s, the magnitude of the stress reaches a peak, and the oscillation is also the biggest; when the speed is higher than this value, the residual stress distribution stays the same.

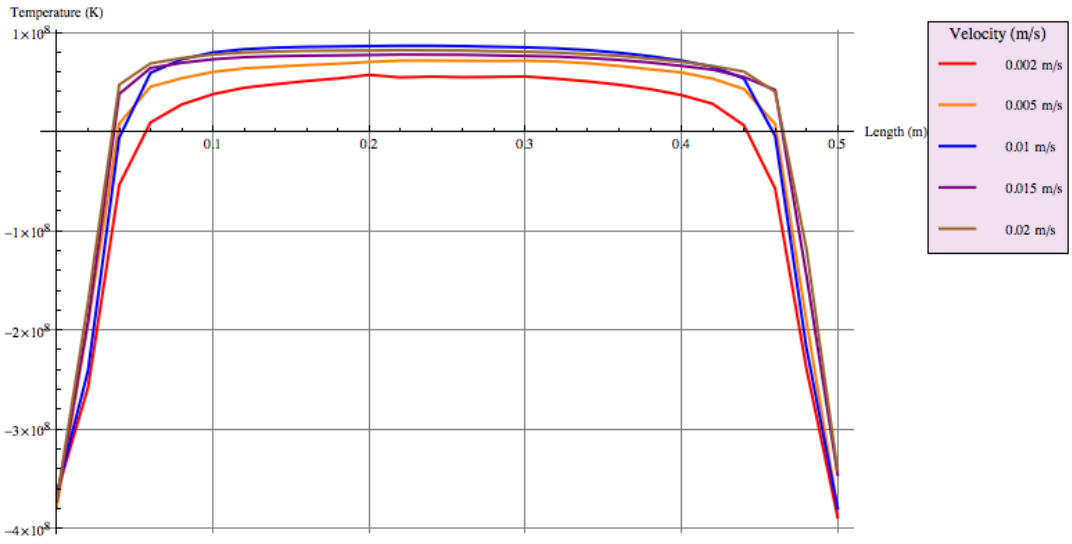

Figure 5-16: Transverse residual stress distribution at welding line under different welding speed

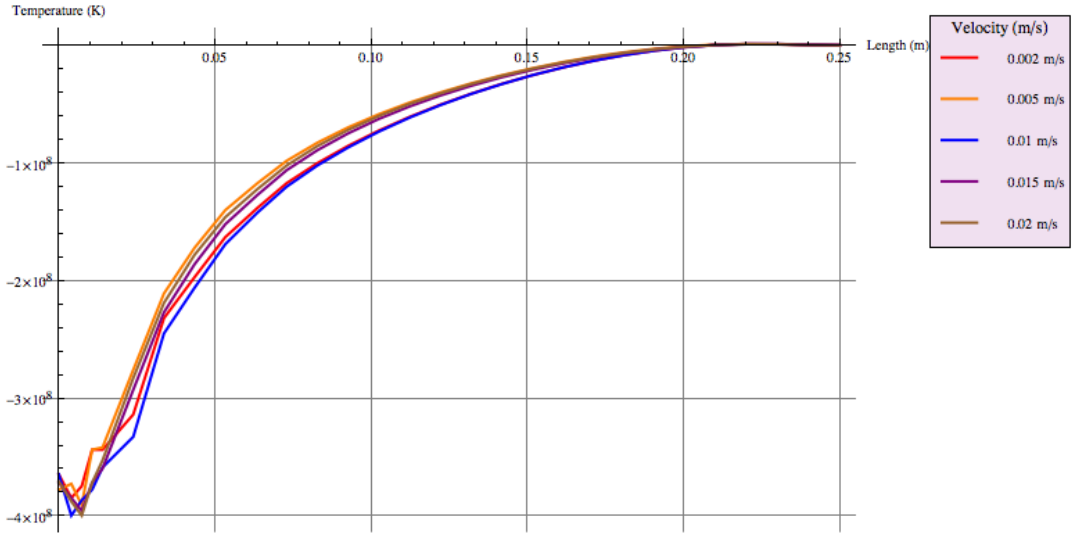

Figure 5-17: Transverse residual stress distribution at the cross section of welding beginning under different welding speed

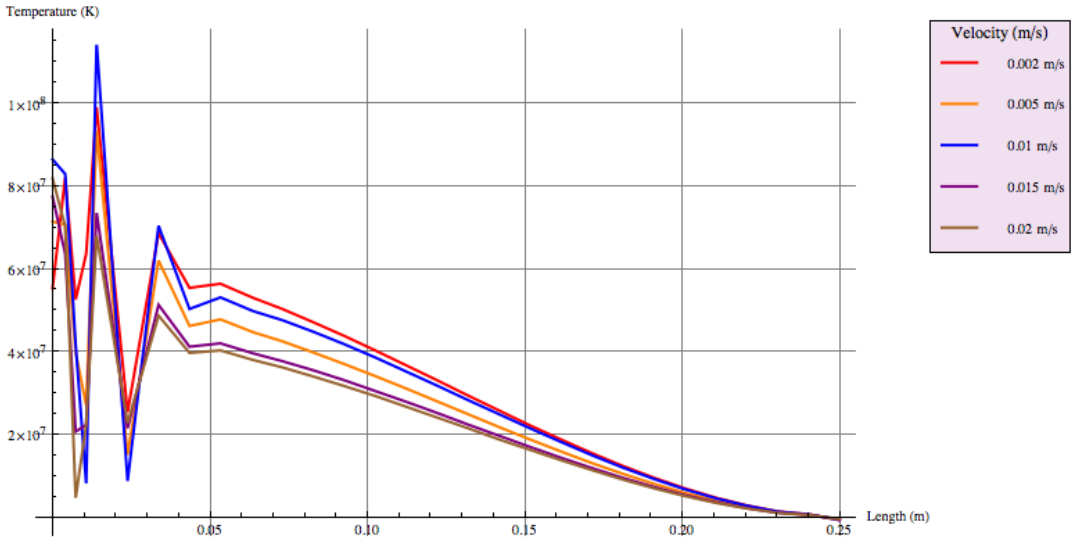

Figure 5-18: Transverse residual stress distribution at the cross section of mid-length under different welding speed

5.3.3 Longitudinal Residual Stress Comparison Under Different Welding Speed

Figure 5-19 shows that the longitudinal residual stress distribution patterns are almost the same in the welding line for the different welding velocity. It can be seen that the tensile

residual stress increased with the welding velocity increasing, and when the velocity is over 0.01 m/s, the stress stays at the same value.

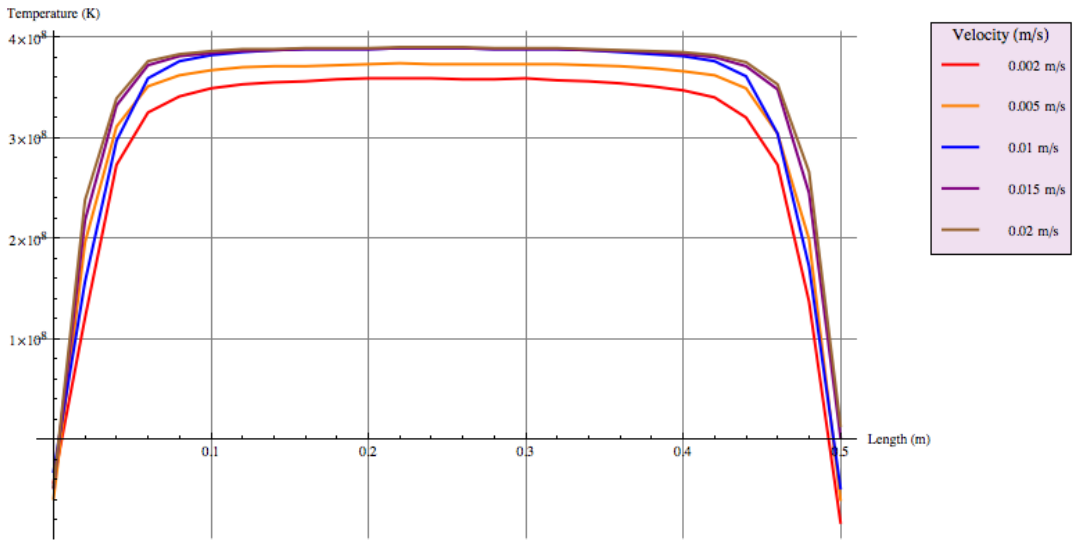

Figure 5-19: Longitudinal residual stress distribution at welding line under different welding speed

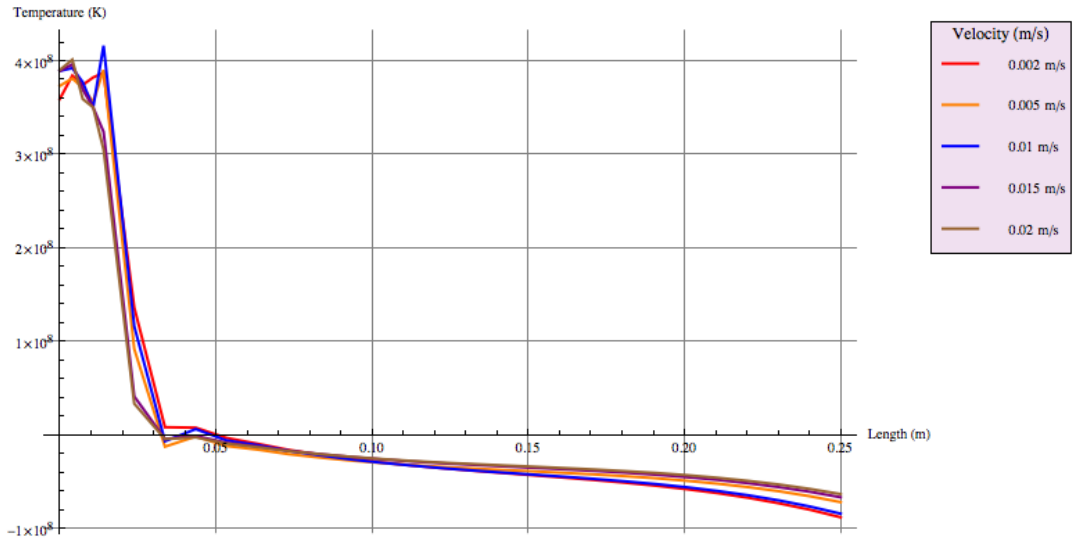

Figure 5-20: Longitudinal residual stress distribution at the cross section of mid-length under different welding speed

According to Figure 5-19 & Figure 5-20, in general, the welding velocity does not significantly affect the longitudinal residual stress distribution in the whole plate,

especially when the velocity is higher than 0.01 m/s, the longitudinal residual stress distribution becomes the same.

5.3.4 Discussion

In this section, the results show that the welds have large differences in their transient temperature field, but when the welding speed over 0.01 m/s, the welding residual stress distribution doesn't have a significant effect. Based on a numerical analysis with different weld powers and weld speeds but constant maximum weld temperature, it is concluded that the ratio of power per unit length of weld does not characterize a weld except in the limit of very high welding speeds.

By combining the analysis in Section 5.2, it is can be conjectured that the duration when the temperature over 1073 K is the key reason for welding residual stress distribution being affected by the temperature profile.

5.4 Plate Length Effect

In this section, the effect of plate length on welding residual stress distribution will be discussed. The different lengths chosen are 0.1 m, 0.3 m, 0.5 m, 1 m, 1.5 m, 2 m and 3 m, other geometry parameters and welding conditions were set the same as the model described in Chapter 4, e.g. the width was 0.5 m and the thickness was 0.006 m, etc.

Due to the welding parameter set in this parametric study, the transient temperature fields during the welding process are exactly the same, so again only the welding residual stresses results will be discussed.

5.4.1 Transverse Residual Stress Comparison Under Different Plate Length

Figure 5-21 shows the transverse residual stress in the welding line for the different plate lengths. It can be seen that when the plate length is smaller than 0.5 m, the lower the plate length, the higher tensile residual stress. Once the plate length is larger than 1 m, it can be seen that the residual stress distributions in the first 0.5 m and the last 0.5 m of the weld are keeping exactly the same, which shows that there is maximum compressive magnitude at the edge and the maximum tensile magnitude at approximately 0.05 m from the edge. The stresses reach a relative smaller constant tensile stress value at the center.

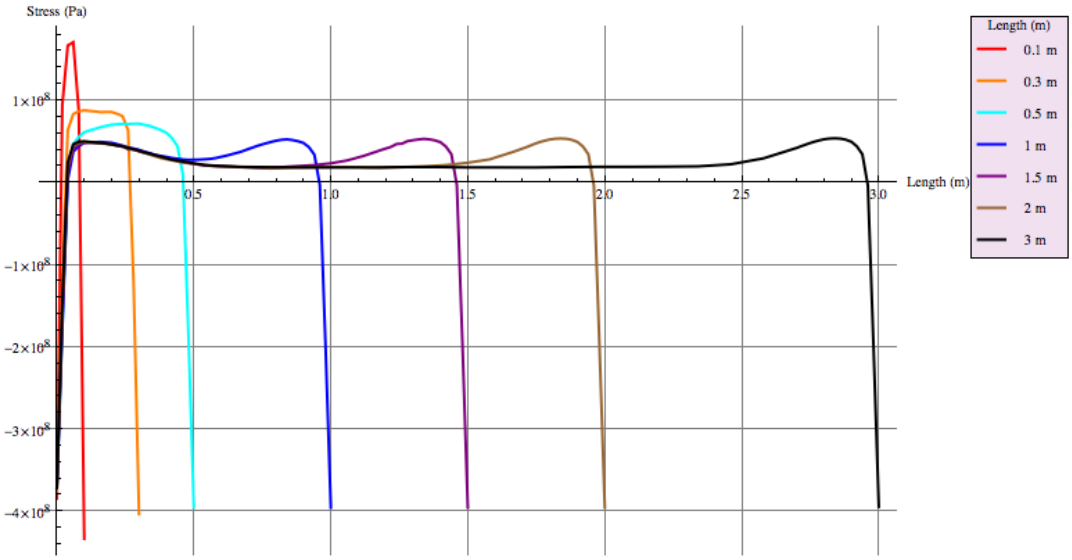

Figure 5-21: Transverse residual stress distribution at welding line under different plate length

Plate Length (M)	Temperature (K)
0.1 m	705 K
0.3 m	542 K
0.5 m	482 K
1 m	418 K
1.5 m	389 K
2 m	371 K
3 m	351 K

Table 5-6: Temperature at the welding beginning when the welding process finishes

The cooling time during welding process for the pre-welded part is different. This is reflected in the different temperature at the position where welding started when the welding process finishes, see Table 5-6.

According to Figure 5-22, the transverse residual stress distributions have the same pattern at the cross section of welding start for a wide range of the different plate length. When the plate length is 0.1 m, the stress magnitudes at each width position are lower than the other cases and the stress changes more rapidly because the plate is short there is still a high temperature at the welding start after welding process, the cooling time during the welding process for the pre-welded part is very short. Also the force equilibrium has to occur over a shorter distance.

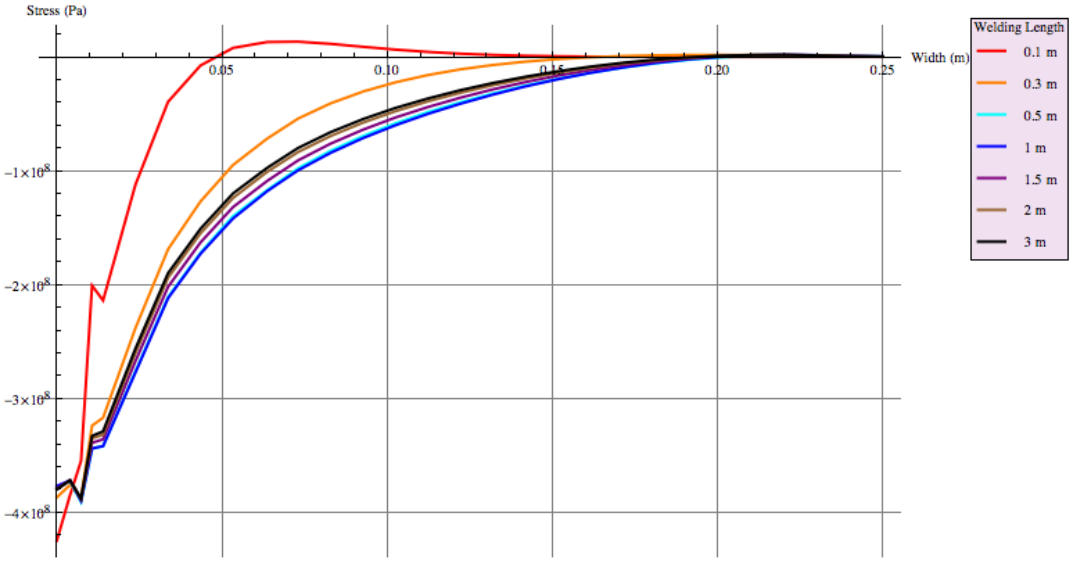

Figure 5-22: Transverse residual stress distribution at the cross section of welding beginning under different plate length

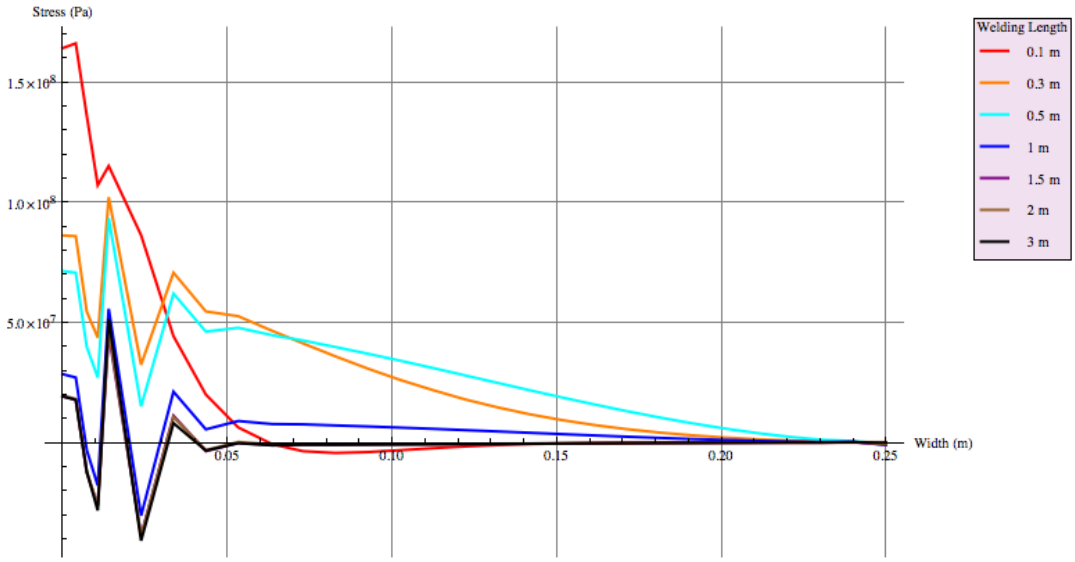

Figure 5-23: Transverse residual stress distribution at the cross section of mid-length under different plate length

In Figure 5-23, the transverse residual stress distribution for the cross section at mid-length for the different plate lengths is shown. While the plate length is smaller than 0.5 m, the maximum tensile residual stress occurs at the mid-length cross section, and the smaller the plate length, the larger the peak stress value. But if the plate length is larger than 1 m, the transverse residual stress distributions at the center part of the length is no longer affected by the plate length effect.

5.4.2 Longitudinal Residual Stress Comparison Under Different Plate Length

Figure 5-24 shows that the longitudinal residual stress distributions along the welding line for different plate length have the same characteristic. It can be seen that when the plate length is smaller than 0.5 m, there is a slightly higher stress than in the other cases; when the plate length is larger than 1 m, it can be seen that the residual stress distributions at the first 0.5 m and the last 0.5 m are exactly the same, which shows that there is a sharp stress increase at the edge and the maximum tensile stress at approximately 0.05 m from the edge, then reaches a slightly smaller constant tensile stress value at the center, the difference is very small compared to the high magnitude of the tensile stress in the middle, which can be neglected in engineering field.

From Figure 5-25, it can be seen that the longitudinal residual stress distributions at the cross section of mid-length are quite different, but the maximum tensile stress magnitudes are exactly the same for different width positions. So generally, the plate length change doesn't affect the peak value of the longitudinal tensile residual stresses.

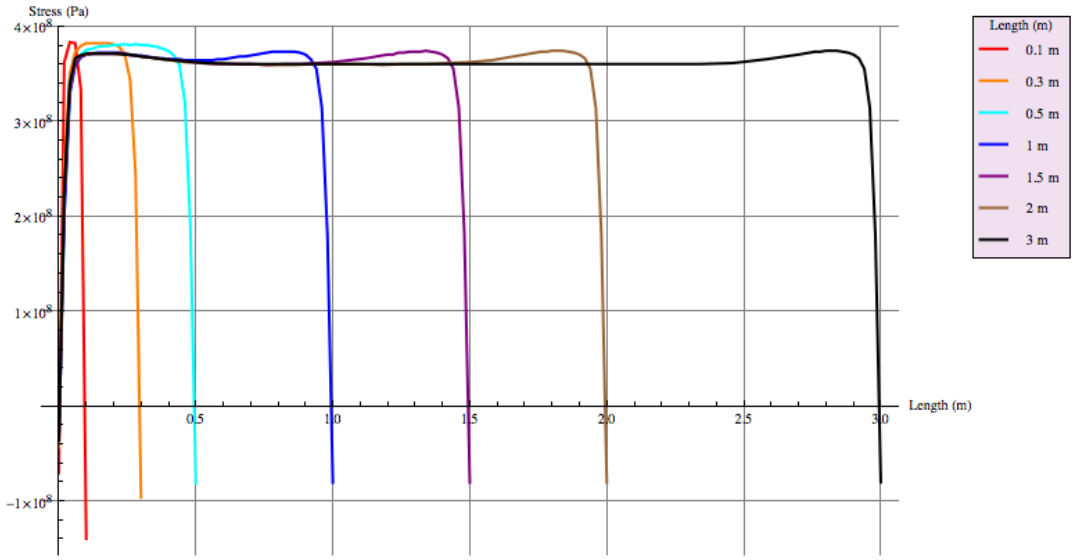

Figure 5-24: Longitudinal residual stress distribution at welding line under different plate length

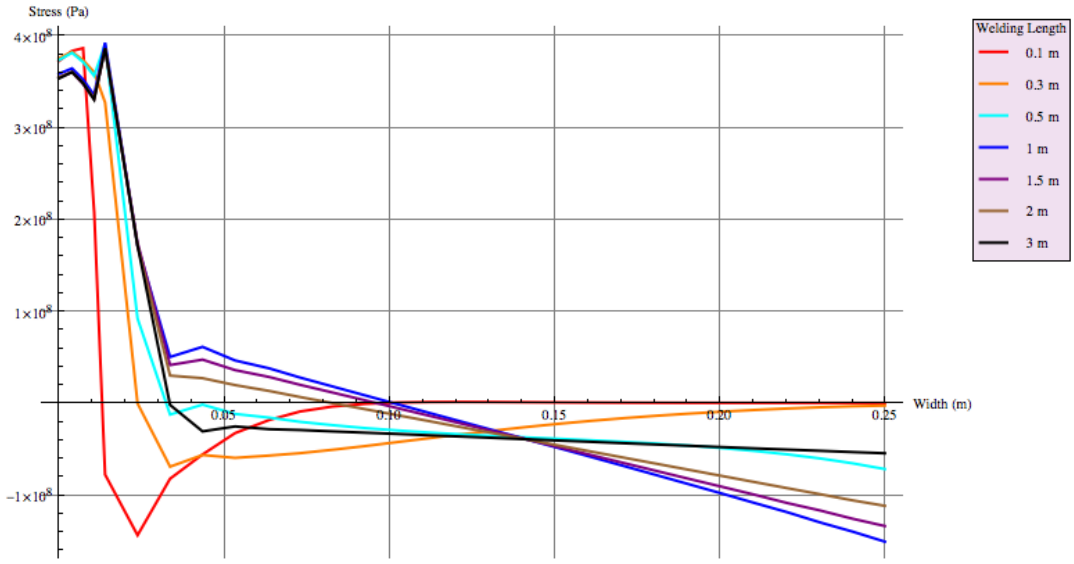

Figure 5-25: Longitudinal residual stress distribution at the cross section of mid-length under different plate length

From Figure 5-24, it can be seen that the longer plate results in a larger transverse moment from the transverse shrinkage (see Figure 4-4), so there needs to be a larger longitudinal moment to balance it, and this is exactly what Figure 5-25 has shown (similar to Figure 5-5). By comparing Figure 5-25 to Figure 4-59, the two figures have got some similarities on the change of stress distributions. Figure 4-59 shows the longitudinal stress distributions at different length positions from 0 m to 0.24 m with 0.2 m tolerance, and Figure 5-25 shows the distributions at the mid-length under different plate length, which also means at different length position at 0.04 m, 0.14 m, 0.24 m, 0.48 m, etc. So the author concludes the main factor affect the longitudinal residual stress distribution in transverse direction is the length position, which may be related to the moment at that position.

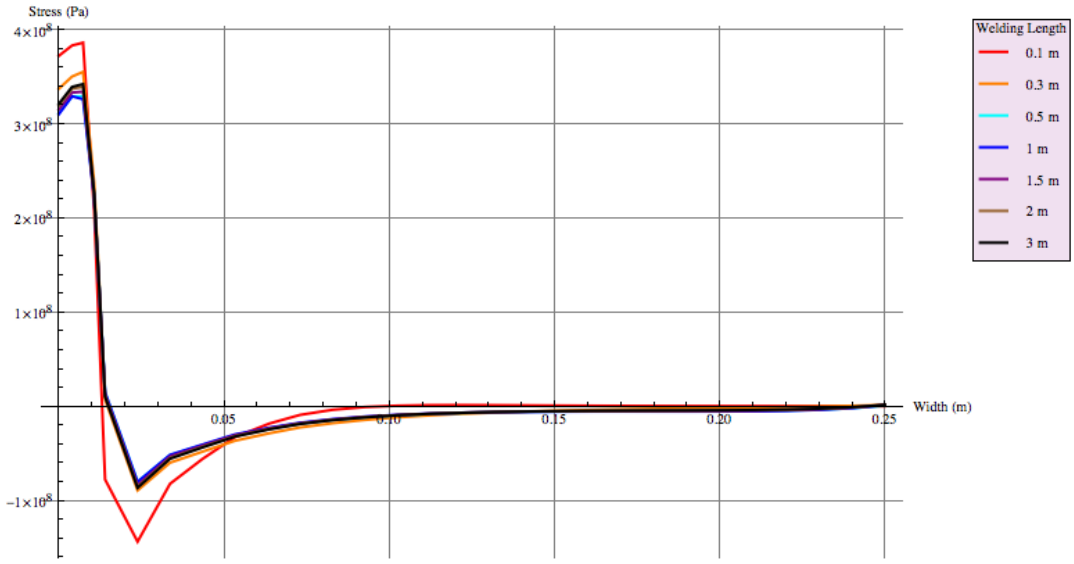

Figure 5-26: Longitudinal residual stress distribution at the cross section of length position 0.04 m under different plate length

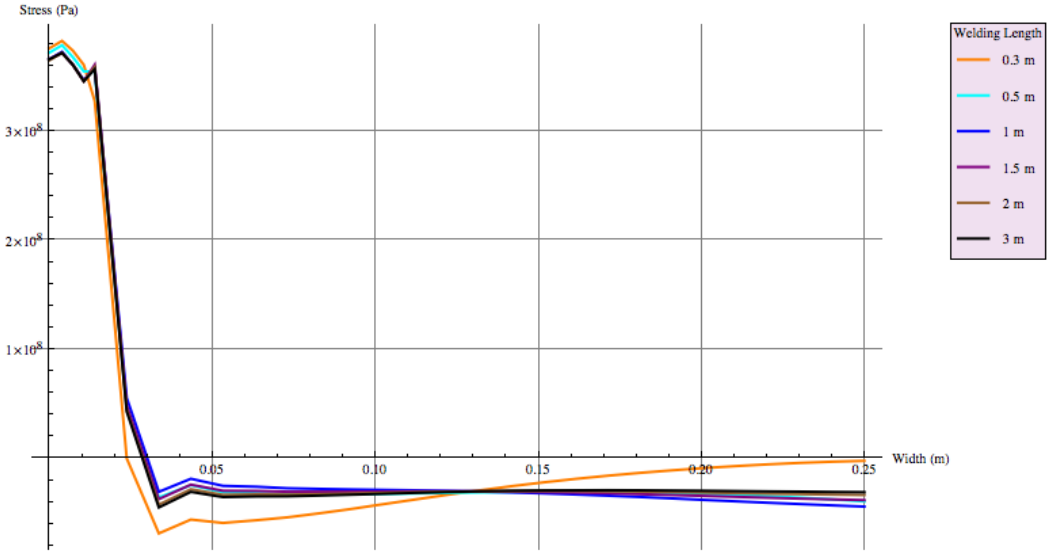

Figure 5-27: Longitudinal residual stress distribution at the cross section of length position 0.14 m under different plate length

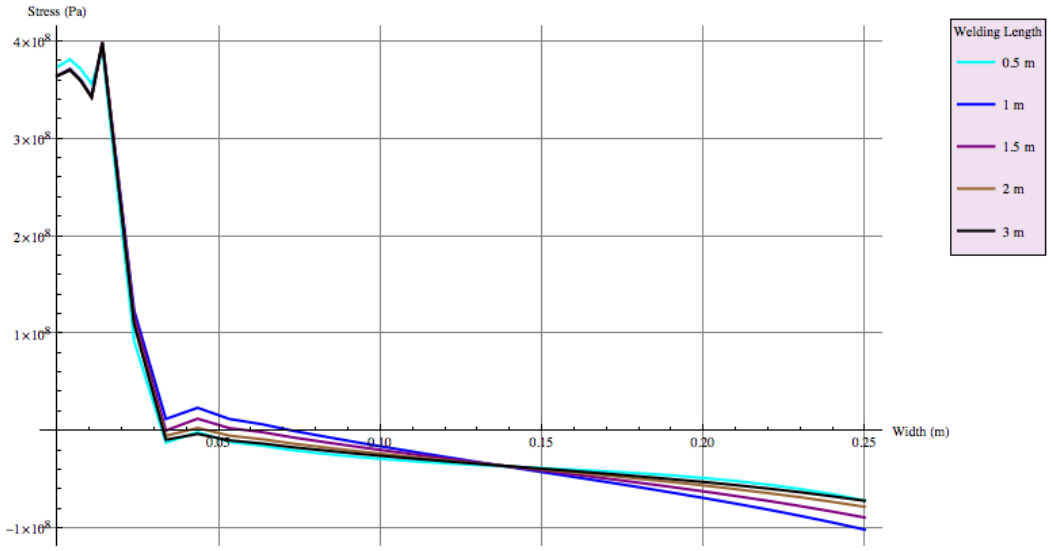

Figure 5-28: Longitudinal residual stress distribution at the cross section of length position 0.24 m under different plate length

According to Figure 5-26, it can be seen that at the cross section of length position 0.04 m, the longitudinal residual stress distributions in transverse direction have the same distribution pattern; only when the plate length is 0.1 m, there is a clear difference, because there is larger transverse moment produced in this case (see Figure 5-21), the

larger longitudinal moment is needed for balancing; and from Figure 5-27, which excludes the case of plate length 0.1 m due to the length is smaller than the length position watched, at the length position 0.14 m, the difference of the longitudinal residual stress distribution is getting smaller regarding to the different plate length, it still can be seen that there is larger longitudinal moment in the case of 0.3 m for the same reason above; then Figure 5-28 shows that at the length position 0.24 m, there is little difference in the stress distribution among the various cases (excluding the case of plate length 0.1 m and 0.3 m).

5.4.3 Discussion

In this section, the plate length effect for the residual stress distributions is presented. It can be seen that when the plate length is smaller than 0.5 m, for transverse residual stress, the large compressive stress at the both edge of the welding line stay as constant, but the stress magnitudes at other locations are affected by the different plate length. It can be concluded that the smaller plate length, the bigger the stress and stress changing rate. For longitudinal residual stress, the stress distribution pattern and the peak value of the tensile stress remains the same, but the stress changing rate in the transverse direction is affected by the different plate length.

When the plate length is larger than 1 m, it can be seen that both the transverse and longitudinal residual stress distributions are exactly the same at the length positions in the first 0.5 m and the last 0.5 m for different plate lengths; and the peak tensile stress at the middle part remains constant.

From the force and moment equilibrium, it can be seen that the longer welding length results in a larger transverse moment; then a larger longitudinal moment is needed for balancing, which is also an important factor for predicting the longitudinal welding residual stress distribution.

Generally, it can be concluded that if the length were great enough, the residual stress distributions would not change with longitudinal direction after some distance from the edge.

5.5 Plate Width Effect

In this section, the effect of plate width on welding residual stress distribution will be discussed. The different plate widths (overall width of both plates) chosen are 0.3 m, 0.5 m, 1 m, 2 m and 3 m, other geometry parameters and welding conditions were set the same as the model described in Chapter 4, e.g. the length was 0.5 m and the thickness was 0.006 m, etc. Due to the welding parameter set in this parametric study, the transient temperature fields in the region near the welding line during the welding process are exactly the same, so again only the welding residual stresses results will be discussed.

5.5.1 Transverse Residual Stress Comparison for Different Plate Widths

Figure 5-29 shows the transverse residual stress in the welding line for different plate widths, which can be seen that the tensile stress distribution pattern were different. When the plate width is 0.3 m, the peak tensile stress value occurred at around 0.08 m from the two edges, which is similar to the stress distribution for the case of plate length 1 m in Section 5.4.1; when the plate width is 0.5 m, the peak tensile stress is located at the mid-length; then once the plate width is larger than 1 m, the transverse stress distribution along the welding line remains the same. From this diagram, it can also be seen that the transverse residual stress induced moments at the mid-length in all cases are almost the same.

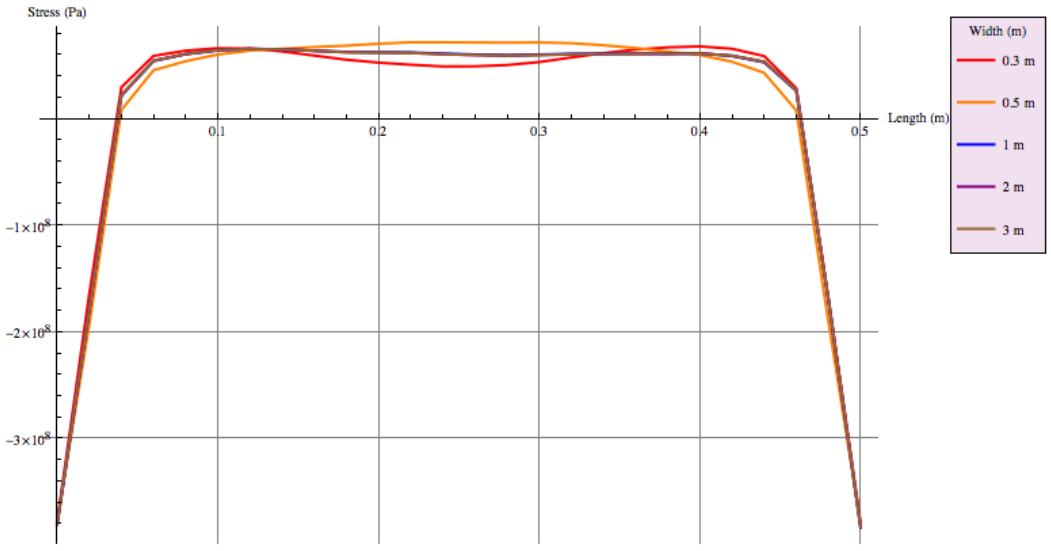

Figure 5-29: Transverse residual stress distribution at welding line under different plate width

From Figure 5-30, in which the width axis margin has been set to stop at 0.42 m in order to see the difference between each other clearly. The transverse residual stress distributions have the same form at the cross section of the welding start irrespective of the different plate widths. There is a very large compressive stress at the welding line due to the edge effect. The stress goes to 0 at a position away from welding seam. The position depends on the plate width and becomes a constant when the plate width is larger than 1 m.

Figure 5-31 shows that, at the cross-section of length position 0.04 m, the transverse residual stress are distributed in the same pattern, but the peak values are different. When the plate width is 0.3 m, the tensile stress is larger and the compressive stress is smaller; with an opposite trend when the plate width is 0.5 m. When the plate width is larger than 1 m, the stress patterns and values are the same and the peak stress is between the 0.3 m and 0.5 m width cases.

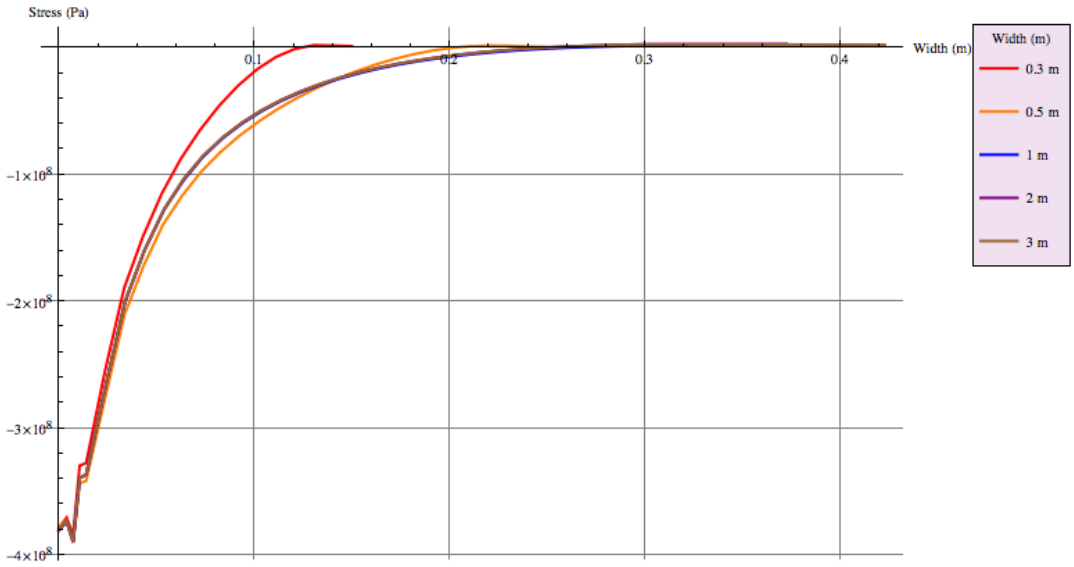

Figure 5-30: Transverse residual stress distribution at the cross section of welding beginning under different plate width

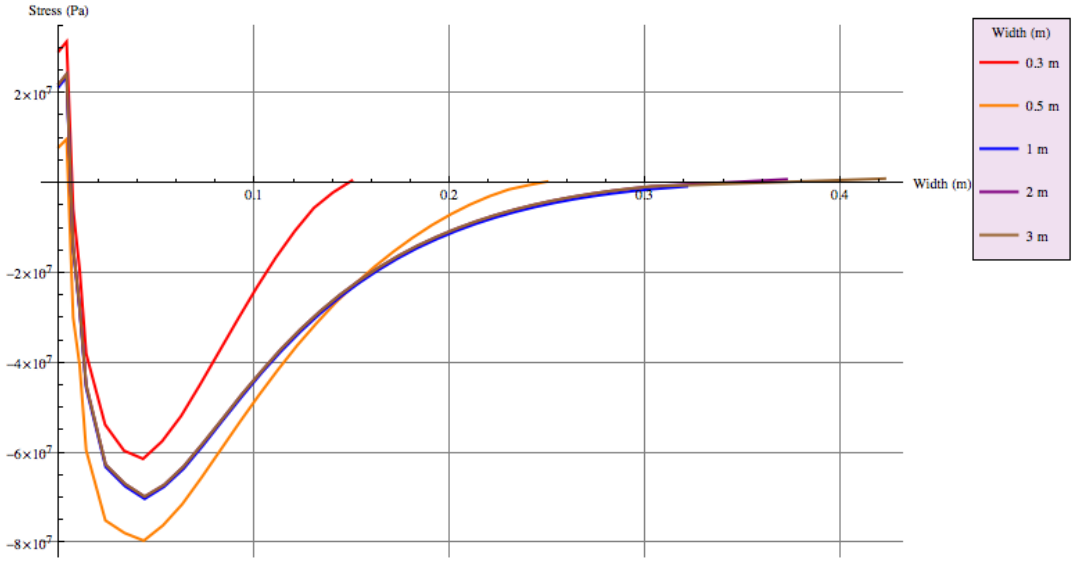

Figure 5-31: Transverse residual stress distribution at the cross section of length position 0.04 m under different plate width

Figure 5-32 shows that the stress distribution also has the same pattern at the cross-section of mid-length, but the changes with plate lengths are opposite to Figure 5-31, which means there is a larger tensile stress and smaller compressive stress when the plate width is 0.5 m; and the opposite when the plate width is 0.3 m. If the plate width is larger than 1 m, the stress remains the same.

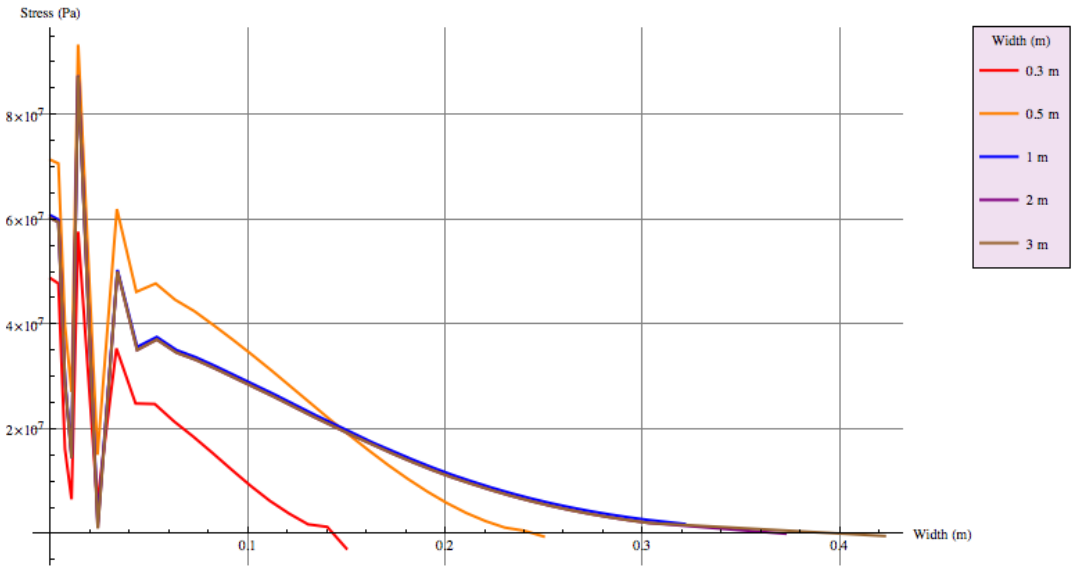

Figure 5-32: Transverse residual stress distribution at the cross section of mid-length under different plate width

In summary, when the plate width is larger than 1 m, the transverse residual stress distribution does not change with the plate width; when the plate length is smaller than 0.5 m, the transverse residual stress distribution maintains the same pattern and the stress are slightly different, although this could often be ignored in practical engineering field.

5.5.2 Longitudinal Residual Stress Comparison Under Different Plate Width

Figure 5-33 shows that the longitudinal residual stress distributions in the welding line under different plate width have exactly the same pattern; there is only a negligible difference in the tensile stress magnitude.

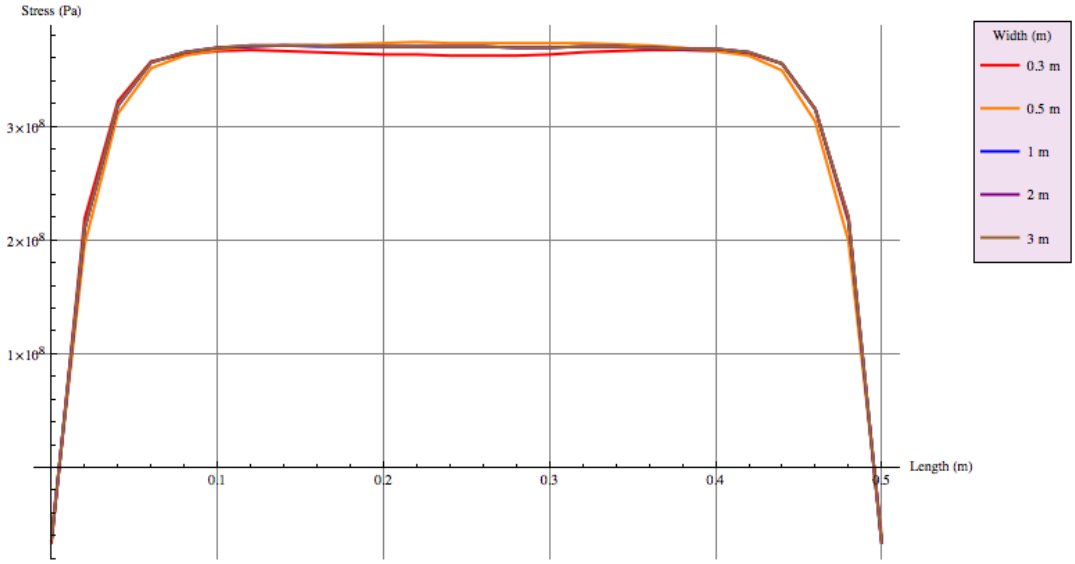

Figure 5-33: Longitudinal residual stress distribution at welding line under different plate width

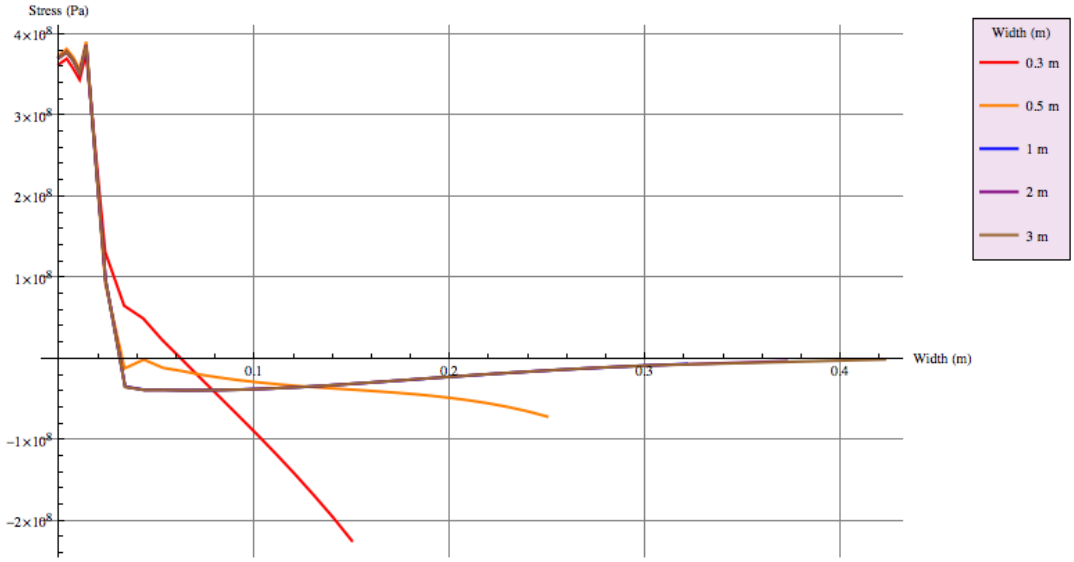

Figure 5-34: Longitudinal residual stress distribution at the cross section of mid-length under different plate width

From Figure 5-34, it can be seen that the longitudinal residual stress distributions at the cross section of mid-length are quite different if the plate width is smaller than 0.5 m, which is mainly embodied at the location away from welding seam. Because the plate length is a constant, so the transverse moment is a constant, which means the longitudinal moment is also a constant. When the plate width is small, there need more force to balance the transverse moment, when the plate length is 0.5 m, the longitudinal moment produced has been already enough to balance, so when the plate width is larger than 0.5 m, the stress distribution remains the same. And in the heat-affected zone, the longitudinal residual stress doesn't change in all cases; but at the location away from HAZ, there is a zero stress at the width edge when the welding width is larger than 1 m; if the plate width is smaller than 0.5 m, the stress at the width edge is turning compressive and the magnitude is increasing as the of the plate width reduces.

By comparing Figure 5-34 to Figure 5-5, it can be seen that there are some similarities between them, which induces the author to suppose that the residual stress distribution should be related to the ratio of welding seam size to the plate width. Based on the results from Section 5.1, the different COT changed not only the maximum temperature, but also the area with the maximum temperature, which can be thought as the 'welding seam'. As mentioned before, the transverse moments for all the cases in this parametric

study are constant as the welding length, so the longitudinal moments needed for balancing are constant. Because the plate widths are different, smaller plate widths will have larger stresses in order to achieve the same longitudinal moment as larger plate width cases.

In general, the longitudinal residual stress distribution in HAZ is not affected by the plate width; the stress distribution is different at the location away from welding seam as the different ratio of welding seam size to the plate width, which shows that the smaller the ratio is, the smaller stress magnitude at the width edge, and it becomes 0 when the ratio is smaller than 0.006.

5.5.3 Discussion

According to the analysis in this section, it can be seen that when the plate width is larger than 1 m, the whole residual stress distribution is maintained the same regardless of the plate widths; but when the plate width is smaller than 0.5 m, the transverse residual stress keeps the same pattern and the values have a slight difference. For longitudinal residual stress, the stress distribution is different at the location away from welding seam, and is determined by where the stress value is heading to at the width edge. Generally, it can be concluded that if the ratio of welding seam size to the plate width is small enough, the residual stress distributions would not change. And the transverse and longitudinal moment produced is a constant, which doesn't change with different plate width once the welding length is constant.

5.6 Conclusions

In this chapter, a detailed parametric study for butt welding residual stress distributions has been performed for different cut-off temperatures, welding power, welding velocity, plate length and plate width. Among these factors, how the temperature history affect the residual stress distribution is reflect on the cut-off-temperature, welding power and welding velocity; the plate length and width expressed the effect of model geometry to the residual stress distribution.

From Section 5.1, when the maximum cut off temperature over 1073 K, the residual stress distribution doesn't change. However if the COT is set lower than 1073 K, the material is too stiff as it does not melt even at the maximum temperature, so the residual stress distribution is changed not only the magnitudes, but also the distribution pattern. As mentioned before, due to the material used in this whole research is ASTM A131, Grade DH36, 1073 K is the materials soften temperature.

In Section 5.2 & 5.3, the results show that the duration when the temperature over 1073 K is the key reason for welding residual stress distribution regarding to the different transient temperature field during the welding process; Section 5.2 also shows that the maximum temperature also has some impacts on the residual stress distribution by affecting the temperature history in HAZ; and Section 5.3 based on a numerical analysis with different weld powers and weld speeds but constant maximum weld temperature, presented that the ratio of power per unit length of weld does not characterize a weld except in the limit of very high welding speeds.

Section 5.4 presents that when the plate length is larger than 1 m, it can be seen that both the transverse and longitudinal residual stress distributions are keeping exactly the same at the length positions in the first 0.5 m and the last 0.5 m regarding to different plate lengths; and the stress distribution at the middle part remains constant, so it can be concluded that if the length were great enough, the residual stress distributions would not change with longitudinal direction after some distance from the edge.

According to the analysis in Section 5.5, it can be seen that when the ratio of welding seam size to the plate width is smaller than 0.006, the whole residual stress distribution is maintain the same regarding to different plate widths, so which can be concluded that if the ratio of welding seam size to the plate width is small enough, the residual stress distributions would not change.

In sum, according to the analysis in Section 5.1, 5.2 and 5.3, it can be seen that the main factor of the temperature history, which affects the stress distribution, is how long the duration when the temperature over the material soften temperature. From the force and moment equilibrium, lower COT makes the material stiffer, which results bigger in-plane bending, so the transverse bending moment became bigger, therefore, larger longitudinal

moment is needed for balancing purpose. A longer welding length results in larger transverse moments, which also increases the longitudinal moment. However, if the welding length is constant, the transverse moment will also be a constant, and the longitudinal stress distribution will depend on the plate width because the longitudinal moment is a constant.

Chapter 6 Optimization of Welding Sequence for a Typical Connection Detail of Marine Structure

Figure 6-2 shows a typical welding connection detail of a marine structures. This kind of structure details suffers fatigue damage frequently, which can be seen in Figure 6-2, and due to the 'shake down' effect, the welding residual stresses are changing all the time during the structures operation and may be beneficial to fatigue crack growth, so it is very worthwhile to carry out an optimization of residual stresses for it. Choosing an optimal sequence from the set of all possible combinations of a welding passes has been always a challenge for designers. The solution of such combinatorial optimization problems is limited by the available resources. For example, having n sub-passes leads to choosing from $2^n \times n!$ possible combinations of the sub-passes, e.g., 10,321,920 for n=8.

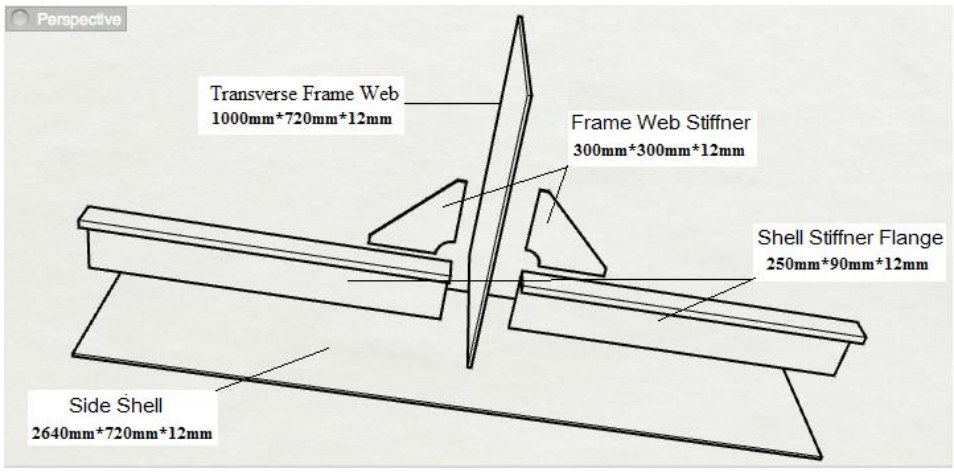

Figure 6-1: Schematic drawing of typical detail of marine structure

From Figure 6-1, it can be seen the model is a relatively complex welding model, which include side shell, transverse frame web, shell stiffeners and frame web stiffeners. There are total 12 sub-passes in this model, so 1.962×10^{12} combinations for optimization of welding sequence could be done for this model. Although prior knowledge can reduce this space, still it is not practically feasible to choose the optimal sequence by evaluating a set of possible combinations either experimentally or by simulation models.

In order to reduce the design space, it is necessary to take the real welding situation into account. From Figure 6-1, the model is symmetrical and all the welding connections in

this model are the double side fillet welding except the frame web stiffeners. According to the IACS (International Association of Classification Societies) regulations for oil tanker in 2006, the welding connections in this kind of details are normally continuous welding, which means there is no break in any sub-pass. The author decided to optimize the double side fillet welding (Figure 6-5) first, and then optimize the welding sequences for the whole model.

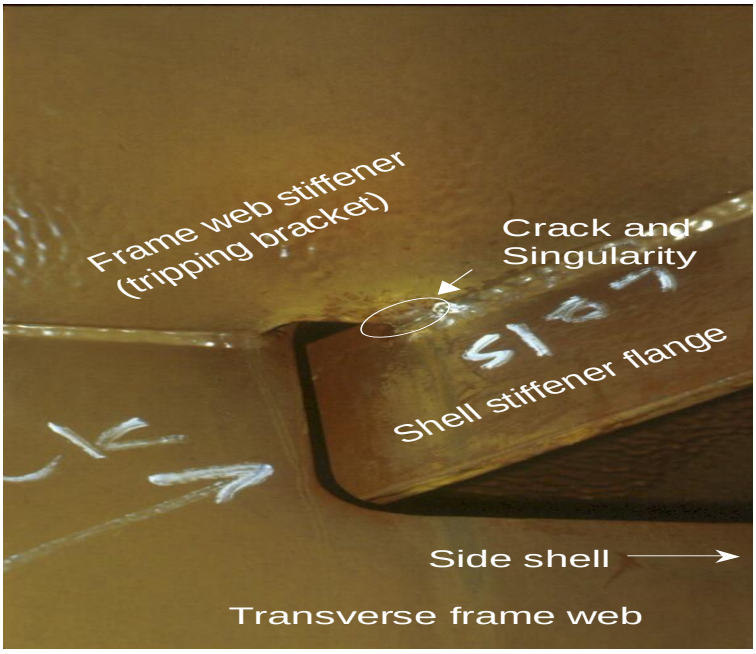

Figure 6-2: Typical ship's side shell connection detail showing positions of singularities

6.1 Computational Setups

All the computational models that include transient thermal and stress analysis are analyzed with VrWeld software. The simulation also consisted of two analyses. The first was a transient thermal analysis where the temperature distribution caused by a travelling heat source was determined. The second step consisted of a nonlinear structural analysis that was solved as a series of sequential load steps. Each load step represented an increment in the position of the heat source in the direction of welding. The temperatures from the thermal analysis associated with each load step were applied as loads in the structural analysis. This process was repeated several times until the welding was completed. The material of all the model is ASTM A131, Grade DH36 steel, for which the temperature dependent material properties have been listed in Chapter 3, the

dimensions of the geometry have been given in Figure 6-1, and the weld sizes are 0.012 m. During the simulation, the element activate and deactivate technique is used to perform the weld metal deposition and the subdomain method (Figure 6-3) is used to increase the calculation efficiency, which has been introduced in Chapter 3.

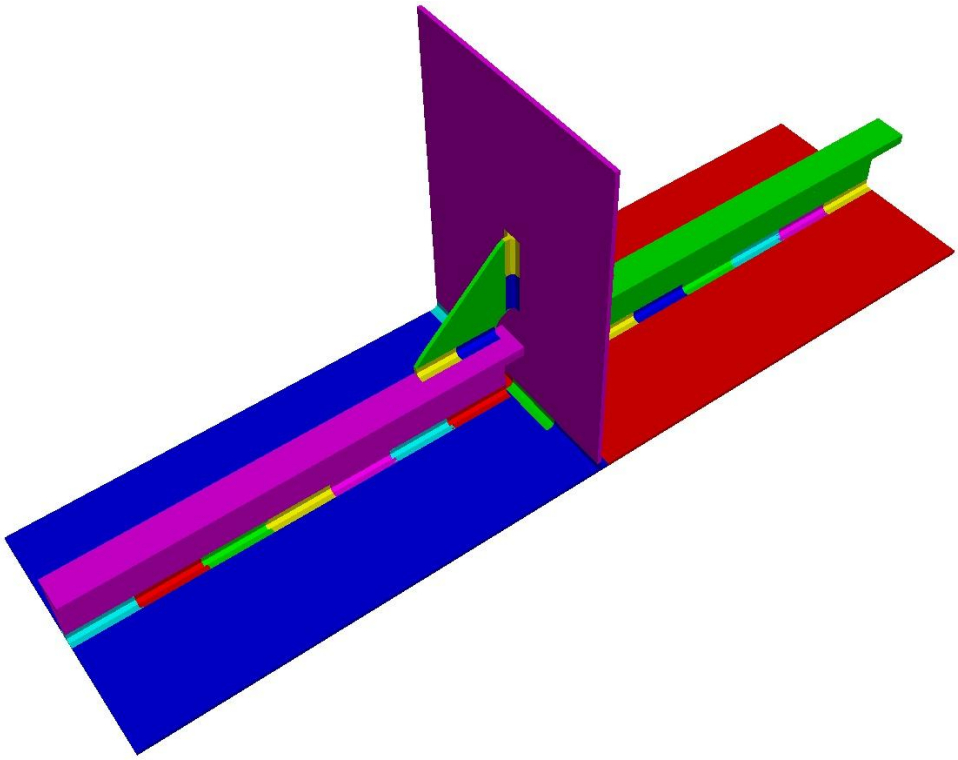

Figure 6-3: Schematic of subdomain method used in the final model

The boundary condition for the model are all using the classic three nodes, six degree of freedoms constraints, which prevent the structure from the rigid body movement but can be stretched and compressed freely. It is likely that the real structure several stiffeners would be fillet at the same time, and constraints against the plates relating about their edges would then be more realistic. The start and end of all the welding passes are pre-tack-welded. The complete model contains approximately 94,890 elements and 94,371 nodes. The finished mesh schematic and totally 12 welding sub-passes are showing in Figure 6-4. From that figure, it can be seen that the advanced mesh technique was used, which represent very fine mesh at the welding joints and coarse mesh at the body part. The moving heat source of all the welding sub-passes is using the double heat ellipsoid power density function and the welding method and parameters are listed in Table 6-1.

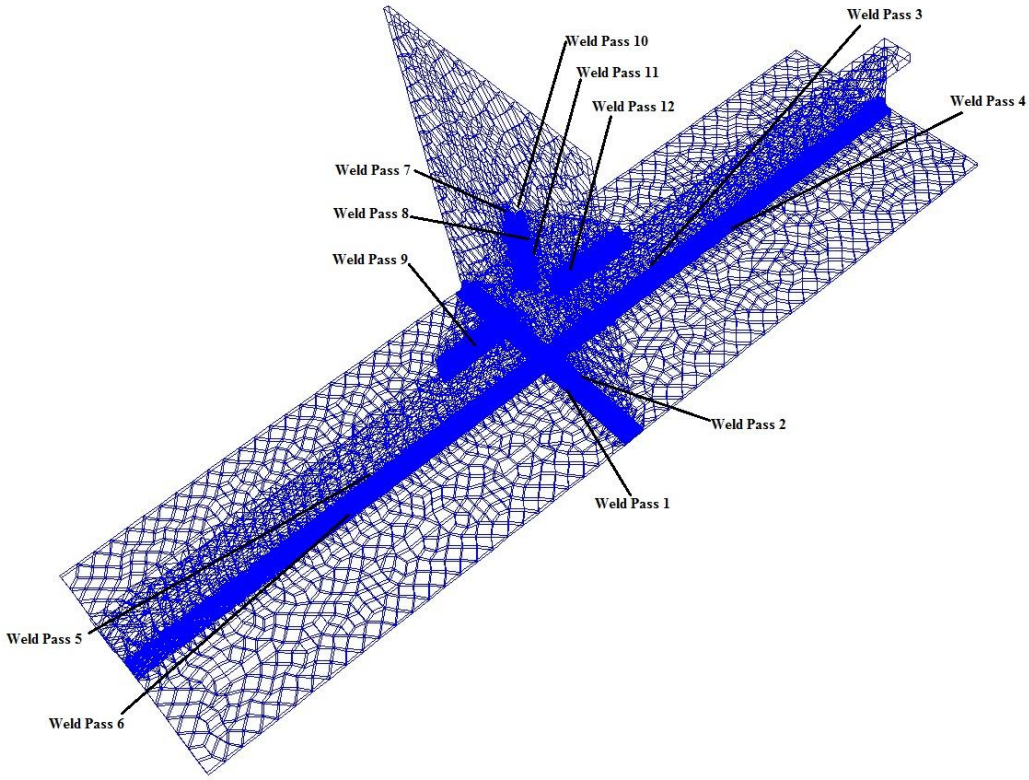

Figure 6-4: Mesh and welding sub-passes schematic of final model

Shielding Gas	Pass Number	Length of welds (m)	Current (A)	Voltage (V)	Speed (m/s)
CO2	1	0.72	300	25	0.01
CO2	2	0.72	300	25	0.01
CO2	3	1.3	300	25	0.01
CO2	4	1.3	300	25	0.01
CO2	5	1.3	300	25	0.01
CO2	6	1.3	300	25	0.01
CO2	7	0.24	300	25	0.01
CO2	8	0.24	300	25	0.01
CO2	9	0.24	300	25	0.01
CO2	10	0.24	300	25	0.01
CO2	11	0.24	300	25	0.01
CO2	12	0.24	300	25	0.01

Table 6-1: Welding method and conditions of final model

6.2 Optimization of Double Side Fillet Welding

As mentioned above, almost all the welding in the final model is continuous double side fillet welding, which needs to be welded sequentially, so it is necessary to analyze how to optimize the continue double side fillet welding, which will dramatically decrease the possible combinations of the final model. In this section, the author modeled the continuous double side fillet welding between the side shell to transverse frame web, the schematic is shown in Figure 6-5. All the welding parameters and modeling procedures used are the same as described in 6.1.

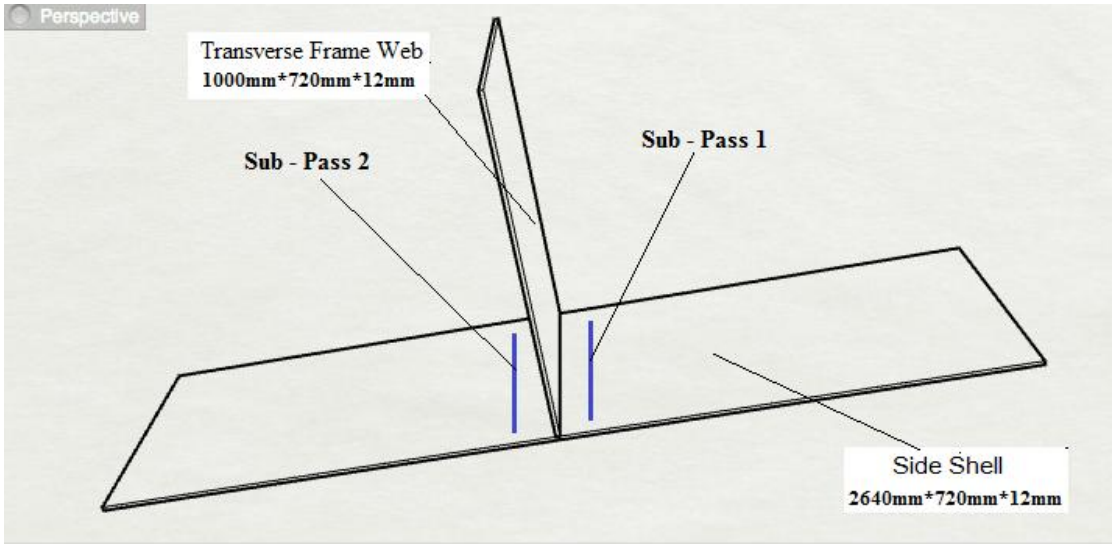

Figure 6-5: Schematic of double side fillet welding model

Due to the welding processes of every pass needs to be continuous, but there are only two passes in this model and the time duration of each pass is 72 seconds, so firstly, whether the welding directions of both passes are in the same or opposite directions need to be decided; then optimum the time lag between the two passes needs to be found. In this research, there are 12 different combinations being chosen, which details listed in Table 6-2

Sub-model No.	Welding Direction Between Both Passes	Lag Time (s)
1	Same	0
2	Same	5
3	Same	9
4	Same	18
5	Same	36
6	Same	72
7	Opposite	0
8	Opposite	5
9	Opposite	9
10	Opposite	18
11	Opposite	36
12	Opposite	72

Table 6-2: Chosen possible welding procedure of sub-models for frame web to side shell weld

6.2.1 Temperature Analysis

In the temperature analysis, the cut-off temperature was set as 1200 K, and the snapshots for the 12 combinations are shown in Figure 6-6 & Figure 6-7. From those figures, it can be seen that when the both sides use the same welding direction, there are two welding pools, which maintain a constant distance (welding velocity * lag time) between each other. This means, after the second welding pool has formed, the temperature profile will keep the same at all the points in the same transverse line; for the opposite welding directions, the lag time determines where both welding pool meet. The utilization of the element activate and deactivate technique is also shown in the figures as described previously.

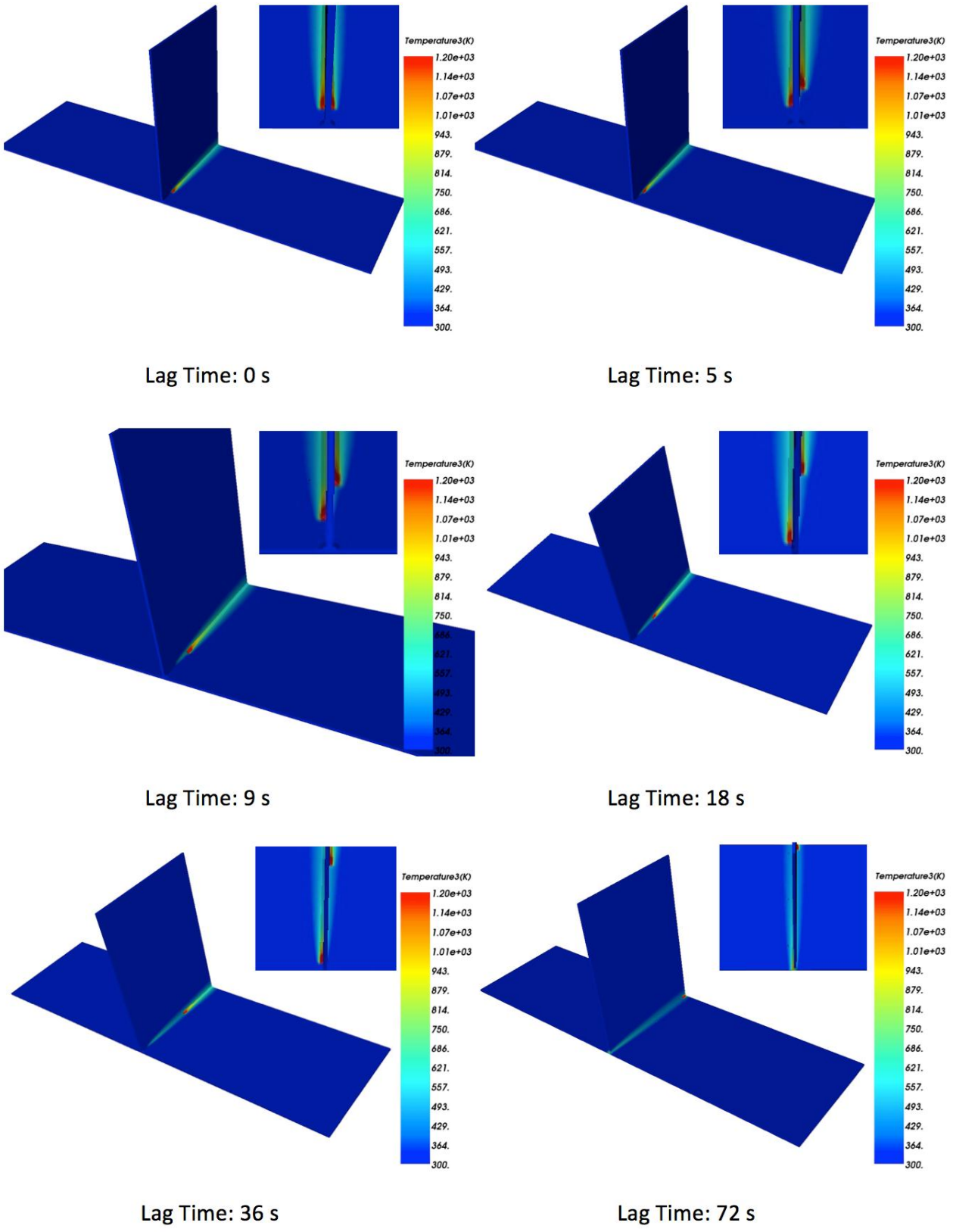

Figure 6-6: Snapshot of temperature distribution of same welding direction

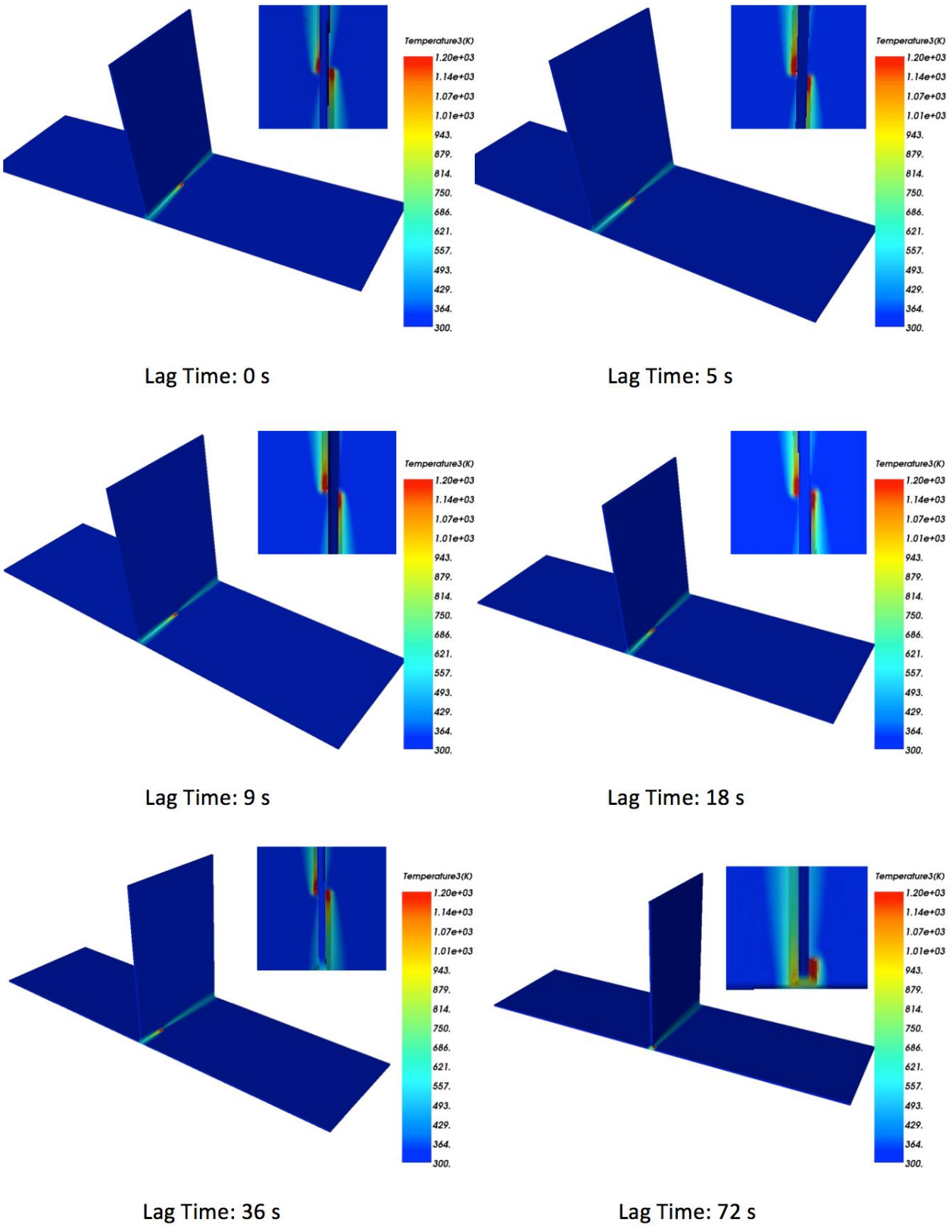

Figure 6-7: Snapshot of temperature distribution of opposite welding direction

6.2.2 Stress Analysis

Although the welding residual stresses caused are three-dimensional, the longitudinal residual stress is usually considered to have the greatest influence on the strength of stiffened plates in ship hulls although there is a possible important influence of transverse residual stresses at the triangular bracket to stiffener connections on fatigue. Due to the highly uneven temperature distribution and the force and moment equilibrium, these residual stresses may result in early yielding of some regions of the longitudinally stiffened plates and consequently cause a reduction in the effective cross-sectional area and moment of inertia leading to the possibility of pre-failure.

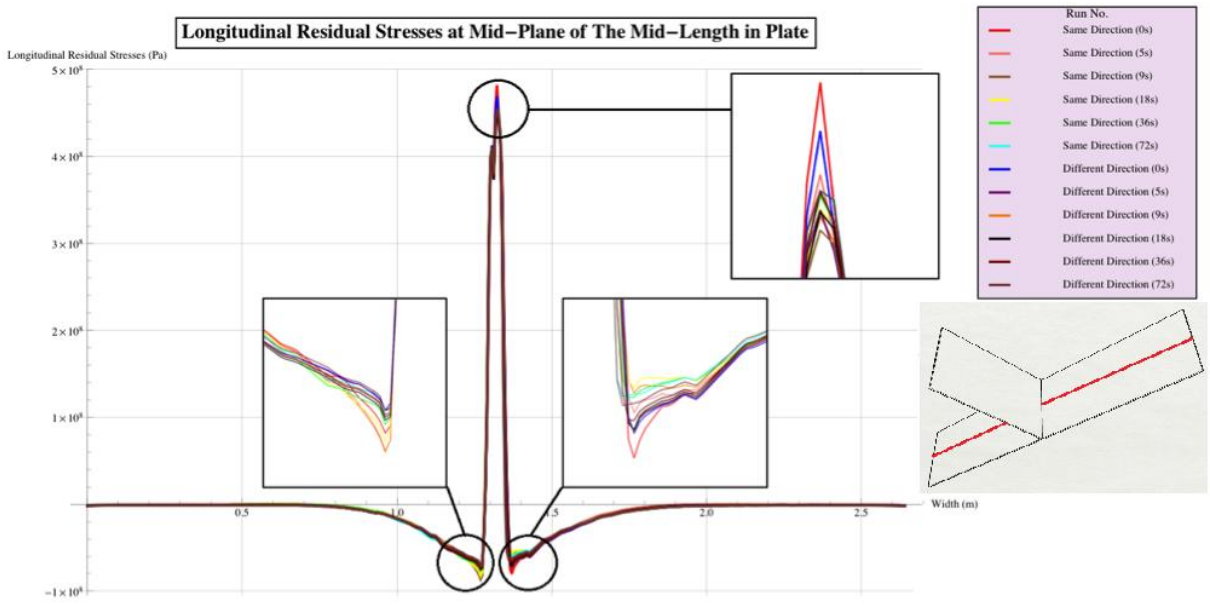

Figure 6-8: Longitudinal residual stress at mid-plane of the mid-length in plate

Figure 6-8 shows the simulated distribution of longitudinal residual stress in the mid-plane of the plate for a transverse section at mid-length for all welding sequences. Overall, the numerical results show that high tensile residual stresses, which are larger than the yield stress of 355 MPa, were present at the location of stiffener attachment acting over a width of approximately 0.07 m, which is almost six times the plate thickness (0.012 m). At this point there is a rapid transition in the residual stress from tension to compression where compressive residual stresses vary in magnitude from about 88 MPa to 0 MPa, and are present at the location of the frame attachment acting and act on a width of approximately 0.5 m to each side of the frame. As the maximum compressive

stresses are relatively small compared to the tensile stresses, optimizing the longitudinal residual stresses can be undertaken by minimizing the maximum tensile stress, because longitudinal residual stress is also determined by transverse residual stress, which means that when minimizing the maximum tensile longitudinal stress, the transverse stress will be minimized too. Figure 6-8 shows the longitudinal stress distribution pattern of all the welding sequence combinations are almost the same. When the double side welding using the same welding direction with a 9 s lagging time in used, there is minimum tensile stress of 437.18 MPa.

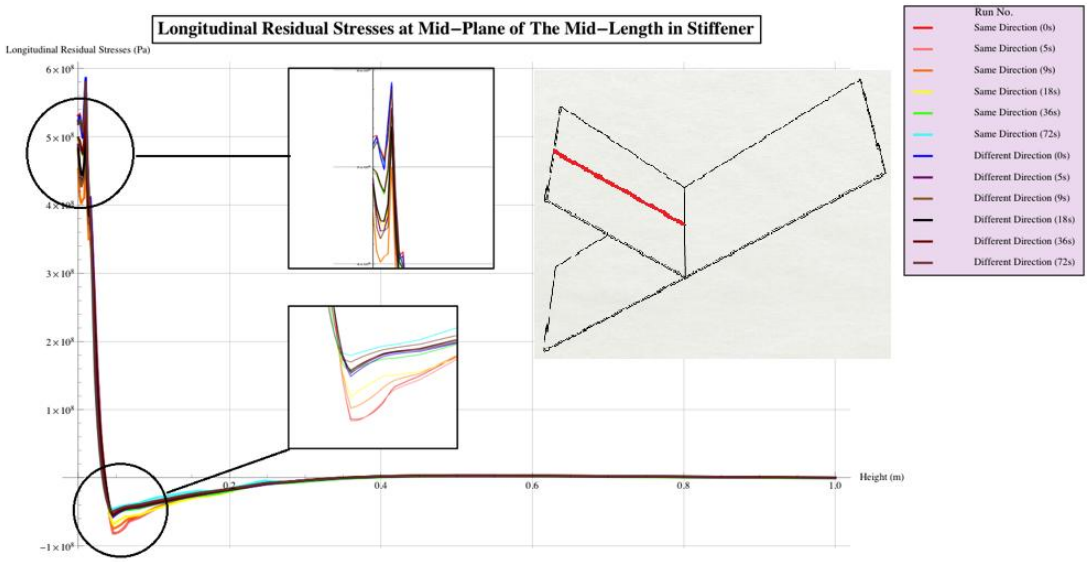

Figure 6-9: Longitudinal residual stresses at mid-plane of the mid-length of the line of the stiffener

Figure 6-9 shows the distribution of longitudinal residual stress along the mid-plane of the side-shell plate along the line of the stiffener. Numerical results show tensile residual stresses also larger than yield near the location of the welds and a rapid transition to compressive residual stress at approximately at 0.048 m from the welding line. From the Figure 6-9, which shows the longitudinal stress distribution pattern of all the welding sequence combinations also are almost the same and with double side welding, using the same welding direction and 9 s lagging time, there is minimum tensile stress of 500.13 MPa, which is higher than the value where plate's because the value used along the stiffener line is located at the welding boundary.

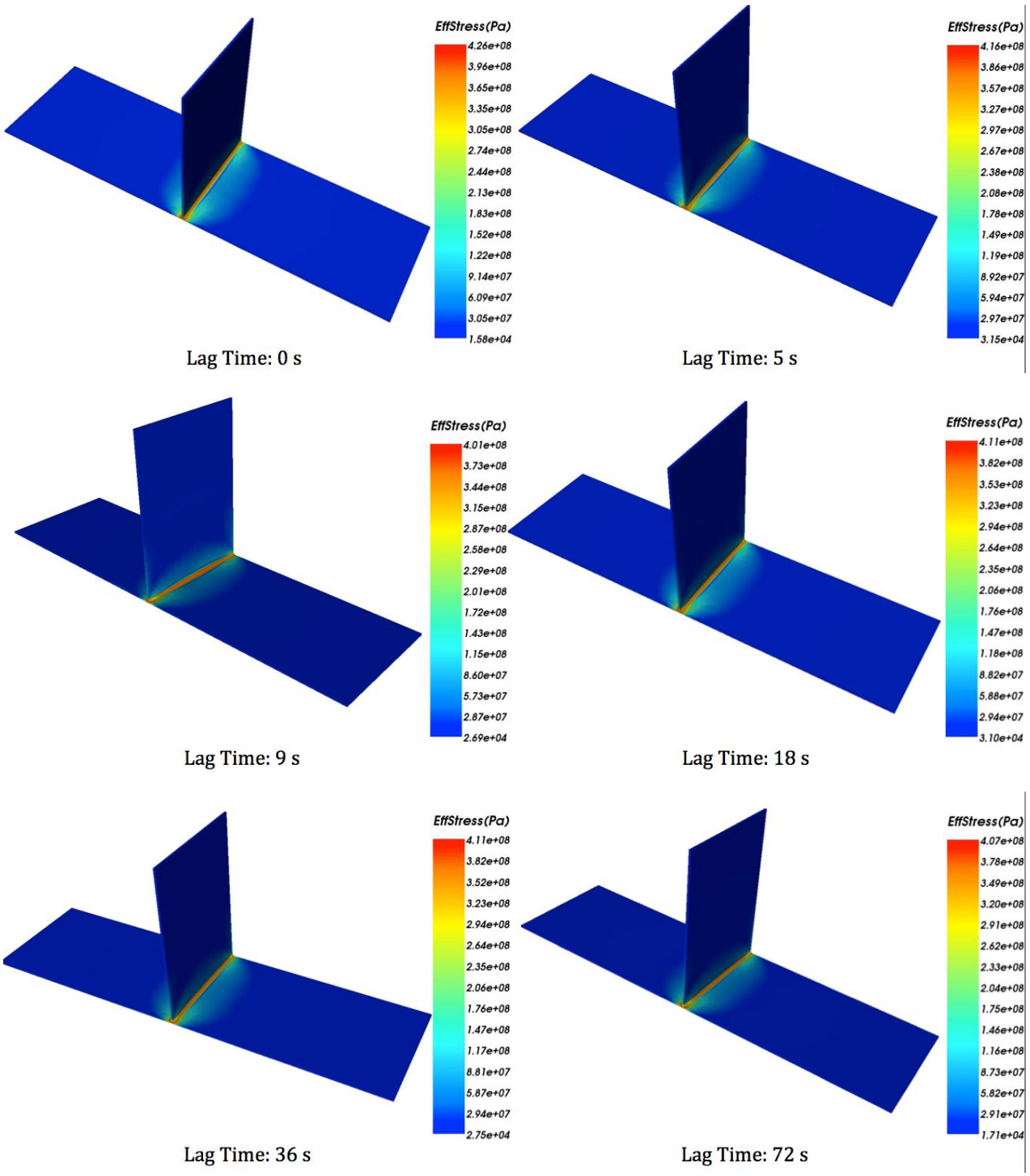

Figure 6-10: Final results of effective stress distribution of same welding direction

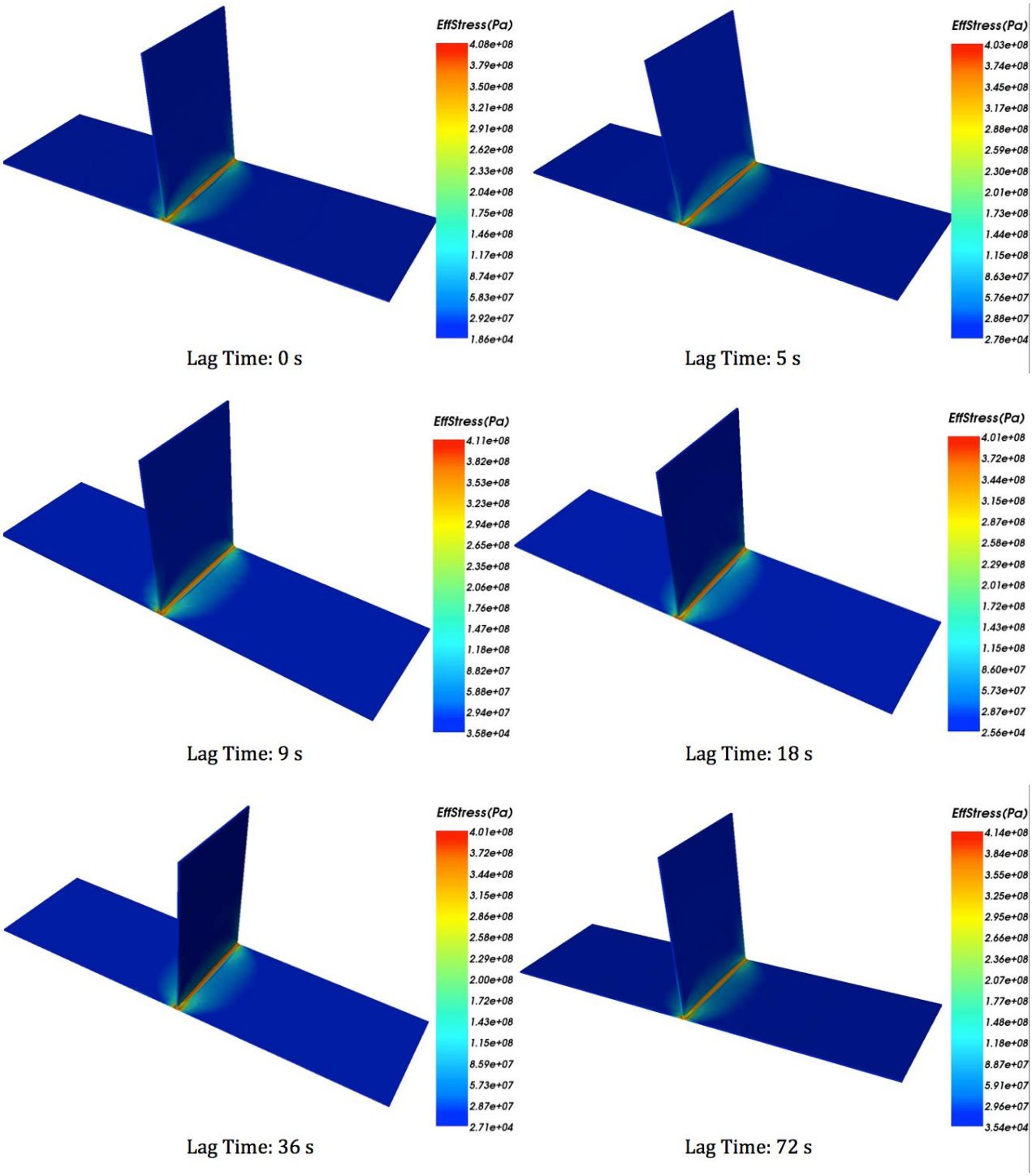

Figure 6-11: Final results of effective stress distribution of opposite welding direction

The final effective residual stresses distributions of all the sub-models is shown in Figure 6-10 & Figure 6-11, which also show the minimum residual stresses occur when double side welding using the same welding direction and 9 s lagging time and has a value of 401 MPa.

6.2.3 Displacement Analysis

Mid-plane vertical deflections of the plate at the mid-length are illustrated in Figure 6-12 for all the combinations. For all combinations, the plate was deformed such that it assumed the 'V' shape that leads to this 'hungry horse' deformation seen in welded stiffened panels of most longitudinally stiffened ship hulls. All the different combinations resulted in asymmetry of the plate vertical deflection about the stiffener. Out-of-plane distortion of the plate contributes to a decrease in the ultimate strength of the plate and consequently, the strength of the stiffened panel (Gordo & Soares, 1993). The minimum magnitude of vertical deflection is approximately 0.024 m, which happened with double side welding using either the same welding direction with 9 s lagging time or using the opposite welding direction with 9 s lagging time.

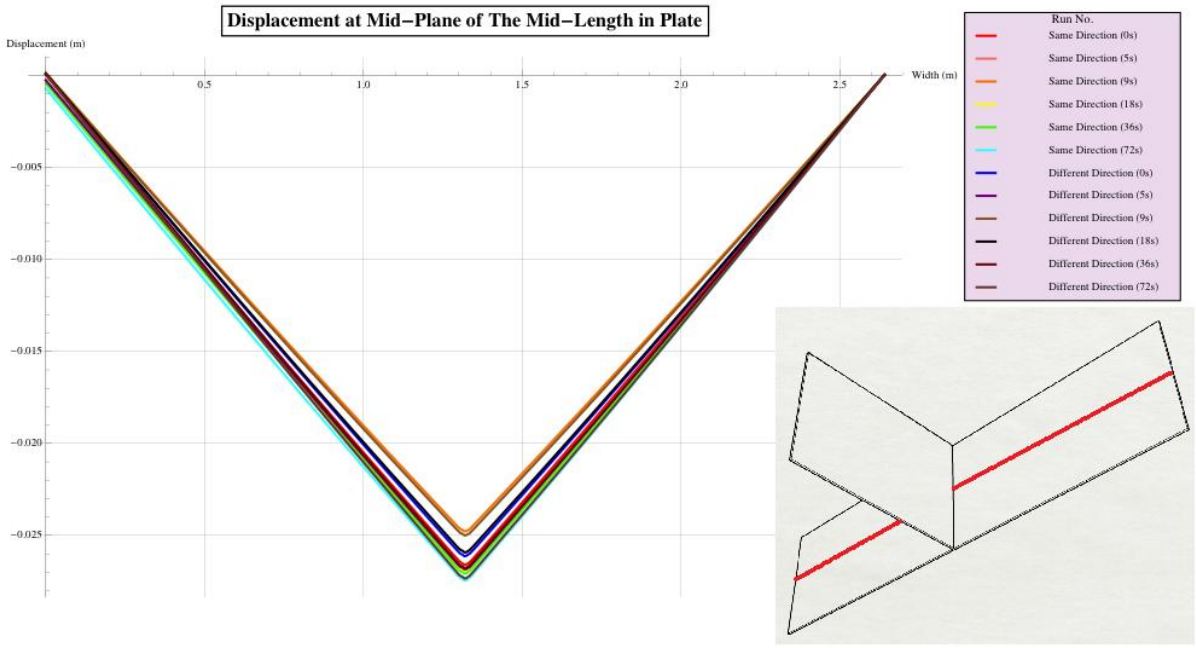

Figure 6-12: Displacement at mid-plane of the mid-length in plate

Mid-plane deflections of the frame at the mid-length are illustrated in Figure 6-12 for all the combinations. The frame displacements of different sub-models varied a lot, even having different directions. The minimum magnitude of vertical deflection is approximately 0.0003 m, which happened when the double side welding using the same welding direction by 5 s lagging time 9 s lagging time, and the displacements in these two sub-models have different directions.

Figure 6-13: Displacement at mid-plane of the mid-length in frame

Figure 6-14 & Figure 6-15 illustrated the final total displacements of all the sub-models, which gave a relatively higher magnitude (around 0.025 m), compare to the fillet model in Chapter 3. Because the size and the width and length ratio of the plate in current model is larger, and there is no constrains applied to prevent the displacement for the model. In order to prove that, the author compared the angular distortion between the model in Chapter 3 (0.02) and the current model (around 0.0196), which shows the same results. According to the results of all the sub-models, the minimum magnitude of total displacement is 0.0255 m, which happened when the double side welding using the same welding direction by 9 s lagging time.

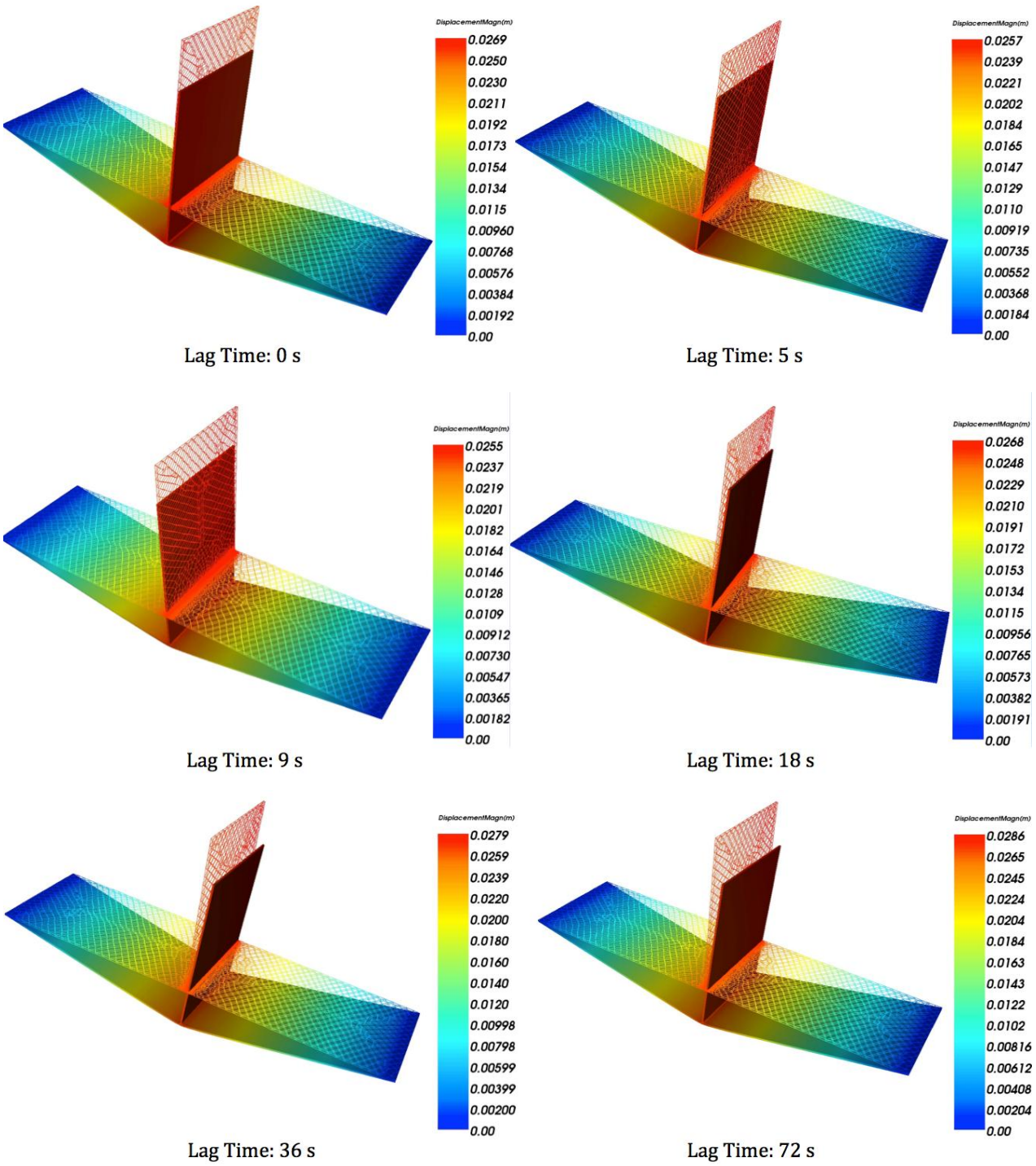

Figure 6-14: Final results of displacement distribution of same welding direction

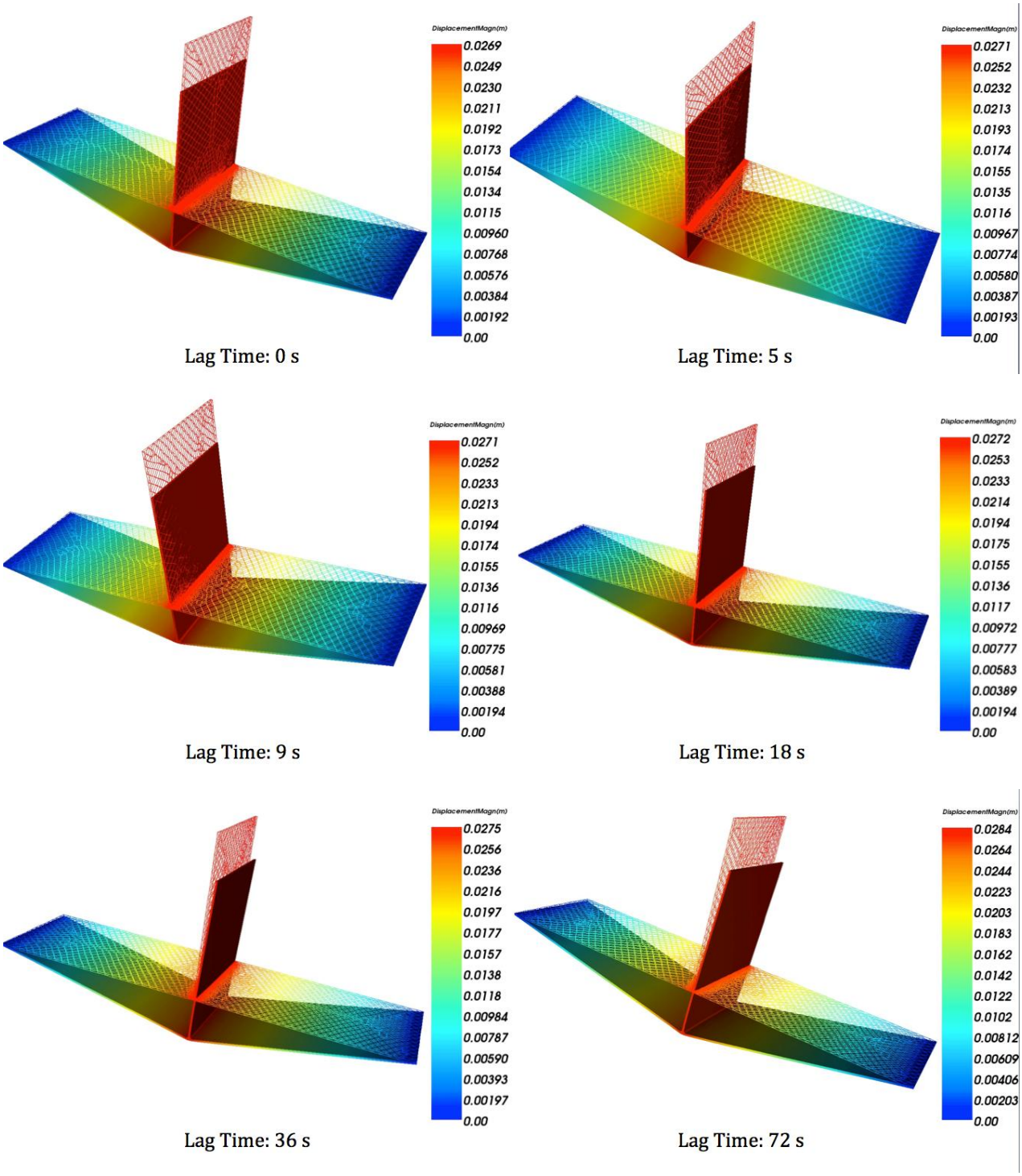

Figure 6-15: Final results of displacement distribution of opposite welding direction

6.2.4 Optimization

From the above analyses, welding sequence did not have a significant influence on the distribution pattern of either the stresses or displacements in both the plate and frame; however it did affect the peak values. In shipyards, optimizing the welding sequences will get significant reduction in weld induced distortions, because in this research, the model is used the boundary condition that allow the plate bending freely, so the limited model can have this kind of results. The objective of the optimization is to minimize the displacement and the residual stresses. The peak value comparison of all the sub-models is shown in Table 6-3, which presents that the minimum peak values of total displacement and effective residual stresses. Both happened in sub-model 3, which showed that best way for the double side fillet welding the frame to the side shell is using the same welding direction by 9 s lagging time.

Sub-Model Number	Total Displacement (m)	Effective Residual Stresses (MPa)
1	0.0269	426
2	0.0257	416
3	0.0255	401
4	0.0268	411
5	0.0279	411
6	0.0286	407
7	0.0269	408
8	0.0271	403
9	0.0271	411
10	0.0272	401
11	0.0275	401
12	0.0284	414

Table 6-3: Peak value comparison of all sub-models

6.3 Optimization of Welding Sequence For Final Model

6.3.1 Design of Optimization Space

According to the discussions above, the final model has a total of 12 weld passes (See Figure 6-4), and continuous double side fillet welding with 9 s lag time is chosen for this model due to the optimization analysis results in Section 6.2, so the 12 weld passes can be sub-grouped as 7 sub-passes:

- Sub-pass 1: Weld Pass 1 and Weld Pass 2
- Sub-pass 2: Weld Pass 3 and Weld Pass 4
- Sub-pass 3: Weld Pass 5 and Weld Pass 6
- Sub-pass 4: Weld Pass 7 and Weld Pass 8
- Sub-pass 5: Weld Pass 9
- Sub-pass 6: Weld Pass 10 and Weld Pass 11
- Sub-pass 7: Weld Pass 12

Even the welding sub pass number was reduced from 12 to 7, there is still 645,120 combinations, which is not possible to carry out an optimization analysis for it either, so the real welding situation need to be taken into account. From Figure 6-1, this structure consists of side shell, transverse stiffener, shell stiffeners and frame web stiffeners; according to the experienced welding engineer, the transverse frame web needs to be welded with the side shell first as if the shell stiffener is welded first, it will obstruct the transverse frame web; and the frame web stiffener needs to be welded last as its function is to connect and stabilize the above two components. The components assemble sequence schematic representation is shown in Figure 6-16, Figure 6-17 and Figure 6-18.

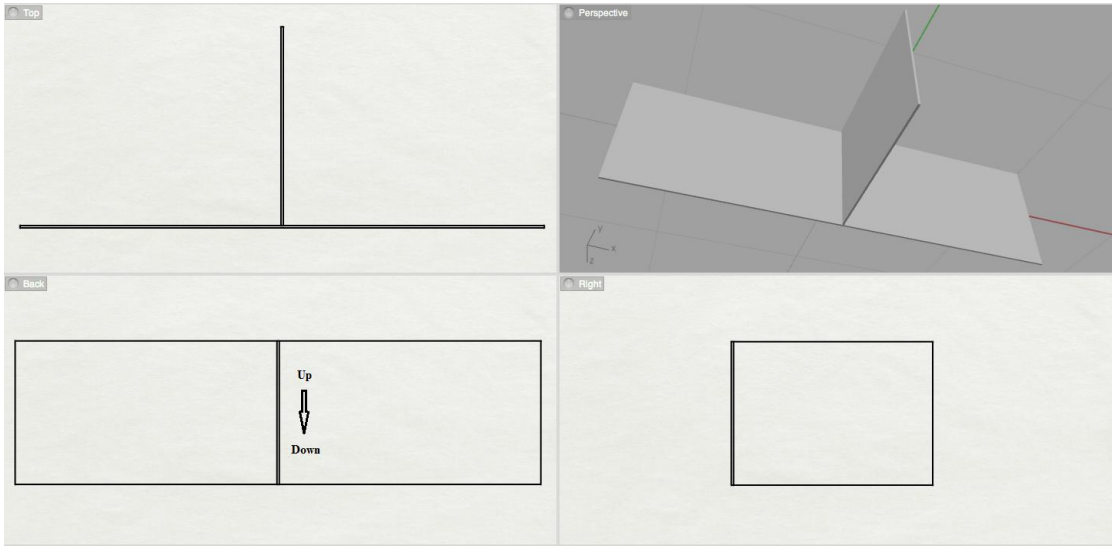

Figure 6-16: Components assembly sequence schematic representation step 1

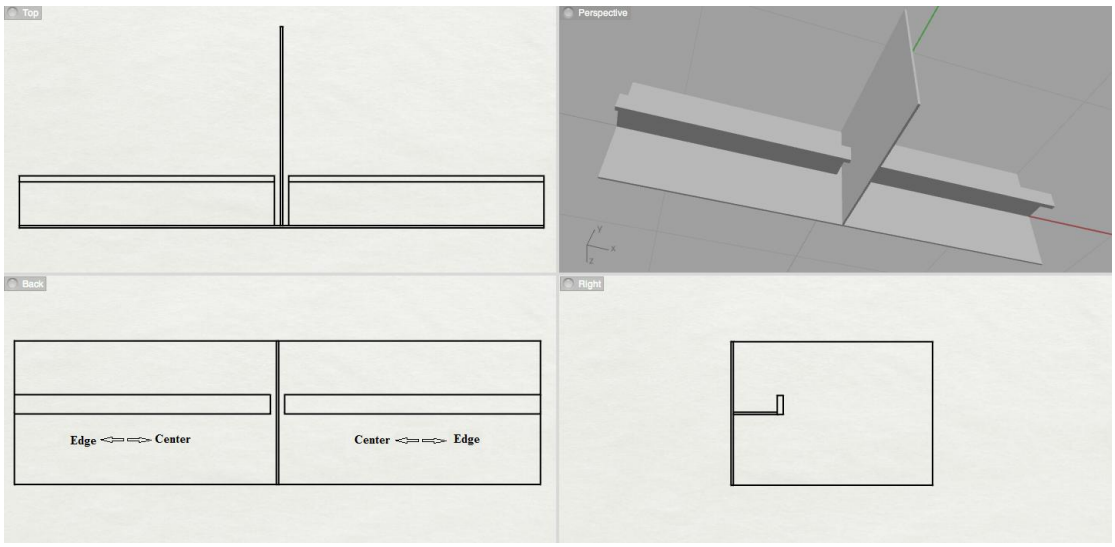

Figure 6-17: Components assembly sequence schematic representation step 2

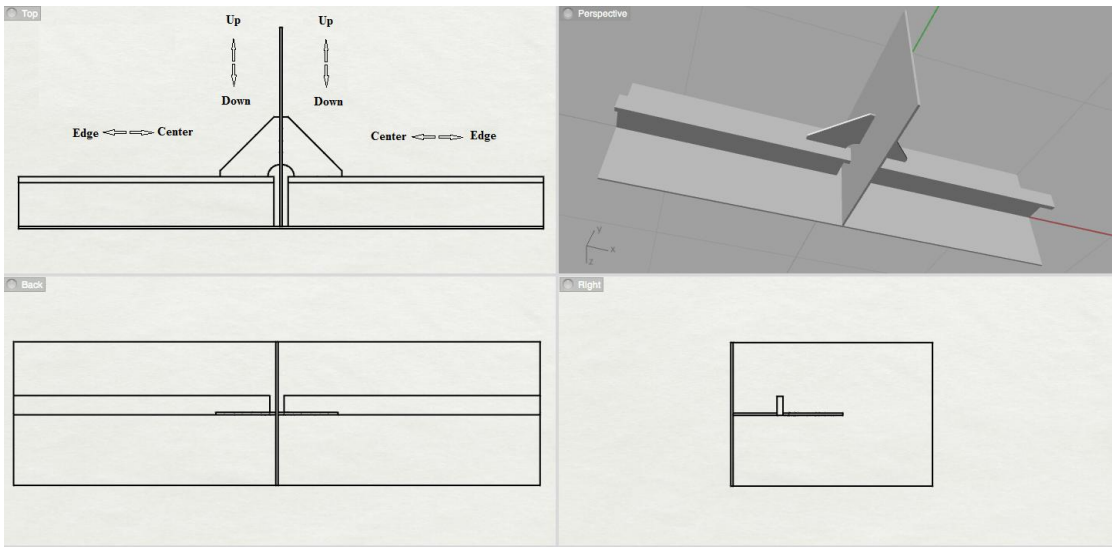

Figure 6-18: Components assembly sequence schematic representation step 3

Because the final model is completely symmetrical along the transverse stiffener web, the design space of the welding sequences need only take the half model into account, for example, it doesn't matter which shell stiffener is first welded to the side shell. According to Figure 6-16, there is only one choice for assemble the side shell and the transverse stiffener web due to the symmetry of the structure; there are two choices for welding the side shell and the shell stiffener: from the center to edge and from the edge to center, which was illustrated in Figure 6-17; from Figure 6-18, it can be seen that there are two choices when welding the frame web stiffener to the transverse stiffener web and also two choices while joining the frame stiffener to the shell stiffener. So after integrating the results from the Section 6.2 and the real welding situation, the welding sequence combination number has been reduced to 8, the details of welding sequence for each sub-model have been given in Table 6-4. Figure 6-19 shows the schematic diagram of welding sequence for sub-model #1 as an example to represent the welding sequences described in Table 6-4.

Sub-Model Number	Sub-Pass 1	Sub-Pass 2	Sub-Pass 3	Sub-Pass 4	Sub-Pass 5	Sub-Pass 6	Sub-Pass 7
#1	Up to Down	Center to Edge	Center to Edge	Down to Up	Center to Edge	Down to Up	Center to Edge
#2	Up to Down	Center to Edge	Center to Edge	Down to Up	Edge to Center	Down to Up	Edge to Center
#3	Up to Down	Center to Edge	Center to Edge	Up to Down	Center to Edge	Up to Down	Center to Edge
#4	Up to Down	Center to Edge	Center to Edge	Up to Down	Edge to Center	Up to Down	Edge to Center
#5	Up to Down	Edge to Center	Edge to Center	Down to Up	Center to Edge	Down to Up	Center to Edge
#6	Up to Down	Edge to Center	Edge to Center	Down to Up	Edge to Center	Down to Up	Edge to Center
#7	Up to Down	Edge to Center	Edge to Center	Up to Down	Center to Edge	Up to Down	Center to Edge
#8	Up to Down	Edge to Center	Edge to Center	Up to Down	Edge to Center	Up to Down	Edge to Center

Table 6-4: Design space of welding sequences for final model

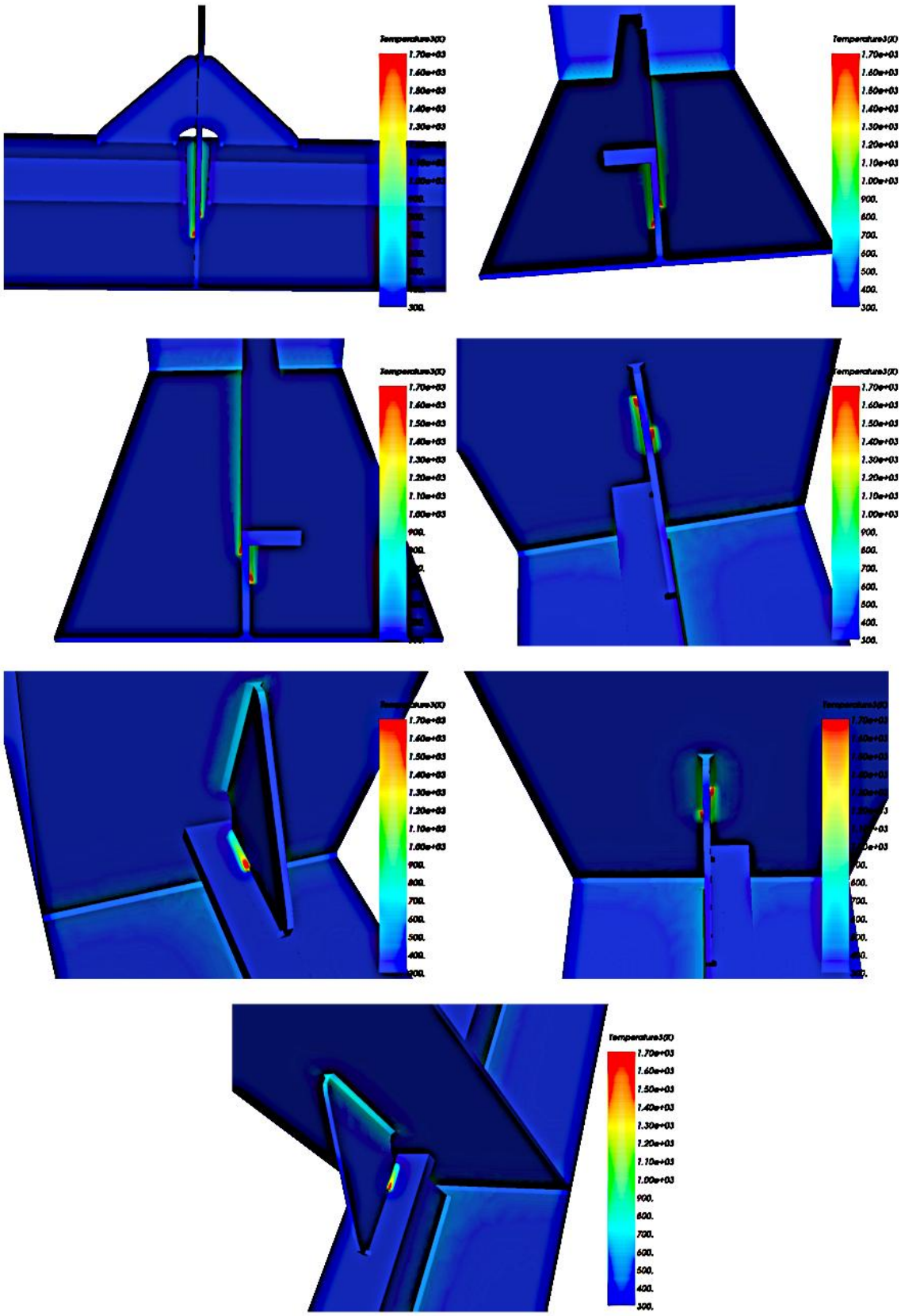

Figure 6-19: Schematic diagram of welding sequence in sub-model #1

6.3.2 Results Discussion

In this analysis, the multi – project mode in VrWeld was employed and used 8 CPUs to run all the cases defined in Table 6-4 in parallel. The whole analysis was completed in two weeks.

Figure 6-20 presents the final effective residual stress distributions for all sub-models. The residual stresses are mainly distributed in the area near the welded joints and the maximum values always appear at the edge of the welding joints. According to the figure, it can be seen that sub-model #1, #2 and #5, #6 have relatively smaller maximum effective residual stress value and there is not a significant difference among those values except sub-model #1, the difference between them and the other four sub-models is the different welding sequences in sub-pass 4 and sub-pass 6 which for sub-passes 4 and 6 introduced welding from down to up. The minimum peak effective welding residual stress happened at sub-model #1 and the value is 541 MPa.

Figure 6-21 shows the final distortions for all the sub-models, which show that the sub-models #5, #6, #7, #8 have the smaller maximum displacement values. The difference between them and the other four sub-models is the different welding sequences in sub-pass 2 and sub-pass 3, when welding the shell stiffeners to side shell, which in sub-models #5 to #8 was welded from edge to center. The minimum peak displacement happened at sub-model #6 and the value is 0.00539 m. By comparing Figure 6-21 with Figure 6-14 & Figure 6-15, it can be seen that the distortion in the final model is much smaller than in the double side fillet welding model. This is because in the final model, all the components have been connected together by tack welds, and the shell stiffeners functioned as constraint to prevent the side shell from the angular distortion.

Often in shipyard practice the frames would be welded without the stiffener present or vice versa as then allow more efficient machine welding. However with robotics welding more compelled fabrication sequences may be practical.

Generally speaking, for this specific structure details, the sequence of welding the shell stiffeners to side shell determined the final peak displacement value and the sequence of welding the frame web stiffeners to transverse frame web determined the final peak effective welding residual stress value.

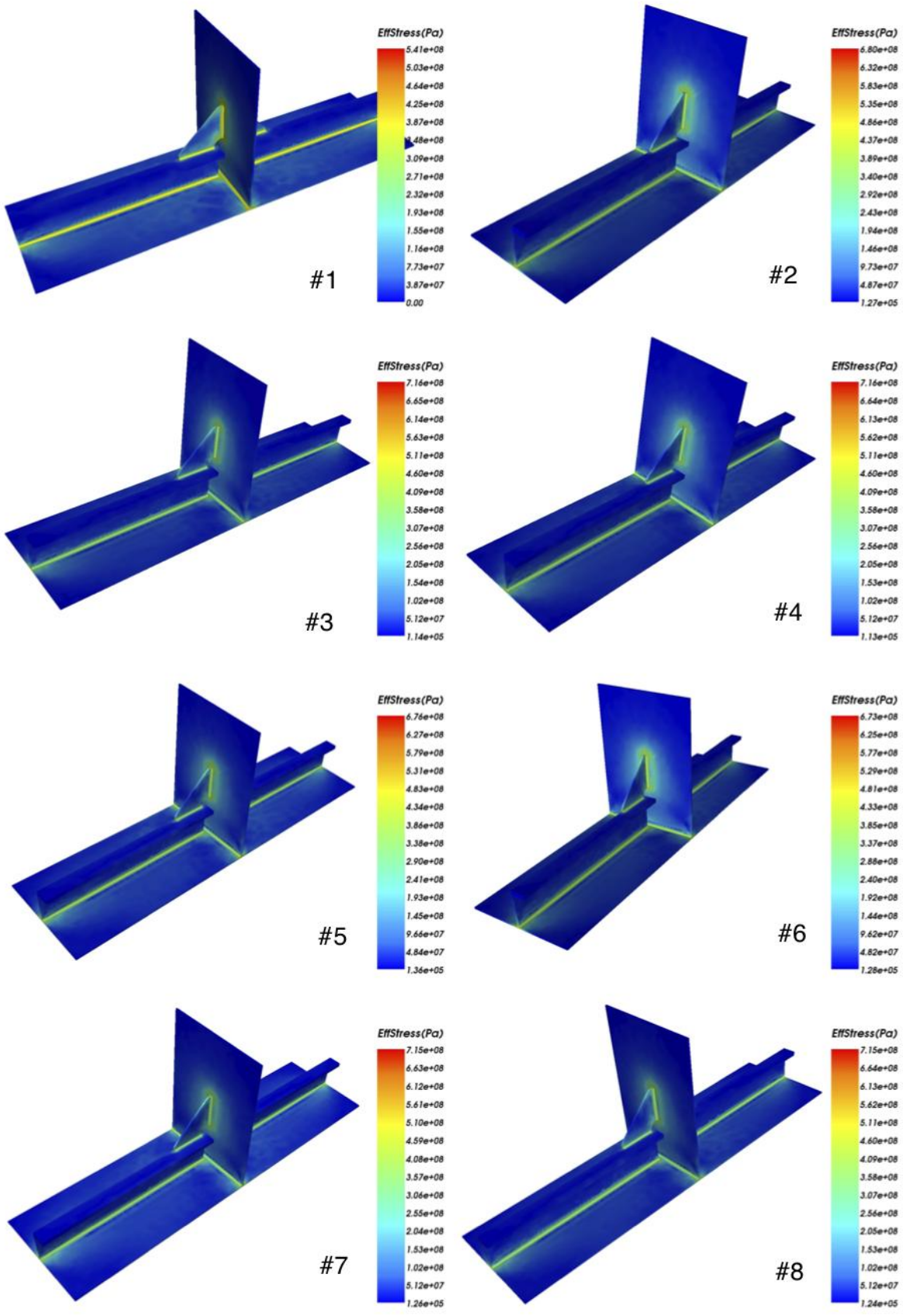

Figure 6-20: Final effective residual stress distribution of all sub-models

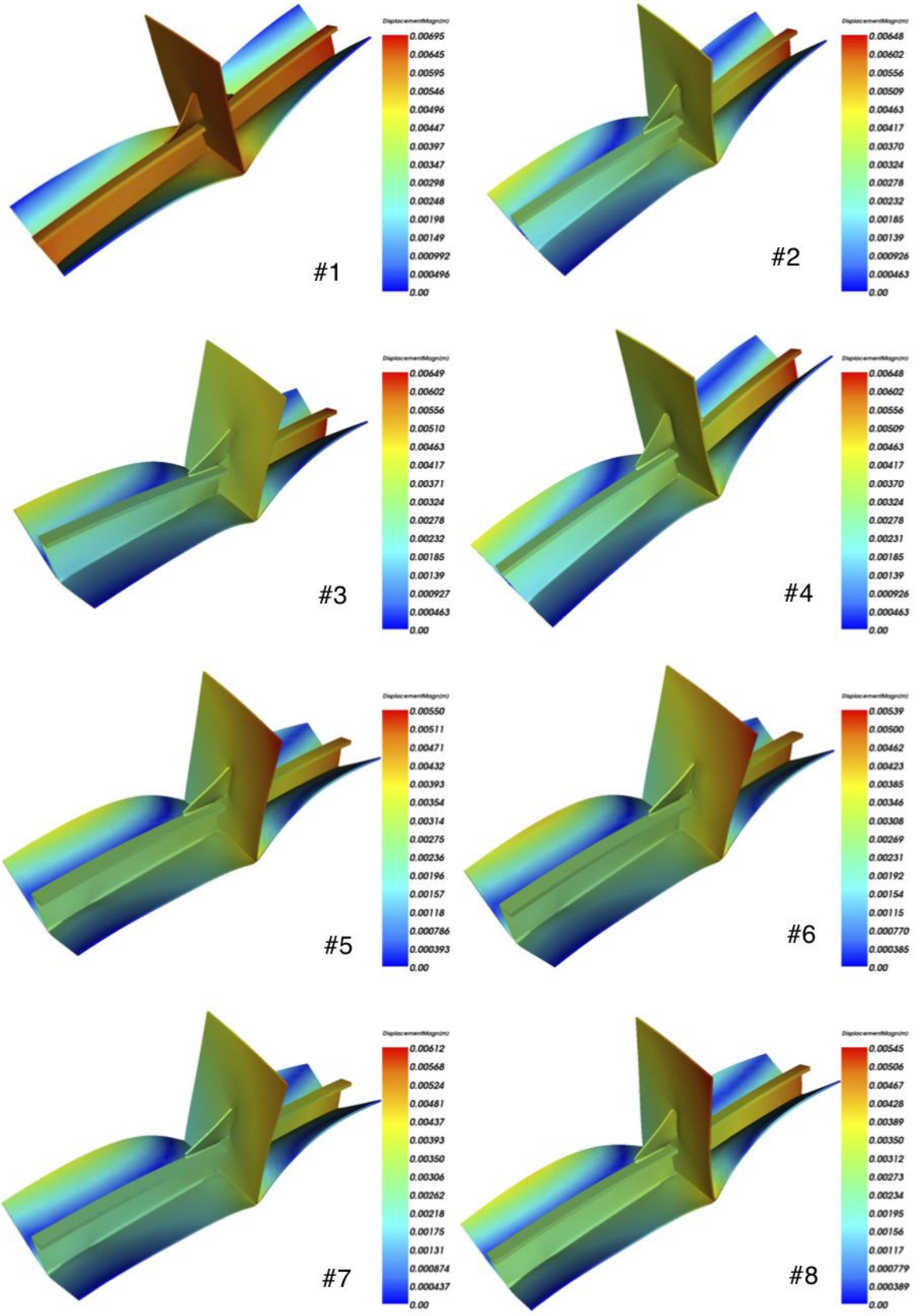

Figure 6-21: Final displacement distribution of all sub-models

6.3.3 Find the Optimum

The optimization objective is to find the best sequence to minimize the residual stress and distortion. From Section 6.3.2, it can be seen that the welding sequences didn't change the pattern of residual stresses and distortions much, but it did affect the peak values of them. According to Table 6-5, sub-model #6 resulted in the minimum peak values of total displacement and sub-model #1 produced the minimum peak values of the effective residual stress.

Sub-Model Number	Total Displacement (m)	Effective Residual Stresses (MPa)
#1	0.00695	541
#2	0.00648	680
#3	0.00649	716
#4	0.00648	716
#5	0.00550	676
#6	0.00539	673
#7	0.00612	715
#8	0.00545	715
Average Value	0.00611	679

Table 6-5: Peak value comparison of all sub-models for final model

From the data, the peak value of displacement and residual stress cannot be optimized at the same time. For this specific case, the optimal welding sequence will be chosen from sub-model #1 and #6. Sub-model #1 gave the minimum peak residual stress of 541 MPa, which is 20% lower than the average value; but the displacement value is 13.7% higher than the average value; sub-model #6 gave the minimum peak displacement value that is 11.8% lower than the average value and the residual stresses value is almost the same as the average value.

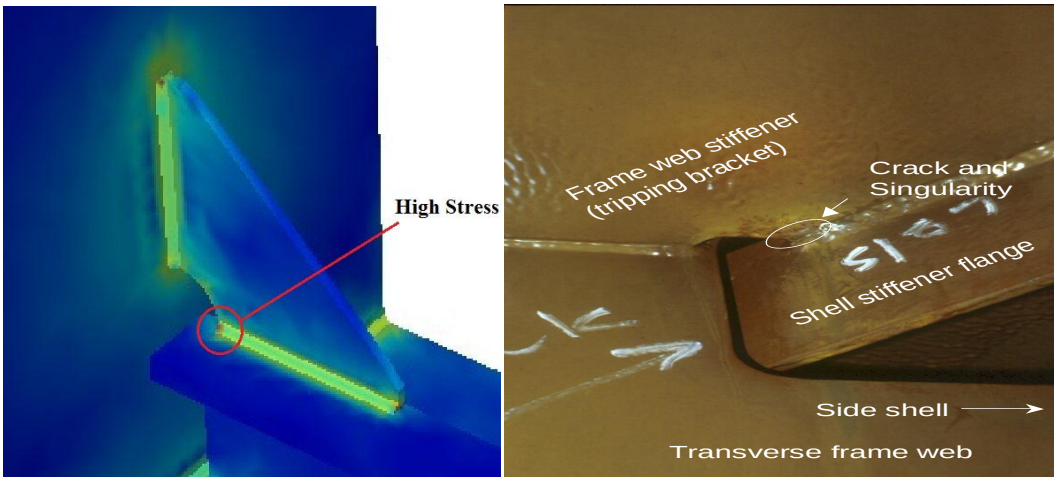

Figure 6-22: Residual stress distribution at typical fatigue crack welding connections

Determining which one is the optimum depends on the preference of the optimization objective. In this research, the author mainly aimed to minimize the residual stresses, and the unit for displacement is millimeter, the 1.5 mm difference can be neglected in marine structures due to the construction size, but the 150 MPa stress reduction may bring a critical benefit to both fracture and fatigue of marine structures, which can be seen in Figure 6-22. According to the right part of Figure 6-22, the position of singularities is often at the edge of welding joints at sharp corners, and the left part also shows there is a very high residual stress at the same location, as mentioned before, some studies reveal that residual stresses are more responsible for fatigue crack growth than any other factors. So the author chose the welding sequence of sub-model #1 as the optimum for this specific structure detail in this research. The schematic diagram of the welding sequence for sub-model #1 has been shown in Figure 6-19, and the final step displacement and effective residual stress distribution have been presented by Figure 6-23 & Figure 6-24.

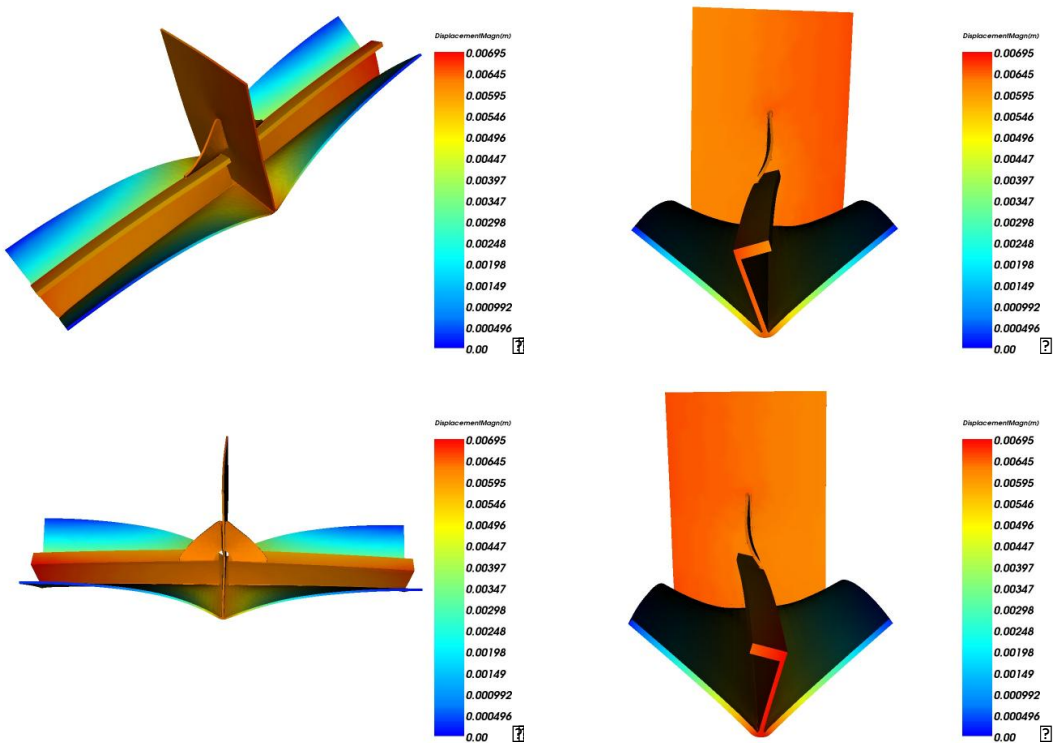

Figure 6-23: Displacement representation from different angles for sub-model #1

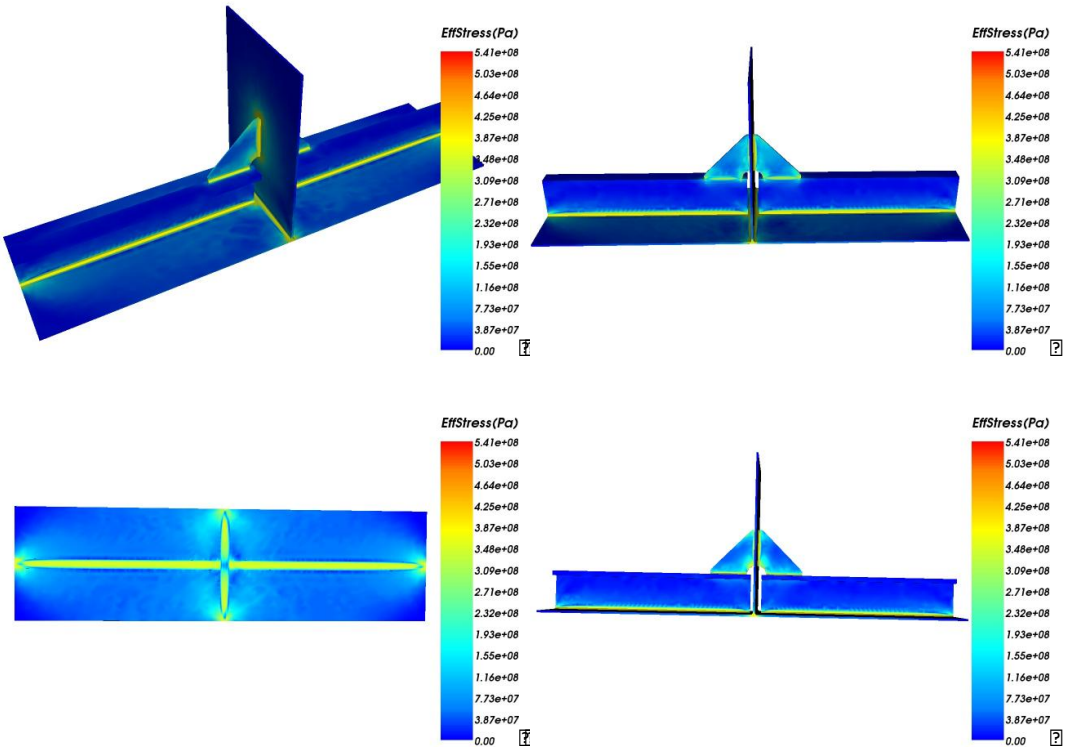

Figure 6-24: Residual stress distribution from different angles for sub-model #1

6.4 Conclusions

This Chapter simulates residual stress and distortion of a fatigue sensitive ship's side shell connection detail, under different welding sequences. The author reduced the welding sequence combinations from billions to eight by optimizing the double side fillet welding sequences and combining the experience from the practical welding situation in shipyard. The advanced welding simulation techniques used, were the same as introduced in Chapter 3. Depending on simulated results, it was found that the sequence of welding the shell stiffeners to side shell determined the final peak displacement value and the sequence of welding the frame web stiffeners to transverse frame web determined the final peak effective welding residual stress value. Comparing the distortion and residual stress under eight welding sequences, the optimal welding sequence was found for this specific marine structure detail.

Chapter 7 Contributions and Recommendations

Conclusions

In this research, a finite element model based on ANSYS and VrWeld software that is capable of simulating the thermo-mechanical welding process was developed and validated by comparison with experimental data. It has been shown that distortions predicted by the finite element model agree well with measured data from previous literature and that the numerically obtained residual stress distribution is compared and agreed by both ANSYS and VrWeld software. In this model, the temperature dependent material properties were used to take the microstructure, material melting and phase changing effect into account; the element activate and deactivate technique, which implemented in both thermal and mechanical simulations, is used for making the simulation more accurate and closer to practical; it is found that the advanced mesh technique and subdomain method is capable of accelerating the simulation speed dramatically by comparing the calculation speed of ANSYS and VrWeld.

And a simple method for predicting the butt-welding residual stresses based on force and moment equilibrium was derived, with results that are a reasonable match with the results from FE analysis. The author also did a detailed analysis for the distribution of transverse and longitudinal residual stresses, which deeply illustrated how the butt-welding residual stresses was distributed and accumulated during the welding process. The boundary condition analyses illustrate the cause of the edge effect graphically, which is due to the longitudinal shrinkage at the two edges of the welding line. The high value residual stresses are located near the welding line, and the following conclusions can be drawn:

- The welding residual stresses are symmetrical in both transverse and longitudinal directions. This results from the use of element activate and deactivate technique and the force and momentum equilibrium effect, which has been detailed explained in Section 4.2.1;

- The main factors dominating the welding residual stress distribution are the heating and cooling during the welding process and the internal force and

moment equilibrium effect; the former mainly dominates the stress produced at the areas near the welding line, which is the origin of the driving force, not substantially affected by the model geometry dimensions; the stresses well away from the weld line are mainly balancing overall forces and moments.

- The maximum residual stress magnitude does not occur at the welding line, but at the position at 0.014 m from the welding line, due to the temperature dependent material properties and performances.

- The transverse welding residual stresses have relatively small tensile value, but a large compressive value, which exceeds the material yield stress, located at the region of both ends of the welding line.

- The longitudinal welding residual stresses have a relatively small compressive value, but a large tensile value, which also exceeds the material yield stress and are located at the region around the welding line.

After that, a detailed parametric study for butt welding residual stress distributions has been performed for different cut-off temperatures, welding power, welding velocity, plate length and plate width. Among these factors, how the temperature history affect the residual stress distribution is reflect on the cut-off-temperature, welding power and welding velocity; the plate length and width expressed the effect of model geometry to the residual stress distribution.

From Section 5.1, when the maximum cut off temperature over 1073 K, the residual stress distribution doesn't change. However if the COT is set lower than 1073 K, the material is too stiff as it does not melt even at the maximum temperature, so the residual stress distribution is changed not only the magnitudes, but also the distribution pattern. As mentioned before, due to the material used in this whole research is ASTM A131, Grade DH36, 1073 K is the materials soften temperature. In Section 5.2 & 5.3, the results show that the duration when the temperature over 1073 K is the key reason for welding residual stress distribution regarding to the different transient temperature field during the welding process; Section 5.2 also shows that the maximum temperature also has some impacts on the residual stress distribution by affecting the temperature history

in HAZ; and Section 5.3 based on a numerical analysis with different weld powers and weld speeds but constant maximum weld temperature, presented that the ratio of power per unit length of weld does not characterize a weld except in the limit of very high welding speeds. In sum, according to the analysis in Section 5.1, 5.2 and 5.3, it can be seen that the main factor of the temperature history, which affects the stress distribution, is how long the duration when the temperature over the material soften temperature.

Section 5.4 presents that when the plate length is larger than 1 m, it can be seen that both the transverse and longitudinal residual stress distributions are keeping exactly the same at the length positions in the first 0.5 m and the last 0.5 m regarding to different plate lengths; and the stress distribution at the middle part remains constant, so it can be concluded that if the length were great enough, the residual stress distributions would not change with longitudinal direction after some distance from the edge. According to the analysis in Section 5.5, it can be seen that when the ratio of welding seam size to the plate width is smaller than 0.006, the whole residual stress distribution is maintain the same regarding to different plate widths, so which can be concluded that if the ratio of welding seam size to the plate width is small enough, the residual stress distributions would not change.

From the force and moment equilibrium, lower COT makes the material stiffer, which results bigger in-plane bending, so the transverse bending moment became bigger, therefore, larger longitudinal moment is needed for balancing purpose. A longer welding length results in larger transverse moments, which also increases the longitudinal moment. However, if the welding length is constant, the transverse moment will also be a constant, and the longitudinal stress distribution will depend on the plate width because the longitudinal moment is a constant.

Lastly, the author simulates residual stress and distortion of a fatigue sensitive ship's side shell connection detail, under different welding sequences. The author reduced the welding sequence combinations from billions to eight by optimizing the double side fillet welding sequences and combining the experience from the practical welding situation in shipyard. The advanced welding simulation techniques used, were the same as introduced in Chapter 3. Depending on simulated results, it was found that the sequence of welding the shell stiffeners to side shell determined the final peak displacement value and the

sequence of welding the frame web stiffeners to transverse frame web determined the final peak effective welding residual stress value. Comparing the distortion and residual stress under eight welding sequences, the optimal welding sequence was found for this specific marine structure detail.

Contributions:

- Finite element simulation of butt and fillet welding processes with advanced simulation techniques was done by ANSYS and VrWeld and validated by comparison with experimental data;

- A detailed analysis for the distribution of transverse and longitudinal residual stresses, which deeply illustrated how the butt-welding residual stresses was distributed and accumulated during the welding process; and how the boundary conditions affect the final results was determined in this study;

- A simplified mathematical model of welding residual stresses based on force and moment equilibrium was derived. The results calculated from this simple method were a useful approximation to the FE results.

- A detailed parametric study for butt welding residual stresses based on 2D butt-welding by using 3D elements was presented. The factors considered in the parametric study involved the cut-off temperature effect, welding power effect, welding velocity effect, plate length effect and plate width effect.

- A simulation and an optimization of welding sequences for residual stress and distortion was carried out for a, fatigue sensitive, ship's side shell connection detail under different welding sequences.

Recommendations for Further works:

The thermal-elastic-plastic FEM computer simulation is quite reliable and is useful for prediction of welding residual stresses, but it is not feasible for very large and

complicated structures because the computation time is too long. The inherent strain method has the ability to predict the welding residual stresses for large structures, but the inherent strains need to be prepared, with values coming from an experiment database. It has limitation that the geometry of the structure has to be in the database, besides, it is still necessary to carry out an elastic FE analysis. The simplified method provided in this thesis is based on first principles and provides an understanding of how the welding residual stresses are produced and distributed. There is no limitation and the results match well with the thermal-elastic-plastic FEM computer simulation. Most importantly, this simple method can be extended to large and complicated structures, for example, each welding pass can be isolated from the complicated structure, and then used in the simple method to calculate the welding residual stresses for each welding pass in the welding sequences; the first calculated welding pass results will be used as boundary condition for the next pass, finally, the results from all welding passes can be added together by using the superposition principle to get the final welding residual stress distribution for the whole structure. The detailed recommendations for further work are as follows:

- Analysis of the effect of welding residual stresses on fatigue and fracture;
- Include transverse residual stress in the optimization;
- Include fatigue, fracture and buckling analysis in the optimization;
- Determine whether there are benefits on fatigue from more compressive residual stresses;
- Analyze fabrication order to balance residual stresses and deformations with cost.
- Extend the simplified methodology to consider longer range stresses as large structure are fabricated. This will be particularly useful for fitness for purpose defect assessment where present practice requires, sometimes very pessimistic, assumptions to be made about residual stress levels.
- Extend the present simplified methodology to calculation of deformations.

Reference:

(n.d.). Retrieved from www.ansys.com.

Asadi, M., & Goldak, J. (2010). Challenges In Verification Of CWM Software To Compute Residual Stress And Distortion In Welds. *Proceeding of 2010 ASME Pressure Vessels & Piping Conference.* Washington.

Bachorski, A., Painter, M. J., Smailes, A. J., & Wahab, M. A. (1999). Finite element prediction of distortion during gas metal arc welding using the shrinkage volume approach. *Journals of Materials Proceeding Technology* , 405-409.

Bathe, K. J. (1996). *Finite element procedures.* Prentice Hall.

Bibby, M., & Goldak, J. (1988). Computational thermal analysis of welds: Current status and future directions. *Modeling and Control of Casting and Welding Processes* , 153-166.

Boley, B. A., & Weiner, J. H. (1960). Theory of Thermal Stresses.

Brian, R., & Salerno, M. (2008). *Welding distortion analysis of hull block using equavalent load method based on inherent strain.* Ship Structure Committee.

Burghardt, M. D., & Harbach, J. A. (1993). *Engineering Thermodynamics.* New York.

Callister, W. J. (1995). *Material Science and Engineering.* NewYork: John Wiley & Sons Inc.

Camilleri, D. 1. (2005). *Support tools for the prediction of distortion in the design and manufacture of thin plate welded structures.* University of Strathclyde, Department of Mechanical Engineering.

Camilleri, D. 2., Comlekci, T., & Gray, T. G. (2004). Use of thermography to calibrate fusion welding procedures in virtual fabrication applications. *Proceeding of Inframation 2004 Conference*, (pp. 121-131). Las Vegas, USA.

Camilleri, D. 3., & Gray, T. G. (2005). Computationally efficient welding distortion simulation techniques. *Modeling Simulation Material Science Engineering* .

Camilleri, D. 4., Comlekci, T., & Gray, T. G. (2005). Computational presiction of out-of plane Welding distortion and experimental investigation. *Journal Strain Analytical Engineering Description* .

Camilleri, D. 5., & Gray, T. G. (2003). Out-of-plane distortion of CMn steel plates during flux-cored CO2/Ar automatic butt welding. *Proceeding International Conference on Metal Fabrication and Welding Technology* .

Camilleri, D. 6., Comlekci, T., & Gray, T. G. (2006). Thermal distortion of stiffened plate due to fillet welds - computational and experimental investication. *Journal of Thermal Stresses* .

Camilleri, D., Comlekci, T., Lee, C. K., Tan, H., & Gray, T. G. (2003). Investigation of temperature transients during flux-cored CO2/Ar butt welding of Cnn steel plates. *Proceeding of International Conference on Metal Fabrication and Welding Technology*. Nottingham, UK.

Carslaw, H. S., & Jaeger, J. C. (1950). *Conduction of heat in Solids*. Oxfard.

Chai, Z., Zhao, H., & Lu, A. (2003). Efficient finite element approach for modelling of actual welded structures. *Science and Technology of Welding & Joining* , 195-204.

Chapman, A. J. (1987). *Fundamentals of Heat Transfer*. London.

Cheng, B. A. (2003). *A posteriori error estimates of finite element solutions*. University of Carleton.

Cifuentes, A. (1992). Performance Study of Tetrahedral and Hexahedral Elements in 3D Finite Element Structural Analysis. *Finite Elements in Analysis and Design* .

Deng, D., Liang, W., & Murakawa, H. (2007). Determination of welding deformation in fillet welded joint by means of numerial simulation and comparison with experimental results. *Journal of Materials Processing Technology* , 219-255.

Deo, M. V., Michaleris, P., & Sun, J. (2003). Prediction of Bulking distortion of welded structures.

Dong, P., Hong, J. K., & Bouchard, P. J. (2005). Analysis of residual stresses at weld repairs. *International Journal of Pressure Vessels and Piping* .

Easterling, K. (1993). *Introduction to the Physical Metallurgy of Welding*. Butterworth Heinemann.

Friedman, E. (1975). Thermo mechanical analysis of the welding process using the finite element method. *American Society of Mechanical Engineer - Journal of Pressure Vessel Technology* , 206-213.

Goldak, J. (2007). Retrieved from Vr Software Suite: www.goldaktec.com

Goldak, J. A. (1989). Modeling thermal stresses and distortions in welds. *Proceeding of the 2nd International Conference on Trends in Welding Research*, (pp. 14-18). Gatlinburg.

Goldak, J., & Akhlaghi, M. (2005). *Computational Welding Mechanics*. Springer.

Goldak, J., Comlekci, A., & Bibby, M. (1984). A new finite element model for welding heat sources. *Journal of Metallurgical Transactions* , 299-305.

Gordo, J., & Soares, C. G. (1993). Approximate load shortening curves for stiffened plates under uniaxial compression. *Proceedings of the fifth international conference on the integrity of offshore structures* (pp. 189-211). Glasgow: Integrity of Offshore Structures.

Gu, M. (1992). *Computational Weld Analysis for Long Welds*. University of Carleton.

Gu, M., & Goldak, J. A. (1993). Steady State Thermal Analysis of Welds with Filler Metal Addition. *Can Metal. Q* , 49-55.

Gu, M., & Goldak, J. (1994). Steady State Formulation for Stress and Distortion of Welds. 467-474.

Hansbo, P. (1946). the characteristic streamline diffusion method for convection diffusion problems. *Computer Methods in Applied Mechanics & Engineering* , 849-865.

Henwood, C., Bibby, M., Goldak, J., & Watt, D. (1988). Coupled Transient Heat Transfer- Microstructure Weld Computations (Part B). *Acta Metall* .

Hsu, T. R. (1986). *The Finite Element Method in Thermomechanics.* Winchester: Allen & Unwin Inc.

Ion, J. C., Easterling, K. E., & Ashby, M. F. (1984). A Second Report on Diagrams of Microstructures and Hardness for Heat-Affected Zones in Welds,. *Acta Metall* .

Jang, C. D., Ryu, H. S., & Lee, C. H. (2004). Prediction and control of welding deformations in stiffened hull blocks using the inherent strain approach. *Proceeding of the Fourteenth International Offshore and Polar Engineering Conference.*

Jiang, W., Yahiaoui, K., Hall, F. R., & Laoui, T. (2005). Comparison of sequentially and fully coupled genralised plane strain FE modeling of mutipass welding. *Best Practices and Visions of Future.* Malta.

Kumar, R., Coulombe, M., Tchernov, S., Goldak, J. A., Johnson, E., & El-Zein, M. (2008). A Model Equation for the Convection Coefficient for Thermal Analysis of Welding Structures. *8th International Trends in Welding Research.* USA.

Lindgen, L. E. (2001). Finite element modeling and simulation of welding. Part 1: Increased Complexity & Part 2: Improved Material Modelling & Part 3: Efficiency and Integration. *Journal of Thermal Stresses* , 141-192 & 305-334.

Lindgren, L. .., Karlsson, L., & Jonsson, M. (1985). Deformation and stresses in butt welding of large plates. *Numerical Methods in Heat Transfer* , 35-57.

Lindgren, L. E. (1986). Temperature fields in simulation of butt-welding of large plates. *Communications in Applied Numerical Methods* , 155-164.

M.F.Ashby, & K.E.Easterling. (1982). A First Report on Diagrams for Grain Growth in the Welds. *Acta Metall* .

Mahyar, A. (2011). *Computational Weld Mechanics (CWM) Framework for Exploring Parametric Design Space to Manage Weld Optimization.* University of Carleton, Ottawa.

Malvem, L. E. (1969). *Introduction To The Mechanics of a Continuous Medium.* NJ: Prentice-Hall, Inc., Englewood Cliffs.

Martin, J. B. (1975). *Plasticity: Fundamentals and General Results.* The MIT Press, Cambridge, MA.

Mashaie, A. (1990). *Error estimates for finite element solution of elliptic boundary valve problems.* University of Carleton .

McDill, J., J., G., J., O., & Bibby, J. (1987). Isoparametric Quadrilaterals and Hexahedrons for Mesh-Grading Algorithms. *Communications in Applied Numerical Methods* .

Michaleris, P., & Debiccari, A. (1997). Prediction of Welding distortion. *Welding Journal* .

Murthy, Y. V., Raot, G. V., & Iyer, P. K. (1996). Numerical simulation of welding and quenching processes using transit thermal and thermo elasto plastic formulations. *Computers and Structures* .

Myhr, O. R., & Grong, O. (1991). Process Modelling Applied to 6082-T6 Aluminium Weldments II. *Acta metall.*

O., Z., & R., T. (1989). The Finite Element Method. *McGraw-Hill* .

Oddy, A. S. (1987). *Three-dimensional, finite deformation, thermal-elasto-plastic finite element analysis.* University of Carleton.

Okerbolm, N. O. (1958). *The calculations of Deformations of Welded Metal Structures.* London: Her Majesty's Stationery Office.

Olden, E., & Leggat, R. (1999). Modelling of residual stresses at girth welds in pipes. *Recent Advances in Welding Simulation.* London: Institution of Mechanical Engineers.

Pilipenko, A. (2001). *Computer simulation of residual stress and distortion of thick plate in multi-electrode submerged arc welding.* Norway: Norwegian University of Science and Technology.

Radaj, D. (1992). *Heat Effects of Welding: Temperature Field Residual Stress Distortion* .

Ragon, S., Nikolaidis, E. K., R., J. E., & Gurdal, Z. (1999). *Methodology For Optimum Design of AAAV Structures: Final Report.* Department of Navy.

Roberts, S. M., Hunziker, O., Reed, R. C., Dye, D., & Stone, H. J. (1999). Nickel based super alloy welding - model for residual stress, distortion and weldability. *Recent Advances in Welding Simulation.* London: Institution of Mechanical Engineers.

Rosenthal, D. (1946). The theory of moving sources of heat and its application to metal treatments. *Transaction of the American Society of Mechanical Engineers* , 846-849.

Rykalin, N. N. (1947). *Thermal Welding Principles.*

Rykalin, R. R. (1974). Energy source for welding. *Welding in the world* , 1-23.

S P Timoshenko, J. N. (1970). *Theory of elasticity.* New York: McGraw-Hill Book Company.

Simo, J. C. (1998). *Numerical Analysis of Classical Plasticity, Handbook for Numerical Analysis.* Elsevier.

Sorensen, M. B. (1999). *Simulation of Welding Distortions in Ship Section.* Technical University of Denmark.

Szabo, B. (1984). Estimation and Control of Error Based on P Convergence. *International Conference on Accuracy Estimates and Adaptive Refinements in Finite Elements Computations.*

Teng, T. L., Fung, C. P., Chang, P., & Yang, W. C. (2001). Analysis of residual stresses and distortions in T Joint fillet welds. *International Jounal of Pressure Vessels and Piping* , 523-538.

Tither, G. (1992). The development and applications of niobium-containing HSLA steels. *Proc. Processing, Properties and Applications*, (pp. 61-80).

Ueda, Y., & Nakacho, K. (1982). Simplifiying methods for analysis of transient and residual stresses and deformations due to multipass welding.

Wahab, M. A., Alam, M. S., Painter, M. J., & Stafford, P. E. (2006). Experimental and numerical simulation of restraining forces in gas metal arc welded joints. *Welding Research - Supplement to the Welding Journal* .

Wahab, M. A., Painter, M. J., & Davies, M. H. (1998). The prediction of the temperature distribution and weld pool geometry in the gas metal arc welding process. *Journal of Materials Processing Technology* , 233-239.

Wang, S. (2005). *Simulation on the Welding Process of Low-Alloy Steel by FEM.* University of Carleton.

Wastberg, S. B. (2006). COMMITEE II 2-Fatigue and Fracture. *Proceeding of 16th International Ship and Offshore Structures Congress* . Southampton.

Well, A. A. (1952). Heat flow in welding. *Welding Journal* , 263-267.

Younan, M. Y., Will, A. S., & Fanous, F. Z. 3D finite element modeling of the welding process using element birth and element movement techniques. *ASME Pressure Vessel and Piping Conference*, (pp. 165-172). Canada.

Zhao, P. C., Wu, C. S., & Zhang, Y. M. (2004). Numerical simulation of the dynamic characteristics of weld pool geometry with step-changes of welding parameters. *Modeling and Simulation in Materials Science and Engineering* , 765-780.

Appendix:

Appendix 1: Program to Estimate Residual Stresses For Butt Welding

Program to estimate average transverse stresses in a linear butt weld

ORIGIN ≡ 1

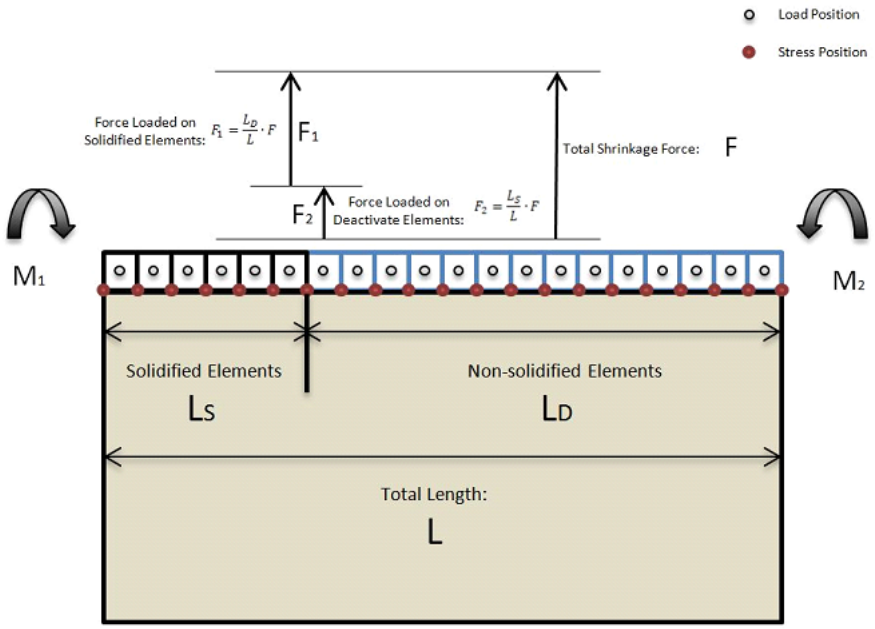

BASIC PARAMETER INPUT:

$Nx := 101$ $L := 0.5 \cdot m$ $t := 6 \cdot mm$ $\sigma_y := 355 \cdot MPa$ $E := 205 \cdot \frac{kN}{mm^2}$

This routine calculates the transverse equilibrium stresses.

$lp := 1 .. Nx$ $\delta L := \frac{L}{Nx - 1}$ $x_{lp} := (lp - 1) \cdot \delta L$ $ls := 1 .. Nx - 1$ $F := \frac{\sigma_y}{2} \cdot t \cdot \delta L$

During the welding and cooling process, the material are always yield and the material properties are temperature dependent, so the yield stress of the material is changing with temperature. And the temperature at the same position are different at different time step, the load can be afforded by the material is the difference of the yield stress between the time steps, in other word, the load can be afforded is the rate of the yield stress to temperature. In linear theotry, once the material is yield, it can't afford any more loads, which means no matter how big the loading is, the maximum load can be applied in the material is the load which can be afforded. The following diagrams show the yield stress and load can be applied at different temperatures. It can be seen that at very high temperature, both yield stress and the load can be applied have very small value close to 0 until the temperature smaller than 1293 K. The yield stress is increasing as the temperature from 1293K to 293K; but the load can be applied is increasing from 1293K to 793K, and decreasing from 793K to 293K.

The most important thing is the load can be afford is the load applied, which is the rate of material yield stress to the temperature!

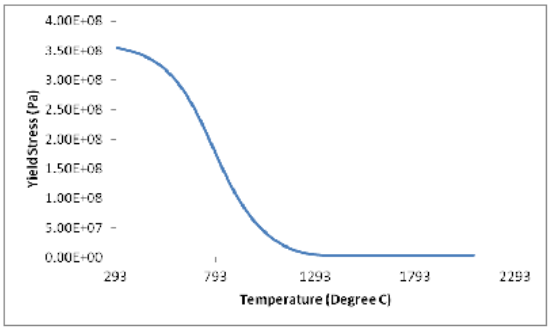

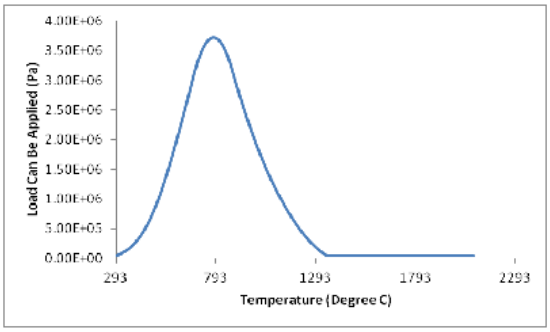

Due to the welds deposit in the welding seam gradually, the element death and birth technique was used in FE method to present that; but in this simple method, the author seperates the welding seam into solidified elements and non-solidified elements at the length position where temperature is 793K, where is the maximum value of load can be applied, from the diagram above, it can be seen that both parts can afford loads, therefore the load applied at each time step will be assigned at both parts in some proportion. From the following diagram, it can be seen that when the welding started, the loads are mainly applied on the solidified element part, but at the end of welding process and the whole cooling process, the loads are mainly applied on the non-solidified element part. And at the dividing line, the load applied is not the maximum value, due to the load applied is the rate of material yield stress to the temperature, which is calculated by integrate the yield stress with the temperature, the value is also depend on the temperature difference between load steps. If the temperature change evenly at each load step, the peak value should appear at the the dividing line, but the temperature changing is uneven, especially at the area near the welding pool. So the peak value of load applied located ahead of the dividing line due to where the temperature change between load step is large.

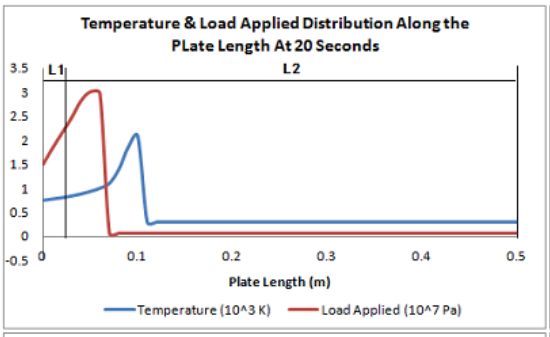

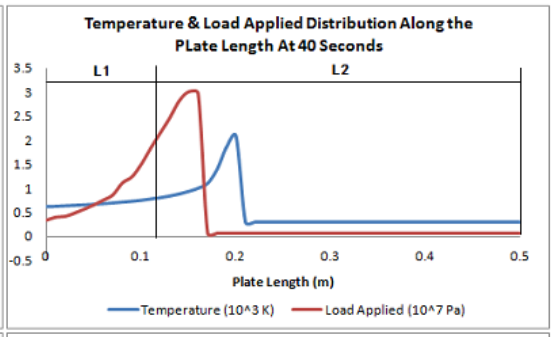

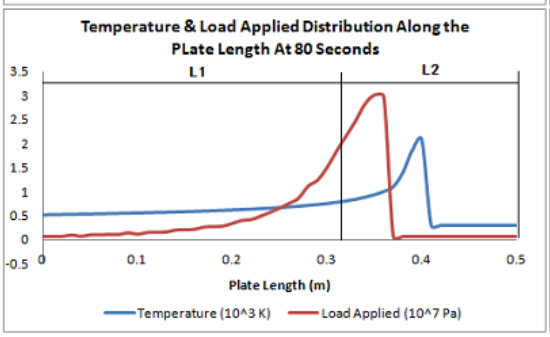

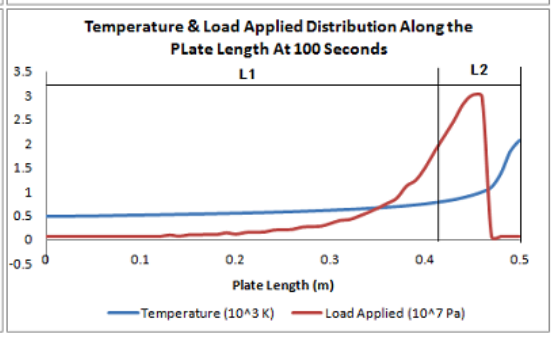

The value of load applied is depend on the temperature at each position, but this simple method don't calculate the temperature during the welding process as keeping its simplicity, in order to present the load distribution at each time step, the author made an assumption for the proportion of the shrinkage force applied on the solidified element part and non-solidified element part: the shrinkage F1, which applied on the solidified element part; and the shrinkage force F2 is also evenly applied on the non-solidified element part. F1 and F2 have the following relationship:

F = F1 + F2

F1 = F * [L2 / (L1+L2)]

F2 = F * [L1 / (L1+L2)]

Stress_Database :=

c ← "Define Matrixes"

for $ix \in 1 .. Nx$

$\sigma 1_{ix,ix} \leftarrow 0$

$\sigma 2_{ix,ix} \leftarrow 0$

$\sigma_{ix,ix} \leftarrow 0$

$stress_{ix,ix} \leftarrow 0$

$stress\_modify1_{ix,ix} \leftarrow 0$

$shear\_force_{ix,ix} \leftarrow 0$

$stress\_modify2_{ix,ix} \leftarrow 0$

c ← "Calculate the residual stresses at each length position and each load step"

for $load\_step \in 2 .. Nx - 1$

c ← "Calculate the stress increment at each length position for solidified elements"

for $position \in 1 .. load\_step$

$$F_1 \leftarrow \frac{Nx - load\_step}{Nx - 1} \cdot F$$

$$M_1 \leftarrow F_1 \cdot \left(x_{load\_step} - \frac{\delta L}{2} - \frac{x_{load\_step}}{2} \right)$$

c ← "My/I is now calculated on the solidified weld material"

$$\sigma 1_{position,load\_step} \leftarrow \frac{M_1 \cdot \left(x_{position} - \frac{x_{load\_step}}{2} \right)}{t \cdot \frac{\left(x_{load\_step} \right)^3}{12}}$$

c ← "Calculate the stress increment at each length position for non-solidified elements"

for $position \in load\_step .. Nx$

$$F_2 \leftarrow \frac{load\_step - 1}{Nx - 1} F$$

$$M_2 \leftarrow F_2 \cdot \left(x_{load\_step} + \frac{\delta L}{2} - \frac{L + x_{load\_step}}{2} \right)$$

c ← "My/I is now calculated on the non-solidified weld material"

$$\sigma 2_{position,load\_step} \leftarrow \frac{M_2 \cdot \left(x_{position} - \frac{L + x_{load\_step}}{2}\right)}{t \cdot \frac{\left[L - \left(x_{load\_step}\right)\right]^3}{12}}$$

c ← "Calculate the stress increment at each length position at each load step for total length"

c ← "Calculate the total stress accumulated at each length position at each load step"

c ← "Modify the plastic effect for compressive total stress accumulated at each load step"

for position ∈ 1 .. Nx

$$\sigma_{position,load\_step} \leftarrow \sigma 1_{position,load\_step} + \sigma 2_{position,load\_step}$$

$$stress_{position,load\_step} \leftarrow \sum_{nn=1}^{load\_step} \sigma_{position,nn}$$

$$stress\_modify1_{position,load\_step} \leftarrow if\left[\left|stress_{(position,load\_step)}\right| \geq -\sigma_y, stress_{position,load\_step}, -\sigma_y\right]$$

c ← "Calculate the shear force and bending moment at each length position at each load step"

for position ∈ 2 .. load_step

$$shear\_force_{1,load\_step} \leftarrow 0$$

$$shear\_force_{position,load\_step} \leftarrow shear\_force_{position-1,load\_step} \cdots + \frac{1}{2} \cdot \delta L \cdot \left(\begin{matrix} stress\_modify1_{position,load\_step} \cdots \\ + stress\_modify1_{position-1,load\_step} \end{matrix}\right) \cdot t$$

$$bending\_moment_{1,load\_step} \leftarrow 0$$

$$bending\_moment_{position,load\_step} \leftarrow bending\_moment_{position-1,load\_step} \cdots + \frac{1}{2} \cdot \delta L \cdot \left(\begin{matrix} shear\_force_{position,load\_step} \cdots \\ + shear\_force_{position-1,load\_step} \end{matrix}\right)$$

c ← "Modify the tensile stress accumulated at each load step for equilibrium"

for position ∈ 1 .. load_step + 1

$$stress\_modify2_{position,load\_step} \leftarrow stress\_modify1_{position,load\_step} \cdots + \left[\begin{matrix} \frac{(-shear\_force)_{load\_step,load\_step}}{x_{load\_step} \cdot t} \cdots \\ + \frac{(-bending\_moment)_{load\_step,load\_step}}{\frac{\left(x_{load\_step} + 0.000001m\right)^3}{12}} \end{matrix}\right]$$

$$\begin{pmatrix} \sigma \\ stress \\ stress\_modify2 \end{pmatrix}$$

Final Result Modification for Equilibrium and Visualization:

$$Q_{ini} := \left| \begin{array}{l} a_1 \leftarrow 0 \\ \text{for } st \in 2..Nx \\ \quad a_{st} \leftarrow a_{st-1} + \frac{1}{2}\cdot\left(x_{st} - x_{st-1}\right)\cdot\left[\left(\text{Stress\_Database}_3\right)_{st,100} + \left(\text{Stress\_Database}_3\right)_{st-1,100}\right]\cdot t \\ a \end{array} \right.$$

$$Mx_{ini} := \left| \begin{array}{l} a_1 \leftarrow 0 \\ \text{for } st \in 2..Nx \\ \quad a_{st} \leftarrow a_{st-1} + \frac{1}{2}\cdot\left(x_{st} - x_{st-1}\right)\cdot\left(Q_{ini_{st}} + Q_{ini_{st-1}}\right) \\ a \end{array} \right.$$

$$\text{Residual\_Stress}_{lp} := \left(\text{Stress\_Database}_3\right)_{lp,100} - \frac{Q_{ini_{Nx}}}{L\cdot t} - \frac{Mx_{ini_{Nx}}}{\left(\frac{L^3}{12}\right)}$$

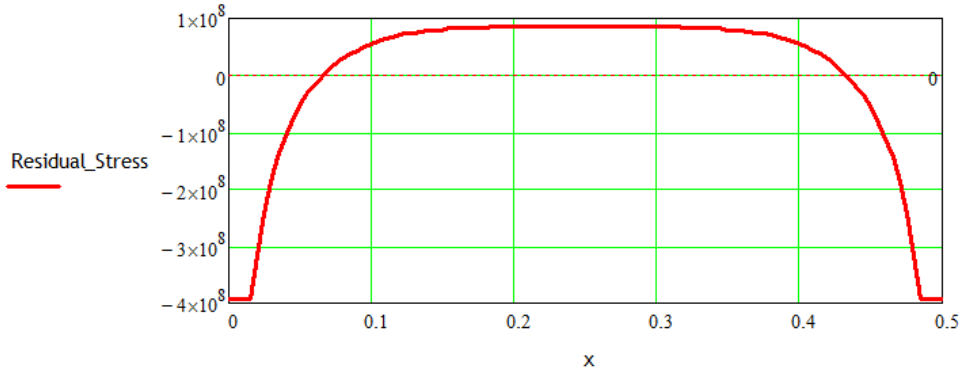

Final Result Verification:

$$Q := \left| \begin{array}{l} a_1 \leftarrow 0 \\ \text{for } st \in 2..Nx \\ \quad a_{st} \leftarrow a_{st-1} + \frac{1}{2}\cdot\left(x_{st} - x_{st-1}\right)\cdot\left(\text{Residual\_Stress}_{st} + \text{Residual\_Stress}_{st-1}\right)\cdot t \\ a \end{array} \right.$$

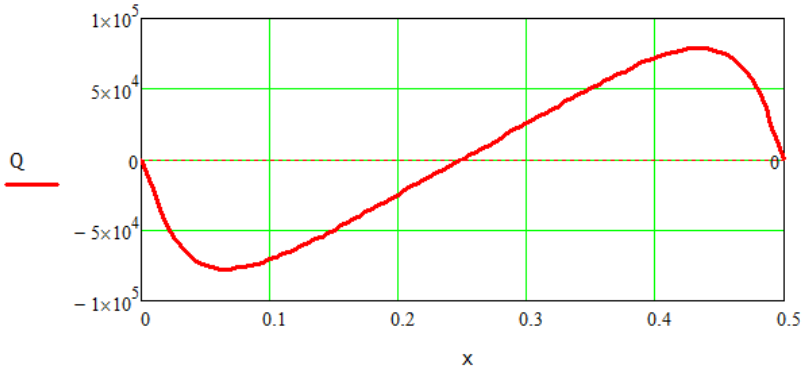

$$Mx := \left| \begin{array}{l} a_1 \leftarrow 0 \\ \text{for } st \in 2 .. Nx \\ \quad a_{st} \leftarrow a_{st-1} + \frac{1}{2} \cdot \left(x_{st} - x_{st-1}\right) \cdot \left(Q_{st} + Q_{st-1}\right) \\ a \end{array} \right.$$

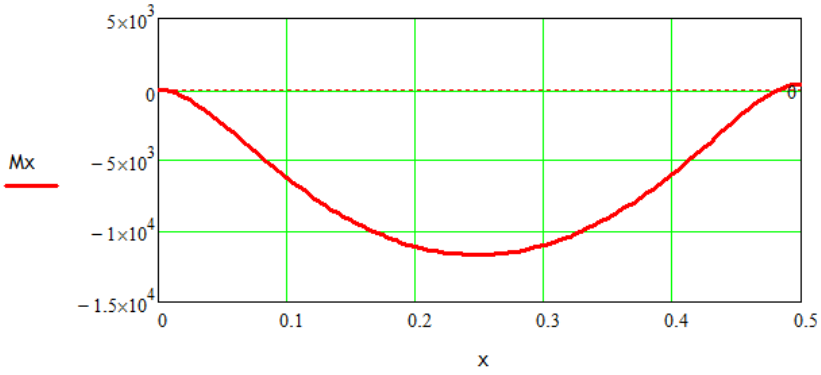

Results Visualization:

Load_Step_Number := 20

$$Stress\_Increment_{lp} := \left(Stress\_Database_1\right)_{lp,\, Load\_Step\_Number}$$

$$Stress\_Accumulated_{lp} := \left(Stress\_Database_2\right)_{lp,\, Load\_Step\_Number}$$

$$Final\_Stress_{lp} := \left(Stress\_Database_3\right)_{lp,\, Load\_Step\_Number}$$

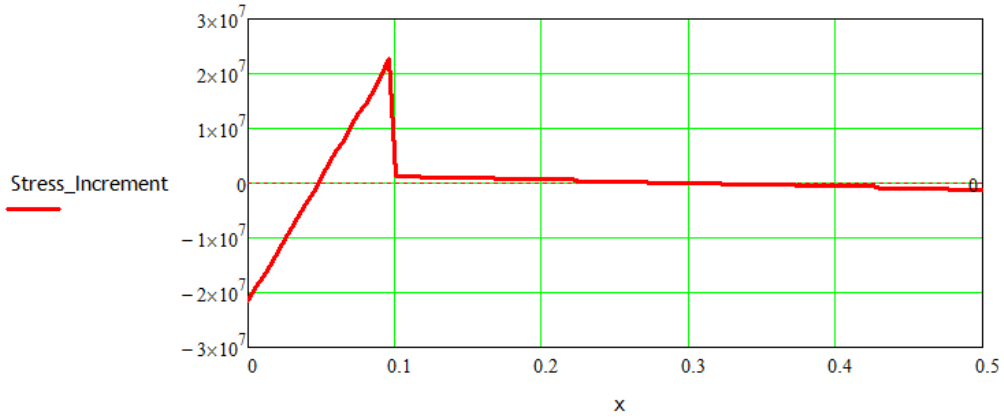
Stress_Increment
3×10^7
2×10^7
1×10^7
0
−1×10^7
−2×10^7
−3×10^7
0
0.1
0.2
0.3
0.4
0.5
x

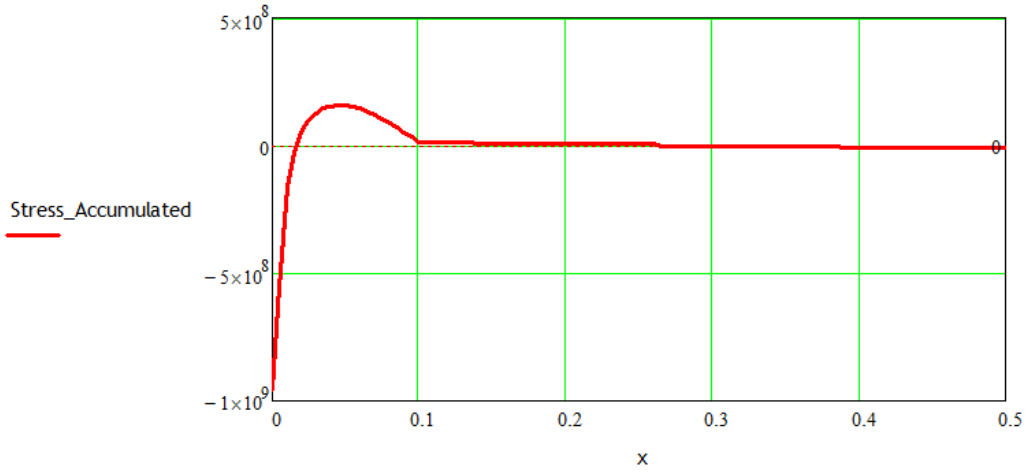
Stress_Accumulated
5×10^8
0
−5×10^8
−1×10^9
0
0.1
0.2
0.3
0.4
0.5
x

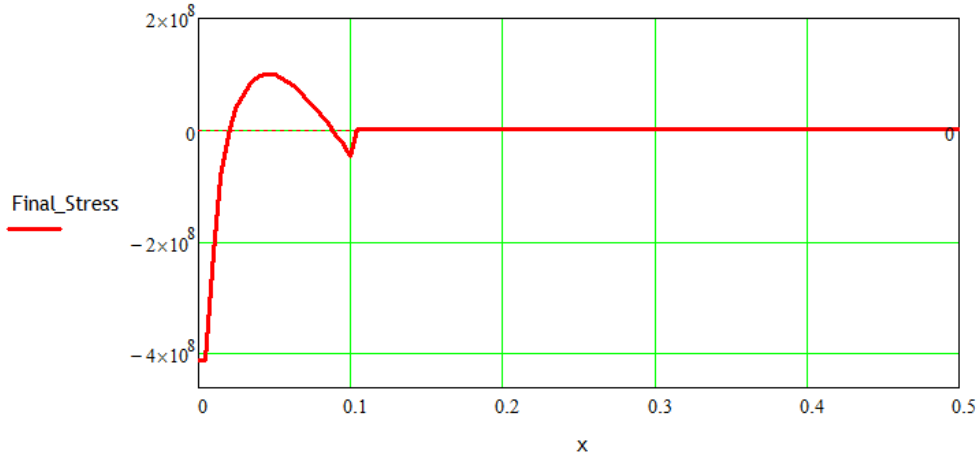
Final_Stress
2×10^8
0
−2×10^8
−4×10^8
0
0.1
0.2
0.3
0.4
0.5
x

Length_Position := 10

$$Stress\_Increment\_History_{ls} := \left(Stress\_Database_1\right)_{Length\_Position,\,ls}$$

$$Stress\_Accumulated\_History_{ls} := \left(Stress\_Database_2\right)_{Length\_Position,\,ls}$$

$$Final\_Stress\_History_{ls} := \left(Stress\_Database_3\right)_{Length\_Position,\,ls}$$

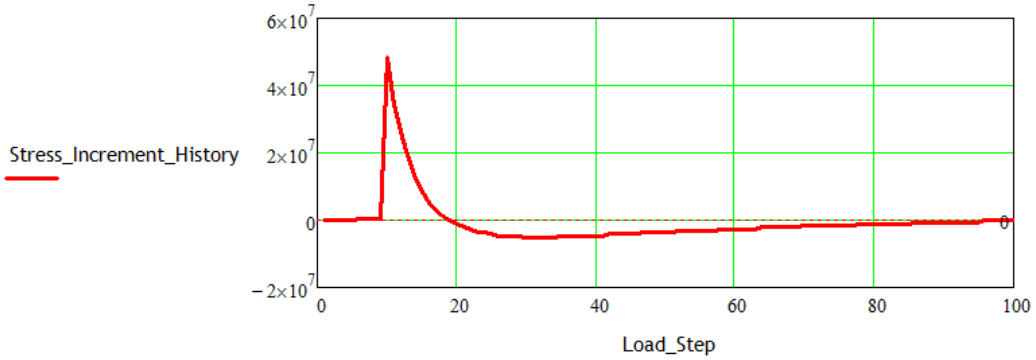

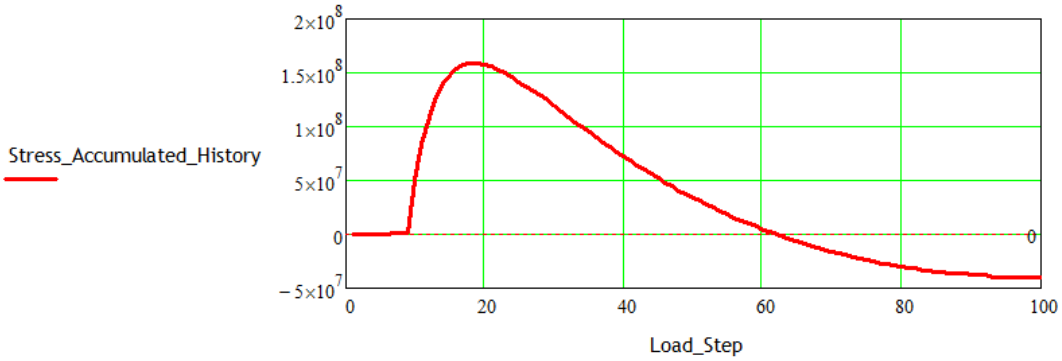

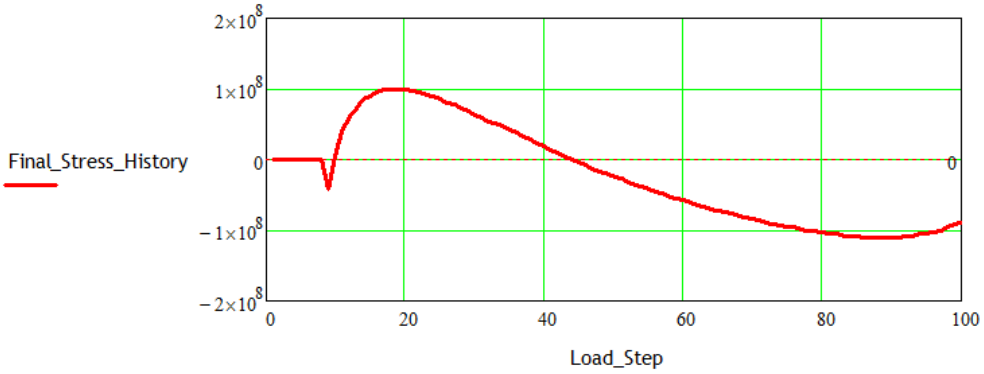

Program to estimate average longitudinal stresses in a linear butt weld

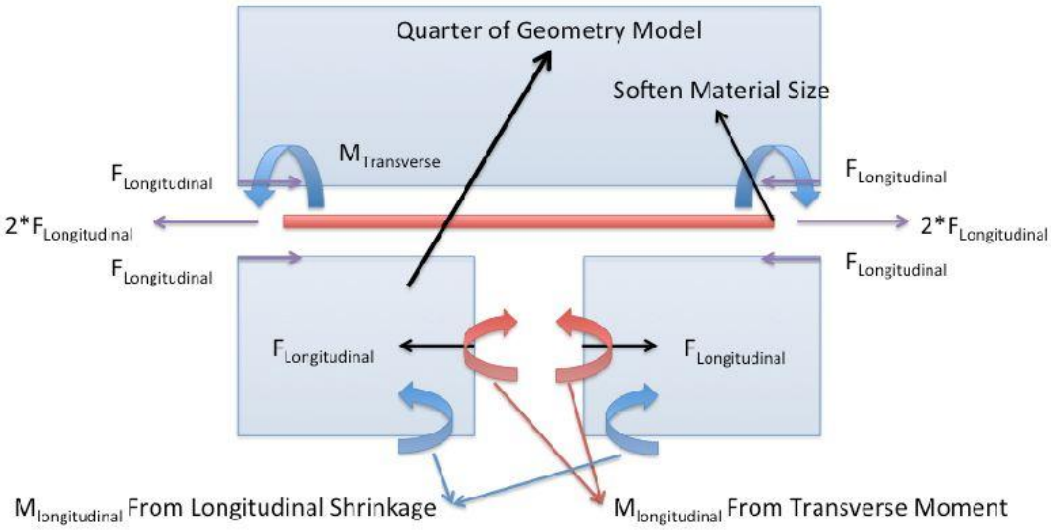

The longitudinal residual stress has two sources, one is the longitudinal shrinkage and the other one is the transverse bending moment. And a simple program to estimate longitudinal residual stresses in a linear butt weld based on force and moment equilibrium has been derived in the following part, which is able to calculate the longitudinal residual stress distribution in different longitudinal positions and the cross section investigated here is located at the mid-length. In this simple method, the size of soften material in transverse direction (Variable 'weld') need to be specified as where the material is yielding. After that, only a quarter of the geometry model was considered due to the model is symmetrical with both transverse and longitudinal directions (see the figure above).

It can be seen that $F_{longitudinal}$ comes from the longitudinal shrinkage and the value is half of the shrinkage force. In order to achieve force equilibrium, there need be a force somewhere to balance $F_{longitudinal}$, if there is tack welding before the welding process, the balance force would act at the tacks; but if there is no tack welding, which means the balance will act on the cross section that investigated evenly. According to , whether the term of F/A exists depends on whether there is tack welding. In this case, the author sets there is no tack welding.

Longitudinal Position Investigated: $LPI := 51$

It can be seen that longitudinal force comes from the longitudinal shrinkage and the value is half of the shrinkage force. In order to achieve force equilibrium, there need be a force somewhere to balance longitudinal force, if there is tack welding before the welding process, the balance force would act at the tacks; but if there is no tack welding, which means the balance will act on the cross section that investigated evenly.

Tack = 1, there is no tack welding

Tack = 0, there is tack welding

$Tack := 1$

$Breadth := 0.25m \qquad weld := 0.028m \qquad B := \begin{cases} Breadth - \frac{weld}{2} & \text{if } Tack = 1 \\ Breadth & \text{otherwise} \end{cases}$

$Ny := 101 \qquad \delta B := \frac{B}{Ny - 1} \qquad CL := 0.25m \qquad iy := 1 .. Ny \qquad y_{iy} := (iy - 1) \cdot \delta B$

This routine calculates the longitudinal shrinkage induced the longitudinal equilibrium stresses.

$$LStress_{LS} := \left| \begin{array}{l} LForce \leftarrow -\sigma_y \cdot t \cdot weld \\ LMoment \leftarrow \dfrac{\dfrac{LForce}{2} \cdot \left(\dfrac{B}{2}\right) \cdot B^3}{\left(x_{LPI}\right)^3 + B^3} \\ \text{for} \quad ixcw \in 1 .. Ny \\ \quad \left| \begin{array}{l} c \leftarrow \text{"P/A +My/I is now calculated on the cross section at length position LPI"} \\ \sigma_{ixcw} \leftarrow \dfrac{LForce}{B \cdot t \cdot 2} \cdot Tack + \dfrac{LMoment \cdot \left(\left(y_{ixcw} - \dfrac{B}{2}\right)\right)}{t \cdot \dfrac{(B)^3}{12}} \end{array} \right. \\ \sigma \end{array} \right.$$

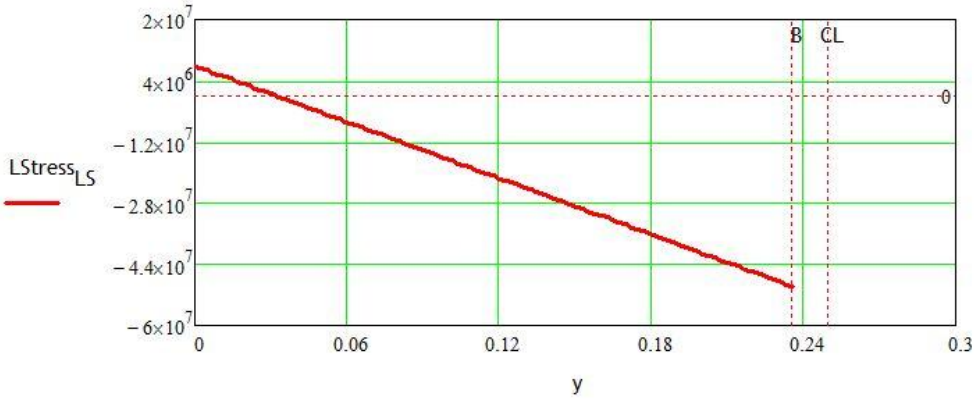

This routine calculates the transverse moment induced the longitudinal equilibrium stresses.

$$LStress_{TS} := \left| \begin{array}{l} LMoment \leftarrow -Mx_{LPI} \\ \text{for} \quad ixcw \in 1 .. Ny \\ \quad \left| \begin{array}{l} c \leftarrow \text{"My/I is now calculated on the cross section at length position LPI"} \\ \sigma_{ixcw} \leftarrow \dfrac{LMoment \cdot \left(\left(y_{ixcw} - \dfrac{B}{2}\right)\right)}{t \cdot \dfrac{(B)^3}{12}} \end{array} \right. \\ \sigma \end{array} \right.$$

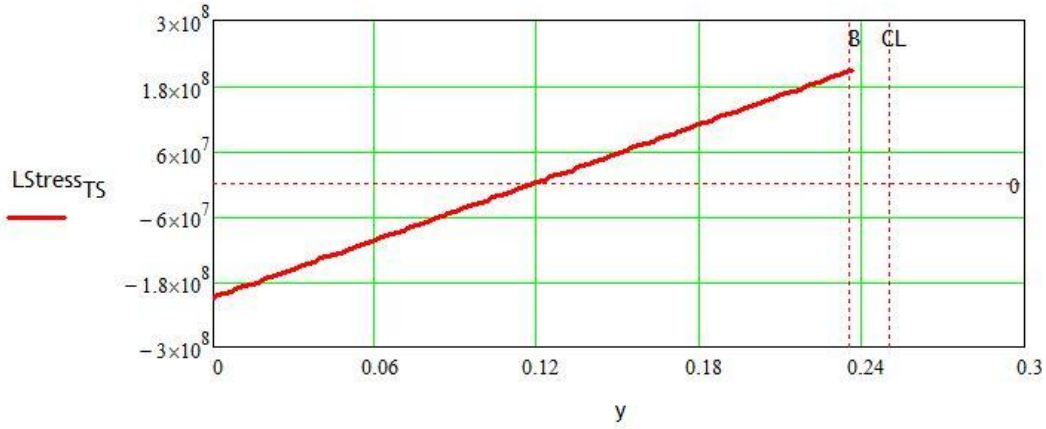

$LStress := LStress_{TS} + LStress_{LS}$

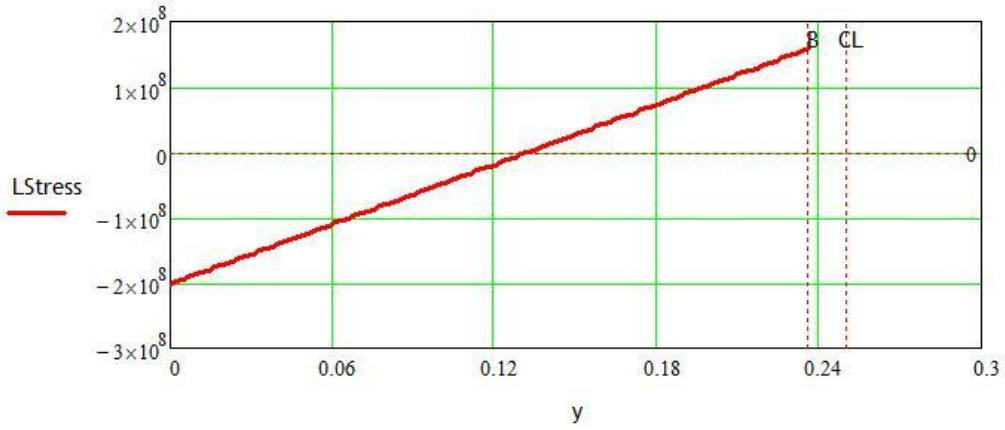

$$LStress_{Ny+1} := \begin{cases} \sigma_y & \text{if } Tack = 1 \\ LStress_{Ny} & \text{otherwise} \end{cases} \qquad LStress_{Ny+2} := \begin{cases} \sigma_y & \text{if } Tack = 1 \\ LStress_{Ny} & \text{otherwise} \end{cases}$$

$y_{Ny+1} := B + 0.0001m \qquad y_{Ny+2} := Breadth$

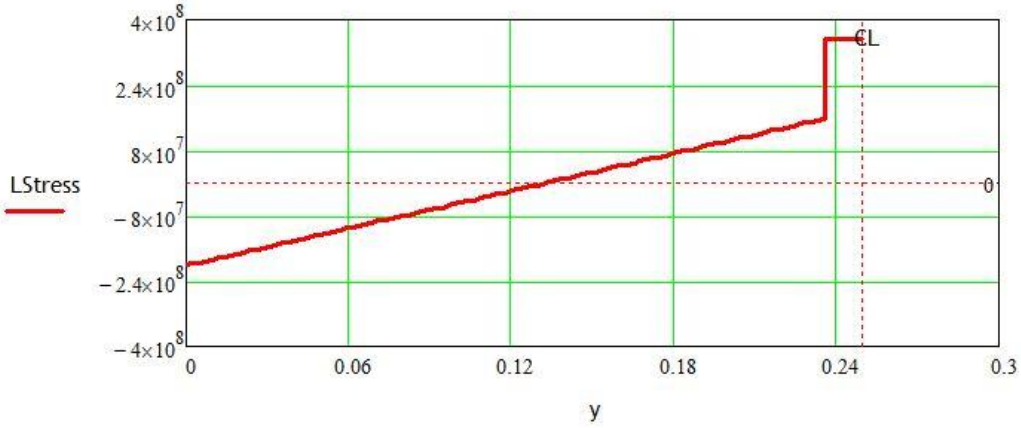

Result

Verification:

$$Q_{yini} := \left| \begin{array}{l} a_1 \leftarrow 0 \\ \text{for } st \in 2..Ny+2 \\ \quad a_{st} \leftarrow a_{st-1} + \frac{1}{2}\cdot\left(y_{st} - y_{st-1}\right)\cdot\left(LStress_{st} + LStress_{st-1}\right)\cdot t \\ a \end{array} \right.$$

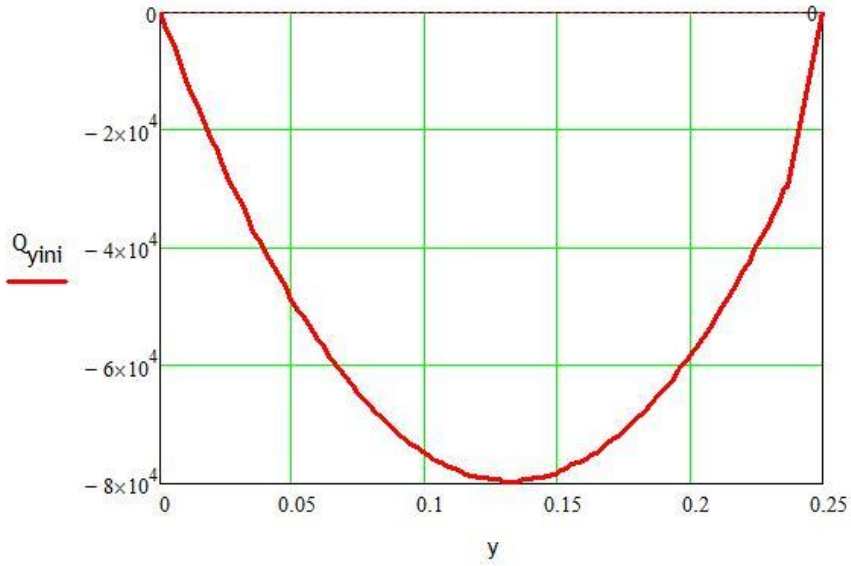

Appendix 2: Residual Stress Distribution of Parametric Study

A2.1 Cut-Off-Temperature Effects

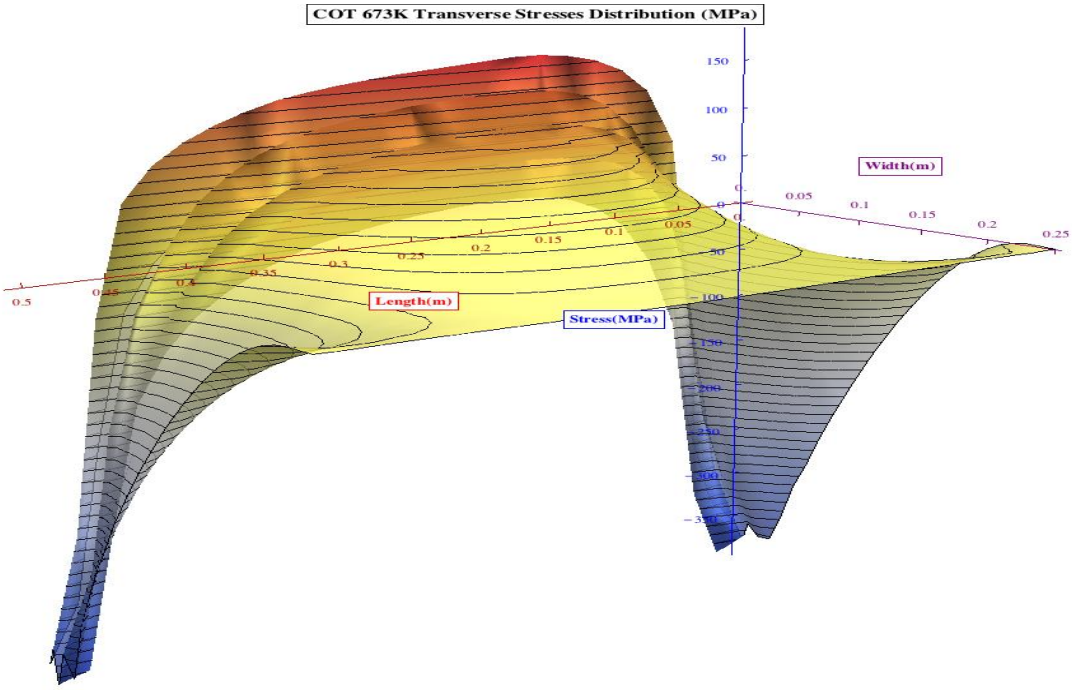

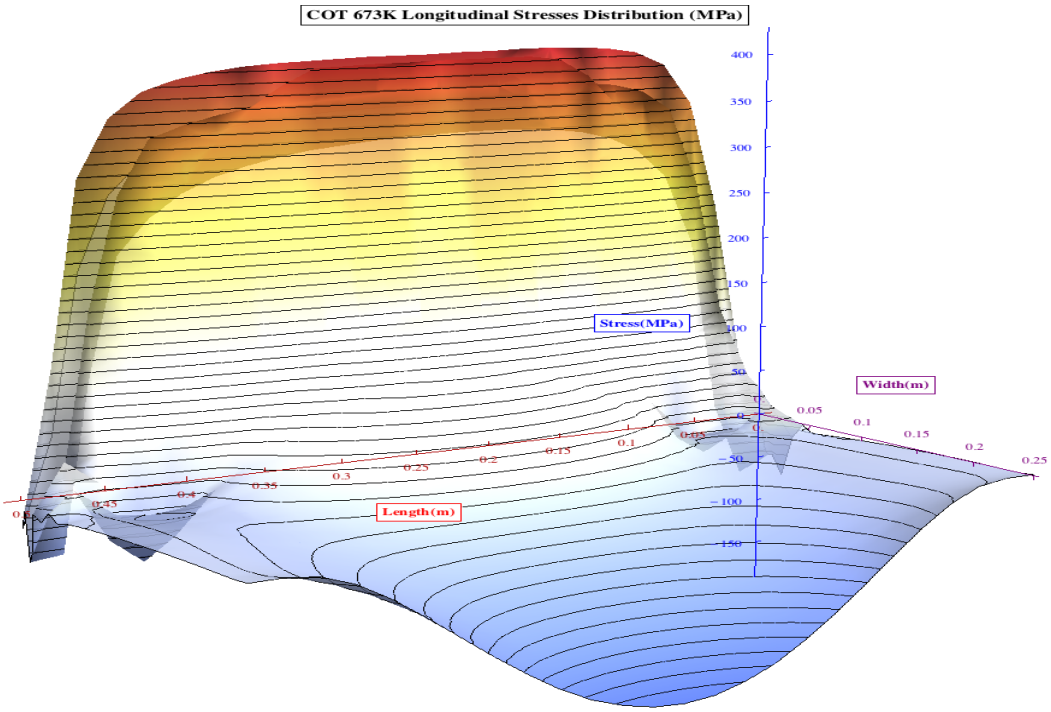

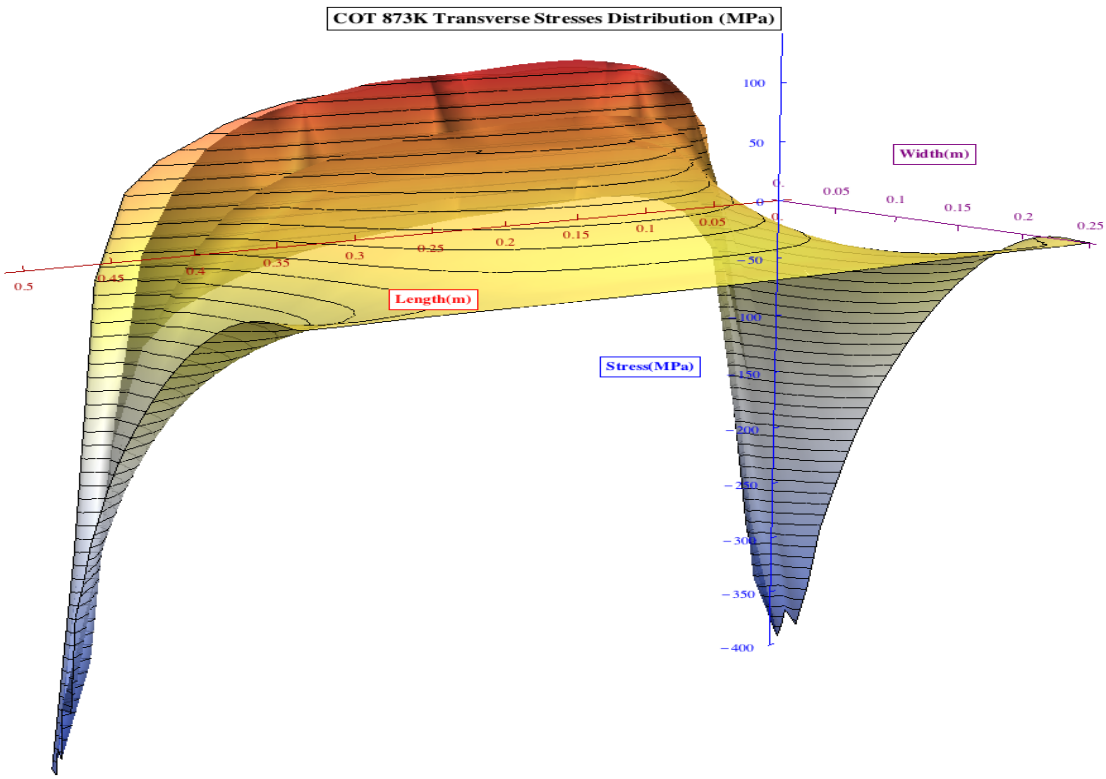
COT 873K Transverse Stresses Distribution (MPa)
Width(m)
Length(m)
Stress(MPa)

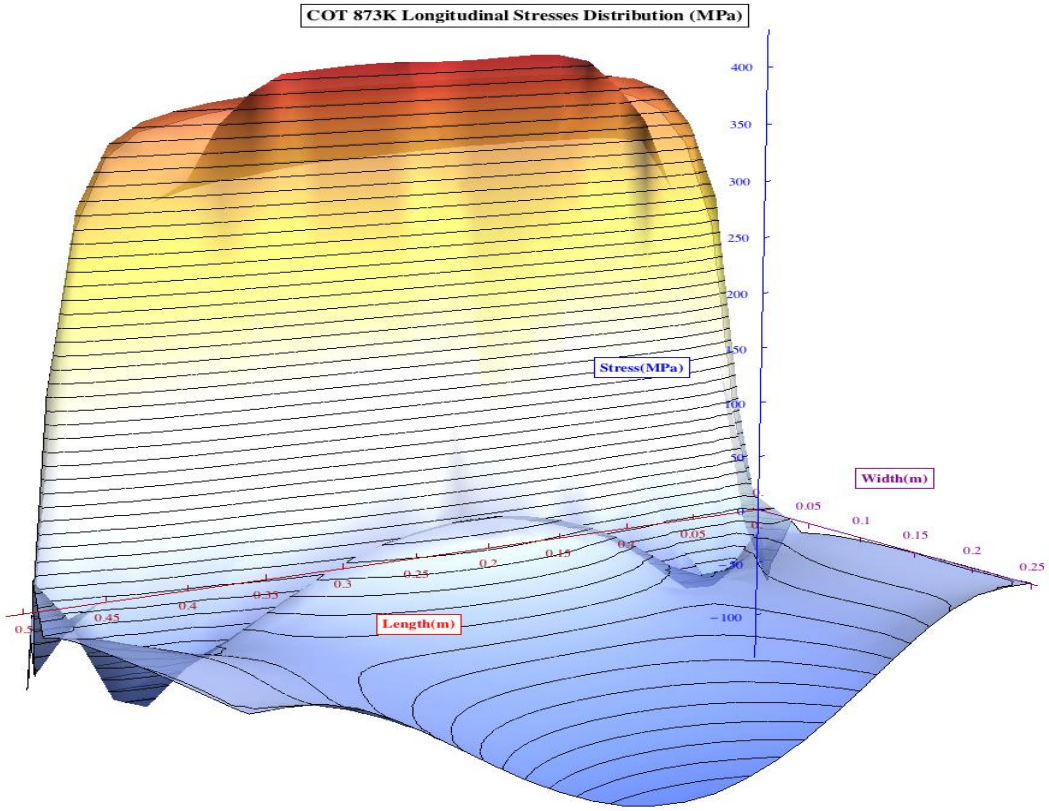
COT 873K Longitudinal Stresses Distribution (MPa)
Stress(MPa)
Width(m)
Length(m)

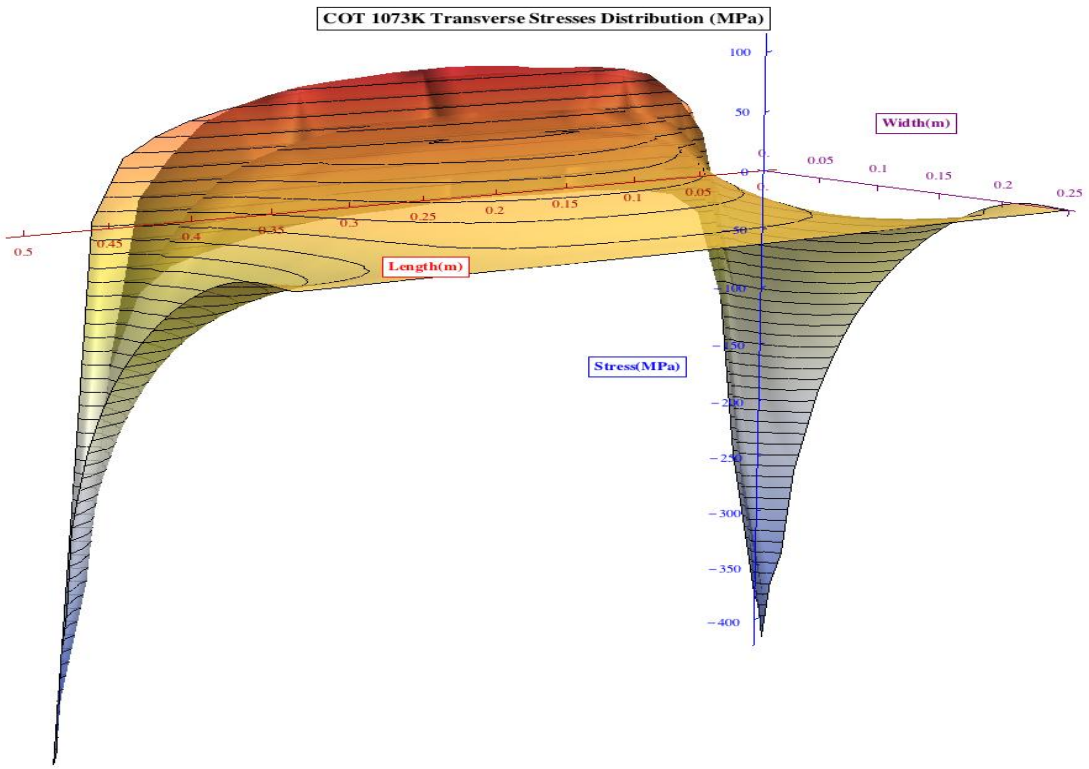
COT 1073K Transverse Stresses Distribution (MPa)
Width(m)
Length(m)
Stress(MPa)

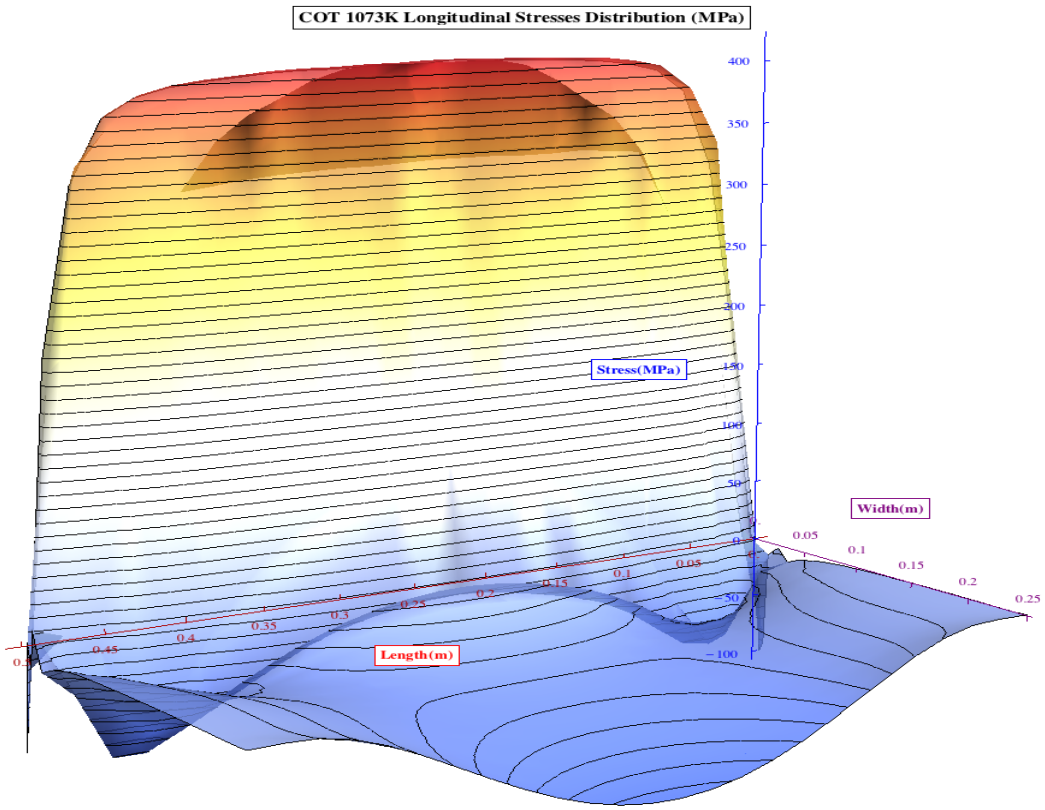
COT 1073K Longitudinal Stresses Distribution (MPa)
Stress(MPa)
Width(m)
Length(m)

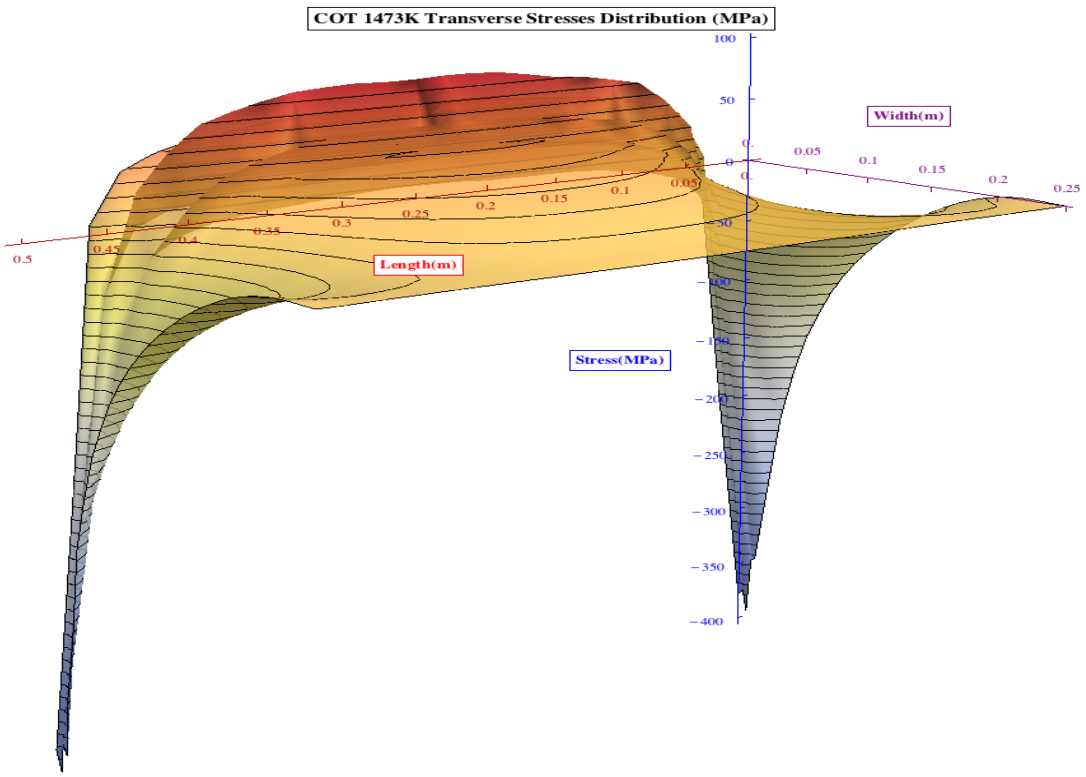
COT 1473K Transverse Stresses Distribution (MPa)
Width(m)
Length(m)
Stress(MPa)

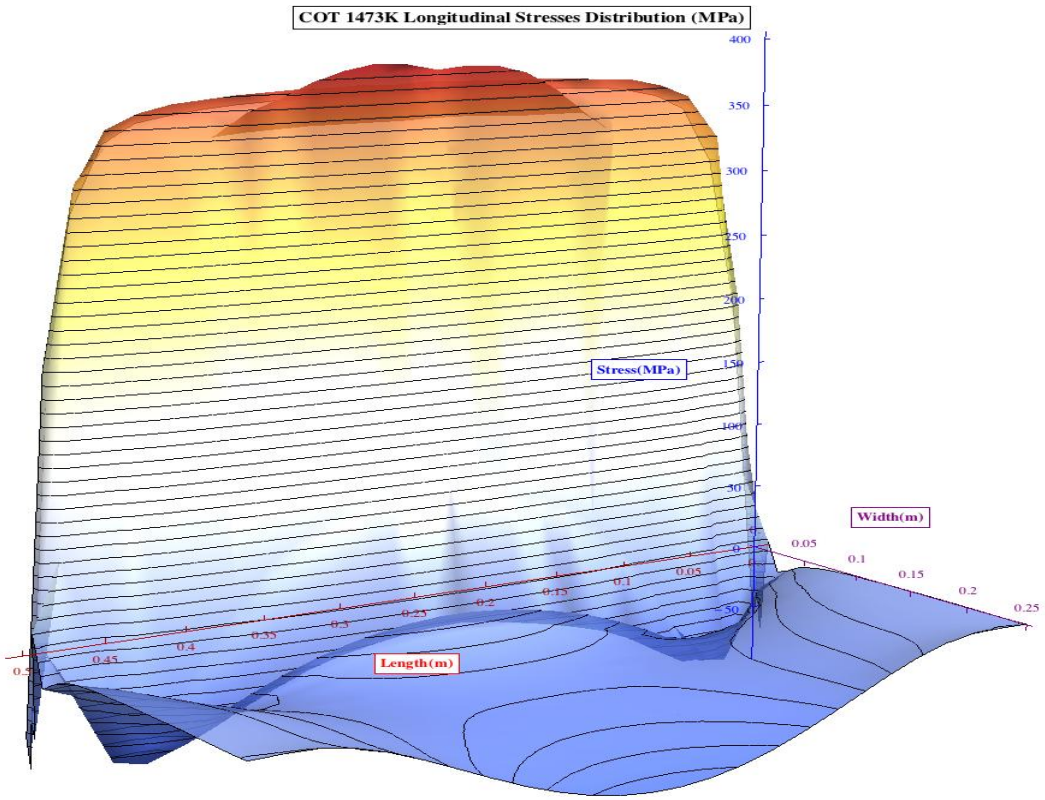
COT 1473K Longitudinal Stresses Distribution (MPa)
Stress(MPa)
Width(m)
Length(m)

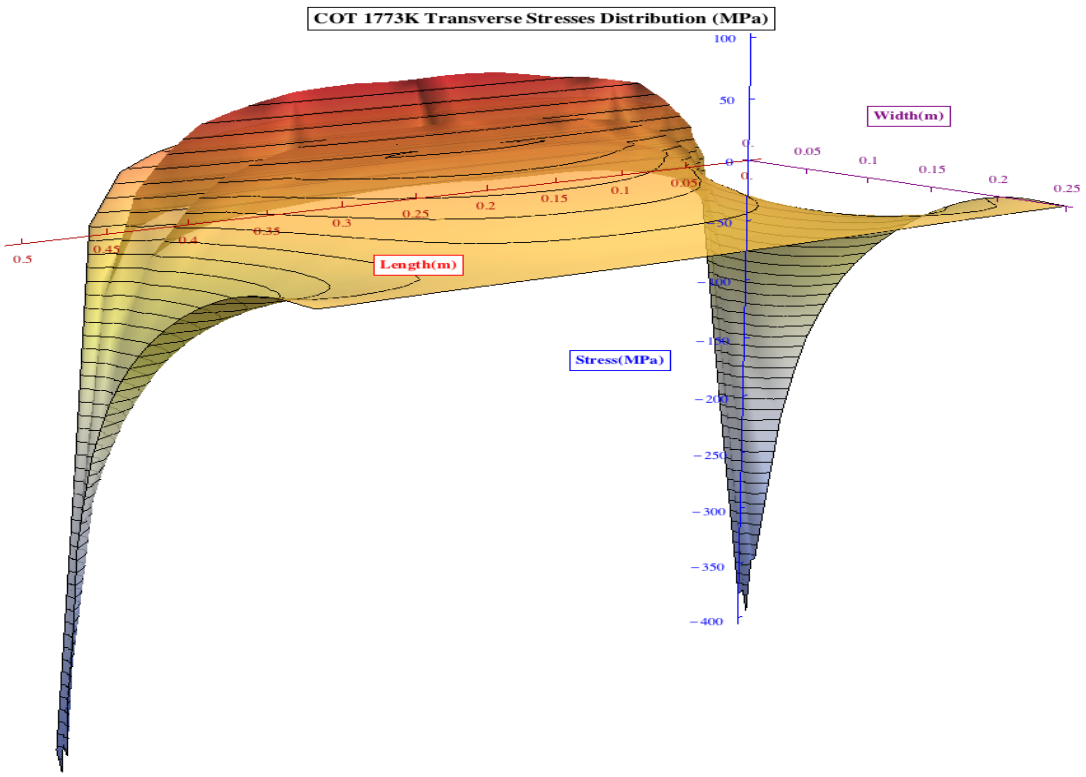
COT 1773K Transverse Stresses Distribution (MPa)
Width(m)
Length(m)
Stress(MPa)

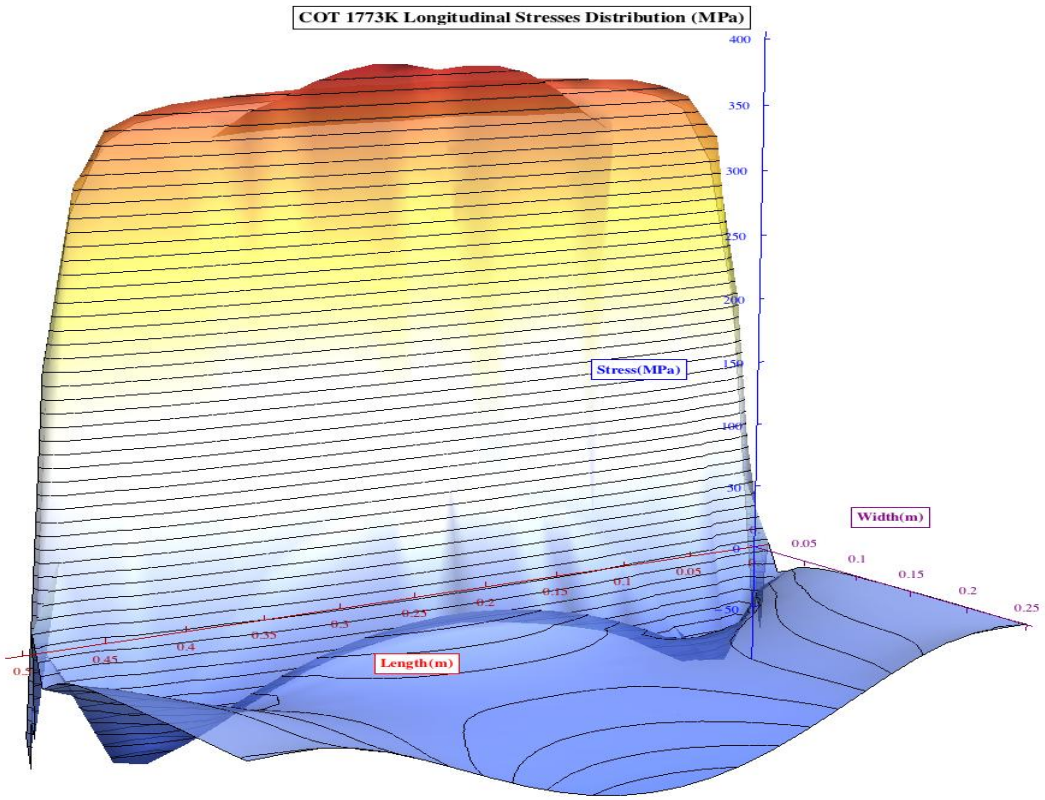
COT 1773K Longitudinal Stresses Distribution (MPa)
Stress(MPa)
Width(m)
Length(m)

A2.2 Welding Power Input Effects

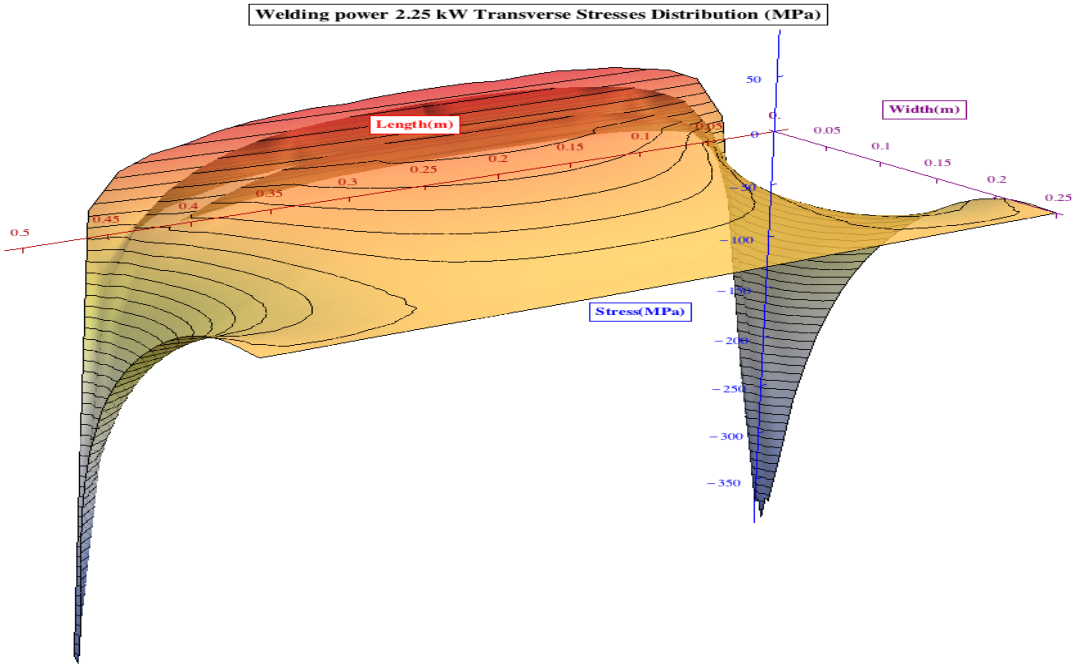

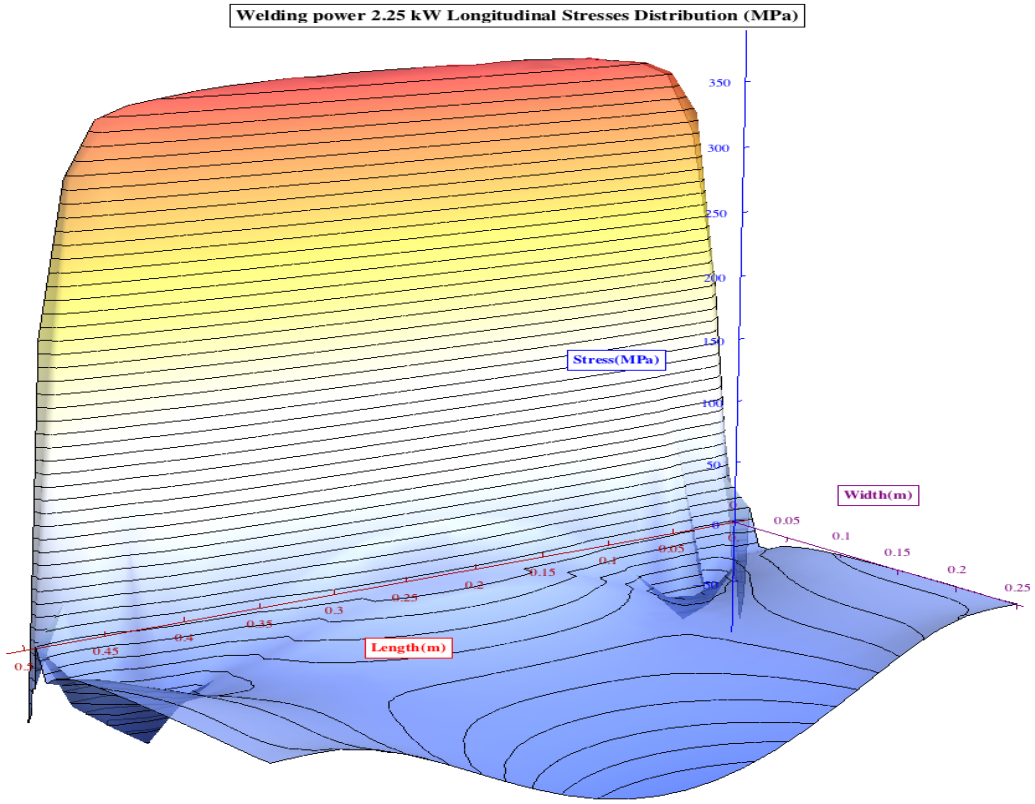

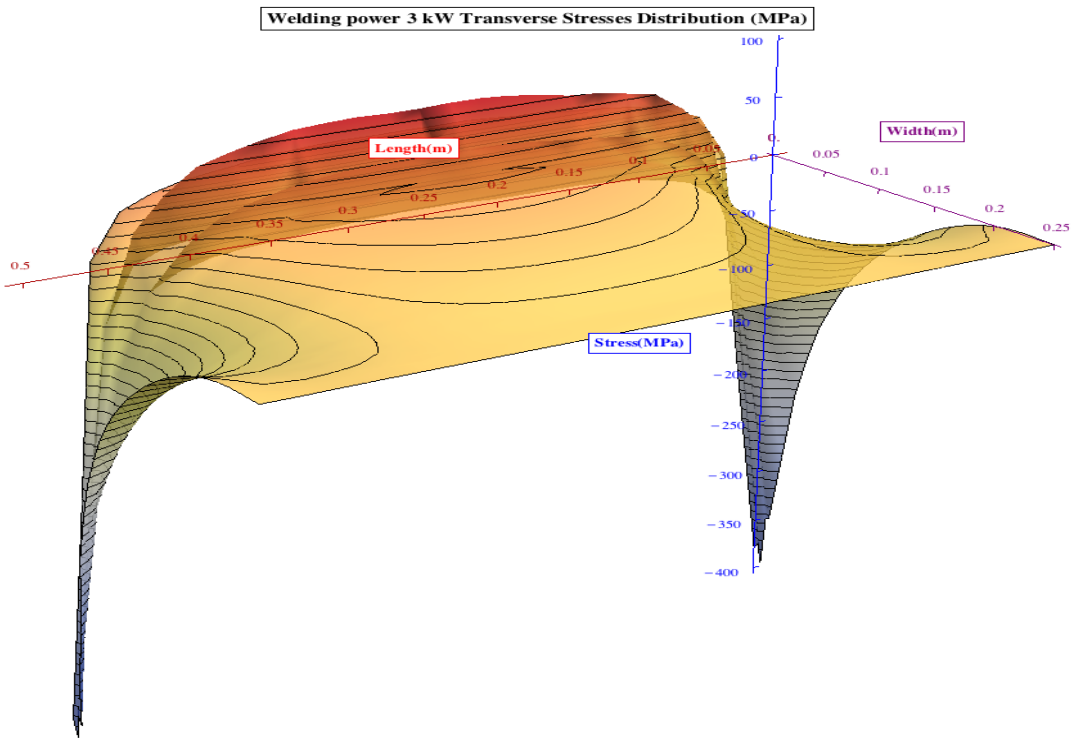
Welding power 3 kW Transverse Stresses Distribution (MPa)
Length(m)
Width(m)
Stress(MPa)

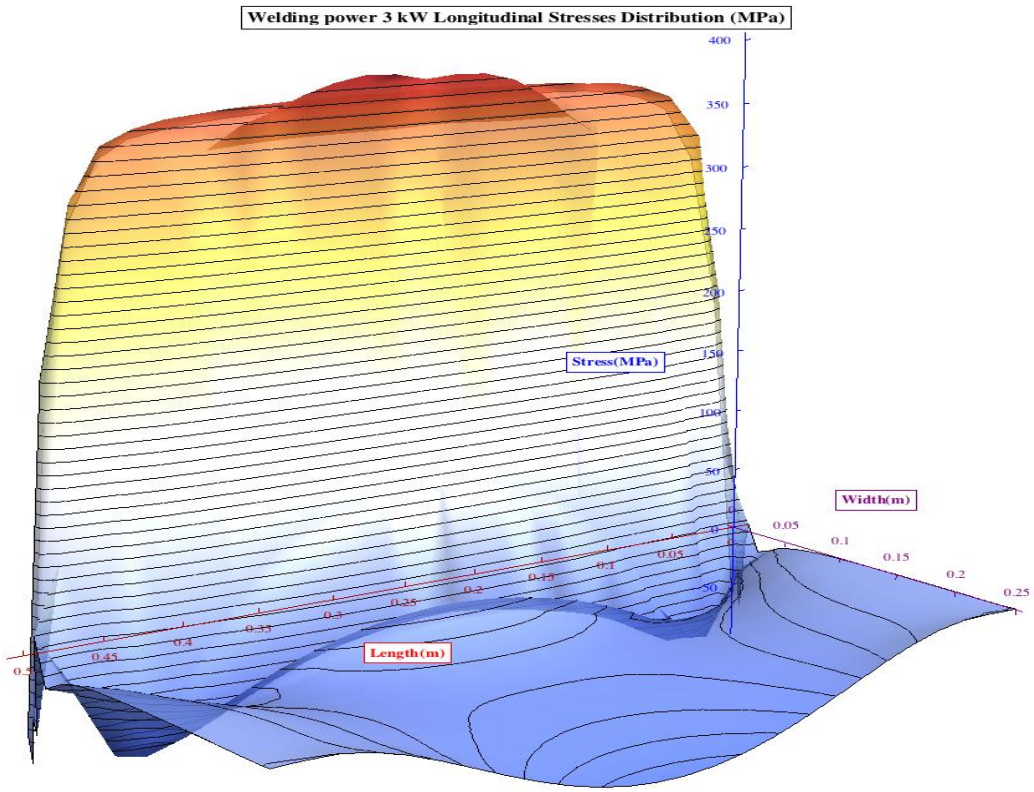
Welding power 3 kW Longitudinal Stresses Distribution (MPa)
Stress(MPa)
Width(m)
Length(m)

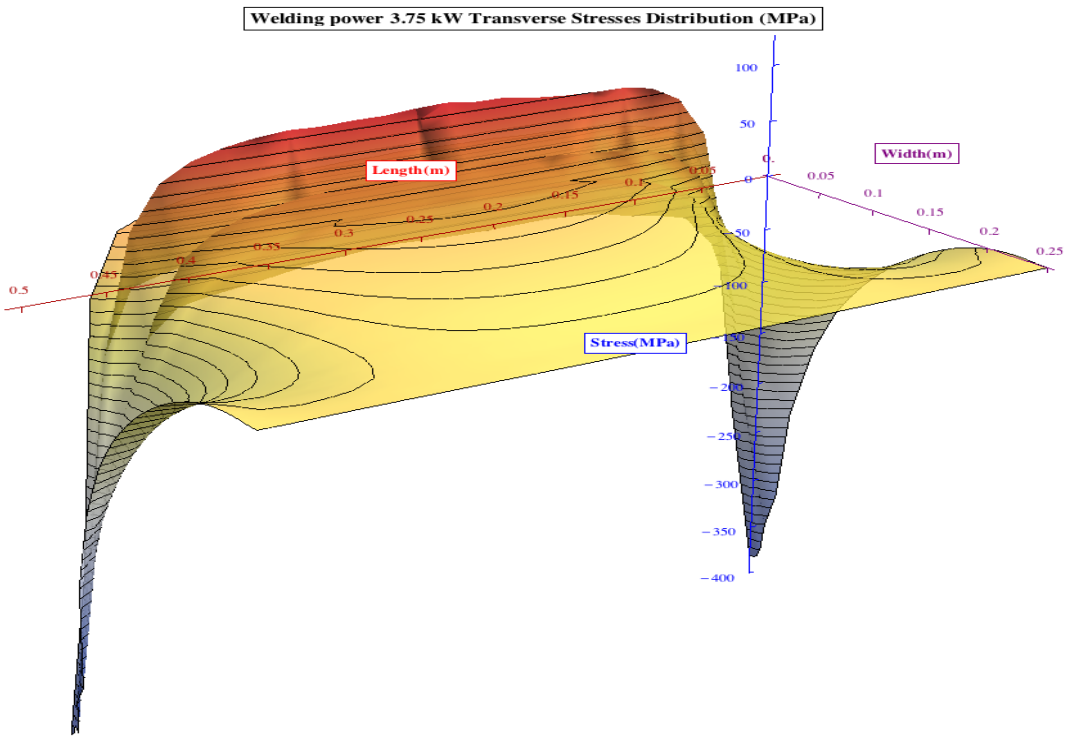
Welding power 3.75 kW Transverse Stresses Distribution (MPa)
Length(m)
Width(m)
Stress(MPa)

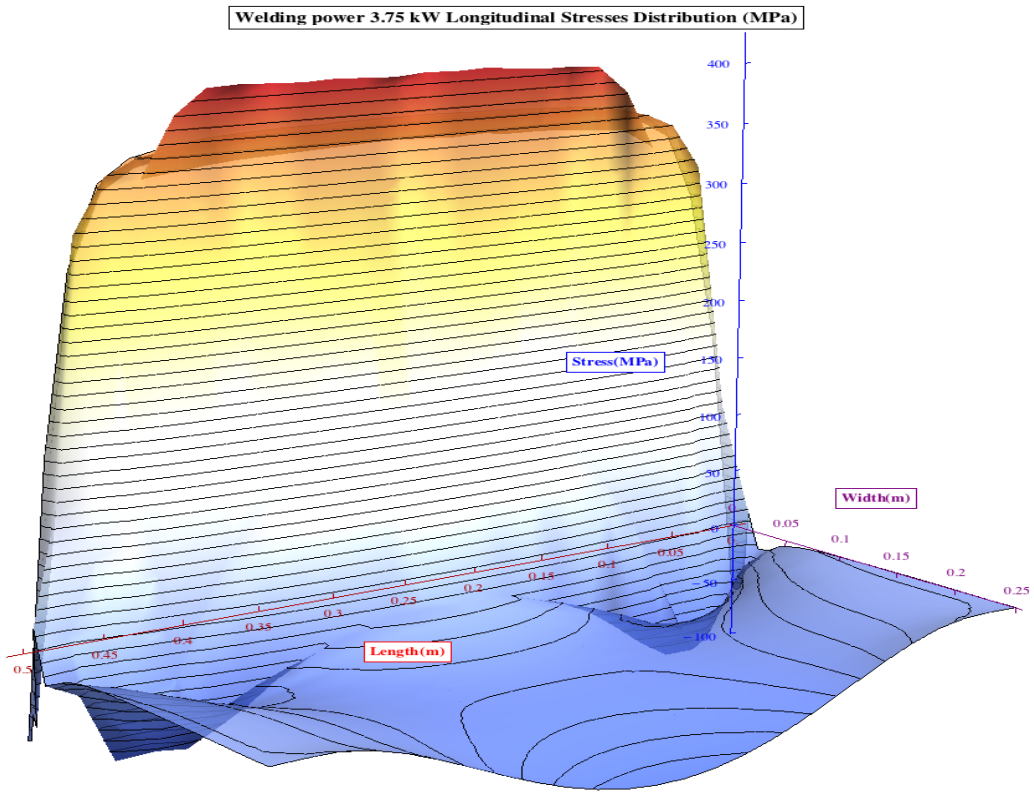
Welding power 3.75 kW Longitudinal Stresses Distribution (MPa)
Stress(MPa)
Width(m)
Length(m)

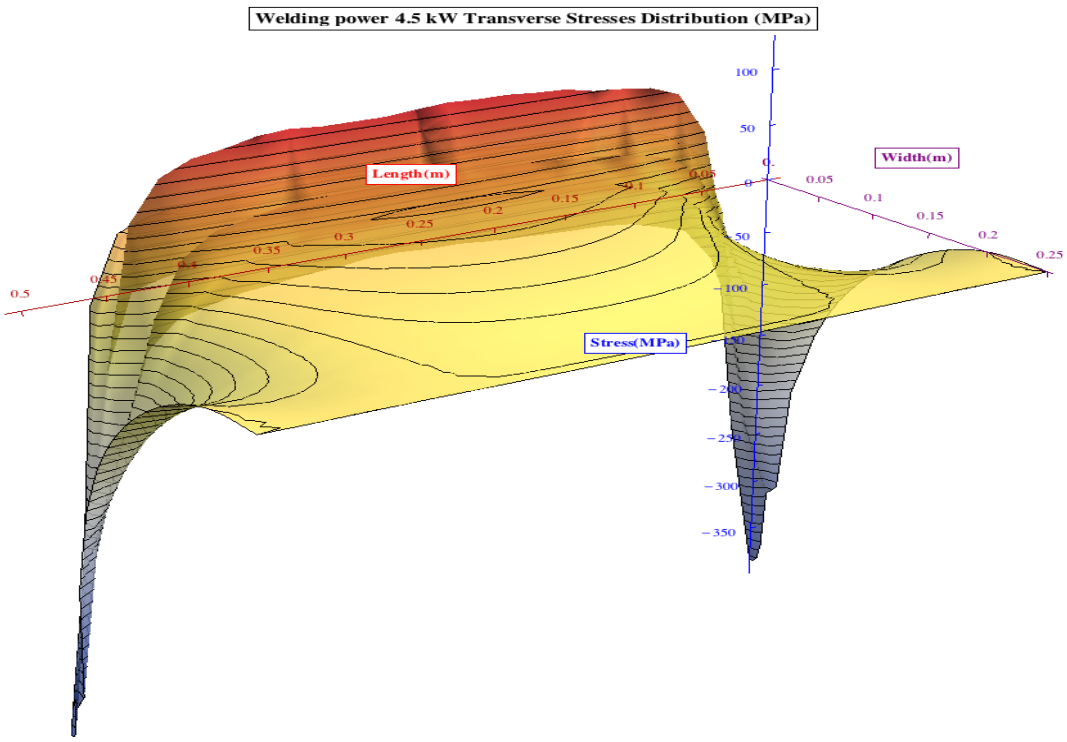
Welding power 4.5 kW Transverse Stresses Distribution (MPa)
Length(m)
Width(m)
Stress(MPa)

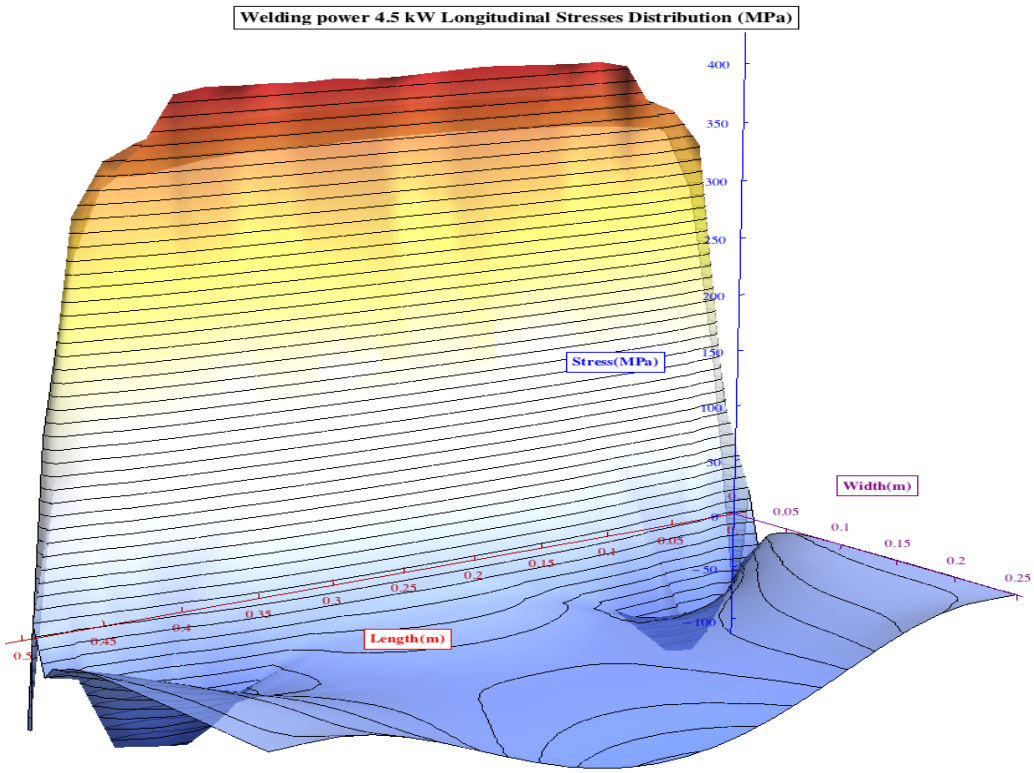
Welding power 4.5 kW Longitudinal Stresses Distribution (MPa)
Stress(MPa)
Width(m)
Length(m)

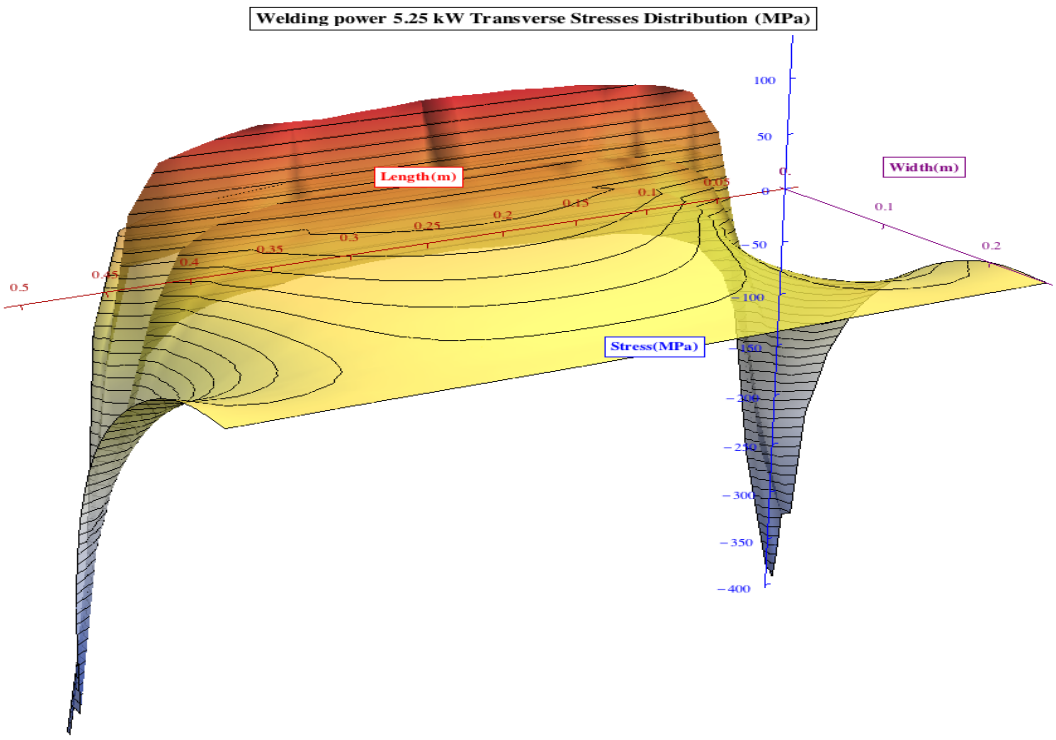
Welding power 5.25 kW Transverse Stresses Distribution (MPa)
Length(m)
Width(m)
Stress(MPa)

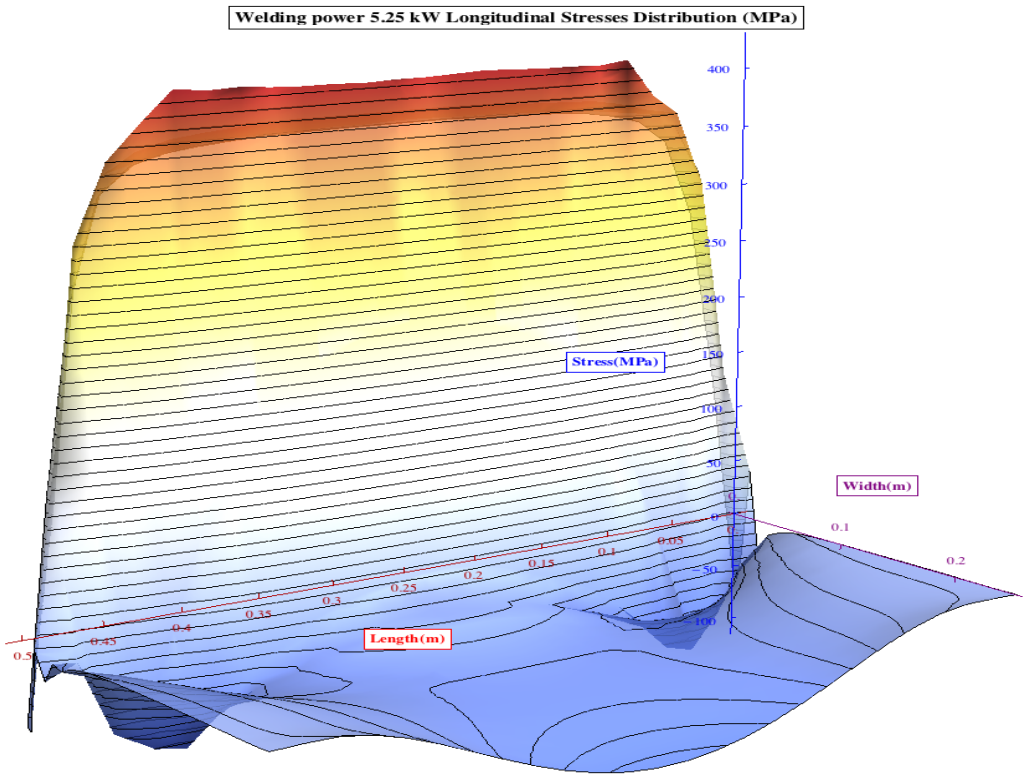
Welding power 5.25 kW Longitudinal Stresses Distribution (MPa)
Stress(MPa)
Width(m)
Length(m)

A2.3 Welding Velocity Effects

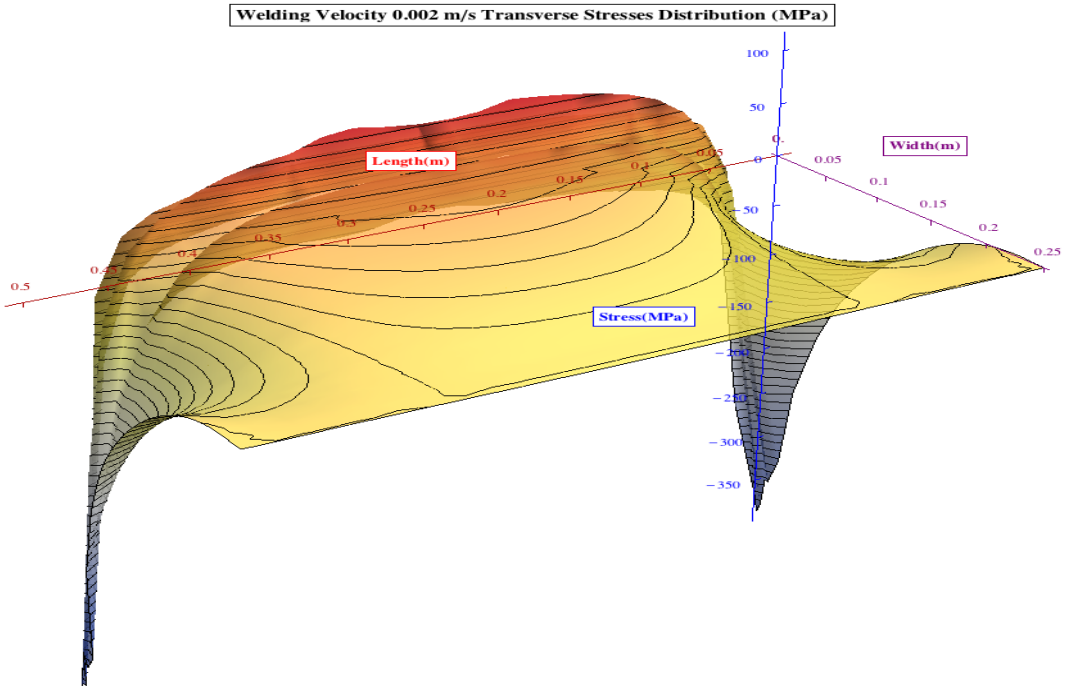

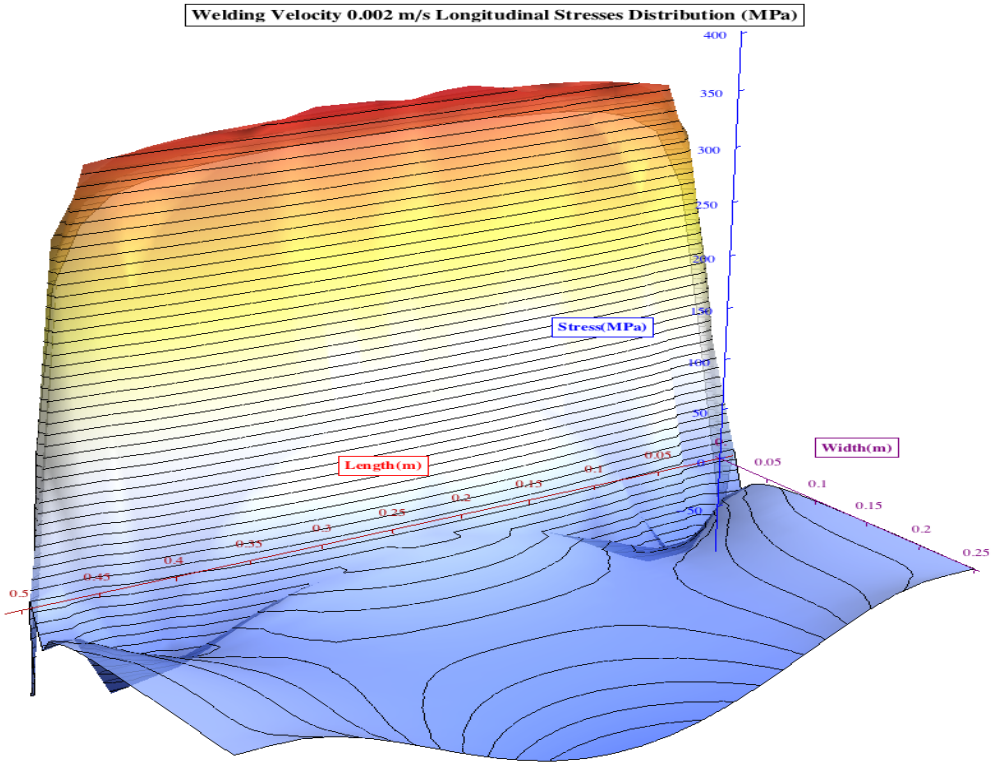

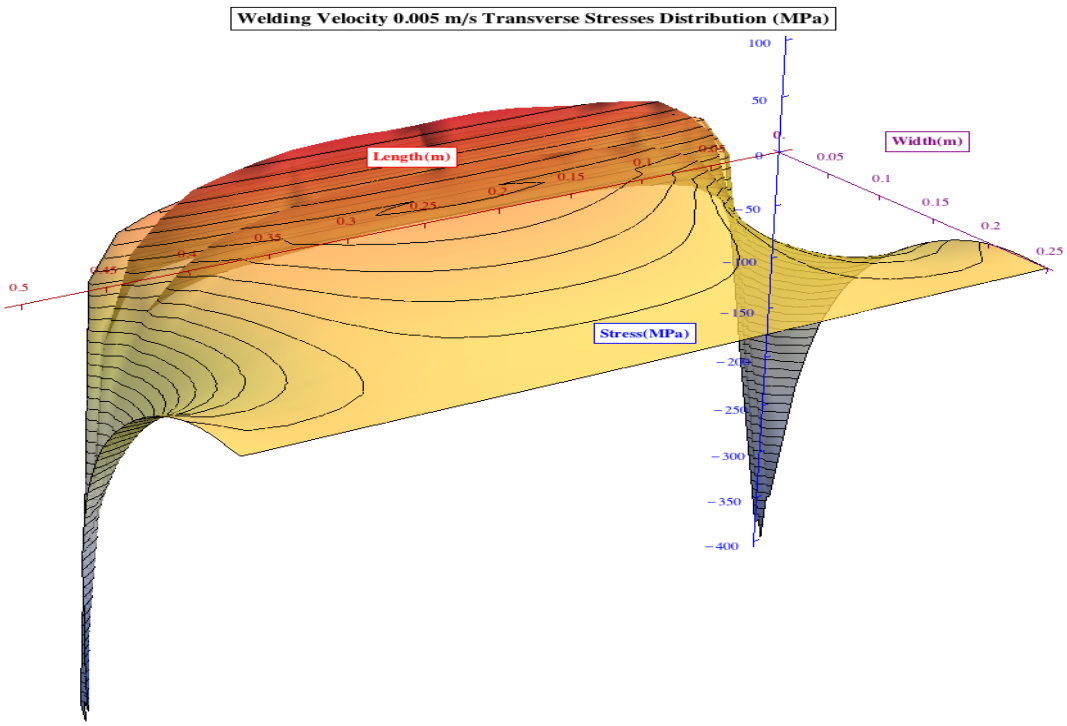
Welding Velocity 0.005 m/s Transverse Stresses Distribution (MPa)
Length(m)
Width(m)
Stress(MPa)

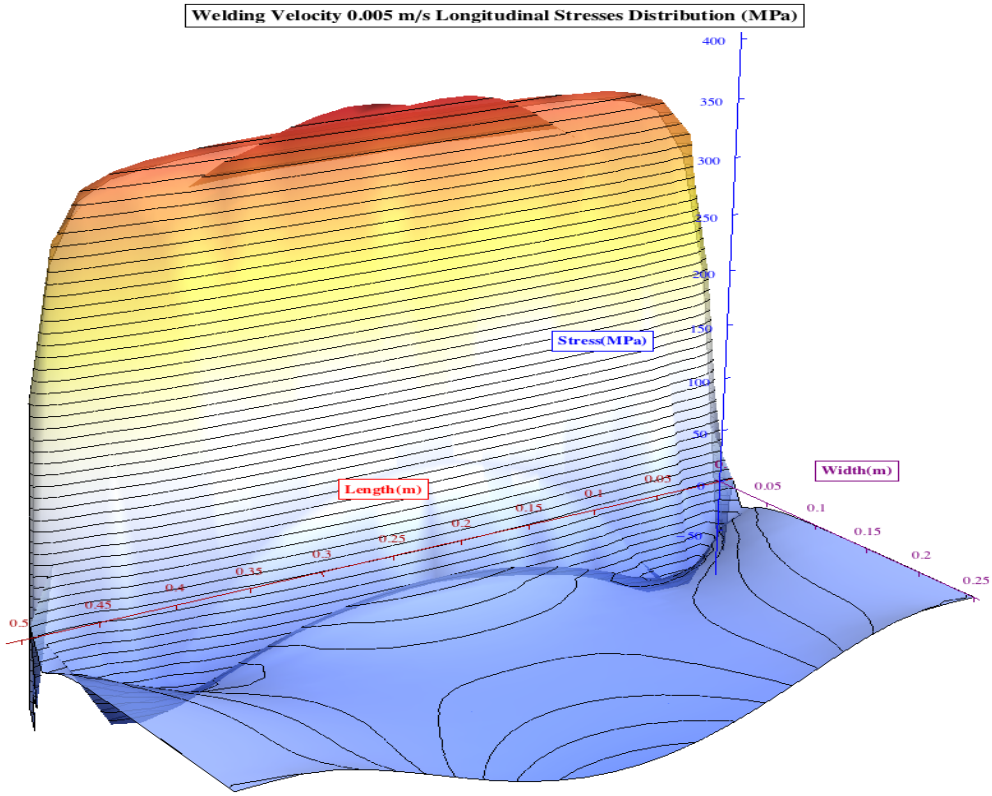
Welding Velocity 0.005 m/s Longitudinal Stresses Distribution (MPa)
Stress(MPa)
Length(m)
Width(m)

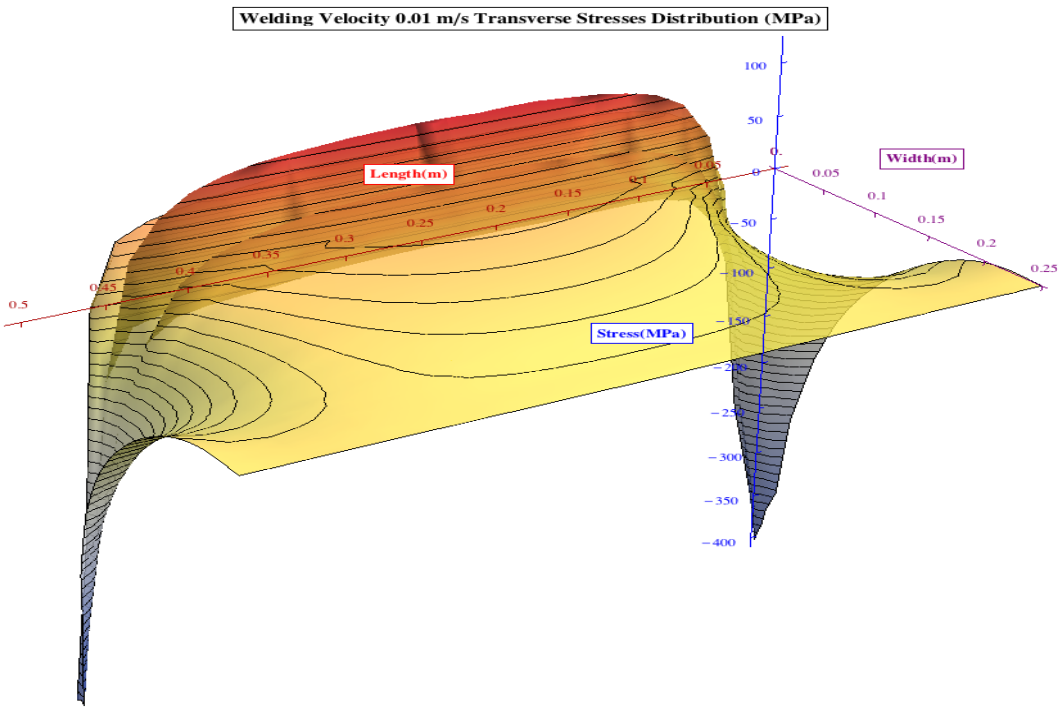
Welding Velocity 0.01 m/s Transverse Stresses Distribution (MPa)
Length(m)
Width(m)
Stress(MPa)

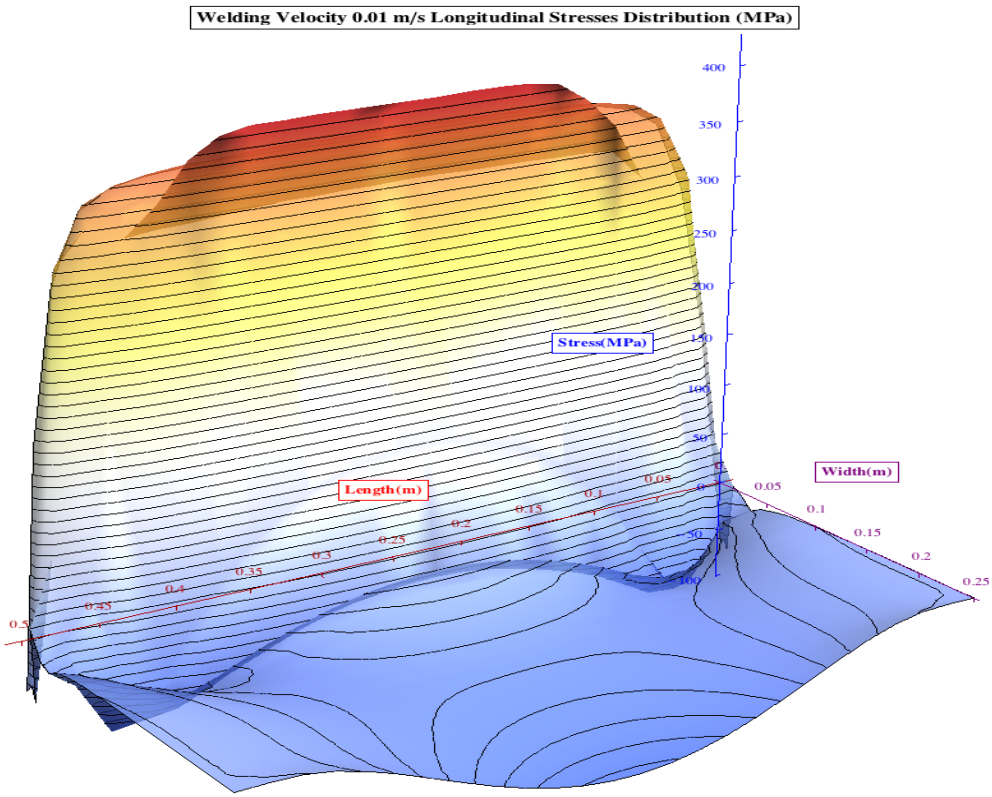
Welding Velocity 0.01 m/s Longitudinal Stresses Distribution (MPa)
Stress(MPa)
Length(m)
Width(m)

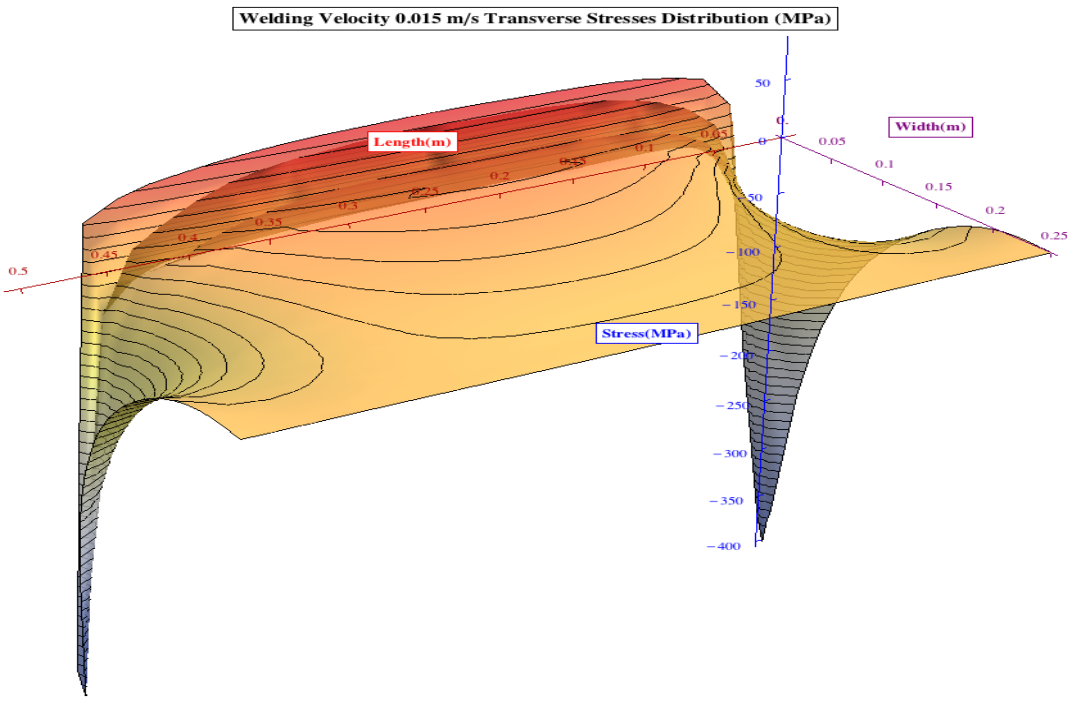
Welding Velocity 0.015 m/s Transverse Stresses Distribution (MPa)
Length(m)
Width(m)
Stress(MPa)
50
0
−50
−100
−150
−200
−250
−300
−350
−400
0.05
0.1
0.15
0.2
0.25
0.5
0.45
0.4
0.35
0.3
0.25
0.2
0.15
0.1
0.05

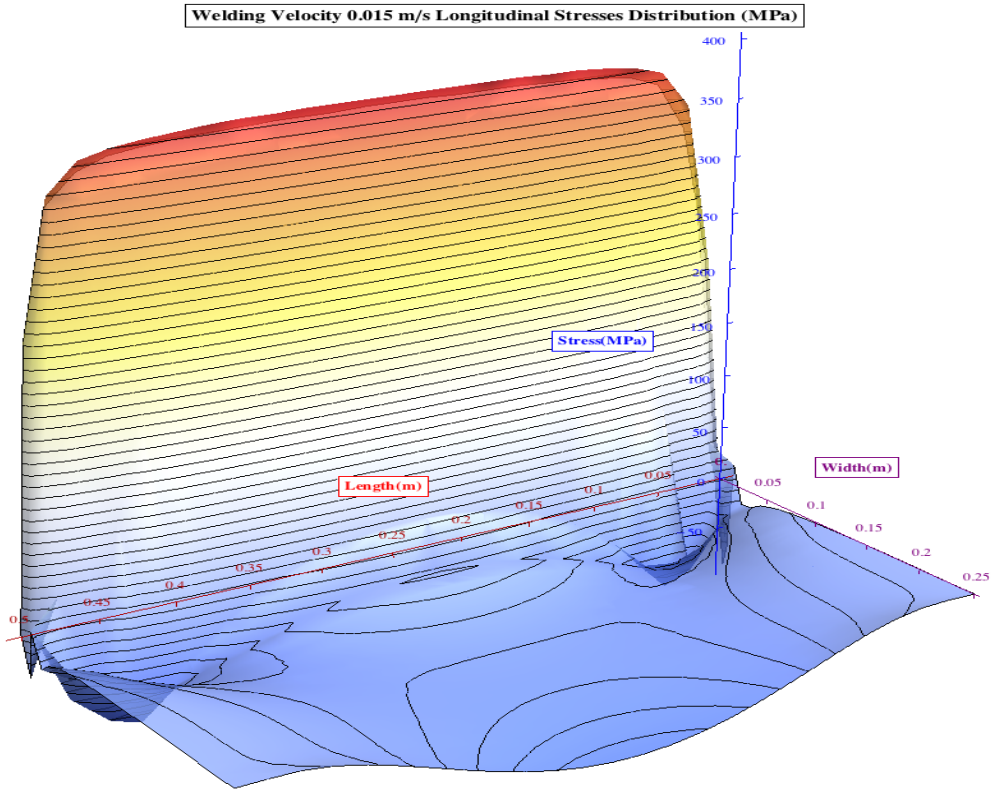
Welding Velocity 0.015 m/s Longitudinal Stresses Distribution (MPa)
Stress(MPa)
Length(m)
Width(m)
400
350
300
250
200
150
100
50
0
0.05
0.1
0.15
0.2
0.25
0.5
0.45
0.4
0.35
0.3
0.25
0.2
0.15
0.1
0.05

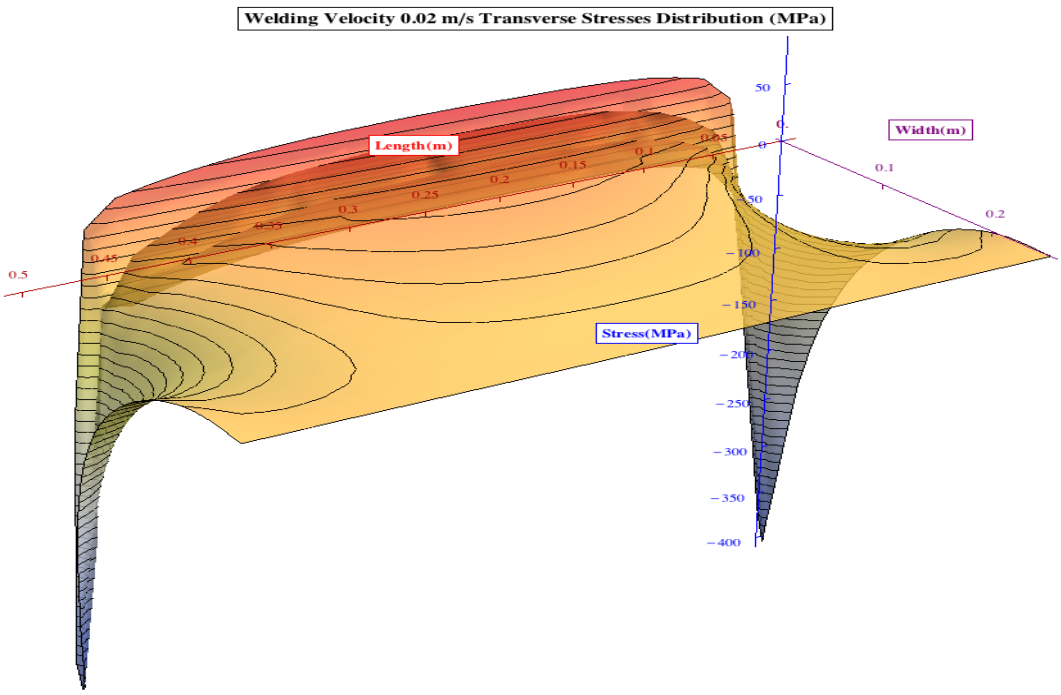
Welding Velocity 0.02 m/s Transverse Stresses Distribution (MPa)
Length(m)
Width(m)
Stress(MPa)
0.5
0.45
0.4
0.35
0.3
0.25
0.2
0.15
0.1
0.05
0
0.1
0.2
50
0
−50
−100
−150
−200
−250
−300
−350
−400

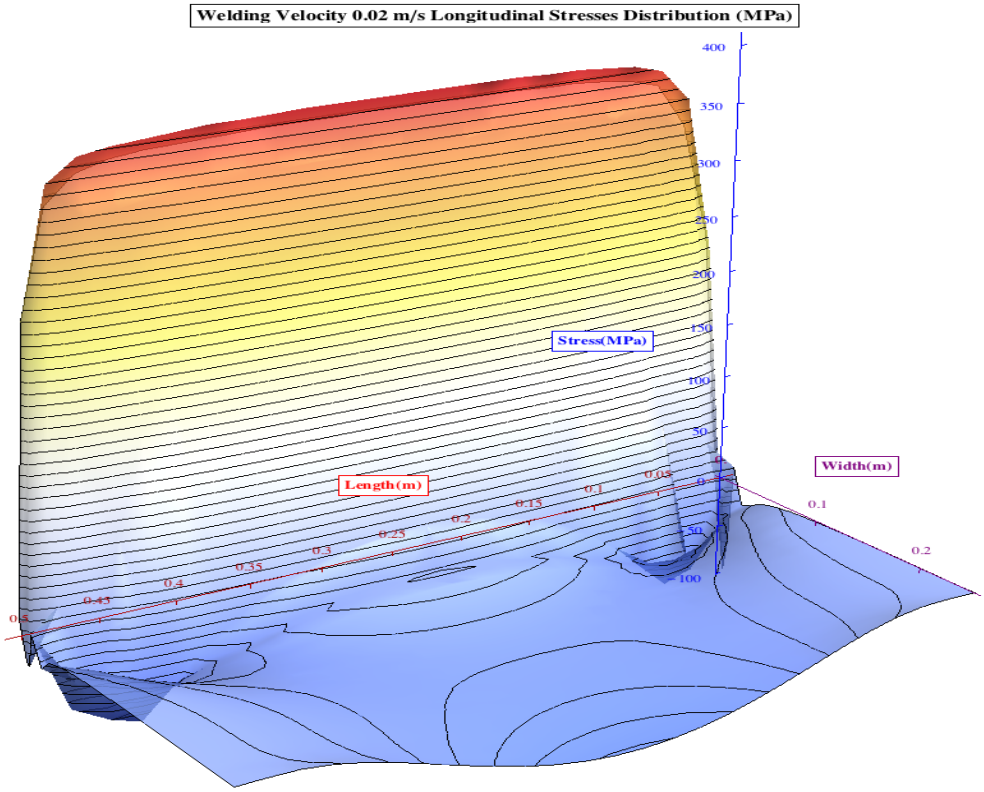
Welding Velocity 0.02 m/s Longitudinal Stresses Distribution (MPa)
Stress(MPa)
Length(m)
Width(m)
400
350
300
250
200
150
100
50
0
0.5
0.43
0.4
0.35
0.3
0.25
0.2
0.15
0.1
0.05
0
0.1
0.2
−50
−100

A2.4 Plate Length Effects

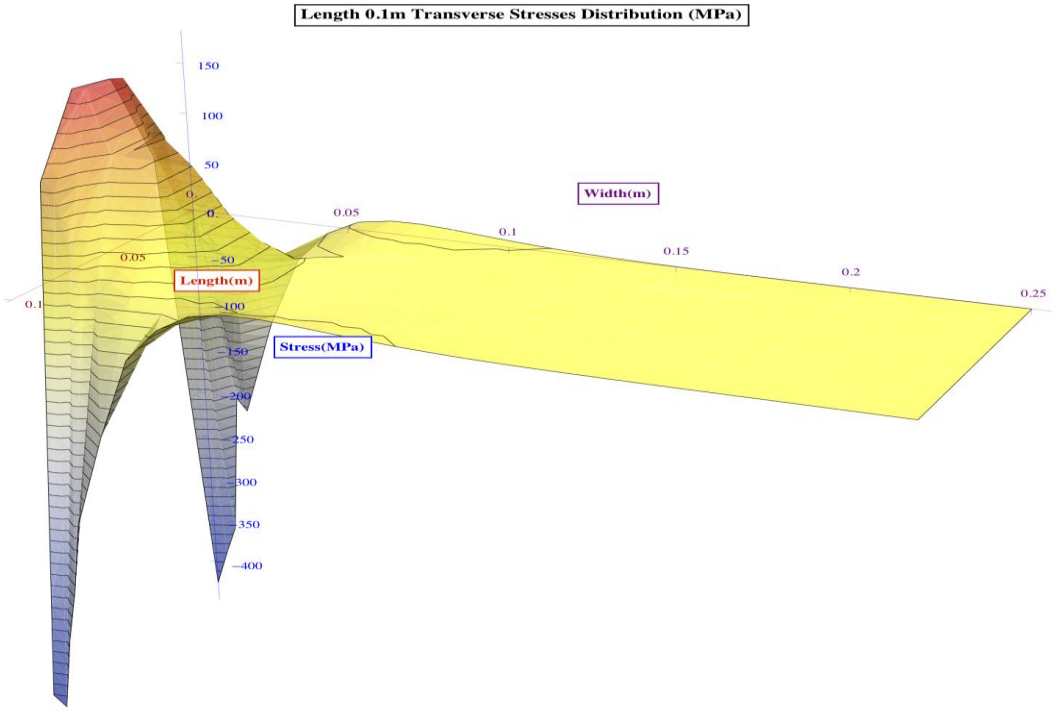

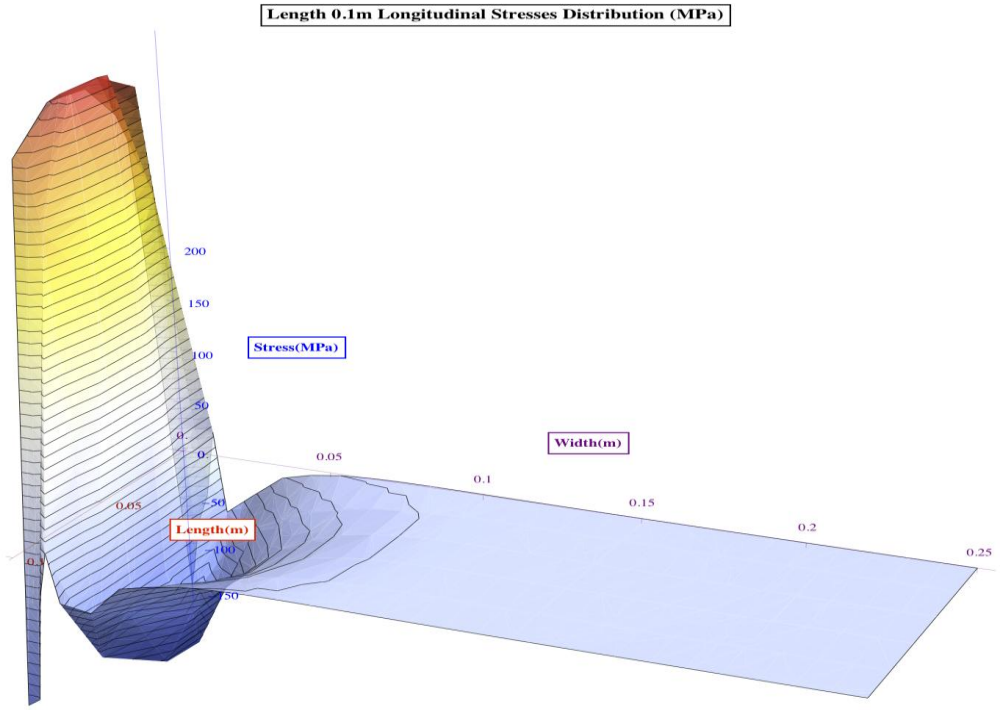

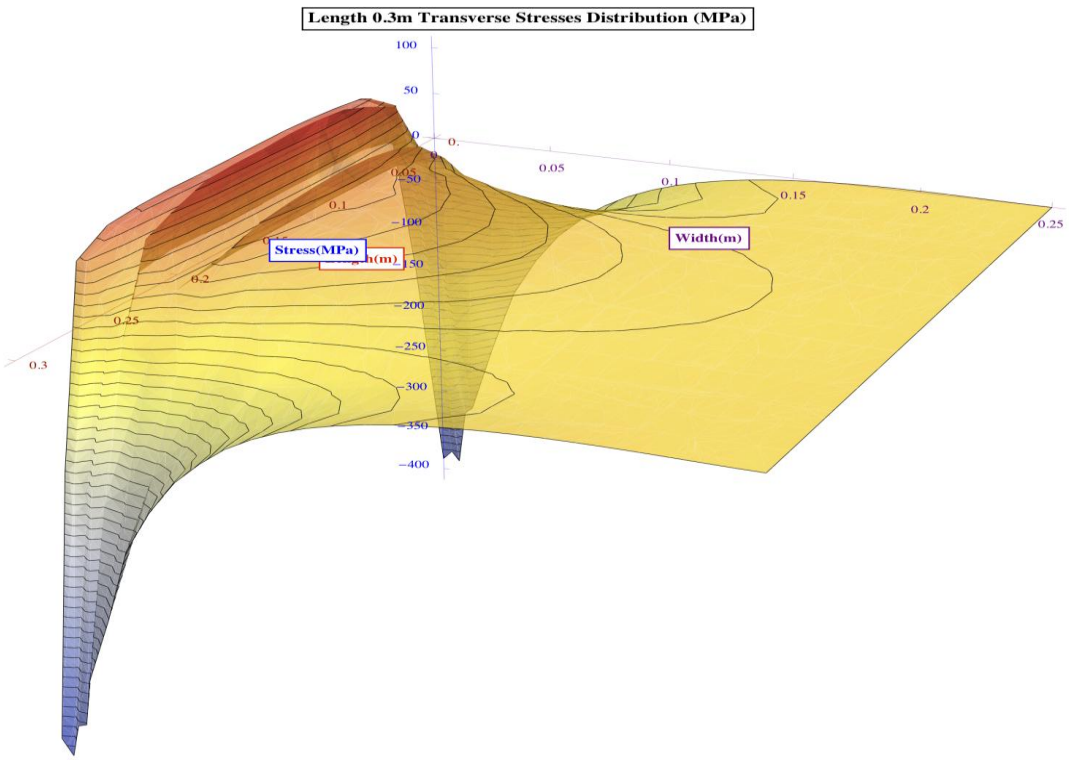
Length 0.3m Transverse Stresses Distribution (MPa)
Stress(MPa)
Width(m)
Length(m)

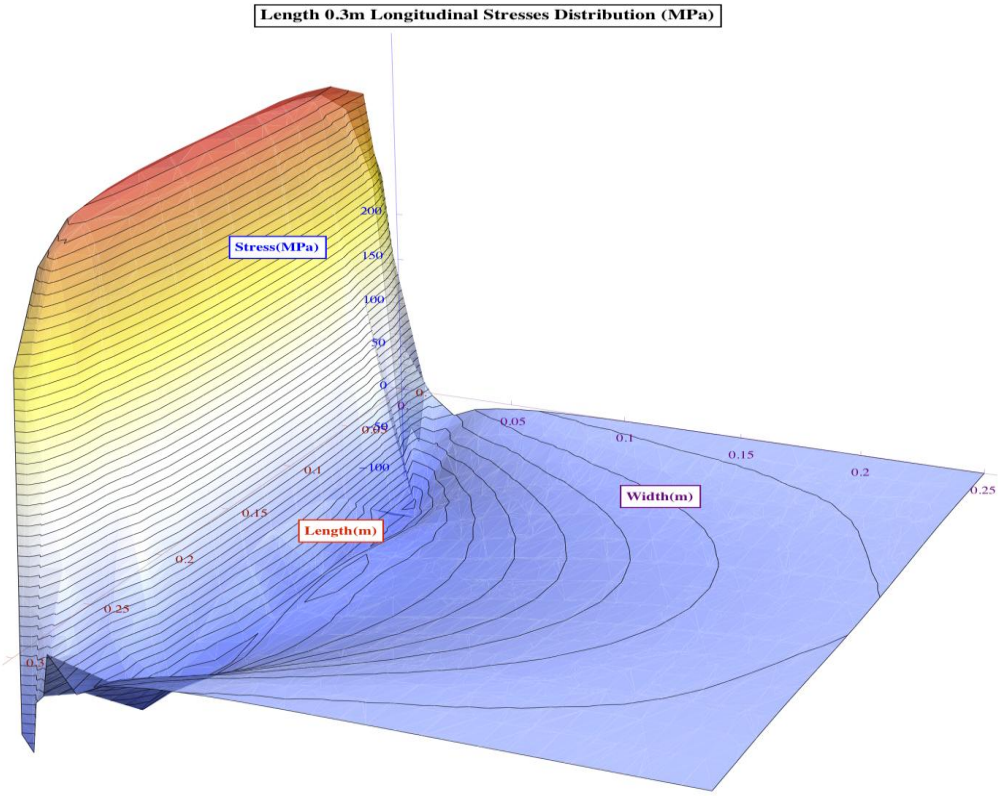
Length 0.3m Longitudinal Stresses Distribution (MPa)
Stress(MPa)
Width(m)
Length(m)

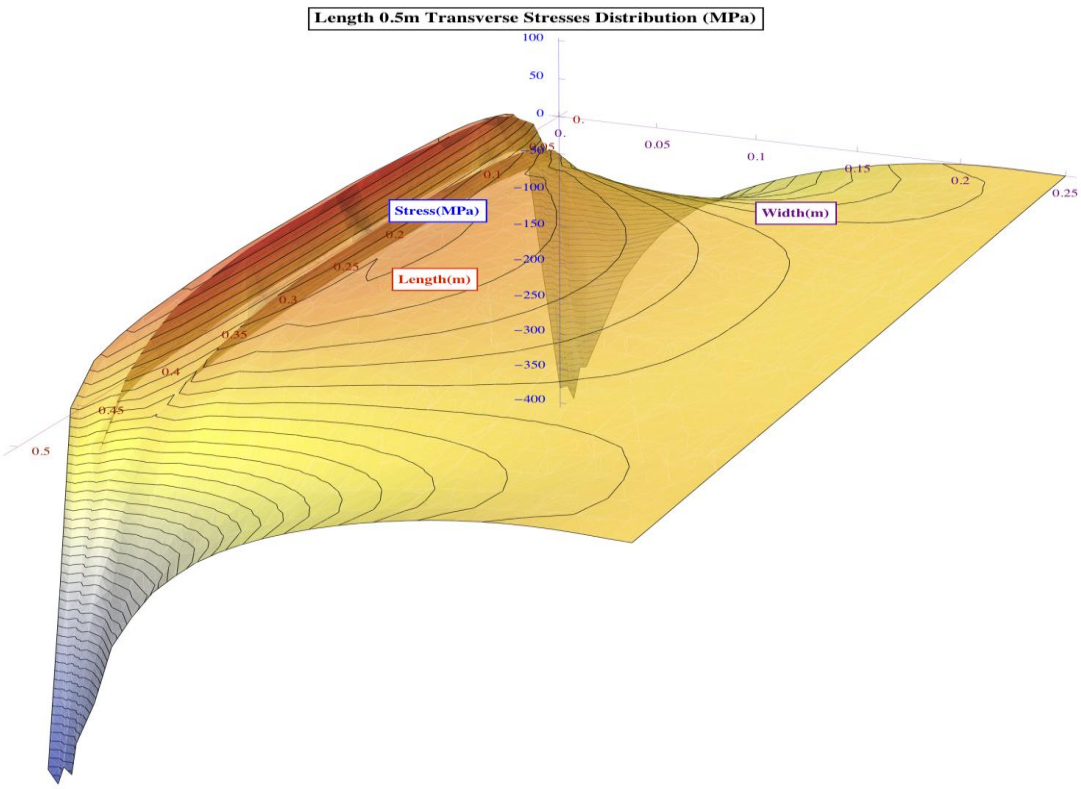
Length 0.5m Transverse Stresses Distribution (MPa)
Stress(MPa)
Width(m)
Length(m)

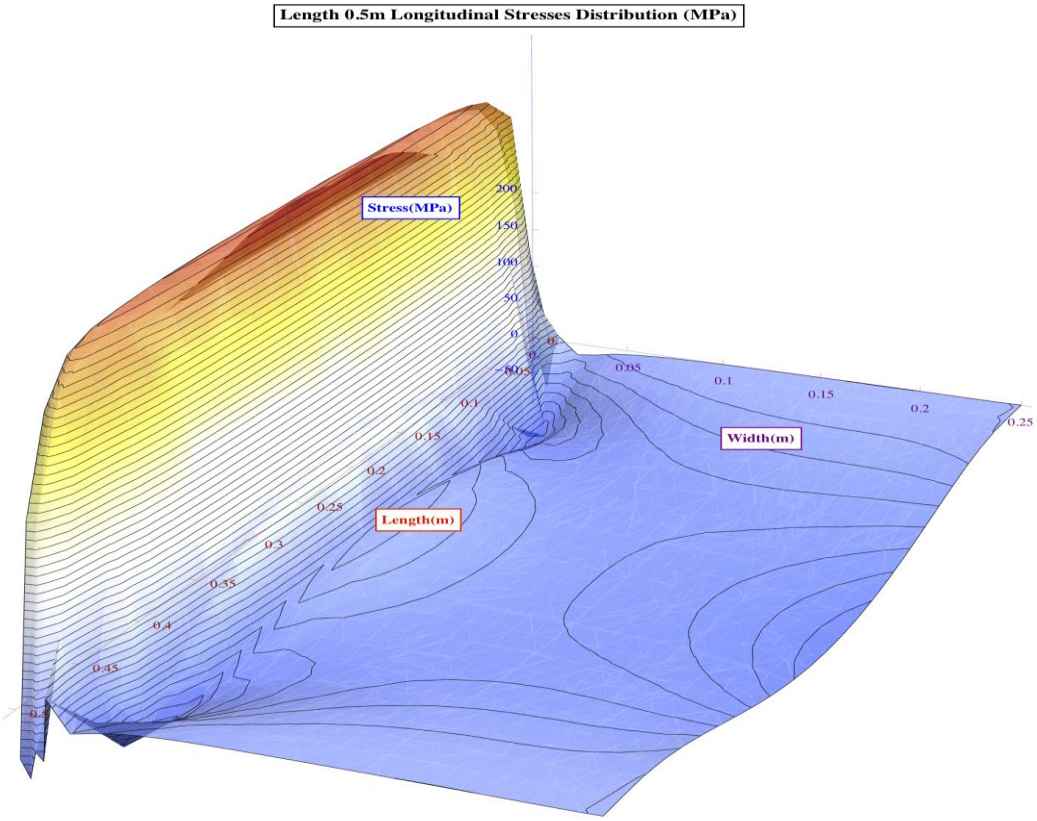
Length 0.5m Longitudinal Stresses Distribution (MPa)
Stress(MPa)
Width(m)
Length(m)

Length 1m Transverse Stresses Distribution (MPa)

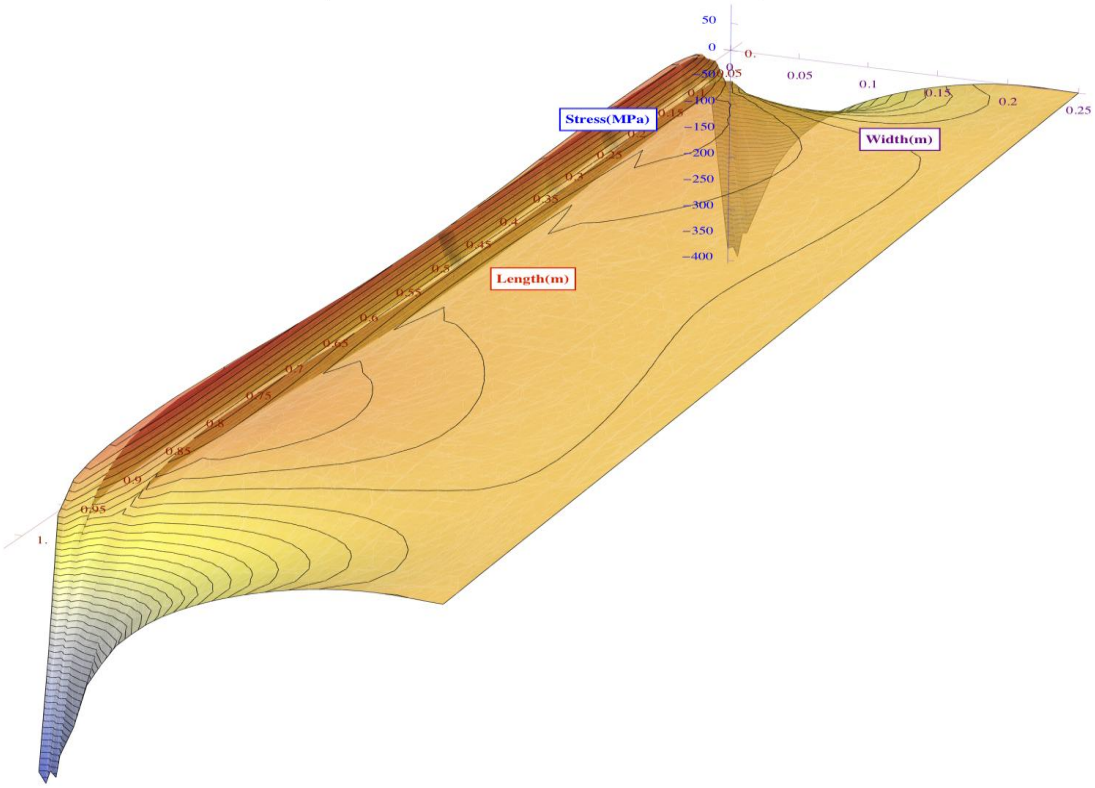

Length 1m Longitudinal Stresses Distribution (MPa)

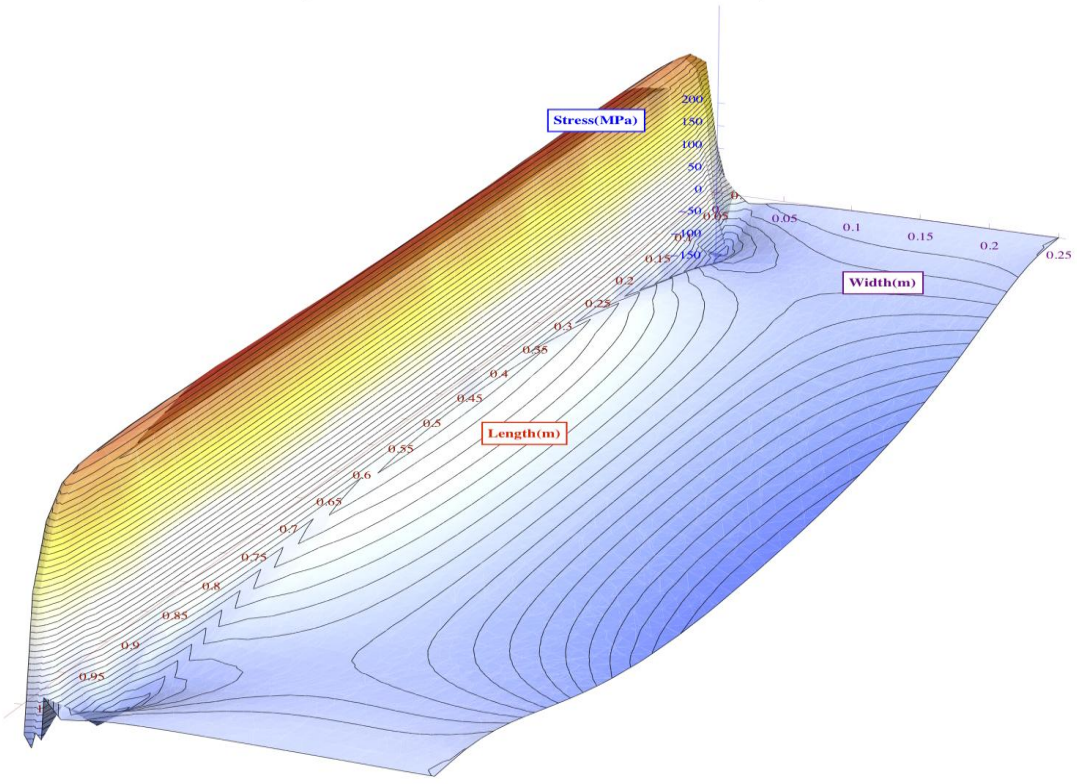

Length 1.5m Transverse Stresses Distribution (MPa)

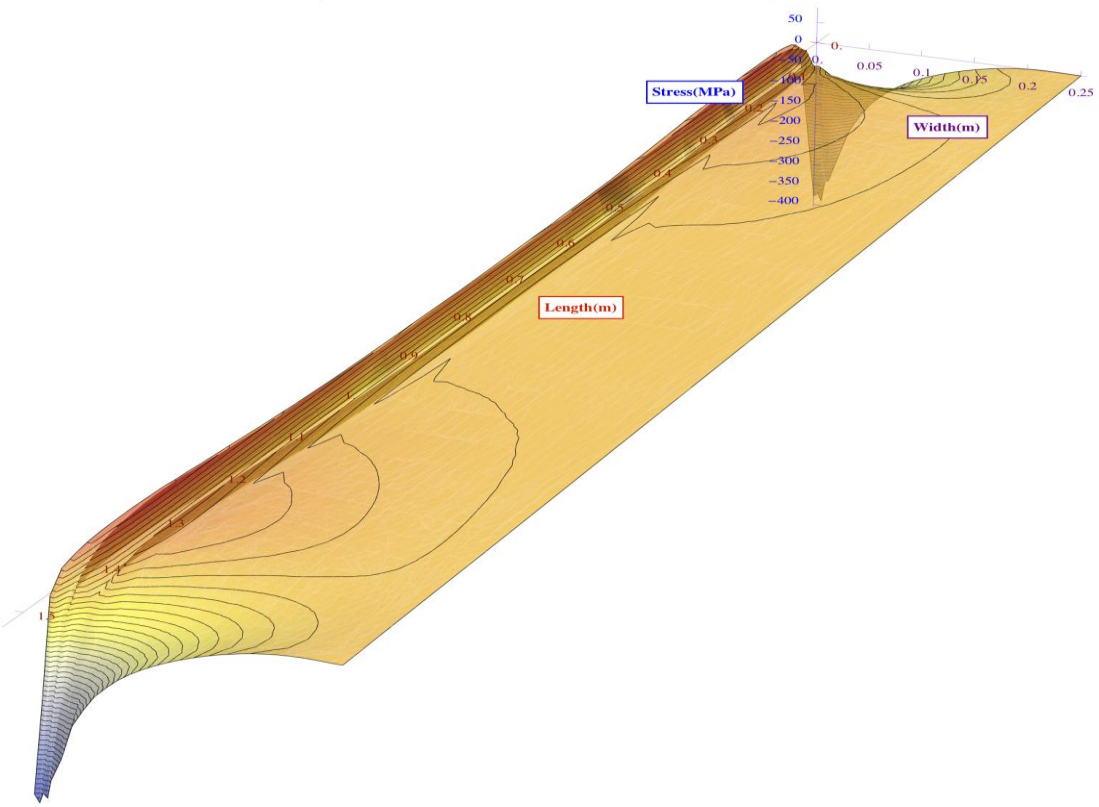

Length 1.5m Longitudinal Stresses Distribution (MPa)

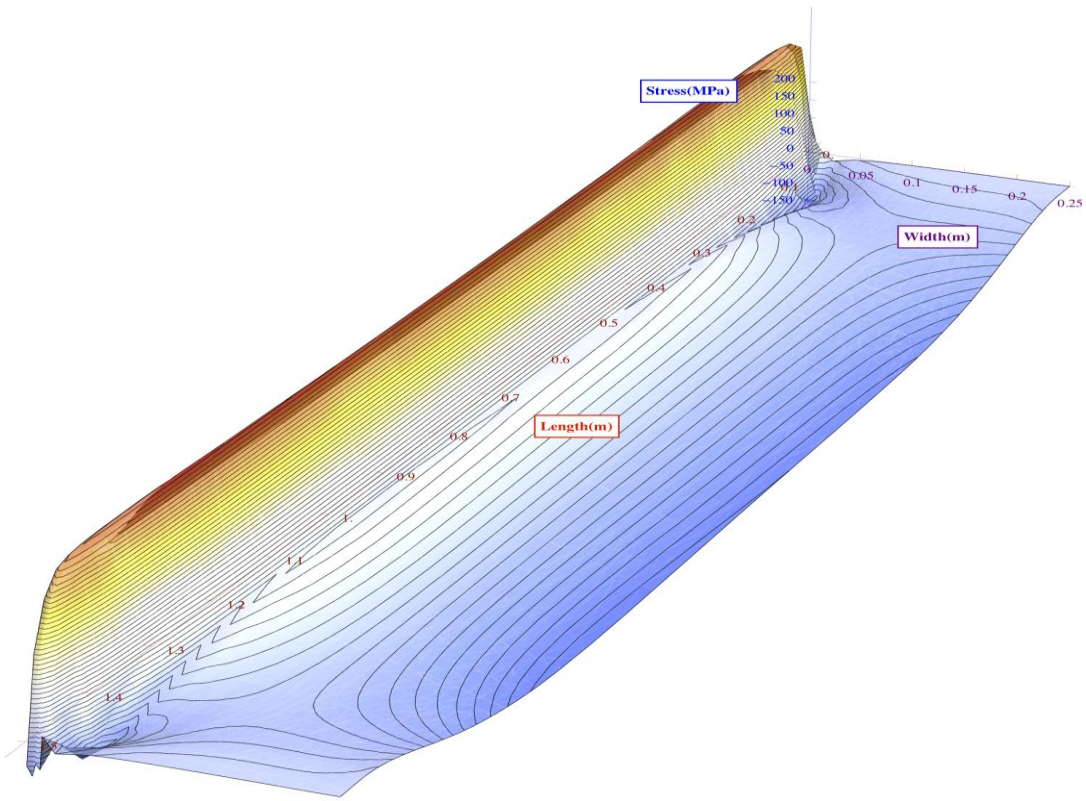

Length 2m Transverse Stresses Distribution (MPa)

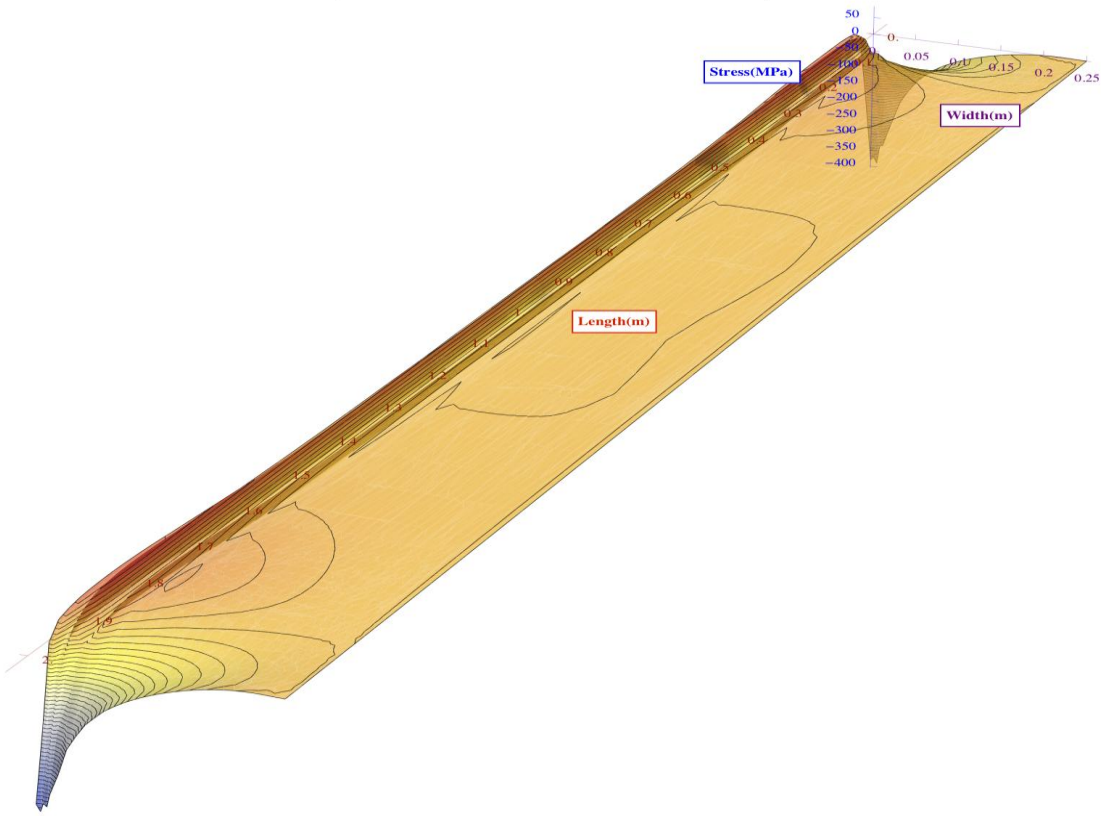

Length 2m Longitudinal Stresses Distribution (MPa)

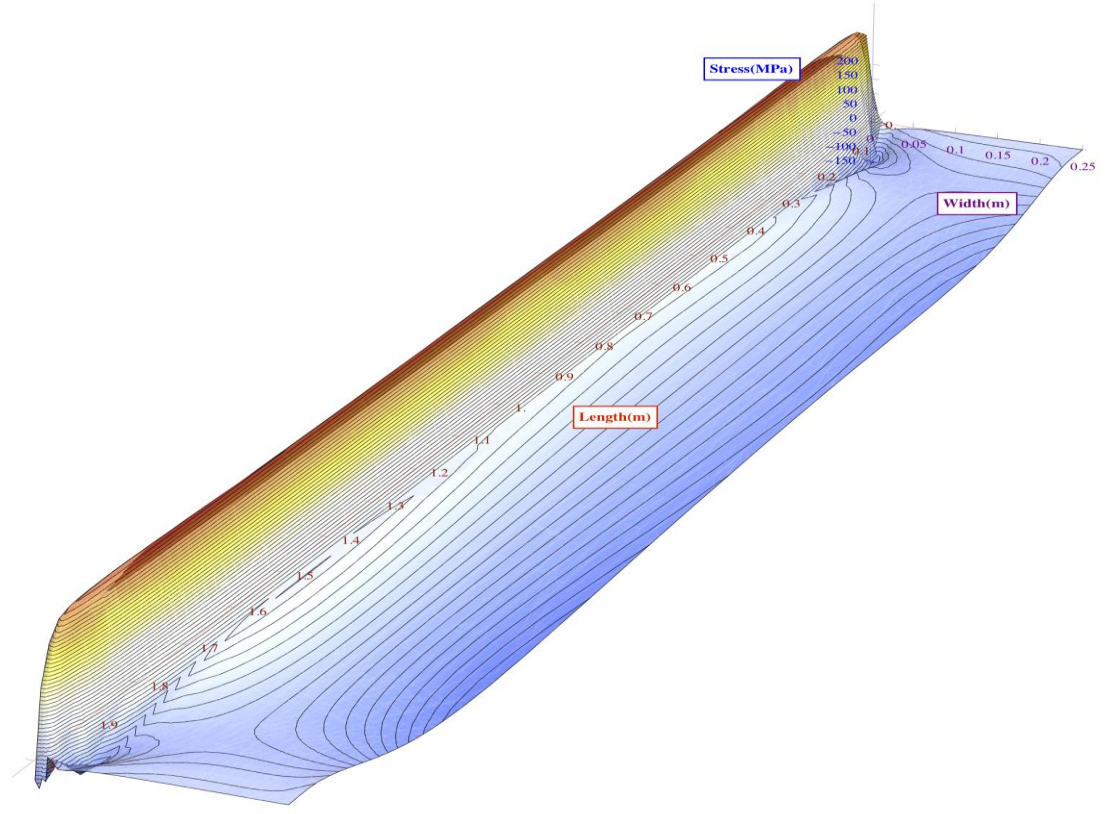

Length 3m Transverse Stresses Distribution (MPa)

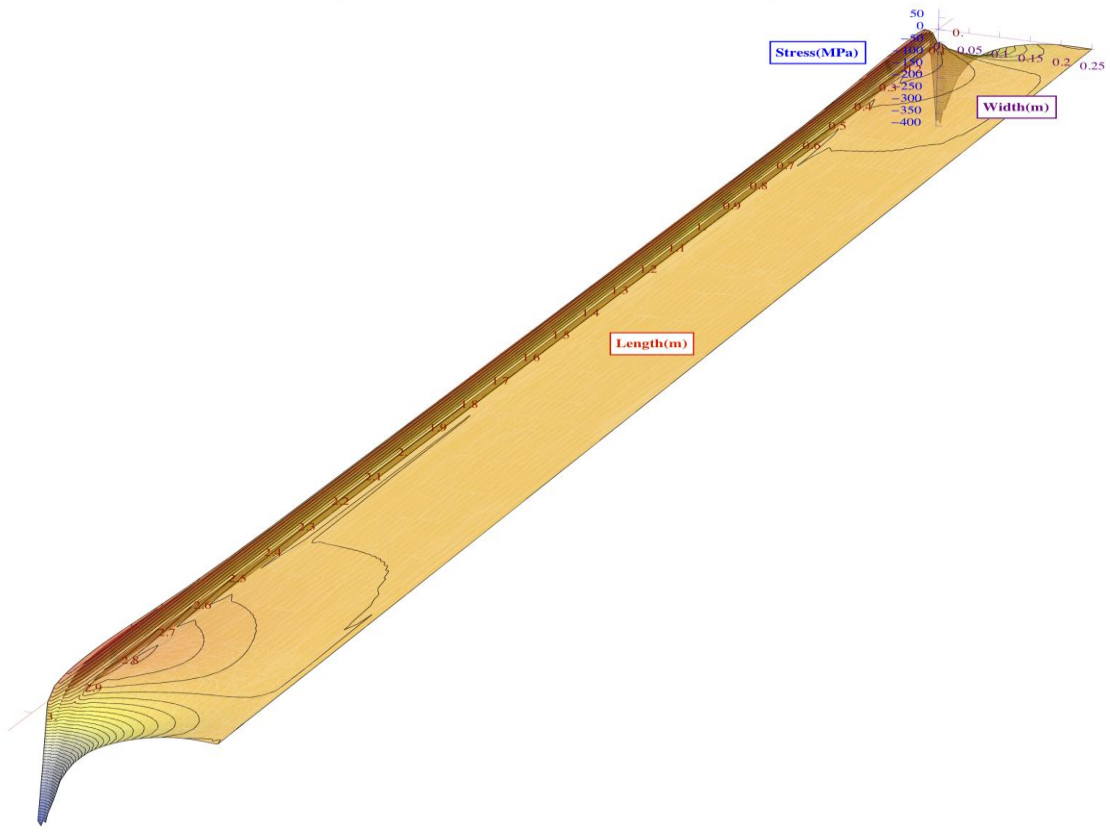

Length 3m Longitudinal Stresses Distribution (MPa)

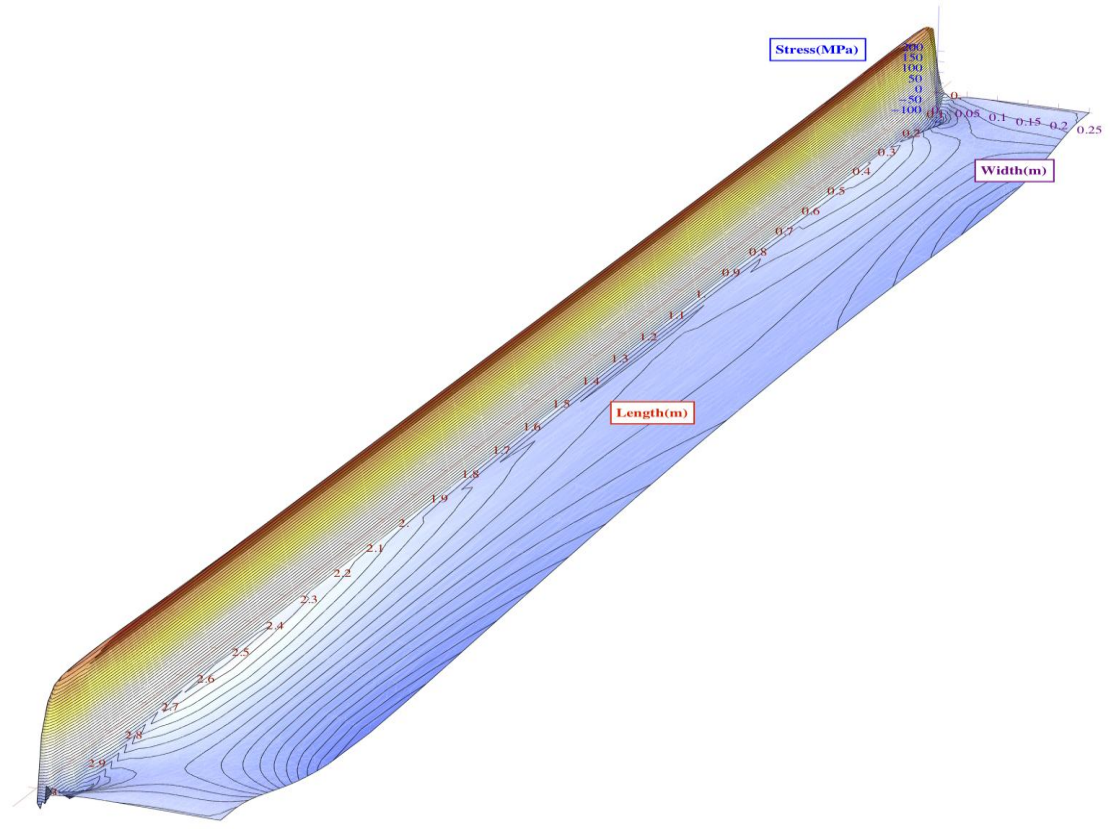

A2.5 Plate Width Effects

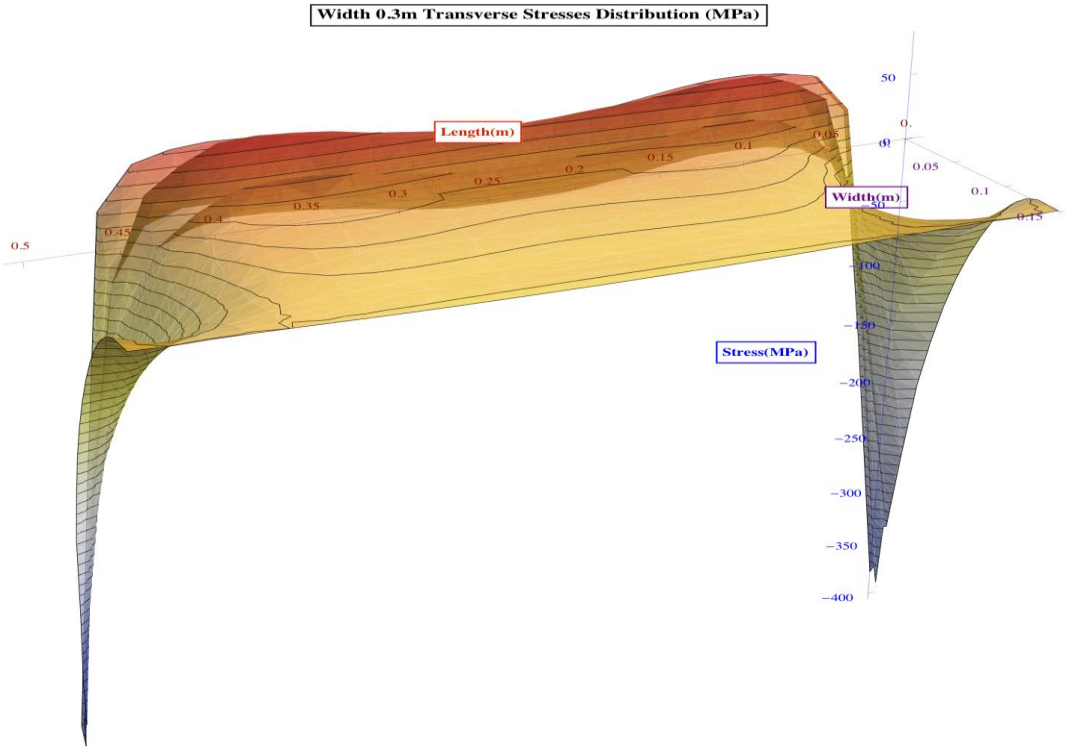

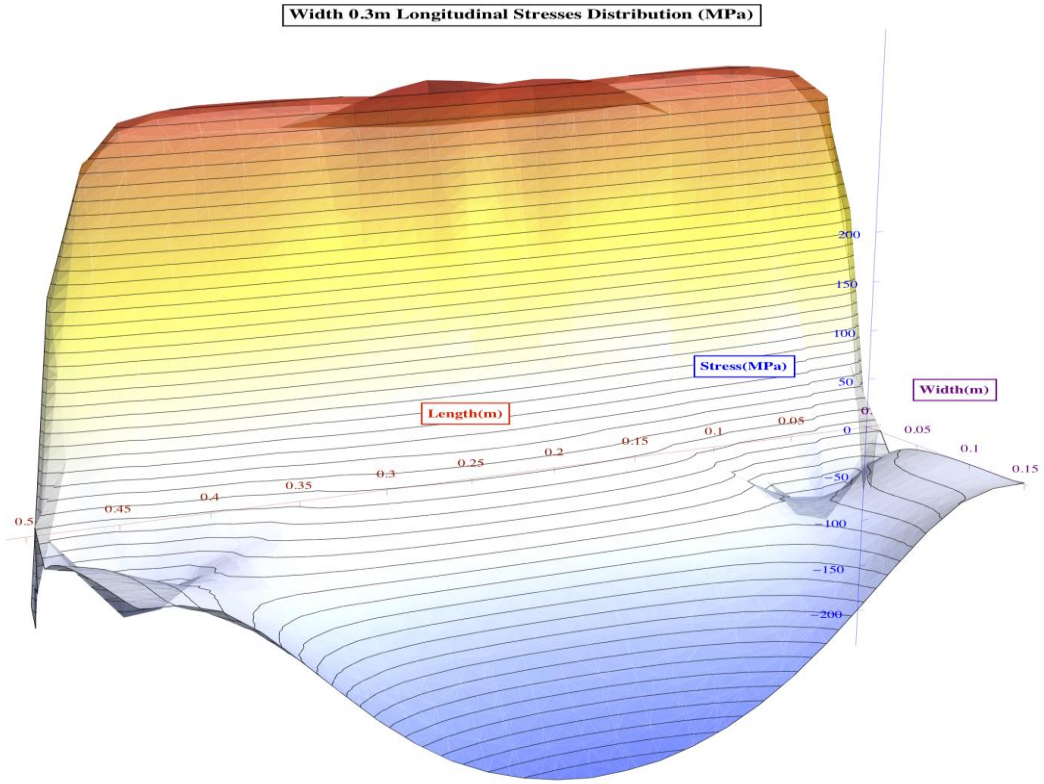

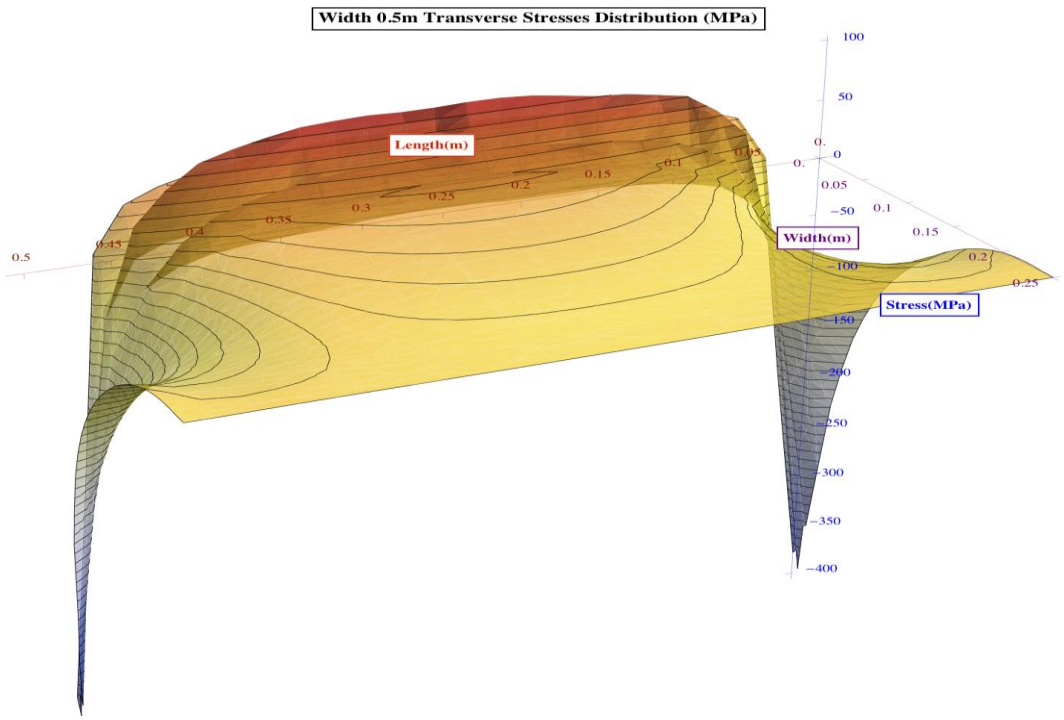
Width 0.5m Transverse Stresses Distribution (MPa)
Length(m)
Width(m)
Stress(MPa)

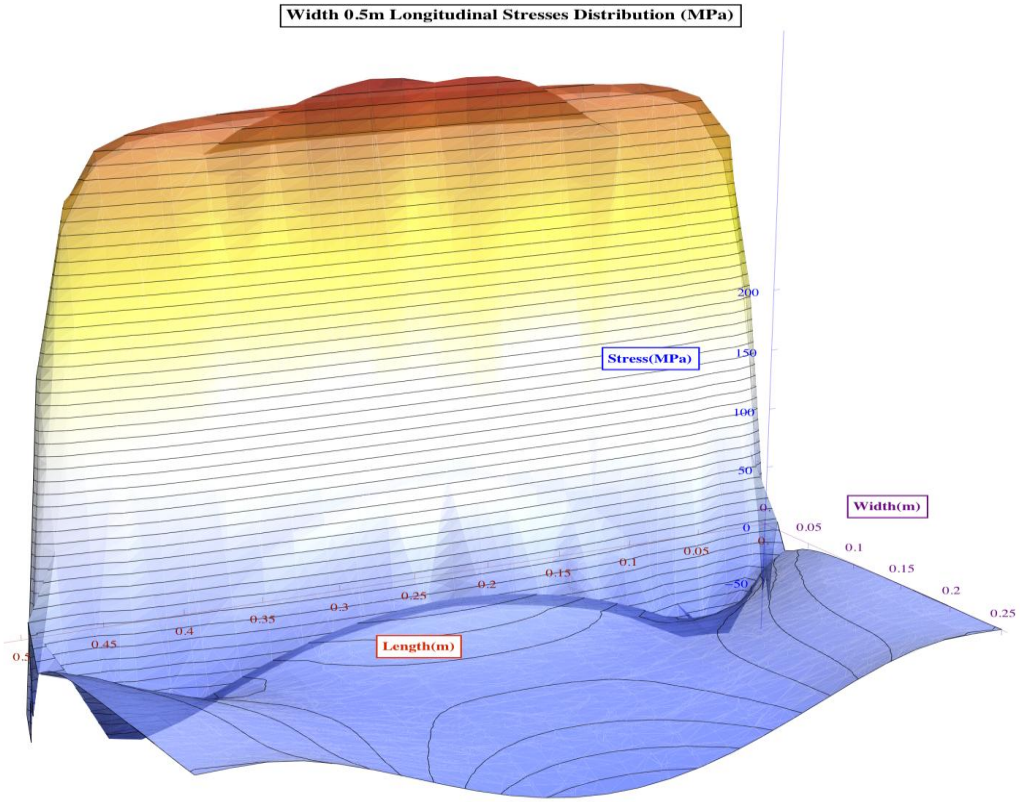
Width 0.5m Longitudinal Stresses Distribution (MPa)
Stress(MPa)
Width(m)
Length(m)

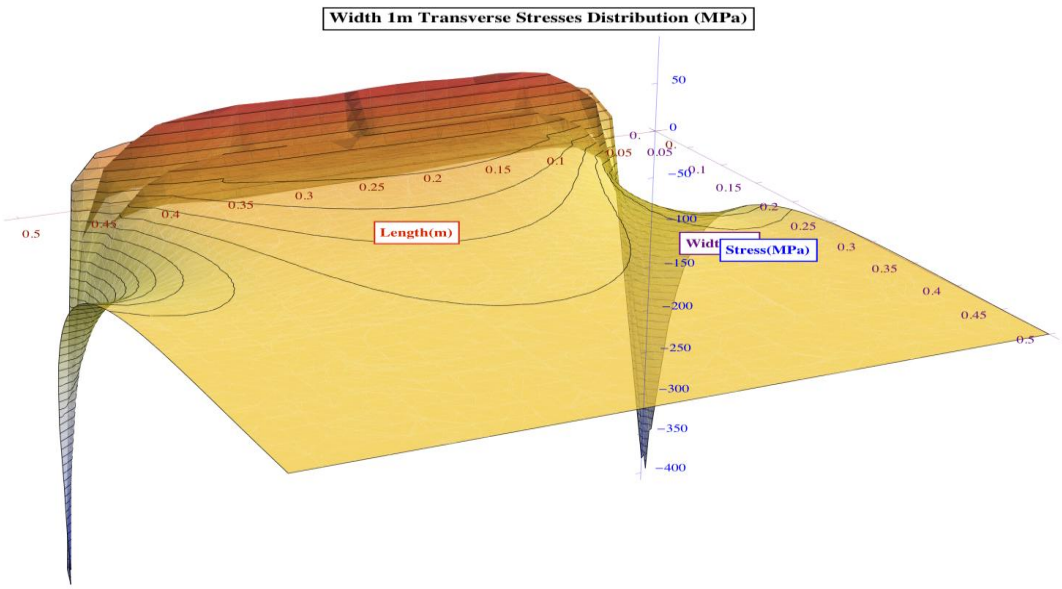
Width 1m Transverse Stresses Distribution (MPa)
Length(m)
Stress(MPa)

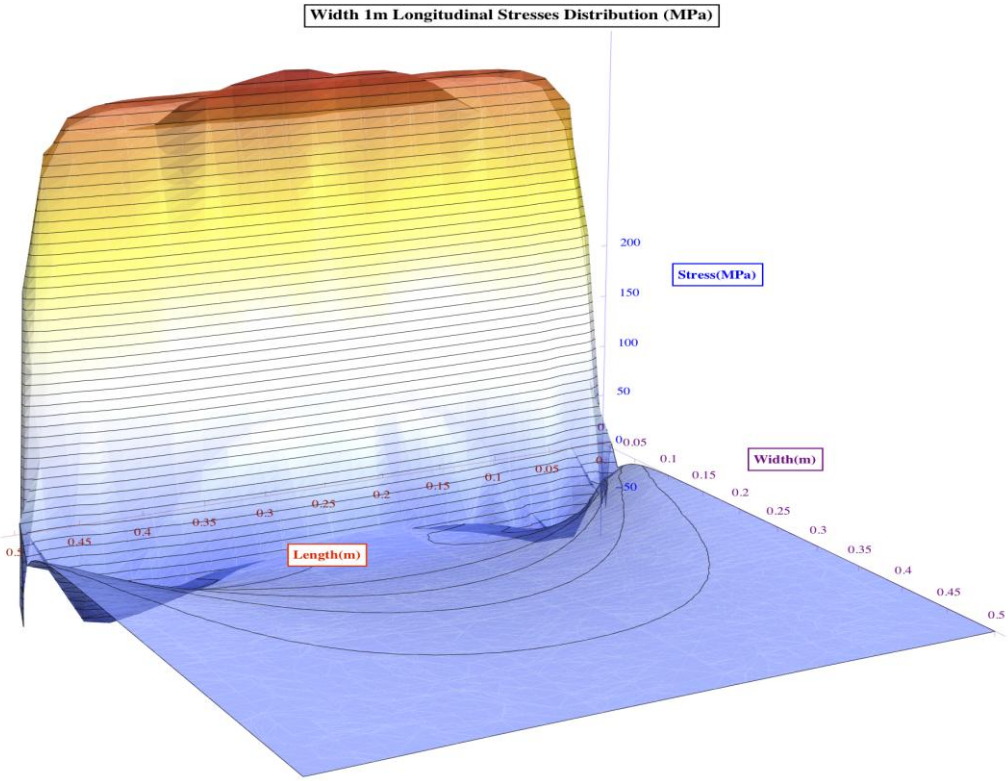
Width 1m Longitudinal Stresses Distribution (MPa)
Stress(MPa)
Width(m)
Length(m)

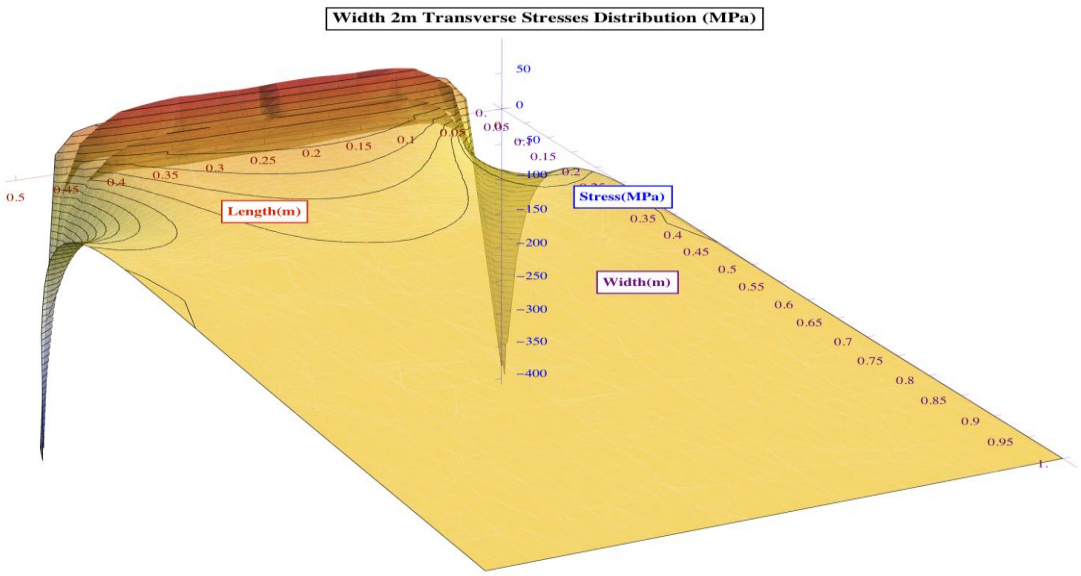
Width 2m Transverse Stresses Distribution (MPa)
Length(m)
Stress(MPa)
Width(m)

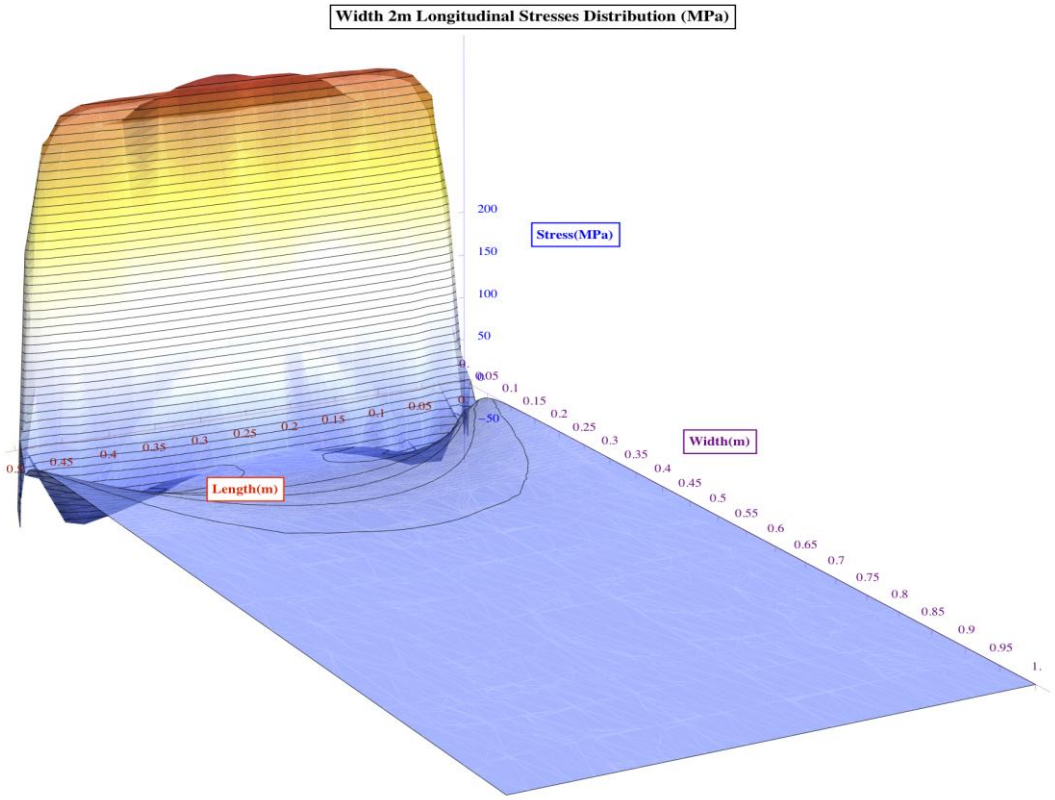
Width 2m Longitudinal Stresses Distribution (MPa)
Length(m)
Stress(MPa)
Width(m)

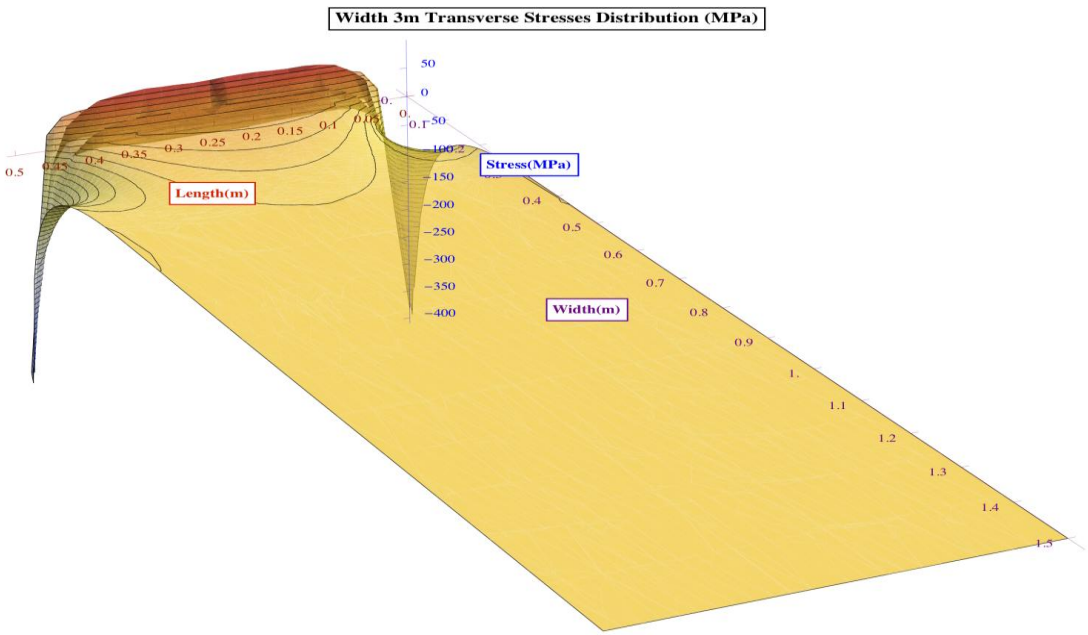
Width 3m Transverse Stresses Distribution (MPa)
Stress(MPa)
Length(m)
Width(m)

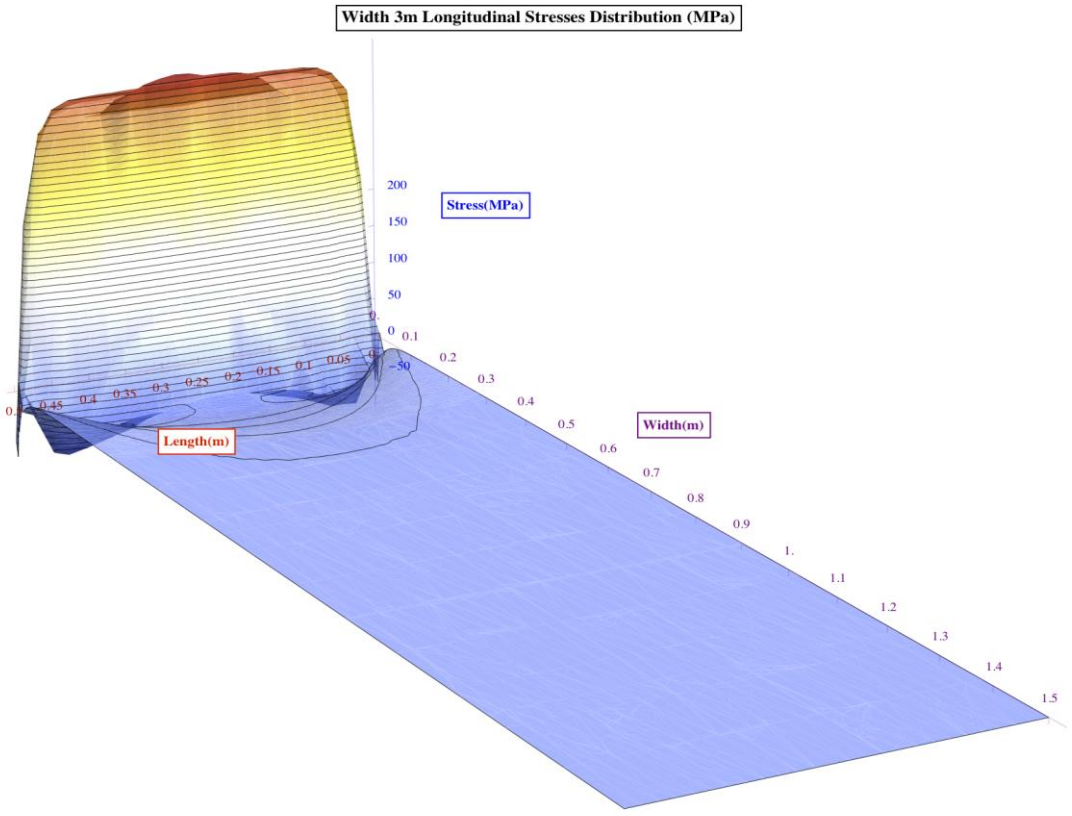
Width 3m Longitudinal Stresses Distribution (MPa)
Stress(MPa)
Length(m)
Width(m)